RADIATION DAMAGE EFFECTS ON X-RAY DETECTORS FOR FUTURE PLANETARY AND ASTRONOMY MISSIONS

Craig Brown

May 18th 2010

Thesis submitted to the University of Leicester

for the degree of Doctor of Philosophy.

University of Leicester

Space Research Centre
Department of Physics and Astronomy
University of Leicester
UK.

ABSTRACT

This thesis describes both theoretical and experimental work conducted to further develop X-ray instrumentation for future planetary and astronomy space missions. Such instruments are used to probe, ever deeper, the high energy Universe; from black holes and active galactic nuclei, to supernovae, galaxy formation and clusters. X-rays can also be used to establish the elemental composition of planetary surfaces from orbit or in situ, furthering our understanding of planetary and moon formation in our solar system.

Chapter 1 introduces X-ray instrumentation and uses the International X-ray Observatory as a case study to explore the many new developments in X-ray instrumentation, both in optics and detectors.

Chapter 2 further explores the field of X-ray optics, particularly the novel Microchannel Plate Optics used on the BepiColombo Mercury Imaging X-ray Spectrometer, MIXS. The characterisation of an MCP optic is presented, demonstrating the best angular resolution measurement of a flat square-pore square-packed Microchannel Plate Optic to date; <2 arcminutes FWHM resolution.

Chapter 3 moves from the X-ray optics used on BepiColombo MIXS to the detectors used in the instrument focal plane; Active Pixel Sensor Depleted Field Effect Transistors (DEPFETs). The solar proton radiation environment around Mercury is one of the most damaging in the solar system due to its proximity to the sun, with ~$3x10^{10}$ 10 MeV equivalent solar protons expected over the mission lifetime. This Chapter presents the proton radiation damage experiments conducted at the Birmingham University Cyclotron, establishing the current related damage rate, α, and dark current increase that can be expected from this radiation damage. The design of the MIXS instrument was changed to include an annealing capability based on the findings of the experiment presented here. A follow-up proton irradiation experiment carried out at the University of Technology in Munich, in collaboration with the Max Planck Institute's Semiconductor Laboratory (MPE-HLL) is also discussed.

Chapters 4 and 5 present the experimental and modelling work carried out in the investigation of X-ray CCDs which, to date, have been the X-ray detectors of choice for many space and terrestrial applications. The aim of this work was to improve the quantum efficiency and spectral resolution of the CCD66, a novel CCD structure initially designed with applications such as the Wide Field Imager of the International X-ray Observatory in mind, by direct manipulation of the device depletion region by applying a negative substrate voltage. Modelling work was also undertaken to investigate the effect of X-ray angle of incidence on spectral resolution and quantum efficiency.

The future of X-ray astronomy and planetary science depends heavily on advances in optics and detector technology. The work presented in this thesis show incremental, yet mission-enabling developments for X-ray instruments likely to fly in the future such as BepiColombo's Mercury Imaging X-ray Spectrometer.

DECLARATION

I hereby declare that no part of this thesis has previously been submitted to this or any other university as part of the requirement for a higher degree. The work described herein was conducted solely by the undersigned except for those colleagues and other workers acknowledged in the text.

Craig Brown

May 18th 2010

For Mam and Nan

My motivation

ACKNOWLEDGEMENTS

There are a number of people who must be acknowledged for their much-appreciated support during my PhD studies over the last five (!) years. This is made tricky by the fact that there are so many people to thank, so profound apologies to anyone who I've missed and feel they should have been included... and also made more difficult to write due to a distinct lack of synonyms for the words 'thank' and 'friendship'.

Firstly, my appreciation goes to my supervisors, Dr Richard Ambrosi and Professor George Fraser. Your patience and guidance have been invaluable. Also, Tony Abbey: your friendship, experience and assistance more than compensated for your lack of patience! I would also like to thank the following people for their support and camaraderie: Jim Pearson, John Lees, Dave Vernon, Chris Whitford, Gillian Butcher, James Carpenter, Alan Hewitt and Dave Bassford.

Great thanks must also go to Helen Yates for her collaboration in the Microchannel Plate Optics work, as well as her friendship over the course of the PhD. I must also give my appreciation to Dr Johannes Treis from the Max Planck Institute for his assistance with my DEPFET Detector work. More thanks need to go to Graeme Hansford and Olivier Godet for their assistance with the CCD modelling work and their invaluable advice. There are many others, too numerous to name, who have helped me in the research contained within this thesis, for all of which I am very grateful.

I must also acknowledge Tone Peacock, for without whose European Space Agency funding in my first 3 years, this PhD would not have been possible! Thanks also to Alan Owens for his encouragement. I also really appreciate the support I received from my colleagues at Astrium: Thanks to Paolo, Marie-Claire, Lisa, Liz, Mick, Matthew, and Ronan, to name but a few.

And finally, there are three people who I must thank in particular, for without them and the motivation they have provided, this thesis would never have been completed. First and foremost, to Matt. You've been there throughout and without you I'm sure I'd have lost the way. Thank you for putting up with the inevitable stress and moodiness that comes as standard with the final stretch of any thesis. Also to my mother for being the main driving force behind my academic and career aspirations. And finally to my Nan. Your friendship, support, encouragement and pride in what I am doing have ensured that I've finally submitted!

Thanks again to all.

PUBLICATIONS RELATING TO THIS THESIS

Craig Brown, Richard M. Ambrosi, Tony Abbey, Olivier Godet, R. O'Brien, M. J. L. Turner, Andrew Holland, Peter Pool, David Burt, David Vernon. "**Improving Quantum Efficiency and Spectral Resolution of a CCD through Direct Manipulation of the Depletion Region**", Proc. SPIE. Vol. 7011, 70113Z (2008)

G. Segneri, C. Brown, J.D. Carpenter, B. Kuhnle, T. Lauf, P. Lechner, G. Lutz, S. Rummel, L. Struder, J. Treis, C. Whitford, "**Measurement of the Current Related Damage Rate at -50°C and Consequences on Macropixel Detector Operation in Space Experiments'**, IEEE Transactions on Nuclear Science, Vol. 56, Issue 6, Pages 3734-3742 (2009)

G.W. Fraser, J.D. Carpenter[a], D.A. Rothery, J.F. Pearson, A. Martindale, J. Huovelin, J. Treis, M. Anand, M. Anttila, M. Ashcroft, J. Benkoff, P. Bland, A. Bowyer, A. Bradley, J. Bridges, C. Brown, C. Bulloch, E.J. Bunce, U. Christensen, M. Evans, R. Fairbend, M. Feasey, F. Giannini, S. Hermann, M. Hesse, M. Hilchenbach, T. Jorden, K. Joy, M. Kaipiainen, I. Kitchingman, P. Lechner, G. Lutz, A. Malkki, K. Muinonen, J. Näränen, P. Portin, M. Prydderch, J. San Juan, E. Sclater, E. Schyns, T.J. Stevenson, L. Strüder, M. Syrjasuo, D. Talboys, P. Thomas, C. Whitford and S. Whitehead. "**The Mercury Imaging X-ray Spectrometer (MIXS) on BepiColombo**", Planetary and Space Science, Vol. 58, Issues 1-2, January 2010, Pages 79-95.

A. Martindale, H. Yates, C. Brown, J.S Lapington, J.F Pearson, J.E. Lees, R. Fairbend, E. Shyns, N.P. Bannister, J.D. Carpenter, G.W. Fraser, "**Improved Imaging Resolution of Square Pore, Square Packed Microchannel plate X-ray Optics**", Nuclear Instruments and Methods in Physics Research A (2010) In prep.

CONTENTS

Abstract		**2**
Declaration		**3**
Acknowledgements		**5**
Publications Relating to This Thesis		**6**
Contents		**7**
List of Figures and Tables		**11**
Executive Summary		**18**
Introduction		**22**
1.1	X-rays in Astronomy and Planetary Science	22
1.2	X-ray Generation	25
1.3	X-ray Focusing	29
1.4	Radiation Damage	34
1.4.1	Atomic Displacement	34
1.4.2	Majority and Minority Carrier Transport Degradation	35
1.5	The International X-ray Observatory	40
1.6	The Subject of this Thesis	40
1.7	Thesis Structure	43
Chapter 2	**Proton Irradiation and Analysis of MIXS Representative Silicon Diodes**	**45**
2.1	The BepiColombo Mission and Radiation Concerns	45
2.1.1	The Current Related Damage Rate	47
2.1.2	Thermal Annealing	48

2.2	MIXS Proton Irradiation Experiment	48
2.2.1	The Mercury Proton Radiation Environment	49
2.2.2	Test Aims	51
2.2.3	The DEPFET Detector	52
2.2.4	DEPFET Diode Samples	53
2.2.5	Pre-Irradiation Tests	56
2.2.6	The Proton Irradiation	59
2.2.7	Radiochromic Film Calibration	64
2.2.8	Proton Irradiation Experiment Results	69
2.2.9	Discussion	74
2.3	The MPI-HLL MIXS Diode Test	79
2.4	Conclusions	81
Chapter 3	**The XMM-Newton Life Test**	**83**
3.1	The XMM-Newton Life Test	83
3.2	XMM-Newton and the EPIC MOS Camera	83
3.3	Background to the XMM-Newton Life Test	85
3.4	Experimental Set-up	90
3.5	The Experiment	92
3.5.1	Test Aims	92
3.5.2	Pre-Irradiation Tests	92
3.5.3	X-ray Irradiation	94
3.5.4	Life Test Damage Analysis	98
3.6	XMM-Life Test Future Work	105

3.7	Summary	105
Chapter 4	**Improving the Performance of X-ray Sensitive CCDs: Direct Depletion Region Manipulation**	**107**
4.1	Development of the CCD66 for Future X-ray Missions	107
4.2	The CCD66	108
4.3	Depletion Depth	110
4.3.1	Depletion in Semi-Conductors	110
4.3.2	Manipulation of Depletion Depth	112
4.4	Investigating Externally Applied Negative V_{ss} and Depletion Depth	113
4.4.1	Experimental Methodology	114
4.4.2	Experimental Results	116
4.4.3	CCD66 Data Analysis	118
4.5	Monte Carlo CCD Simulation	122
4.5.1	The CCD22 Swift-XRT and the CCD66 Models	122
4.5.2	CCD66 Depletion Depth Modelling Results	125
4.5.3	CCD66 Quantum Efficiency Modelling Results	128
4.6	Conclusions	129
Chapter 5	**Improving the Performance of X-ray Sensitive CCDs: Investigating the X-ray Angle of Incidence**	**131**
5.1	X-ray Angle of Incidence	131
5.2	Effective Depletion Depth	133
5.3	Spatial Resolution	135
5.4	CCD Model Assumptions	136

5.5	Verification of the Model	139
5.6	Modelling Results and Discussion	140
5.6.1	Quantum Efficiency (QE)	140
5.6.2	Energy Resolution and Multi-Pixel Events	141
5.7	Experimental Work	143
5.7.1	The Experimental Set-up	143
5.7.2	The Experimental Method	143
5.7.3	Results	144
5.7.4	Experiment Discussion	146
5.7.5	Conclusion	148
5.8	Summary	148
Chapter 6	**Concluding Remarks**	**149**
Annex 1	**Mission Case Study: The International X-ray Observatory**	**151**
Annex 2	**Microchannel Plate Optics for X-ray Focussing**	**176**
Appendix 1	**I-V Curves Measured in the MIXS Diode Irradiation**	**209**
Appendix 2	**X-ray Spectra Taken with the CCD66 at Different Negative Substrate Voltages**	**224**
References		**230**

LIST OF FIGURES AND TABLES

FIGURES

Figure 1.1	The Aluminium/Silicon abundance ratio maps created by the Apollo 15 and 16 X-ray Fluorescence Spectrometer experiment from lunar orbit. It can be seen that only a very small fraction of the Lunar surface was measured during the Apollo missions.	24
Figure 1.2	Coverage maps for the BepiColombo X-ray fluorescence spectrometers left: MIXS-T and right: MIXS-C. The figure shows that the MIXS instrument will provide global coverage of Mercury.	25
Figure 1.3	A schematic diagram of the electron shell model, showing the source of Kα, Kβ, Lα and Lβ X-ray fluorescence emission lines. Note only 4 of the 8 N shell electrons are shown.	28
Figure 1.4	The three Wolter X-ray focussing geometries [Giacconi et al, 1969] where a), b) and c) show the Wolter I, II and III configurations respectively.	31
Figure 1.5	Top left: The Chandra nested optics, Top right: The XMM-Newton nested optics, Bottom left: The IXO Silicon Pore Optics currently under development and Bottom right: Microchannel Plate Optics as used for the BepiColombo MIXS Instrument [Beijersbergen et al, 2004].	32
Figure 1.6	Sources of radiation damage and their long-lived and transient effects	34
Figure 1.7	A schematic diagram of a MOSFET	36
Figure 2.1	The expected proton fluence at different energies expected during the transfer and operation phases of BepiColombo. Modelled data taken from [BepiColombo MIXS Environment Specification Part II, 2006], modelled using the JPL-91 model [Feynman, 1993]	49
Figure 2.2	The NIEL equivalent 10MeV proton fluence experienced by BepiColombo for different Al shielding thickness for the two main phases of the mission. Modelled data taken from [BepiColombo MIXS Environment Specification Part II, 2006], modelled using the JPL-91 model [Feynman, 1993]	50
Figure 2.3	Left: A schematic showing the DEPFET structure. Right: A potential distribution along a cut across the wafer in the gate region of the device. [Zhang, 2006]	52
Figure 2.4	A Silicon Drift Detector with an integrated J-FET. [Zhang, 2006]	53
Figure 2.5	Aluminium mask of a test die, showing the sample layout. The sample consists of three diodes, D1, D2 and D3, and one test capacitor, C1	54
Figure 2.6	Diode Sample Pin-out diagram and table	54

Figure 2.7	Photographs of sample C05 mounted on a PCB	55
Figure 2.8	The test sample mounted inside the die-cast box used for dark current measurements	57
Figure 2.9	An example set of I-V curves for one of the diodes tested. Comparison is made between the results achieved at Leicester and MPE-HLL	57
Figure 2.10	I-V curve for diode D1, sample C07, showing breakdown in the device	58
Figure 2.11	Schematic diagram of the test setup, showing the path of the protons from beam exit window to target. This information is required in order to calculate the energy degradation of the protons from exit to target	59
Figure 2.12	Stopping power of air for high energy protons, calculated using SRIM [Ziegler et al, 2010]	59
Figure 2.13	Stopping power of Aluminium for high energy protons, calculated using SRIM [Ziegler et al, 2010]	60
Figure 2.14	Stopping power of Mylar for high energy protons, calculated using SRIM [Ziegler et al, 2010]. Radiochromic film is made of polyester, plus an unknown active agent which is the self developing component of the material	60
Figure 2.15	The beamline interface mount at the Birmingham Cyclotron Facility	63
Figure 2.16	The test sample mounted on the PCB and irradiation test jig	63
Figure 2.17	Left, radiochromic film exposed to approximately $1x10^{10}$ 10MeV Protons and right, a 3D profile of the film exposure, showing the non-uniformity of the proton beam. The exposed area is ~$1.5x1.5cm^2$. The vertical axis in the 3D plot is grey-scale, from 0-254 where 0 is black and 254 is white.	65
Figure 2.18	The two scanned images showing calibration films 004-007, the exposures taken during the diode irradiations, 008-011 and the black-white step function used to establish the contrast level	66
Figure 2.19	I-V curves for D2 on sample C03 taken at 20°C before and after irradiation	70
Figure 2.20	Plot of I/κV versus proton fluence, used to establish the value of α	71
Figure 2.21	Isothermal annealing results from diode D3 on sample C07. The diode was kept at 60 ± 0.5°C for the duration of the experiment	73
Figure 2.22	Separate α curves for D1 and D2 & D3	74

Figure 2.23	Image of the 10MeV proton beam used in the Munich Proton Irradiation experiment. Image was taken using the GAFCHROMIC HD-810 radiochromic film. Right: Intensity beam profile in arbitrary units obtained from the film analysis	79
Figure 3.1	The XMM-Newton Spacecraft (Credit: NASA)	83
Figure 3.2	Photograph of an EPIC MOS focal plane camera. The camera consists of seven distinct MOS CCDs	83
Figure 3.3	Two observations of a typical X-ray Source, 2.5 years apart, using the central region of the XMM-Newton EPIC-MOS camera [Read and Abbey, 2007]. Note the spectral redistribution in the more recent data set	85
Figure 3.4	Spectra taken at a synchrotron radiation source [Read and Abbey, 2007] demonstrating the low energy spectral redistribution which the XMM Life Test attempts to recreate. Each 'snapshot' is taken using a different X-ray photon energy.	86
Figure 3.5	Modelled potential within a CCD showing the variation of potential with depth. Charge generated in the CCD will be swept to the buried channel (V_{max})	87
Figure 3.6	Plots, courtesy of A. Read, showing the energy deposited and X-ray counts accumulated over the XMM-Newton mission from launch to 2007. Note that 1 revolution, or orbit, takes 2 days.	88
Figure 3.7	The XMM-Newton Life Test Facility	89
Figure 3.8	The XMM-Life Test facility – comprising an electron gun X-ray source, crystal monochromator, MCP optic and a CCD22 detector	90
Figure 3.9	CCD22 Dark Current Image taken at -100°C prior to any X-ray Irradiation. Image is 2.5x2.5cm^2.	92
Figure 3.10	CCD22 Dark Current Image taken at -100°C after 24 hours of annealing at +100°C. This image was taken at twice the gain and twice the exposure time of Figure 3.10. Image is 2.5x2.5cm^2.	92
Figure 3.11	The MCP Optic is used to focus X-rays onto the CCD. This image is 2.5cm x 2.5cm.	93
Figure 3.12	The first dark frame taken without X-rays incident on the CCD22 after the first irradiation. Note the high dark current and dead columns towards the centre of the CCD. Image is 2.5x2.5cm^2.	94
Figure 3.13	CuL X-ray image taken with the CCD22 after the first irradiation.	95
Figure 3.14	'Warm' dark images taken at -50°C. The image on the left was taken as the CCD was warmed up from -100° while the image on the right was taken when cooling the device down after a 13-hour room temperature anneal. Each image is Image is 2.5x2.5cm^2.	95

Figure 3.15	Histogram showing the normalised events measured before irradiation, after irradiation and after the high temperature anneal. The more damaged a device, the more multipixel events will be registered.	96
Figure 3.16	Isolated Event Spectrum taken using the damaged CCD22 and the XMM-Life Test facility. The monochromator is used to select the Nitrogen line (0.39keV). A series of Gaussian curves is used to approximate the main components of the spectrum. The X-ray lines have been redistributed to lower energies.	98
Figure 3.17	CCD22 Image showing the Regions of Interest (ROIs) investigated on the damaged CCD22. Note the X-rays directed by the MCP Optic to the areas less exposed during the irradiation.	99
Figure 3.18	CCD image split into Region of Interests with the associated redistribution factor, R. The greater the value of R, the less redistribution and therefore the less damage has occurred.	101
Figure 3.19	Horizontal Bi-pixel X-ray Event Image	103
Figure 3.20	Vertical Bi-Pixel X-ray Events. These events MUST occur in the open electrode part of the pixel.	103

Figure 4.1	The XXM-Newton EPIC MOS 1(left) and p-n camera (right) Quantum Efficiency Curves	106
Figure 4.2	Photograph of the CCD66 chip. The two different pixel regions are labelled and marked using a dashed line	108
Figure 4.3	Diagram of the CCD66 pixel layout, showing the supplementary channel in the serial direction	109
Figure 4.4	The 1-D depletion depth, as calculated using equation (4.1), versus ΔV (V_{bi}-V). The resistivity used is 1500 Ω.cm and the channel potential, V_{bi}, is 5.5V	112
Figure 4.5	Photographs of the EPIC/Swift CCD Test facility, showing the experimental setup used to test the CCD66 device. This picture shows the X-ray generating equipment and material target wheel	113
Figure 4.6	Photograph of the EPIC/Swift CCD Test facility, showing the experimental setup used to test the CCD66 device. This picture shows the camera chamber end of the facility	114
Figure 4.7	Isolated Cu K spectrum taken with the CCD66 with no additional external negative substrate voltage. The Cu Kα and Kβ peaks are well separated	116
Figure 4.8	Isolated Cu K spectrum taken with the CCD66 with 15V external negative substrate voltage	116

Figure 4.9	Event size histograms showing how multipixel events are effected by increasing negative substrate voltage. Increased negative substrate voltage increases the percentage of total counts interacting within the depletion region (1-4 pixels)	117
Figure 4.10	Percentage of Cu Kα X-rays interacting within the depletion region (1-4 pixel events) versus negative substrate voltage	118
Figure 4.11	Summed (1-4 events) Cu Kα spectrum taken with the CCD66 with 20V external negative substrate voltage	119
Figure 4.12	A flow diagram summarising the CCD Monte Carlo model architecture that was used to investigate the CCD66. This has been modified from the CCD22 Swift XRT model architecture from [Godet, 2009] and details the changes made from the original code to make the new model	122
Figure 4.13	Microscope photograph of the CCD66 pixel structure, overlaid with the pixel dimensions. Note that the central CCD finger has been simplified as a regular column when, in fact, the actual finger is tapered	123
Figure 4.14	A schematic showing the two different sized pixels used on the CCD66 and their dimensions (in microns) as used in the model	123
Figure 4.15	Comparison between Cu Kα data taken with V_{ss} = 0V and simulated data using the CCD66 model	124
Figure 4.16	Depletion depth versus the percentage of all counts interacting within the depletion layer of the device, as simulated using the CCD66 model	125
Figure 4.17	Plot of the CCD66 depletion depth versus negative substrate voltage, showing both the physical model and the Monte Carlo model results. A logistic curve was found to fit the data very well and is used to establish the depletion depth for a given V_{ss}	126
Figure 4.18	Modelled QE curves for CCD66 isolated events corresponding to a V_{ss} of 0V, 20V and a hypothetical 80μm depletion depth	127
Figure 5.1	The geometry of the International X-ray Observatory, showing that X-rays entering the CCD are not normal to the CCD surface when entering the detector. A range of angles can be expected dependant on the X-ray energy and the radius of interaction with the X-ray mirror	130
Figure 5.2	Early CAD model of the X-ray Diffractometer (XRD) ExoMars Instrument. Note that the detector plane is curved rather than flat	131
Figure 5.3	A diagram showing the effective depletion depth, d_{eff}, due to an X-ray incident at an angle θ_i from the CCD normal	133

Figure 5.4	Schematic diagram of electron diffusion within a CCD pixel, resulting in a split-pixel event	134
Figure 5.5	A schematic showing how an event can enter one pixel at an angle, yet still register as an isolated event in the adjacent pixel. This can result in image blur.	135
Figure 5.6	Dimensions and transmission coefficients of the various regions of the CCD22 pixel, as used in the Monte Carlo model. From [Godet, 2009]	137
Figure 5.7	Left: Microscope image of the CCD22 electrodes, showing the main elements. Right: Electron microscope image of the CCD22 etched pixel showing the different pixel constituents at the etched interface. Images provided by e2v. From [Godet, 2009]	137
Figure 5.8	Comparing the Monte Carlo model results to experimental data, using CuKα X-rays (8.05 KeV)	138
Figure 5.9	Modelled CCD22 ^{55}Fe (MnKα) X-ray quantum efficiency (QE) curves for isolated and summed events with varying incident angle, θ_i, from the Z-axis which is normal to the CCD surface	139
Figure 5.10	Isolated event quantum efficiency curves modelled for the CCD22 at 0°, 20°, 40°, 80° and 89° for energies ranging from 3keV to 24keV	140
Figure 5.11	Modelled ^{55}Fe (MnKα) summed event spectra for 0°, 50° and 86°. A large reduction in spectral redistribution is observed as the incident angle approaches 90° from the z-axis	141
Figure 5.12	The fraction of summed events occurring in the photo peak as a function of angle	141
Figure 5.13	Photograph of the experimental setup, showing the radioactive source mounted at an angle to the CCD22	143
Figure 5.14	^{109}Cd data compared with the equivalent model outputs. The spectra were normalised to the peak counts in both cases	144
Figure 5.15	Modelled ^{109}Cd spectrum compared with experimental data. Experimental data are normalised to the modelled value at 45°	144
Figure 5.16	The spectral redistribution of the ^{109}Cd peak can be fit with two Gaussian curves	146

TABLES

Table 1.1	Key satellite performance parameters for a number of X-ray Astronomy missions	23
Table 1.2	Energies of X-ray emission lines for some elements mentioned in this thesis.	29
Table 1.3	10MeV Proton NIEL Scaling in Silicon (from Holmes-Seidle & Adams, 1993 and calculated by Burke, 1986)	39
Table 2.1	Diode designations and approximate radiation fluence to be administered during the test.	56
Table 2.2	Table showing the proton energy required to achieve 10 MeV protons at the test diodes. The protons leave the exit beam and travel through aluminium, air and a polyester-based radiochromic film	61
Table 2.3	Coarse dosimetry for each of the irradiated diode samples based on beam current measurements prior to and after irradiation	68
Table 2.4	The measured leakage current of diodes irradiated in the current related damage rate (α) experiment. The proton fluence used to irradiate each diode is also shown	70
Table 2.5	Fraction of time measured in various flare states during years analogous to possible years of operation for BepiColombo at Mercury [Carpenter and Fraser, 2006]	76
Table 2.6	Summary of the Current Related Damage Rate Experiments Mentioned in the chapter.	80
Table 3.1	Summary of counts in each spectrum peak and the calculated value of R for each region of interest	100
Table 3.2	Summary of peak positions on the x-axis and the FWHM values of the main peaks for each ROI. The position of Nk_{α} was fixed and the position of the other peaks allowed to vary.	100
Table 4.1	Summary of the CCD66 Voltage optimisation used when collecting data and during noise calibration	115
Table 4.2	Analysis of the Cu Kα and Cu Kβ lines for 15 V and 20 V negative substrate voltage and redistribution of counts	120
Table 4.3	The FWHM Spectral Resolution of Cu Kα summed (1-4 pixel) spectra taken at negative substrate voltages (V_{ss}) of 0V-20V in 5V steps	120
Table 4.4	The depletion depths inferred from the comparison of CCD66 data and the CCD Monte Carlo modelling results	125

EXECUTIVE SUMMARY

Chapter 1 opens the thesis by discussing X-rays from astronomical and planetary bodies and providing some of the mechanisms of X-ray generation in these objects. The importance of a mission's radiation environment is discussed in the context of achieving mission requirements as well as an introduction to types of damage and how instruments can mitigate and recover from such damage in order to achieve the end-of-life mission requirements.

Chapter 2 is concerned with the BepiColombo mission to Mercury and the Mercury Imaging X-ray Spectrometer, MIXS. The Chapter details the proton damage experiments conducted on a series of MIXS-representative diodes manufactured on silicon wafers from which the focal-plane DEPFET detectors were fabricated. The results of the radiation damage experiments provide confidence in the ability of the MIXS DEPFET detectors to meet the BepiColombo mission requirements. The radiation damage experiments show that, by conducting two detector anneals, a spectral resolution better than the 200eV@1 keV requirement can be met at the end of the mission.

The current-related damage factor, α, is also shown to be similar for the 450µm-thick DEPFETs as thinner 300µm silicon devices. This should allow good damage estimates of DEPFETs to be made based on damage experiments conducted using 300µm devices. It is expected that the DEPFETs will undergo further proton damage experiments, utilising flight-like devices rather than represented diodes cut from DEPFET wafers as presented in this thesis.

The use of radiochromic film as a measure of proton beam uniformity was demonstrated in two proton irradiation experiments: one conducted at the University of Birmingham Cyclotron and another at the Garching Tandem Accelerator of the Maier-Leibnitz-Laboratory of the Technical University in Munich. Both of these experiments are discussed in the chapter. With accurate calibration, this film could potentially provide dosimetry with very accurate positional information. Unfortunately, insufficient calibration data were obtained for the film to function in this capacity in the experiments presented.

Chapter 3 of this thesis describes an experiment designed to replicate the ionising radiation damage experienced by the XMM-Newton CCD22 detectors over the course of the mission. The results of this experiment show that a device based on an open electrode structure is highly

susceptible to ionizing damage from X-rays incident on the detector. This knowledge can be applied to future instruments in order to decide whether such a device is acceptable for the application at hand. Should a long-lifetime detector be required which will, over its lifetime, be subject to a high X-ray fluence, it might be preferable to use a thinned, back-illuminated, closed electrode device in place of an open electrode. The XMM Life Test Experiment continues with Tony Abbey at the University of Leicester and contributes to the EPIC Camera Calibration Team's activities related to the radiation damage modelling of the EPIC MOS CCDs.

Chapter 4 discusses the work carried out during the PhD on the CCD66, a new CCD detector designed with the XEUS/IXO mission in mind, where the ability to increase high energy quantum efficiency through the application of a negative substrate voltage is both demonstrated and quantified. The experiment shows that a significant reduction in large-scale multipixel events is achieved by increasing the negative substrate voltage, and the number of events occurring within the depletion region, resulting in events of 1-4 pixels, is increased. In addition, the achieved depletion depth is quantified through Monte Carlo simulation.

The modified CCD66 Monte Carlo code, originally developed for XMM-Newton and Swift CCD22 devices, is used to calculate the expected depletion depth of a CCD66 when such substrate voltages are used. The modelling work demonstrates that calculations of CCD depletion depths under negative substrate voltage using the standard 1-dimensional equation will significantly overestimate the depletion depths achieved for a given potential difference. The 1D equation predicts a depletion of ~55µm for a negative substrate voltage of 20V, for example. An increase in depletion depth from 28.4µm for 0V to 34.7µm for -20V on the substrate is demonstrated using the Monte Carlo model. This, in turn, results in ~7.8% increase in the number of events interacting in the device depletion region. The application of a relatively small voltage to the substrate of a CCD is shown to result in a significant improvement in QE.

In Chapter 5, the simulation results of an investigation into the effect of X-ray angle of incidence are reported. This work used the Monte Carlo code developed for the CCD66 experiment, and described in Chapter 4, to investigate the effect of X-ray angle of incidence on quantum efficiency. It is found from this work that X-rays entering a CCD at shallower angles are more likely to interact in the depletion region of a device and, therefore, QE is improved for higher energy X-rays. Initial experimental results attempting to demonstrate this effect in the laboratory are also reported, although proved inconclusive due to limitations introduced by the experimental setup.

A number of annexes have been included in this thesis which describe additional work conducted during the course of this PhD in the field of X-ray instrumentation. In Annex I, a case study based on the author's work as the System Engineer on the International X-ray Observatory Assessment Study is presented, outlining the very diverse range of instrumentation used in the mission. Both Depleted Field Effect Transistors and CCDs are used in the mission payload, both of which are studied as part of this thesis.

Annex II deviates from the rest of this thesis, which is primarily concerned with the radiation damage of X-ray detectors, by reporting the early work conducted during this PhD in the field of Microchannel Plate (MCP) X-ray Optics. The Annex publishes the highest resolution image yet achieved by a flat square-pore, square-packed MCP optic. The development of MCP optics is ongoing, with the optics due to fly, for the first time, on the BepiColombo mission to Mercury. These optics will enable the high-resolution imaging of Mercury's surface in the X-ray, providing planetary scientists with the information they require to establish the surface composition of one of the least-explored planets in the solar system. The optics were also key in the experiment reported in Chapter 3 of this thesis, the X-ray radiation damage of the CCD22. Such an optic was used to focus X-rays onto a small region of the device, thus shortening the exposure time required to achieve a mission-level dose and also allowing the investigation of different regions of the CCD.

One of the key questions often asked is 'what is the best X-ray detector to use?' The answer to this question is 'it depends greatly on the application'. There are many different types of detector that provide very different capabilities which can achieve a wide variety of science goals. Many of these detectors have been discussed, particularly in the context of the International X-ray Observatory in Annex I. Some detectors provide excellent spatial resolution, others excellent spectral resolution. Others still need to maximise the quantum efficiency of a detector within a particular energy band. Some are sensitive to the polarization of X-rays, others not. Some detectors, such as the DEPFET, are capable of providing good 'all round' performance, with good QE (>80%) over a broad energy range (0.1-10 keV), good spectral performance, such as for BepiColombo, despite a high dose of radiation (~$3x10^{10}$ 10 MeV protons) and can also be made to have a large field of view. Such a detector, however, is unable to provide very high resolution spectroscopy as is achieved using a Transition Edge Sensor (~10eV for energies <6 keV). The main message is that there is no one detector that can do all things. It is necessary to tailor your detector to the application.

Knowledge of the radiation environment of each space mission, and how this environment will affect the vital components of instrument payloads, is vital for mission success. Confidence in the ability of payloads to withstand such environments can be achieved through experiment and simulation of radiation effects. The usefulness of this approach is demonstrated in this thesis by the influence on the BepiColombo MIXS instrument design with the inclusion of detector annealing capability, as well as the greater understanding of ionising radiation effects on open electrode CCDs.

CHAPTER 1

INTRODUCTION

1.1 X-RAYS IN ASTRONOMY AND PLANETARY SCIENCE

The measurement of X-ray sources in space began in the 1940s when sounding rockets were used to lift Geiger counters above the Earth's atmosphere, looking for high energy photons. Giacconi et al (1962) showed, for the first time, X-ray emission with an extra-solar system origin when an experiment to measure the X-ray fluorescence from the Moon proved unsuccessful due to what was originally interpreted as high background noise. The source of this perceived 'noise', originally concluded to be diffuse background with a discrete source imposed on it, was shown to be Sco-X1.

Modern X-ray Astronomy is carried out entirely by space-borne telescopes, the most recent missions being the NASA Swift mission [Gehrels et al, 2004], the NASA Chandra telescope [Weisskopf, 2004], the ESA XMM-Newton (where XMM stands for X-ray Multi-Mirror) telescope [Jansen et al, 2001] and JAXA's Suzaku mission (also known as Astro-E2) [Mitsuda, 2007].

Table 1.1 summarises the key telescope parameters for a number of X-ray missions. In the table, RGS refers to the XMM-Newton Refection Grating Spectrometer, ACIS-S the Advanced CCD Imaging Spectrometer on Chandra, HETG is the Chandra High Energy Transmission Grating, XIS is Suzaku's X-ray Imaging Spectrometer and XRT refers to Swift's X-ray Telescope.

Chandra's main aim was to provide unprecedented angular resolution of X-ray sources using high-precision zero-expansion glass ceramic shell mirrors [Zhao et al, 2004][Hartmann and Morian, 2003] in the Wolter-I configuration [Mangus and Underwood, 1969]. Chandra's mirrors and X-ray detectors (the Advanced CCD Imaging Spectrometer (ACIS) [Garmire, 2003], the position sensitive microchannel plate detector and the High Resolution Camera (HRC) [Murray et al, 2000]), achieve better than 1 arc-second angular resolution (~0.2'') [Dahlem et al, 1999].

XMM-Newton's primary scientific goal is sensitive spectroscopy of faint X-ray sources and therefore was designed with collecting area as a primary concern. The X-ray mirrors on XMM-Newton are nested inside each other, resulting in an effective area more than 8 times that of

Chandra at 1keV [Dahlem et al, 1999]. The FWHM energy resolution of XMM is just ~6 arcseconds, however, compared to Chandra's 0.2 arcseconds [Jansen et al, 2001][Jerius et al, 2000].

Suzaku turned its attention to harder X-rays than Chandra and XMM-Newton, making use of a Hard X-ray Detector (HXD) with sensitivity from 10 keV to 600 keV [Yamaoka et al, 2009]. The X-ray mirrors on Suzaku use light-weight thin foil shells nested to a very high density, providing large collecting efficiency with a moderate imaging capability from 0.2-12 keV. Higher energy X-rays are not focussed onto the HXD. HXD is a collimated instrument with a scintillator detector array, surrounded by a BGO anticoincidence shield to ensure all X-rays detected at the focal plane have their origins within the telescope field of view [Yamaoka et al, 2009]. Each of these missions complements each other greatly, with slightly different emphases on spectral resolution, spatial resolution and energy of interest.

Satellite	Mirror PSF[1] (" FWHM)	Mirror PSF[1] (" HEW)	Energy Range (keV)	Effective Area at 1keV (cm^2)	Energy Resolution At 1 keV (eV)
XMM-Newton	6	15	0.15 – 15	4650	4 (RGS)[2]
Chandra	0.2	1.5	0.1 – 10	555 (ACIS-S)	1 (HETG)[3]
Suzaku	108	120	0.2 – 600	1760 (XIS)	50
Rosat	3.5	7	0.1 – 2.4	400	500
Swift	8.8	18 (@1.5 keV)	0.2 – 10 (XRT)	133.5	70

[1] *PSF is the acronym for Point Spread Function*
[2] *RGS is the acronym for XMM's Reflection Grating Spectrometer*
[3] *HETG is the acronym for Chandra's High Energy Transmission Grating*

Table 1.1 Key satellite performance parameters for a number of X-ray Astronomy missions

X-ray fluorescence from the Moon was first measured from lunar orbit on the NASA Apollo 15 and 16 missions [Adler et al, 1973], establishing aluminium-to-silicon and magnesium-to-silicon ratios of a number of lunar features. Such abundance ratios have been found to correlate with certain lunar surface features: for example, a correlation was found between optical albedo measurements and Si/Al ratios on the moon [Adler et al, 1973]. Figure 1.1 shows the aluminium-to-silicon ratio map that was created by the X-ray Fluorescence Spectrometer on Apollo 15 and 16. It was not until ROSAT in 1990, however, when the technology to achieve an adequate signal to noise ratio was available, that an X-ray image of this fluorescence was taken from Earth orbit

[Schmitt et al, 1991]. As is evident from Figure 1.1, X-ray emission from only a very small fraction of the Moon's surface was measured. Ideally, a global abundance map with high spectral and spatial resolution is desirable. The introduction of a focusing element to such an instrument greatly improves the sensitivity by decoupling the detector area from the collecting area of the telescope. Non-imaging telescopes have a collecting area limited by the area of the detector. The BepiColombo mission to Mercury, using the Mercury Imaging X-ray Spectrometer (MIXS), will make use of recent developments in microchannel plate X-ray optics to measure the elemental composition of the planet's surface [Fraser et al, 2010]. Microchannel plate (MCP) optics is the main topic of Chapter 2 and is discussed there in more detail. Figure 1.2 shows a pair of BepiColombo calculated coverage maps from Fraser et al (2010) produced for the MIXS-T and MIXS-C instruments, where MIXS-C is a collimator and MIXS-T is an imaging telescope. The figure shows the time spent viewing different areas of Mercury with the two instrument channels over the total mission duration of two years. It can be seen in Figure 1.2 that over the course of the mission, complete global coverage of the planet will be achieved, with the majority of time being spent over the planet poles.

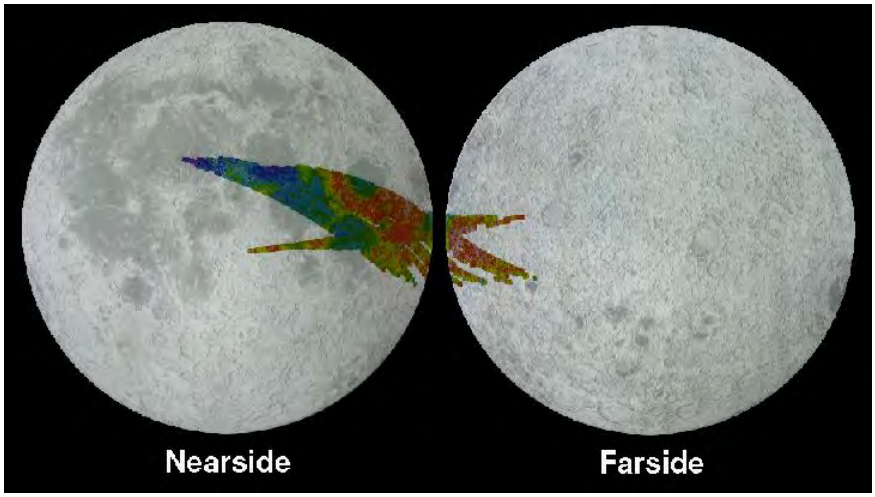

Figure 1.1 The Aluminium/Silicon abundance ratio maps created by the Apollo 15 and 16 X-ray Fluorescence Spectrometer experiment from lunar orbit. It can be seen that only a very small fraction of the Lunar surface was measured during the Apollo missions.

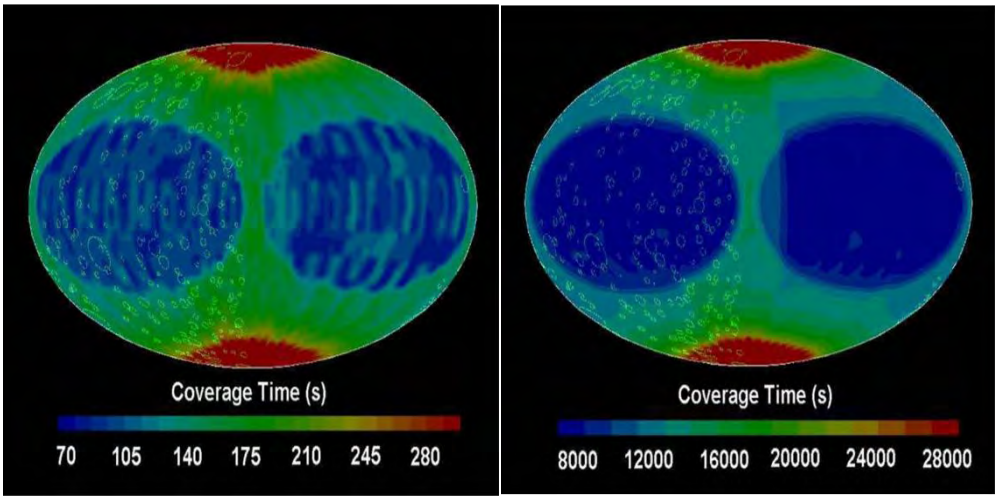

Figure 1.2 Coverage maps for the BepiColombo X-ray fluorescence spectrometers left: MIXS-T and right: MIXS-C. The figure shows that the MIXS instrument will provide global coverage of Mercury.

MIXS-C will result in a surface pixel size of ~70km at periherm (~400km orbital altitude) and ~270km at apoherm (~1500 km orbital altitude). MIXS-T, during solar flares, where the solar X-ray flux and, hence, fluorescent X-ray flux, is at its highest, will result in a surface pixel resolution of <1km at periherm and ~4km at apoherm [Fraser et al, 2010].

X-ray measurements will play a very important role in many astrophysics and planetary missions. This thesis considers the requirements for X-ray instruments of the future and investigates some specific traits of devices such as radiation damage and how to improve key features such as spectral resolution and quantum efficiency.

1.2 X-RAY GENERATION

Many astronomical and solar system objects can be detected in the X-ray band: photons in the range of 0.1keV to 100 keV. For example, in our solar system, the sun, planets, moons, asteroids, planetary coronae and the rings of Saturn can all be seen using X-ray telescopes [Bhardwaj et al, 2007]. Other examples of astronomical X-ray sources which can be observed include hot plasmas such as the interstellar medium [Lequeux, 2005], stars, the accretion disks around compact objects [Camenzind, 2007], star clusters [Allison, 2006] and supernova remnants [Marcaide and Weiler, 2005]. X-ray emission can be categorised into two types: Line emission, consisting of X-rays emitted over a narrow energy band and continuum emission, broad band emission of X-rays.

There are a variety of physical mechanisms that result in X-ray emission from planetary surfaces. [Bhardwaj et al, 2007]. These include:

1) Collisional excitation of neutral species and ions by charged particle and high energy photon impact followed by line emission, often known as secondary emission or X-ray fluorescence

2) Electron collisions with neutral species and ions resulting in continuum bremsstrahlung emission

3) Photon scattering from neutral species and ions in planetary atmospheres

4) Charge exchange of solar wind ions with neutral species

5) X-ray production from the charge exchange of energetic heavy ions of planetary magnetospheres with neutrals or direct excitation of ions in collisions with neutrals.

6) X-ray production from charged particles accelerated by magnetic fields (known as cyclotron radiation or synchrotron radiation at relativistic speeds).

Cosmic X-ray sources include thermal processes such as black-body radiation and bremsstrahlung emission, synchrotron radiation from energetic cosmic ray electrons moving under the influence of magnetic fields and inverse Compton scattering of cosmic ray electrons colliding with starlight or microwave photons [Adams, 1980]

For a black-body source, the energy of a photon is related to the temperature of the photon emitter, the spectrum of which is defined by Planck's function, equation (1.1), giving the intensity (I) of radiation at a temperature (T) as a function of wavelength (λ). In the equation, h is Planck's constant, c is the speed of light in a vacuum and k is Boltzmann's constant. X-rays are often quoted in terms of energy (E) rather than wavelength, where equation (1.2) shows how the conversion between energy, wavelength and frequency (ν) is easily calculated.

$$I(\lambda, T) = \frac{2hc^2}{\lambda^5} \frac{1}{e^{hc/\lambda kT} - 1} \tag{1.1}$$

$$E = \frac{hc}{\lambda} = h\nu \tag{1.2}$$

$$E(keV) = \frac{12.4}{\lambda(\text{Å})} \tag{1.3}$$

Equation (1.4) is known as Wien's displacement law and is used to relate the peak of the Planck function to temperature, where the peak wavelength, λ_{max}, is given in meters, b is Wien's displacement (2.898×10^{-3} mK) and the temperature, T, is in Kelvin. Combining (1.4) and (1.2) allows Wien's law to be expressed in terms of energy and is shown in equation (1.5). q_e is the electronic charge (1.602×10^{-19} Coulombs) and is used to express E_{max} in terms of electron volts (eV); 1eV is equivalent to 1.602×10^{-19} Joules.

$$\lambda_{max} = \frac{b}{T} \tag{1.4}$$

$$E_{max} = \frac{Thc}{bq_e} \tag{1.5}$$

From (1.5) it can be calculated that for peak X-ray energies of 0.1 keV and 100keV, the black body temperature due to Wien's law is 2.3×10^5K and 2.3×10^8K respectively. Any objects in the night sky which have a temperature in this range will emit X-rays which can be detected in orbit by a spacecraft, provided that the signal to noise ratio is large enough. These X-rays, along with bremsstrahlung radiation, make up the X-ray continuum.

Bremsstrahlung radiation is a key mechanism which contributes to broad X-ray continuum emission [Bhardwaj et al, 2007] and is the result of high energy charged particles, such as electrons, being slowed down when they interact with other charged species, such as the nucleus of an atom. Other mechanisms such as Compton and Inverse Compton scattering affect the energy of X-ray photons as they travel from the object source to the observer. This, too, can be used as a diagnostic of the environment around astronomical high energy photon emitters.

X-ray fluorescence is an important generation mechanism in X-ray planetary science. X-ray fluorescence, often called secondary emission, is key to the BepiColombo MIXS instrument discussed in Chapter 2. X-ray fluorescence occurs when a high energy X-ray or particle interacts with a target material and excites an electron from one of the target atoms into a higher energy state. Usually, the excess energy is taken up by the ejection of an Auger electron from the atom. Sometimes, however, an outer-shell electron falls back to the now vacant lower energy state. When this happens, energy equivalent to the difference between the higher and lower shell energies is released in the form of a photon. The fluorescent X-ray yield for such interactions is small. For example, the X-ray photon yield for oxygen is only ~0.2% in the soft X-ray part of the spectrum (0.53 keV) [Bhardwaj et al, 2007]. Figure 1.3 shows this process in a schematic

diagram, where electrons falling from higher to lower energy shells result in the emission of X-ray photons with characteristic energies.

Moseley's Law states that the wavelength of a spectral line is related to the atomic number, Z, of the element emitting that line (Khare and Swarup, 2007). As each of the elements has different shell energies, the X-ray energy of the released photon is characteristic of that particular element. Detection and measurement of the energy of this photon can be used as a diagnostic method to determine the element emitting the photon. Table 1.2 summarises the X-ray emission energies of some elements mentioned in this thesis. The values in this table are taken from the X-ray Data Booklet [Thompson, 2001].

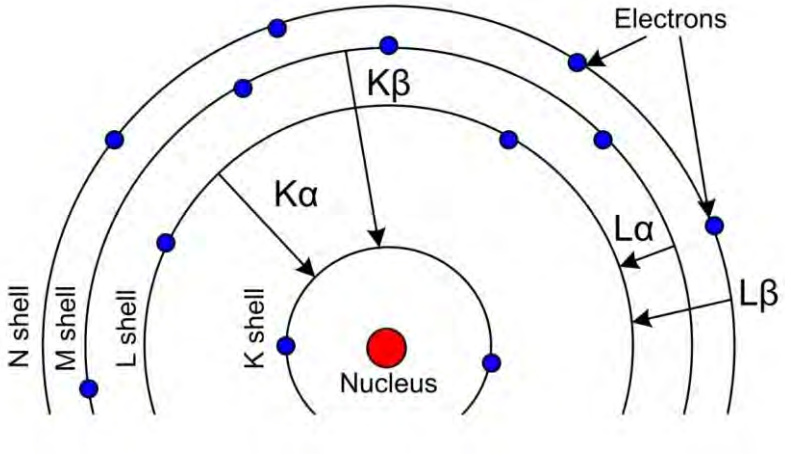

Figure 1.3 A schematic diagram of the electron shell model, showing the source of Kα, Kβ, Lα and Lβ X-ray fluorescence emission lines. Note only 4 of the 8 N shell electrons are shown.

There are four main areas of X-ray diagnosis that can be used in astronomy and planetary science: imaging, spectroscopy, photometry and polarimetry [Cash, 2001]. Each of these diagnosis tools provides different insights into astronomical or planetary X-ray sources. Spectroscopy is measurement of the energy or frequency of detected X-rays, allowing the observer to determine the elemental material of the source. Imaging techniques determine the direction of incoming X-rays and provide information on source structure; they also provide the astronomer with the amazing images and pictures for which the subject of Astronomy is famed. Photometry, the counting of photons from a source, can reveal how these objects change with time. And finally,

polarization measurements allow astronomers to extract three-dimensional information from high energy photon sources which also have strong magnetic fields.

Element	Kα (keV)	Kβ (keV)	Lα (keV)	Lβ (keV)
^{6}C	0.2770	-	-	-
^{7}N	0.3924	-	-	-
^{8}O	0.5249	-	-	-
^{13}Al	1.48670	1.55745	-	-
^{14}Si	1.73998	1.83594	-	-
^{22}Ti	4.51084	4.93181	0.4522	0.4584
^{25}Mn	5.89875	6.49045	0.6374	0.6488
^{26}Fe	6.40384	7.05798	0.7050	0.7185
^{28}Ni	7.47815	8.26466	0.8515	0.8688
^{29}Cu	8.04778	8.90529	0.9297	0.9498
^{47}Ag	22.16292	24.9424	2.97821	3.34781
^{48}Cd	23.1736	26.0955	3.13373	3.31657
^{79}Au	68.8037	77.984	9.7133	11.4423

Table 1.2 Energies of X-ray emission lines for some elements mentioned in this thesis. Values from [Thompson, 2001]

The following sections address the practical aspects of X-ray instrumentation; focusing X-rays and X-ray detection.

1.3 X-RAY FOCUSING

The need for X-ray focussing optics results from the necessity for greatly improved signal to noise ratio. The flux of X-ray photons from celestial sources is, for the most part, very small. For example, taking the average of ~500 X-ray sources chosen at random in the NASA Master X-ray Catalogue [Smale, 2010] gives just ~1.5×10^{-1} X-ray counts per second. This low photon rate results in the need for photon counting, particularly in the observation of distant sources which tend to be less bright. There is also a diffuse X-ray background above 0.3keV across the whole sky which largely originates from unresolved extragalactic X-ray sources [Shanks et al, 1991]. It is also possible that some component of the diffuse X-ray background originates from inverse Compton

photons from cosmic rays interacting with the microwave background [Charles and Seward, 1995]. This background signal acts as noise when trying to resolve the signal from discrete X-ray sources.

X-ray noise, which is made up of this diffuse background as well as fluorescent X-rays from the spacecraft, particle-induced background, plus internal factors such as leakage current in the case of CCDs and other solid state detectors, can swamp this very small signal. As the noise is proportional to detector area, a small detector area is desired. For non-focusing instruments, however, such as collimated or coded-mask detector systems, reducing the detector area also proportionately reduces the X-ray signal. A focussing element introduced to an instrument decouples the signal and noise, allowing a large area of X-ray flux to be focussed onto a detector of small area and, therefore, less noise results. The signal-to-noise ratio can therefore be greatly improved, increasing the sensitivity of the instrument and allowing fainter objects to be observed.

X-ray optics do not work like conventional optics, which focus visible light by refraction through a material or by reflection from concave mirrors. Instead, X-ray optics work by reflecting X-rays at shallow grazing angles. High energy photons such as hard X-rays or gamma rays can also be focused using Bragg or Laue diffraction.

The reflectance of a material depends on the material composition and surface properties such as surface roughness. A number of geometries can be used in X-ray optics to achieve a focus, such as the Kirkpatrick Baez [Kirkpatrick and Baez, 1948] or the Wolter I, II and III geometries (Figure 1.4). The most widely used geometry is the Wolter I configuration, consisting of a hyperbolic and a parabolic mirror. It is also the most suited for wide-field imaging as Type II and Type III telescopes do not focus off-axis sources well. Type I also allows nesting of the optics in concentric shells, greatly increasing the effective area of the optic. The Type II is more suited to high spatial resolution imaging and small field of view applications such as transmission spectroscopy.

There are a number of technologies currently favoured for X-ray focussing optics (Figure 1.5): replicated nickel shell optics [Spiller, 1999], such as those used on XMM-Newton [Aschenbach et al, 2000], ceramic shell optics such as used on Chandra [Jerius et al, 2000], microchannel plate optics [Martindale, 2008a], such as will be used on the BepiColombo Mercury Imaging X-ray Spectrometer [Fraser, 2010], and Silicon Pore Optics [Ackermann et al, 2009] which are currently under development as a possible optic technology for the International X-ray Observatory [Parmar, 2009].

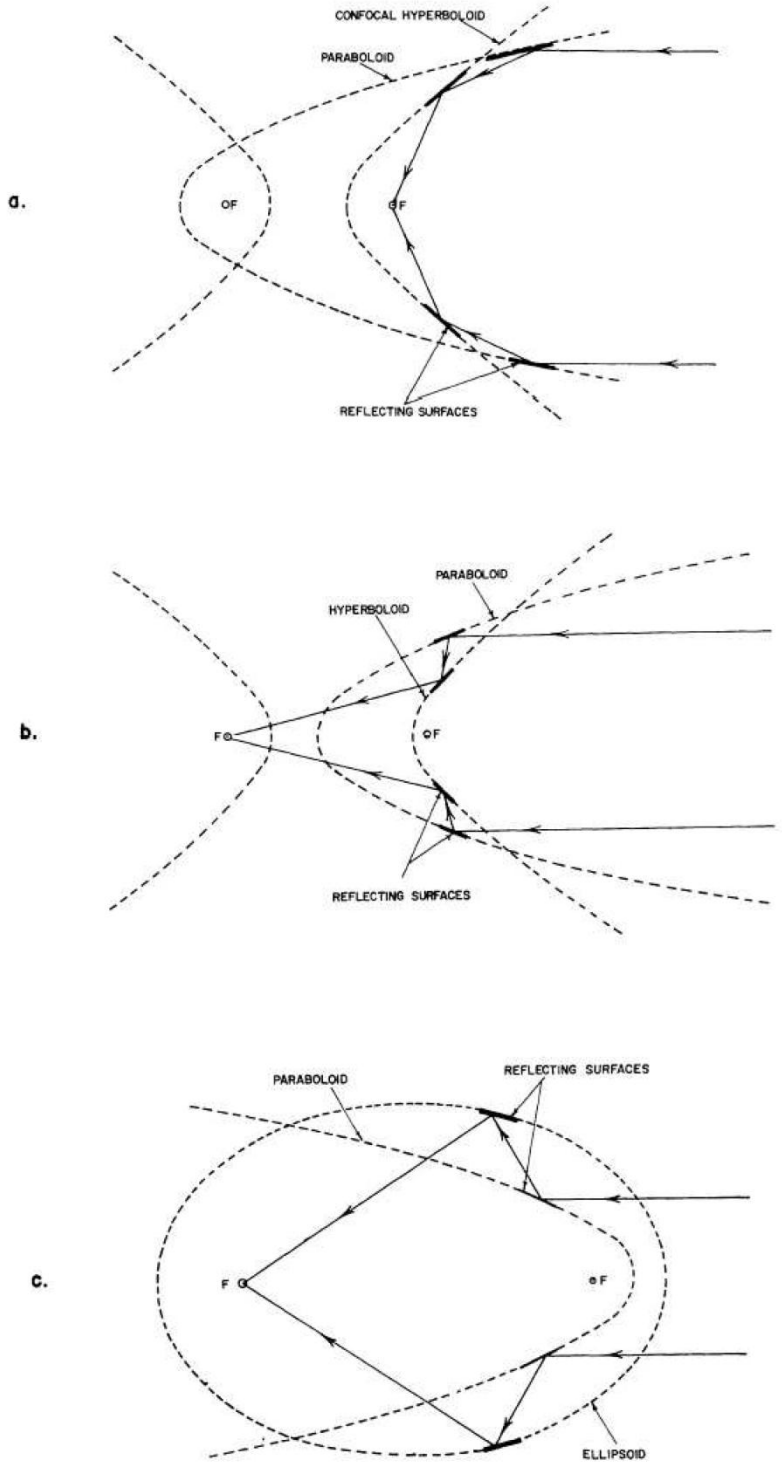

Figure 1.4 The three Wolter X-ray focussing geometries [Giacconi et al, 1969] where a), b) and c) show the Wolter I, II and III configurations respectively.

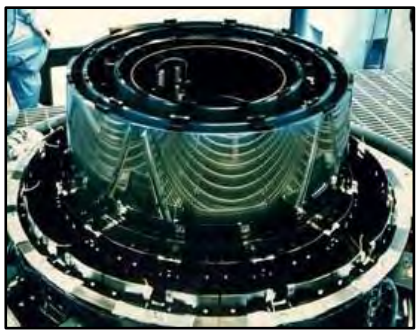

Chandra Shell Optics
≥0.2'' FWHM Angular Resolution
18,500 kg/m^2 A_{eff} @ 1keV

XMM-Newton Shell Optics
≥6'' FWHM Angular Resolution
2300 kg/m^2 A_{eff} @ 1keV

IXO Silicon Pore Optics
≥5'' FWHM Angular Resolution
200 kg/m^2 A_{eff} @ 1keV

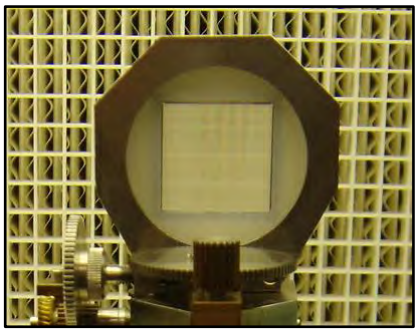

Microchannel Plate Optics
≥30'' FWHM Angular Resolution
25 kg/m^2 A_{eff} @ 1keV

Figure 1.5 Top left: The Chandra nested optics, Top right: The XMM-Newton nested optics, Bottom left: The IXO Silicon Pore Optics currently under development and Bottom right: Microchannel Plate Optics as used for the BepiColombo MIXS Instrument [*Beijersbergen et al, 2004*].

X-ray shell optics manufactured from different materials have a great deal of heritage in X-ray Astronomy, having flown on all of the major X-ray Astronomy missions in recent times: ESA's XMM-Newton, NASA's Chandra and Swift missions, and JAXA's Suzaku. XMM-Newton provides the largest effective area of any X-ray spacecraft using this mirror technology, achieved by nesting 58 Wolter-I nickel shells in each of the three distinct mirror modules. The effective area achieved is 4300cm^2 at 1.5 keV [Gabriel et al, 2006].

A major drawback of nested shell optics, where nesting is the close-packing of concentric mirror shells, is their mass-to-effective area ratio, with the XMM-Newton optics achieving just 2300kg per m^2 at 1keV [ESA Advanced Studies and Payloads, 2010]. More recent developments in nested shell optic technology make use of much thinner foil shells rather than heavier ceramic glass or nickel based mirrors. Suzaku used such mirrors, with 175 replicated foil shells nested over 4 separate telescopes [JAXA Suzaku X-ray Telescopes, 2010]. This technology results in lower

effective area (450cm^2 at 1keV) and angular resolution (60'' HEW) than would be achievable using the heavier nested nickel shells [JAXA Suzaku X-ray Telescopes, 2010].

ESA, with the Brera Astronomical Observatory – INAF in Italy, and NASA's Goddard Space Flight Centre are independently considering a new slumped glass optic option for the IXO mission. Both groups are currently pursuing research and development activities in order to ensure the 3m^2 at 1keV effective area and 5'' FWHM angular resolution requirements are met, ready for mission launch in 2020 [Ghigo et al, 2008][Zhang et al, 2009]. These very low-mass slumped glass optics will need to have an effective area to mass ratio of 20cm^2 per kg if the 3m^2 at 1.25 keV requirement is to be met within the launch mass envelope [NASA IXO flight Mirrors, 2010].

The BepiColombo MIXS Instrument [Fraser, 2010], the subject of Chapter 2 of this thesis, uses the Microchannel Plate (MCP) Optic to focus X-rays onto the focal plane detector. The primary reason for the use of MCP optics for planetary instruments is the very low mass per unit effective area achievable. The 70cm^2 effective area requirement for the MIXS Telescope can be met with an optic consisting of just 0.175kg of microchannel plates. Two MCP geometries are employed by the MIXS instrument: the collimating square-pore, square-packed microchannel plate [Chapman, Nugent and Wilkins, 1991] and the radially packed Wolter-I geometry microchannel plate optic [Price, 2002]. These are discussed in more detail in Annex 2 of this thesis.

Silicon pore optics [Beijersbergen et al, 2004] is a new technology developed in Europe by ESA for the IXO mission which will compete against the slumped glass optic technology to be the X-ray focussing element of the spacecraft. The optics are manufactured using off-the-shelf 'super-polished' silicon wafers, scored to create regular channels along the wafer length, and then stacked to create a solid volume of silicon with regular pores. The silicon pore optics are then slumped to the correct radii to establish a Wolter-I geometry, allowing true X-ray imaging [Gunther et al, 2006].

Advances in slumped glass and silicon pore optics will enable the next generation of X-ray observatory, while the development of light-weight microchannel plate optics has opened up the field of high angular resolution (≤8' FWHM) X-ray imaging and spectroscopy of planetary bodies. Developments of multilayer coatings [Contoneo et al, 2009], and even crystal diffraction lenses [Brown et al, 2008][Ferrari et al, 2009], will increase the capability of hard X-ray and gamma ray imaging for high energy instruments of the future.

1.4 RADIATION DAMAGE

High energy photons and particles passing through matter lose energy through various scattering and interaction processes, resulting in two main types of damage: Ionizing damage and displacement damage (also known as non-ionizing damage). Figure 1.6 shows a flow diagram summarising some of the effects of both types of damage [Holmes-Seidle & Adams, 1993].

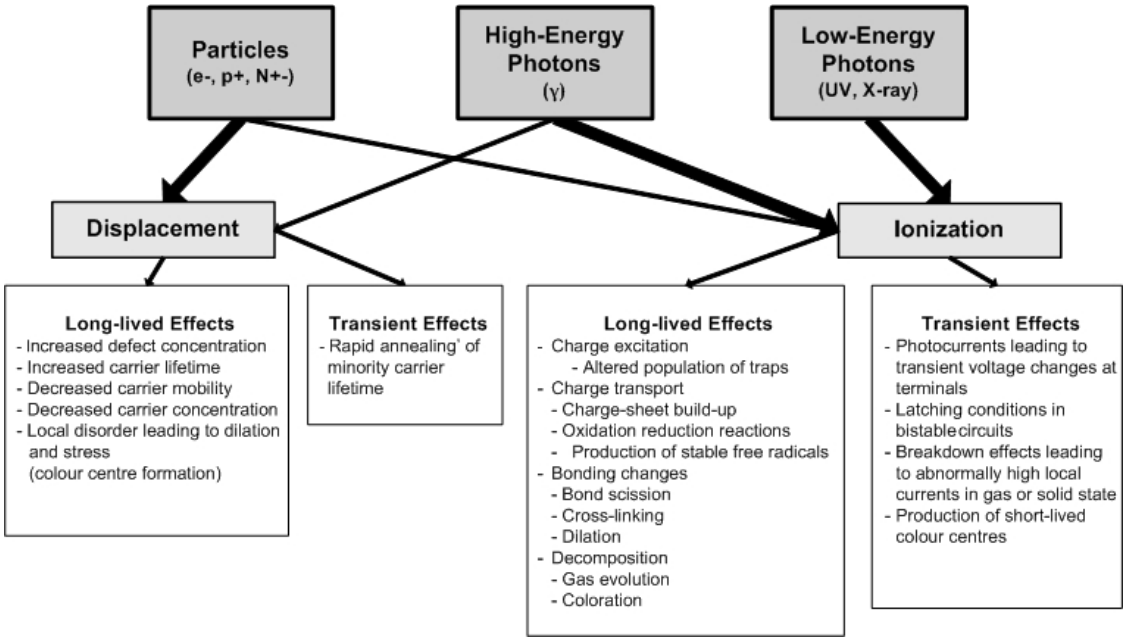

Figure 1.6 Sources of radiation damage and their long-lived and transient effects

1.4.1 ATOMIC DISPLACEMENT

High energy particles interacting with matter cause displacement of atoms from their equilibrium position within the crystal lattice. This displaced atom may recombine with its original position in the lattice, as the newly created lattice vacancy is a position of stability for a displaced atom, or it may migrate to another site of stability such as the surface of the material or a second defect within the material. Whether an atom migrates or returns to its original position in the lattice depends on how much energy is imparted to it as well as the internal electric fields within the material. Displaced atoms are a significant source of damage effects in semiconductor devices such as CCDs [Holmes-Seidle & Adams, 1993 [Moll, 1999][Janesick, 2001].

The main effect caused by displacement damage is the construction of trapping sites affecting majority and minority carriers in the semiconductor. An incident particle transfers momentum to an atom in the target material. Given that the energy imparted to the target atom is greater than

the displacement energy, E_d (in the order of 10-50eV) [Averback and Diaz de la Rubia, 1998], the atom leaves its normal position in the lattice and becomes a Primary Knock-on Atom (PKA).

A particle of incident energy E_I colliding with any atom of mass A (28 for silicon), in which the particle is deflected though an angle θ, will transfer an energy of ΔE [Holmes-Seidle & Adams, 1993] to the PKA such that;

$$\Delta E = 4A/(1+A)^2 . sin^2(\theta/2) \quad (1.6)$$

A 1MeV neutron, for example, can transfer up to 130 keV to a silicon atom. The PKA may collide many times with other atoms in the lattice, potentially causing a cascade of atoms leaving their nominal positions. The space left behind by the atoms is known as a vacancy. The theory of Kinchin and Pease (1955) states that the number of pairs of simple defects (or a Frenkel pair, consisting of a single vacancy and a single interstitial atom) is proportional to the energy imparted to the PKA, ΔE. Each displaced atom will recombine with a vacancy in the lattice or become lodged between atoms in an interstitial state.

Vacancies within the lattice are mobile and can combine with impurity atoms or cluster with other vacancies. These clusters are usually electronically active; depending on their vacancy and impurity constituents, they can act in the same way as dopants and provide carriers in the semi-conductor. They can also act as traps for carriers and increase the number of collisions of carriers within the semiconductor [Holmes-Seidle & Adams, 1993]. Displacement, or 'bulk' damage, although complex, can be modelled accurately using software such as SRIM (Stopping Range of Ions in Matter) [Ziegler et al, 2010].

1.4.2 MAJORITY AND MINORITY CARRIER TRANSPORT DEGRADATION

The majority and minority carriers in a semiconductor are the most abundant and least abundant carriers of charge, respectively. In p-type semiconductor material, holes are the majority carriers and in n-type materials the majority carriers are electrons. In a device such as a MOSFET (Metal Oxide Semiconductor Field Effect Transistor) (Figure 1.7), which contains both n- and p-type materials, the role of minority and majority carriers is more complicated.

The transistor action in a MOSFET device involves the majority carriers of the source and drain but as these carriers traverse the body of the device through the opposite n-type material, they are minority carriers. One of the most important actions of particle-induced traps in a material is the

recombination of minority carriers which carry the electric signal [Holmes-Seidle & Adams, 1993] through the body of the device.

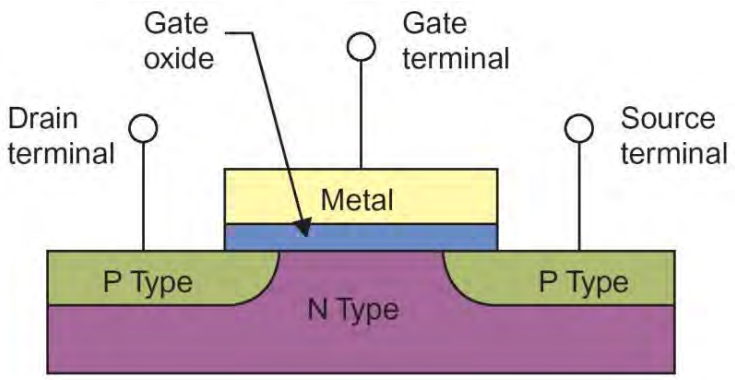

Figure 1.7 A schematic diagram of a MOSFET

Dark current, current which is thermally generated under completely dark conditions, is increased in silicon through damage of the silicon lattice and the creation of lattice defects. Dark current carriers are generated when defects are created within the lattice that result in the introduction of energy levels within the forbidden band gap of the silicon [Janesick, 2001]. Such states in the forbidden band gap act as steps for electrons to more easily move from the valence to the conduction band of the semiconductor.

Generation and recombination of electrons and holes within a semiconductor occurs in four processes. These are electron capture and electron emission, and hole capture and hole emission [Holmes-Seidle & Adams, 1993]. Electron and hole capture are required for recombination, something which rarely occurs within a CCD as signal charge is contained within a potential well where no majority carrier charges can enter and recombine with the signal charge [Janesick, 2001]. Dark current is generated by electron and hole emission. Hole emission is the transition of an electron from the valence band to the centre of the band gap, leaving a hole in the valence band. Electron emission is the transition of the electron from the trap at the centre of the band gap to the conduction band. Once in the conduction band, the electron contributes to the signal in the device as dark current. The hole that is made leaves the CCD through the device substrate [Janesick, 2001]. In order for dark current to be generated, both hole and electron emission must occur near-simultaneously. Energy states with the band gap from silicon defects will more likely

contribute to dark current when they are in the centre of the band gap, where hole and electron transmission from the valence and conduction bands are equally probable.

Shockley-Read-Hall (SRH) theory describes the statistics of electron and hole recombination [Shockley & Read, 1952][Hall, 1952][Janesick, 2001][Holmes-Seidle & Adams, 1993]. The Shockley-Read-Hall equation (1.7) is used to establish the net carrier generation/recombination, U. N_T is the concentration of traps at energy level E_t, E_t-E_i is the energy of the defect level with respect to the Fermi-level, E_i, σ_p and σ_n are hole and electron cross sections (which for simplicity sake are often assumed to be equal) and n and p are the absolute number of electrons and holes respectively. v_{th} is the thermal recombination velocity.

$$U = \frac{\sigma_p \sigma_n V_{th} (pn - n_i^2) N_T}{\sigma_n \left[n + n_i exp\left(\frac{E_t - E_i}{kT}\right)\right] + \sigma_p \left[p + n_i exp\left(\frac{E_i - E_t}{kT}\right)\right]} \tag{1.7}$$

For a CCD in thermal equilibrium, $pn = n^2$ and $U = 0$ indicating that generation and recombination are equal. Negative U suggests a net generation rate of electron-hole pairs whereas a positive U indicates a net recombination rate [Janesick, 2001].

The SRH theory predicts that, for few excess carriers, diffusion lengths and minority carrier lifetimes in silicon vary according to equations (1.8) and (1.9), where τ is the minority carrier lifetime after irradiation, τ_0 is the initial minority carrier lifetime, K_τ is the minority carrier lifetime damage constant (dependent on material, particle type and temperature), L is the diffusion length after irradiation, L_0 the initial diffusion length, K_L is the minority carrier diffusion length damage constant (also dependant on material, particle type, injection level and temperature) and Φ is the particle fluence [Holmes-Seidle & Adams, 1993].

$$\frac{1}{\tau} - \frac{1}{\tau_0} = K_\tau \Phi \tag{1.8}$$

$$\frac{1}{L^2} - \frac{1}{L_0^2} = K_L \Phi \tag{1.9}$$

The damage factors K_τ and K_L are practical factors determined by experiment that are used to linearise degradation of diffusion length or minority carrier lifetime over the range of interest. T and L are inversely proportional to Φ when K_τ and K_L are applied. This can then be used to normalise test results for different particle fluences. It is standard in many damage experiments

to quote the fluence in terms of 1MeV neutrons so the SRH theory is important when comparing test results, such as those reported in Chapter 2 which use 10MeV protons, and other experiments in the literature [Segneri, 2009] [Bortoletto, 2006][Moll, 1999][ROSE, 1999]. This is called NIEL scaling and is discussed in the following section.

In a CCD, the reduction in the number of charge carriers due to trapping sites and recombination results in the loss of measured charge. When X-ray photon counting, this effect is enhanced as a small fraction of charge loss results in significant degradation of spectral resolution. Redistribution effects and reduced charge transfer efficiency, as discussed in Chapter 2 and Chapter 4, are major problems in radiation damaged CCDs.

The DEPFET devices discussed in the chapter, however, are considered to be more radiation hard than CCDs due to the way in which they are read out. Rather than transferring charge from pixel-to-pixel as with a CCD [Treis, 2007], the DEPFET is an active pixel sensor and reads out the X-ray-generated charge in each pixel. Trapping sites generated in the silicon do not, therefore, have such a large effect on the DEPFET as charge transfer efficiency from pixel-to-pixel is not an issue.

1.4.2.1 NON IONIZING ENERGY LOSS (NIEL) SCALING

Non-Ionizing Energy Loss (NIEL) scaling is used to model the effect of broad energy spectra, of different particles, interacting with semiconductor devices. The scaling allows a broad spectrum to be equated with a fluence of a single energy and particle type. This is very useful when conducting damage experiments, allowing the use of monoenergetic particles to represent broad mixed-particle spectra such as those seen in orbit by satellites.

The PKA energy spectra for various incident particles and energies are very different. Despite this difference, a very good linear relationship exists between NIEL (energy deposited by radiation per unit target mass) and device degradation. It is found [Dale and Marshall, 1991] that the original energy spectrum is lost and the resultant stable defects throughout the material are similar for electrons, protons and neutrons over a wide range of energies.

Table 1.3 shows the calculated values [Burke, 1986][Holmes-Seidle & Adams, 1993] of NIEL scaling for protons, normalised to 10MeV. The Mercury Environmental Specification document [BepiColombo Environmental Specification, 2006] uses this scaling to convert the expected broad energy proton spectrum for the BepiColombo mission to an equivalent 10MeV and 60MeV proton

fluence. The 10MeV equivalent proton fluence provided by ESA was used in the presented proton damage experiment presented in Chapter 2 to establish the proton dose needed for conducting a representative irradiation of the MIXS diodes. NIEL(E)/NIEL(10) is the scaling of NIEL at a given energy to NIEL at 10 MeV.

Proton Energy (MeV)	NIEL in Si (KeV cm^2g^{-1})	$\frac{\mathbf{NIEL(E)}}{\mathbf{NIEL(10)}}$
0.01	2000	290
0.02	1300	188
0.03	1000	145
0.05	690	100
0.07	540	78.2
0.1	410	59.4
0.2	240	34.8
0.3	170	24.6
0.5	110	15.9
0.7	85	12.3
1.0	63	9.13
2.0	32	4.64
3.0	22	3.10
5.0	14	2.03
7.0	9.8	1.42
10	6.9	1.0
20	4.7	0.681
30	4.3	0.623
50	3.7	0.536
70	3.3	0.478
100	3.0	0.434
200	2.4	0.348
300	2.2	0.319
500	2.0	0.290
700	1.7	0.246

Table 1.3 10MeV Proton NIEL Scaling in Silicon
(from Holmes-Seidle & Adams, 1993 and calculated by Burke, 1986)

1.5 THE INTERNATIONAL X-RAY OBSERVATORY

The International X-ray Observatory (IXO) [Bavdaz et al, 2009][ESA, 2009] is a large X-ray telescope mission currently being assessed by the European Space Agency and NASA as a potential future mission concept. The author of this thesis is currently employed by Astrium Ltd in the UK as the System Engineer for the ESA IXO Assessment Study, with particular responsibility for the payload complement. IXO is an ideal case study for investigating the current state-of-the-art optics and detector technologies. The telescope utilizes a complement of six focal plane detectors, each using a different detector technology. The large range of science goals of the mission requires an extremely diverse capability from the detectors. IXO is described in detail in Annex I, outlining the science case, payload contingent and X-ray optics.

The IXO detectors are sensitive to radiation damage. The silicon-based Wide Field Imager uses a Depleted Field Effect Transistor (DEPFET) Active Pixel Sensor (APS) array [Treis, 2007], similar to that used on the BepiColombo MIXS instrument. The experiments outlined in the following Chapter investigate the radiation hardness of the DEPFET APS detector, with the results directly applicable to the WFI detector on IXO. The ability to recover some detector performance from thermal annealing is also demonstrated.

1.6 THE SUBJECT OF THIS THESIS

X-ray astronomy can only be conducted from space due to the Earth's atmosphere's opacity to photons at this energy. As such, space-based telescopes are necessary in order to observe X-ray emitting objects. There are a number of desirable features that scientist require from their instruments, depending on the application:

- Good spectral resolution. This parameter is very application specific, ranging from a few eV @ 1keV such as for the X-ray Microcalorimeter Spectrometer on IXO to a few hundred eV @ 1keV such as for BepiColombo MIXS.
- Good spatial resolution. As X-ray optics improve, it is necessary to ensure that detectors have a compatible spatial resolution. It is important that the detectors do not limit the ability to resolve target features when imaging.
- Good temporal resolution: Many observations require fast detectors in order to view objects with a very high count rate. Also, some objects change rapidly with time.

- Polarization sensitivity: The least explored aspect of X-ray astrophysics, polarization provides a great deal of information on the geometry of X-ray emitting objects.
- Good quantum efficiency at low energies: Very soft X-rays <300keV are of great interest to scientists. Such soft X-rays are very easily absorbed by filters and the detector layers in front of the active region of the device. Pushing quantum efficiency up at lower energies is very desirable.
- Good quantum efficiency at high energies: Hard X-rays (>20keV) are also of interest to astronomers. These X-rays have a tendency to pass through X-ray detectors with no interaction with the device active layer. Also, often a successful interaction will result in a very large multipixel event being registered with its associated reduction in spectral resolution due to device thresholding.
- Radiation hardness: Instruments exposed to radiation in the space environment will degrade. The ability to resist such damage is very desirable for such detectors.

The space environment is very challenging for spacecraft systems and instruments, with spacecraft experiencing significant temperature variations and gradients as well as a challenging radiation environment.

Radiation damage is one of the most significant challenges of the space environment. Unlike telescopes on the ground, there is no ready means to change or repair damaged equipment. It is therefore vital to manage the damage devices receive over their operational lifetime. This will ensure that the instrument end-of-life operational requirements are met.

There are a number of aspects related to radiation that must be known if radiation damage is to be managed. Firstly, it is important to establish the radiation environment that the spacecraft will be subject to. This can be done either by establishing the environment via in situ measurements or by employing modelling tools, such as the ESA SPENVIS package, as used in this thesis when considering the BepiColombo mission to Mercury. Once the environment is better understood, the effect of radiation on the instrument must be established to estimate the extent of the radiation damage the device will suffer over the course of the mission. Again, this can be done via measurement, such as done in Chapter 2 of this thesis, or by modelling using such packages as SRIM [Ziegler et al, 2010].

The following Thesis Chapters discuss the research conducted as part of this thesis into X-ray detectors for future missions, focusing particularly on the effects of radiation damage and its mitigation. In addition, methods to improve the quantum efficiency and spectral resolution of X-ray detectors are investigated.

X-ray science in space is not just limited to astrophysics such as in the context of the International X-ray Observatory [Parmar, 2009], but is also a useful tool in planetary science, both from orbit, as used in the Mercury Imaging X-ray Spectrometer experiment on BepiColombo, or in situ on a planet's surface, such as the X-ray Diffractometer (XRD) instrument proposed for the ExoMars rover. The constant improvement of X-ray Instrumentation is necessary to ensure that technology is sufficiently developed for implementation on future planetary science and astrophysics missions.

The radiation environment for X-ray missions has a broad range from the relatively benign (though not insignificant) environment of the second Lagrange point (L2) to the extreme harsh radiation environment in orbit around Mercury which is in close proximity to the sun. Knowledge of how such environments affect the detectors used in radiation-sensitive detectors is essential if mission requirements are to be met towards the end of the mission lifetime. The DEPFET detectors used on BepiColobo's MIXS instrument, for example, has an end-of-life spectral resolution requirement of 200eV @ 1keV. Proton damage experienced by the detectors, both in transit to Mercury as well as in the planet's orbit, will result in a degradation of the spectral resolution beyond this requirement, necessitating a detector anneal in order to recover device performance. This is discussed in detail in the next Chapter.

The research presented herein has been used in the development of the MIXS focal plane detectors. Research into the radiation damage experienced by the XMM-Newton detectors and a novel CCD structure with potential applications for a future wide field imager, such as the WFI of the IXO mission, was also undertaken and is reported. Monte Carlo modelling of the spectral response and quantum efficiency of this new device was coupled with laboratory experiment in order to determine the CCD depletion depth. Modelling was also conducted to investigate the scenario of non-normal incidence X-rays to the CCD surface and its effect on detector spectral response.

1.7 THESIS STRUCTURE

This thesis consists of four further Chapters. Chapter 2 introduces the Mercury Instrument X-ray Spectrometer (MIXS) [Fraser, 2010] and the Depleted Field Effect Transistor (DEPFET) Active Pixel Sensor (APS) [Treis, 2008], and presents the research conducted as part of this thesis into the radiation tolerance of diodes manufactured on DEPFET wafers. The increased leakage current resulting from a proton irradiation experiment, representative of the fluence expected during the BepiColombo mission, was established. An annealing experiment showed that a significant improvement in spectral resolution can be achieved post-irradiation if an annealing programme is followed, and, from this experiment, the recommendation that the BepiColombo MIXS detectors are annealed at least once during the mission was made.

Chapter 3 follows with the research carried out in the investigation of X-ray radiation damage observed by the XMM-Newton spacecraft. A Microchannel Plate Optic was used to simulate ionizing damage seen in orbit to an XMM CCD22. The results from this experiment shed new light onto the mechanism of this damage and are currently being used by the XMM-Newton Instrument Calibration Team in their detector response modelling.

Chapter 4 presents experimental work investigating a novel CCD structure, the CCD66. The experiment attempted to improve two of the key characteristics of the CCD, the quantum efficiency and spectral resolution, by applying an external negative substrate voltage to the device. The response of the device to this negative substrate voltage was obtained and improvements in QE and spectral resolution were shown. A Monte-Carlo model was used to investigate the manipulation of the CCD66 depletion region and the results of this modelling work are presented in the chapter.

Chapter 5 reports on the investigation of CCD response to X-ray angle of incidence. The model used to investigate the CCD66 response in Chapter 5 was modified to establish the effect of changing the angle of incidence and the results are presented in the chapter. Initial laboratory results of an experiment conducted by Huawei Su, another current postgraduate student at the University of Leicester, investigating the response of a CCD to X-ray angle, are also presented and compared with the modelling work.

Chapter 6 provides some concluding remarks.

In addition to the main content of the thesis, two annexes are provided which contain further information and work conducted during the PhD which are related to the subject of X-ray Instrumentation but fall slightly outside of the context of the subject at hand. Annex 1 provides a case study, detailing the scientific payload for the International X-ray Observatory. This information puts the work presented in this thesis into the context of the next large X-ray telescope likely to be placed in orbit. The mission uses many different types of X-ray instrument, from a gas-based polarimeter to a high spectral resolution camera which uses a cryogenic transition edge sensor. IXO demonstrates the diverse range of detector requirements that must be met for future X-ray astronomy.

Annex 2 describes work carried out by the author in the field of X-ray optics. Included here is the characterisation of a microchannel plate optic which, for the first time, demonstrates an intrinsic spatial resolution which meets the requirements of many future X-ray mission such as BepiColombo MIXS.

CHAPTER 2

PROTON IRRADIATION AND ANALYSIS OF MIXS REPRESENTATIVE SILICON DIODES

2.1 THE BEPICOLOMBO MISSION AND RADIATION CONCERNS

The BepiColombo mission to Mercury, introduced in Chapter 1, will experience a harsh radiation environment over the duration of its life; 6 years of interplanetary transit in the inner solar system and 2 years in orbit around Mercury. The Mercury Environment Specification document [BepiColombo MIXS Environment Specification Part II, 2006] provided by the European Space Agency (ESA) details the expected radiation doses the spacecraft will receive during transit and operations from both ionizing and non-ionizing sources.

The MIXS instrument [Fraser et al, 2010] uses a silicon-based Depleted Field Effect Transistor (DEPFET) Active Pixel Sensor (APS) array [Treis et al, 2007] in the focal plane of each optic element. A key mission concern is the ability of the DEPFET array to withstand the expected radiation environment at Mercury. The radiation environment is dominated by low energy (10-1000 keV) electrons and (0.1-60MeV) solar protons, with a lesser contribution from galactic cosmic rays [BepiColombo MIXS Environment Specification Part II, 2006]. Mission radiation specifications have been obtained using the JPL-1991 Standard Solar Particle Event Model for protons [Feynman et al, 1993] and the NASA/GSFC Trapped Electron Model for electrons [Vette, 1991]. A $1/r^2$ scaling, where r is the distance of the spacecraft to the sun, was employed by ESA to obtain the radiation values at Mercury. It is noted that this is a simplification, yet worst case assumption, of the actual radiation environment due to the highly elliptical orbit of spacecraft around Mercury. The radiation environment for the BepiColombo mission [BepiColombo MIXS Environment Specification Part II, 2006] is discussed in more detail in Section 2.2.1.

The protons will cause displacement damage in the silicon detectors, where silicon atoms are displaced from their nominal positions in the crystal lattice, resulting in an increase in dark current. Displacement damage results in energy levels being created in the band gap of the semiconductor, allowing easy promotion of charge carriers into the conduction band, thereby

leading to the dark current increase [Holmes-Seidle & Adams, 1993]. Both electrons and protons also cause ionisation damage, but this is expected to be less serious, with displacement dominating the radiation damage [BepiColombo MIXS Environment Specification Part II, 2006]. This displacement damage is expected to cause an elevation of dark current within the detectors, thereby limiting the end-of-life energy resolution of the instruments. An energy resolution of at least 200eV in the band 0.5 to 2keV is needed at the end of the detector life in order to achieve the mission science requirements [Carpenter and Fraser, 2007]. This resolution is required in order to distinguish between important spectral lines: For example, Mg-Kα, Al-Kα and Si-Kα [Fraser et al, 2010].

The radiation damage in similar detectors has been measured in the context of instruments for particle physics [Moll, 1999], but the applicability of the results to the BepiColombo mission needs to be verified by experiment. It is common practice to represent the intensity of particle irradiation by its equivalent fluence of 1 MeV neutrons [ROSE, 1999], with proton damage subsequently inferred by using a scaling factor. Furthermore, most measurements have been made with 300 µm thick samples, whereas the MIXS detectors use 450 µm thick silicon. The MIXS DEPFET devices are limited to 450 µm thick silicon by the wafer manufacturing and implantation methods.

This Chapter discusses the preliminary radiation test programme undertaken to test the behaviour of silicon diode devices, manufactured using the same processes as the MIXS DEPFET devices, exposed to radiation damage corresponding to the Mercury environment. The proton radiation dose used in these tests was established using the mission Environment Specification [BepiColombo MIXS Environment Specification Part II, 2006] which employs a standard bulk damage equivalence, Non Ionizing Energy Loss scaling, in order to express the total mission dose in terms of 10 MeV protons. The purpose of these tests is to measure the susceptibility of devices representative of the macropixel arrays to low energy (10 MeV) protons.

Large area diodes (0.5cmx0.5cm and 0.32cmx0.32cm), manufactured on the same n-type silicon bulk material as the real DEPFET detectors, using identical manufacturing processes, were utilised in the test. When a set of DEPFET devices are manufactured, spare areas of the silicon wafer are used to create test diodes. The data presented in the chapter were collected when testing such test diodes. Future tests will be conducted using more representative, flight-type devices in the

context of the BepiColombo MIXS programme, with DEPFET devices also undergoing a similar development programme for the International X-ray Observatory [Treis, 2009].

The experiment used 10 MeV protons with a range of fluences up to ~1x10^{11} prot.cm^{-2}. The detectors used for the BepiColombo mission will accumulate ~3x10^{10} prot.cm^{-2}, calculated using the aforementioned bulk damage equivalence in the environmental specification. The first half of this dose will be accumulated during the 6-year transit period between Earth and Mercury, the second half during the 2-year nominal operation of the spacecraft around the planet [BepiColombo MIXS Environment Specification Part II, 2006].

2.1.1 THE CURRENT RELATED DAMAGE RATE

The current related damage rate, α, is defined by:

$$I = \alpha \Phi_{\mathrm{eq}} \mathrm{V} \tag{2.1}$$

Where I is the measured dark current, Φ_{eq} is the 1MeV neutron equivalent irradiation fluence (per cm^2) and V is the sensitive volume. The hardness factor, κ, analogous to the damage factors K_τ and K_L in equations (1.8) and (1.9), can be used to convert the 1 MeV neutron equivalent fluence to a 10MeV proton fluence, Φ_{prot}, given the appropriate value of κ.

$$I = \alpha \kappa \Phi_{\mathrm{prot}} \mathrm{V} \tag{2.2}$$

It has been found that α is independent of doping species and concentration in Silicon used for high energy particle detectors [ROSE, 1999]. In equation (2.2), the proportionality of I with V depends on the assumption that the damage incurred is uniform along the particle track. This assumption, however, is not true for low (<1MeV) energies [ROSE, 1999]. The energy deposition becomes non-uniform, depositing more energy at the end of the track. At low energy the nature of the radiation-induced damage changes from defect clusters to point defects. These are less generation-active; that is, they produce less dark current. The majority of silicon devices tested for particle radiation damage have a thickness of 300 µm. The MIXS detectors, however, use a 450 µm silicon wafer. It is necessary, therefore, to establish the damage rate for this thicker silicon as the effective α in 450 µm silicon may not be the same as in 300 µm silicon [Treis, 2007]. The accepted value of α is (3.99±0.03)x10^{-17} Acm^{-1} for 300 µm silicon-based semiconductor detectors as measured by the RD48 collaboration [ROSE, 1999]. An experiment to determine the value of α for the BepiColombo MIXS diodes was conducted and is reported in Section 2.2.

2.1.2 THERMAL ANNEALING

Bulk damage can be reversed by applying thermal energy to the crystal lattice, thereby increasing the motion of atoms within the material, allowing trapped interstitials to return to vacant sites. Repairing the crystal lattice in this way can recover some of the performance of semiconductor detectors, such as CCDs [Rose, 2004][Holmes-Seidle & Adams, 1993][Moll, 1999].

Thermal annealing can also be employed as a diagnostic tool for determining radiation damage, as different types of lattice defects anneal at different temperatures. The material temperature is raised in incremental amounts at regular time intervals, the radiation effects being measured after each temperature change. This method of defect diagnosis is known as an *isochronal anneal*. As certain defects tend to anneal out at quite specific temperatures it is often possible to establish the type of defects present by measuring macroscopic properties of the device such as leakage current [Moll, 1999][Lindstrom, 2001].

Damage, when incurred at low temperature (~80K) is frozen into the crystal lattice. When the temperature is raised, the damage sites migrate through the lattice, combining to form a series of complexes. The electronic property of each complex can differ, resulting in an initial increased dark current. This is known as *reverse annealing*. Recovery of device performance can be achieved by holding the device at a high temperature (>50°) [Holmes-Seidle & Adams, 1993]. Despite initial reverse annealing effects, performance will be recovered if the temperature is great enough. Holding a device at a steady high temperature is known as an *isothermal anneal*. The experiment described in Section 2.2.8.3 makes use of an isothermal anneal in order to establish and quantify the ability to recover MIXS detector performance after a significant dose of proton radiation.

2.2 MIXS PROTON IRRADIATION EXPERIMENT

The most critical effect of the radiation damage to the devices is the increase in bulk leakage current. This directly affects the energy resolution of the devices. The increase in dark current through bulk damage results in an increase in noise and, therefore, a degradation of the spectral resolution obtained by the device. The two other major effects, namely bulk donation change, which is the gradual inversion of conductivity type through the inactivation of dopants in the material [Holmes-Seidle & Adams, 1993], and ionizing damage, are less critical for the given radiation levels of the mission [Holmes-Seidle & Adams, 1993][Janesick, 2001].

Most of the published results (e.g. [ROSE, 1999][Moll, 1999][Vasilescu, 1998][Glaser et al, 1999][Lindstrom, 2001]) have been measured with samples 300 µm thick and, in initial modelling of the DEPFET detectors performed by the Max Planck Institute Semiconductor Laboratory (MPI-HLL) in Munich, it is assumed that the damage scales with volume, independent of the sample thickness. It is known that the damage is dependent on the type and energy of the particle. It is also known that the damage can be partially reversed by annealing at elevated temperature [ROSE, 2004][Holmes-Seidle & Adams, 1993][Janesick, 2001].

2.2.1 THE MERCURY PROTON RADIATION ENVIRONMENT

The BepiColombo Environmental Specification (2006) is provided by ESA as a reference document to academia and industry involved in payload and spacecraft development. The document gives guidance on the expected environmental factors expected at Mercury based on the SPENVIS (Space Environment Information System) models [SPENVIS, 2010]. Information is given on modelled solar and planetary electromagnetic radiation, plasma, particulates and energetic particle radiation.

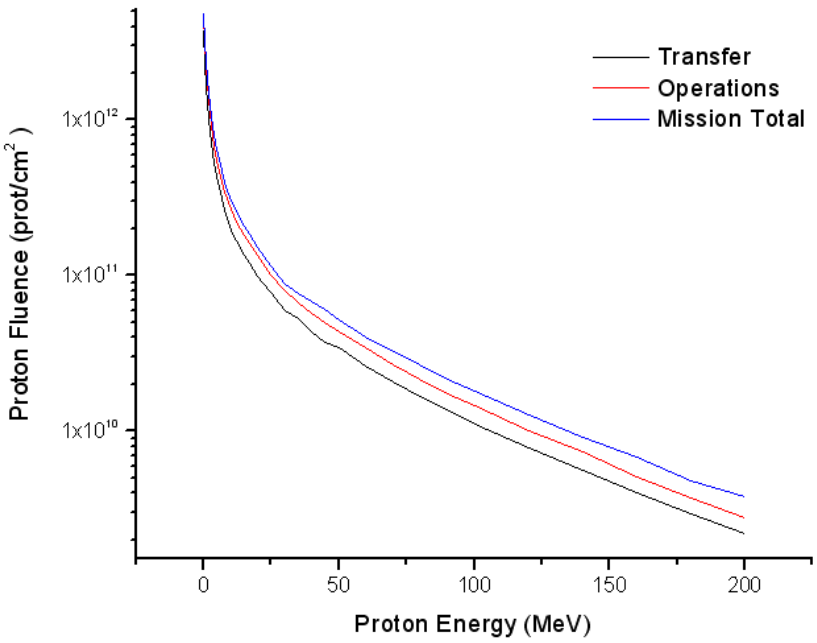

Figure 2.1 The expected proton fluence at different energies expected during the transfer and operation phases of BepiColombo. Modelled data taken from [BepiColombo MIXS Environment Specification Part II, 2006], modelled using the JPL-91 model [Feynman, 1993]

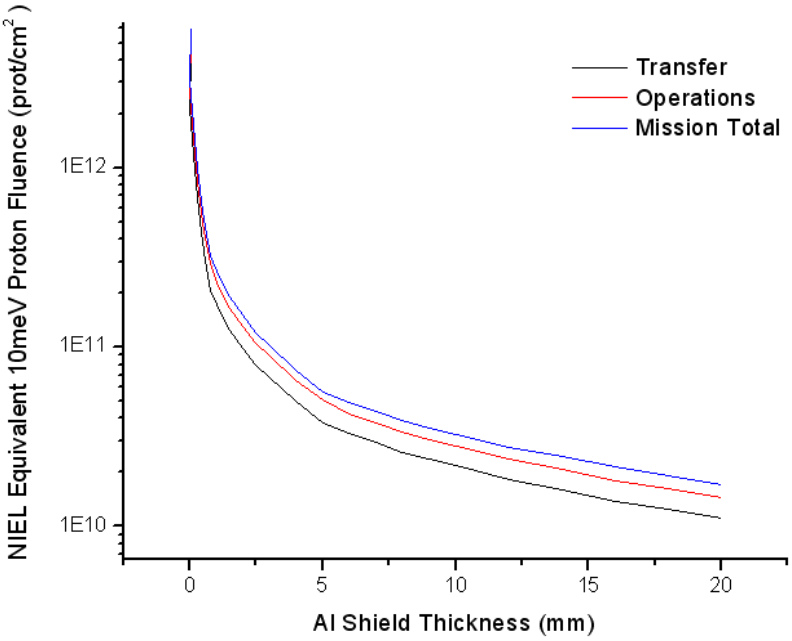

Figure 2.2 The NIEL equivalent 10MeV proton fluence experienced by BepiColombo for different Al shielding thickness for the two main phases of the mission. Modelled data taken from [BepiColombo MIXS Environment Specification Part II, 2006], modelled using the JPL-91 model [Feynman, 1993]

Figure 2.1 shows the expected proton fluence at different energies for the BepiColombo mission during the two main phases; transfer to Mercury and mission operations. The total fluence (protons per cm^2) is also shown. The proton spectrum is dominated by lower energy protons (<50MeV) and therefore the radiation shielding of the spacecraft and sensitive instruments will need to take these energies into account.

Using the NIEL scaling, the NIEL equivalent 10MeV proton fluence is calculated for the whole proton spectrum. Figure 2.2 shows this equivalent fluence for different thicknesses of aluminium shield. The aluminium shield changes the spectrum of protons such that the majority of lower energy protons (<50MeV) are stopped.

For the purpose of this experiment, it is assumed that the equivalent of 5mm of aluminium shielding is present in all directions around the DEPFET detector. In practice, this cannot be true as the entrance window to the detector cannot be covered by any shielding. A particle diverter is required to deflect low energy protons (up to ~90keV) but higher energy protons will hit the detector from this side. The field of view of the detector to particles will also be limited somewhat by the telescope baffle which connects the optics to the focal plane assembly.

In order to establish a more accurate radiation dose to the DEPFET detector, a more complex model using a tool such as GEANT4 [Agostinelli, 2003][Allison, 2006] could be used, but in order to get a meaningful dose estimate from such a package, a more accurate configuration model for the BepiColombo spacecraft was needed. Prior to this experiment, this was not available so the assumption of an equivalent 5mm omni-directional Al shield was made.

From Figure 2.2, this assumption results in a proton fluence of ~$3x10^{10}$ protons per cm^2 during the mission. Note that the total mission dose presented is *not* equal to the sum of the two mission phases. This is due to two separate models being used to produce the data for the separate phases and the total mission [BepiColombo MIXS Environment Specification Part II, 2006]. The diodes tested in this experiment will be irradiated up to ~$1x10^{11}$ protons per cm^2 at 10MeV in order to provide a representative damage effect analysis.

2.2.2 TEST AIMS

There were three primary aims of the MIXS Proton Irradiation Experiment:

1) to measure the damage rate, α, which relates the increase in leakage current to the proton fluence, using a representative 450 μm thickness of silicon and 10 MeV protons. Knowledge of α will be directly useful for estimating the damage in the BepiColombo mission. It will also determine whether the results are consistent with the assumed scaling laws with energy and particle type.

2) to measure the effect of annealing. Previously reported results have all applied some annealing to the test samples at elevated temperature. The MIXS detectors, on the other hand, will be at <~–40°C for the whole of the mission, unless specific provision is made for annealing. A measurement of the annealing effect will assist in correlating results with previous work, and determine if annealing during the mission will be beneficial, feeding directly into the instrument design.

3) to determine the temperature required for significant annealing.

2.2.3 THE DEPFET DETECTOR

The experiment reported in the chapter use diode samples rather than a full DEPFET detector. It is necessary, however, to discuss the complete DEPFET detectors in more detail.

A DEPFET detector consists of a p-channel field effect transistor and an n-type clear contact placed on a fully depleted n-type silicon substrate. The substrate is fully depleted by the large diode on the back side of the wafer and the p+ contacts of the FET. A potential minimum for electrons is thus formed beneath the channel of the transistor, as shown in potential distribution diagram in Figure 2.3. A deep n- implantation layer underneath the transistor region in actual DEPFET devices is used to further confine the potential minimum.

Electrons created by ionizing radiation are collected in the internal gate. The signal charge can then be removed from the internal gate by applying a positive voltage pulse into the clear contact. The DEPFET has the combined function of sensor and amplifier. Optimized noise performance is achieved, as well as the prevention of baseline shift and internal gate overflow, by completely removing the electrons in the internal gate by a clear pulse (~15V) after an integration cycle.

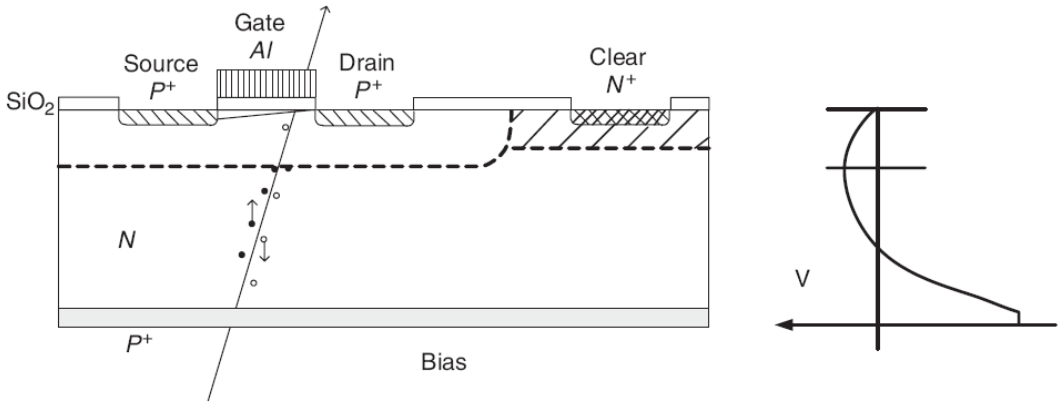

Figure 2.3 Left: A schematic showing the DEPFET structure. Right: A potential distribution along a cut across the wafer in the gate region of the device. [Zhang, 2006]

In order to increase the sensitive area of a DEPFET pixel, a drift diode is used to collect signal charge and then transport the charge to the DEPFET internal gate using the sideways depletion principle [Lechner, 2004]. Figure 2.4 shows a Silicon Drift Detector (SDD) which uses this principle. Electrons created in the silicon by incident radiation move upwards towards the front of the device while also drifting towards the centre of the detector. The electrons are then collected by

the collection anode which is connected to the gate of the J-FET. This is analogous to a single DEPFET pixel, where the silicon drift rings surround a DEPFET gate, and is the principle behind the macropixel concept. In principle, the number of pixels on a DEPFET Macropixel Detector is limited only by the size of the silicon wafer on which the detector is made. [Zhang, 2006] The macropixel concept also allows relatively large pixels to be constructed. The two identical MIXS DEPFET detectors each consist of 64x64 pixels, each pixel 300µm x 300 µm in size.

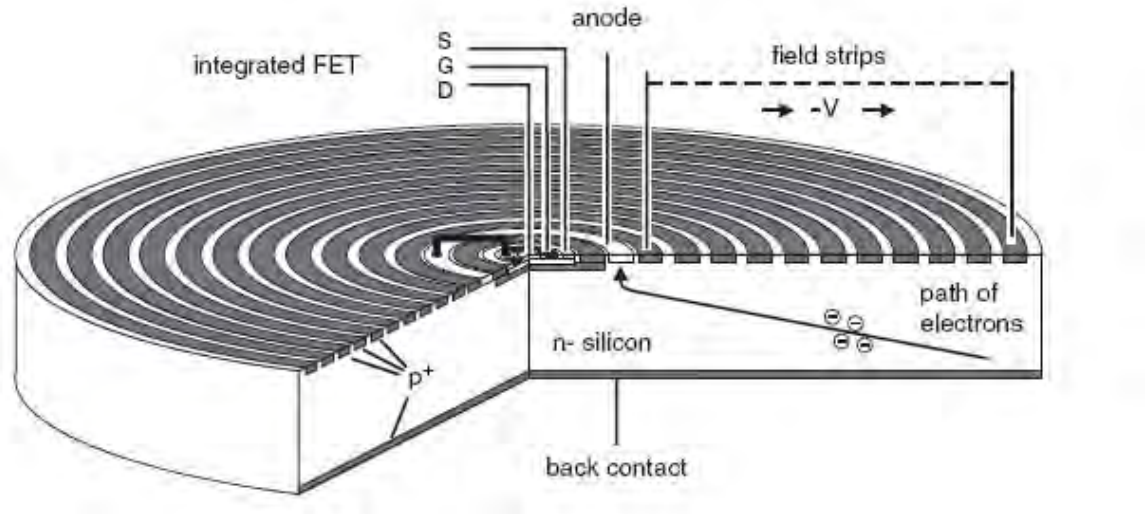

Figure 2.4 A Silicon Drift Detector with an integrated J-FET. [Zhang, 2006]

2.2.4 DEPFET DIODE SAMPLES

The DEPFET detectors that will be used on BepiColombo MIXS are printed and processed on large silicon wafers by the Max Planck Institute Semiconductor Laboratory (MPI-HLL) in Munich, Germany. In order to maximise the use of individual wafers, test diodes are printed in the small regions around the larger detectors. These diodes undergo manufacturing processes identical to the main devices on the wafer and are an equal thickness of 450µm. Five such diodes are used in this experiment.

Each test sample used is a single die with three diodes and one Metal Oxide Semiconductor (MOS) capacitor. The MOS capacitor, labelled C1 in Figure 2.5, is not used in these tests. Each sample is 1.2 cm × 1.2 cm. D1 is 5 mm × 5 mm and D2 and D3 are both 3.2 mm × 3.2 mm. This size difference was accounted for in the analysis of the dark current data. All three diodes were irradiated simultaneously in a proton beam at the University of Birmingham Cyclotron facility by

the author. The proton beam had a cross-section larger than the diode sample. The samples were delivered on a silicon substrate with the connections bonded to a header as shown in Figure 2.6.

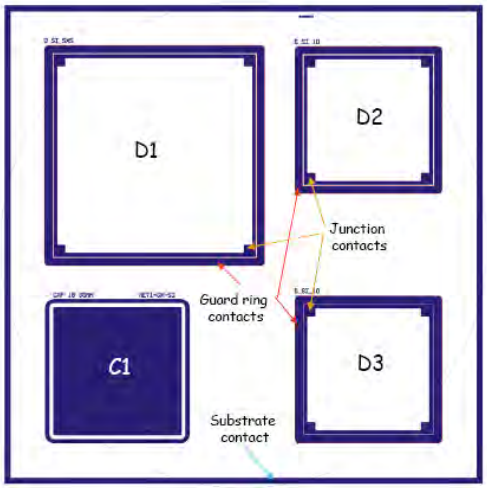

Figure 2.5 Aluminium mask of a test die, showing the sample layout. The sample consists of three diodes, D1, D2 and D3, and one test capacitor, C1

The samples were each mounted onto a printed circuit board (PCB). The PCB was used to fix the sample to the irradiation test jig fabricated to interface the diodes to the University of Birmingham's Medical Physics Department Cyclotron. Figure 2.7 shows two photographs of the diode sample C05 mounted on the PCB.

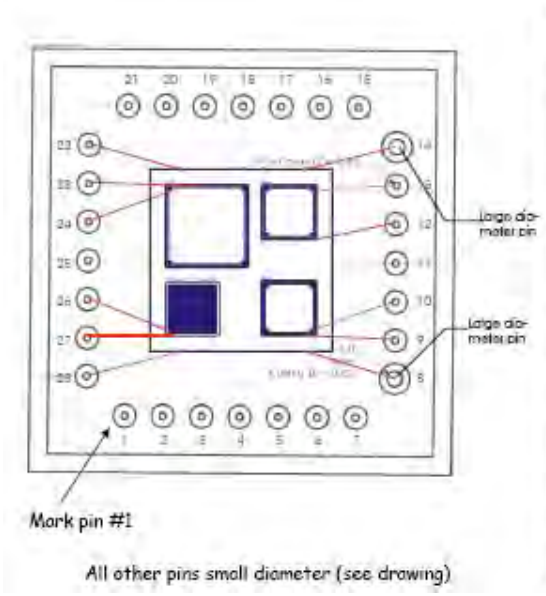

Pin #	Contact	Comment
8	Substrate	Common N bulk
9	D3_GRD	Guard ring for D3
10	D3_P	P contact for D3
12	D2_GRD	Guard ring for D2
13	D2_P	P contact for D2
14	Substrate	Common N bulk
22	Substrate	Common N bulk
23	D1_GRD	Guard ring for D1
24	D1_P	P contact for D1
26	C1_C	Capacitor C1
27	C1_GRD	Guard ring for C1
28	Substrate	Common N bulk
Any other	Floating / GP	Not connected

Figure 2.6 Diode Sample Pin-out diagram and table

Irradiation with energetic protons results in a measurable increase in dark current production, so the damage will be determined by a measurement of the leakage current of a diode with a Keithley electrometer. The electrometer had to be able to measure very small currents down to the picoamp range.

In order to achieve the aims set out in section 2.2.2, the following tests were carried out:

1) Pre-Irradiation measurements of leakage current at room temperature (20°C) and at –40°C of all diode samples
2) Damage factor measurement of three samples, irradiated using different fluences
3) Annealing properties test of a single sample, with one irradiated sample held in reserve for further annealing tests if required.

Table 2.1 shows the designation of each test sample and the corresponding dose given to each. Note that during pre-irradiation tests one of the diodes failed, resulting in only four samples being irradiated. The methods employed in the tests were used by the ROSE collaboration and are fully reported in [ROSE, 1999].

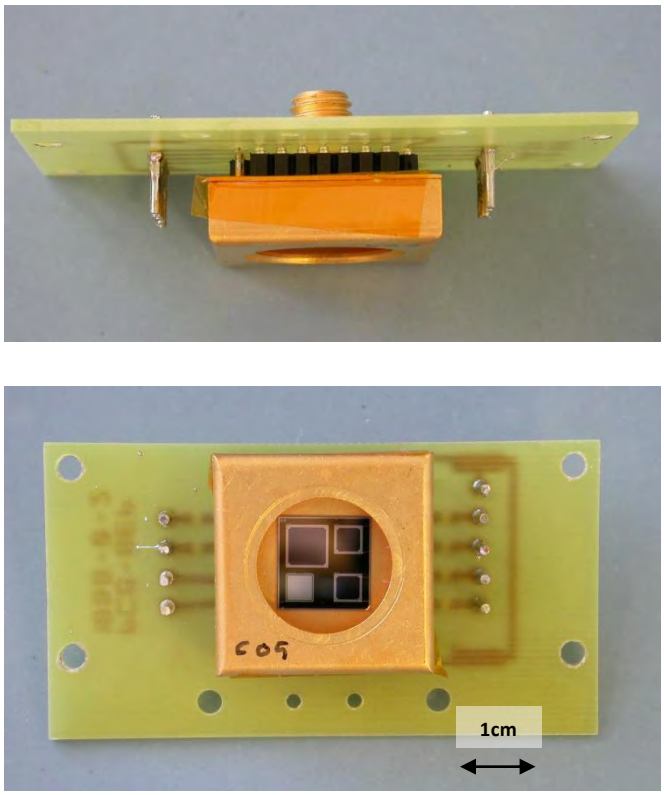

Figure 2.7 Photographs of sample C05 mounted on a PCB

Diode Name	Approximate Irradiation Dose	Test
C07	$3x10^{10}$ Protons	Annealing
C05*	$3x10^{10}$ Protons	Annealing
G03	$1x10^{10}$ Protons	α determination
E05	$5x10^{10}$ Protons	α determination
C03	$1x10^{11}$ Protons	α determination

Table 2.1 Diode designations and approximate radiation fluence to be administered during the test. *Sample C05 was non-operational so was not irradiated or tested in the experiment

2.2.5 PRE-IRRADIATION TESTS

Each of the diodes were initially characterised by MPI-HLL before being delivered to the University of Leicester. In order to establish the correct bias voltages required to fully deplete the devices, a capacitance versus voltage (CV) curve was also established for each diode by MPI-HLL. A depletion voltage of 140V was observed. The RD50 Consortium, a group which conducts damage experimentation for CERN, has compiled a standard set of procedures for damage testing silicon devices [ROSE, 2004]. Following one of these procedures, the diodes used in this test are biased at 190V, 50V above the depletion voltage. This over-bias ensures that diodes are completely depleted at all times throughout the experiment.

The diode characterisation was repeated at the University of Leicester, both at 20°C and at -40°C. As the diodes are light sensitive, the samples were mounted in a die cast aluminium box containing a Platinum Resistance Thermometer (PRT), with the temperature controlled using an environmental chamber. Dry nitrogen was pumped into the chamber and through the aluminium box to prevent condensation. Figure 2.8 shows a sample in the die cast box.

Figure 2.9 shows an example I-V curve measured at Leicester with the accompanying MPI-HLL data for comparison. Approximately a difference of a factor of two is seen between the two sets of measurements, true of all I-V curves taken using these diodes at the University of Leicester and MPI-HLL. The currents being measured, however, are so small that this difference is insignificant. The shape of the curve taken at Leicester is consistent with standard I-V curves for a diode of this type. All pre-irradiation I-V curves produced at Leicester and MPI-HLL are in Appendix II.

During the pre-irradiation tests, sample C05 failed to work. Inspection of the device under a microscope was inconclusive as all bond wires appeared to be attached correctly. In addition to this, D1 on C07 showed evidence of breakdown in the I-V curve. Figure 2.10 shows this I-V curve. Due to this problem D1 on C07 was not used and sample C07 was used only for the less crucial annealing test.

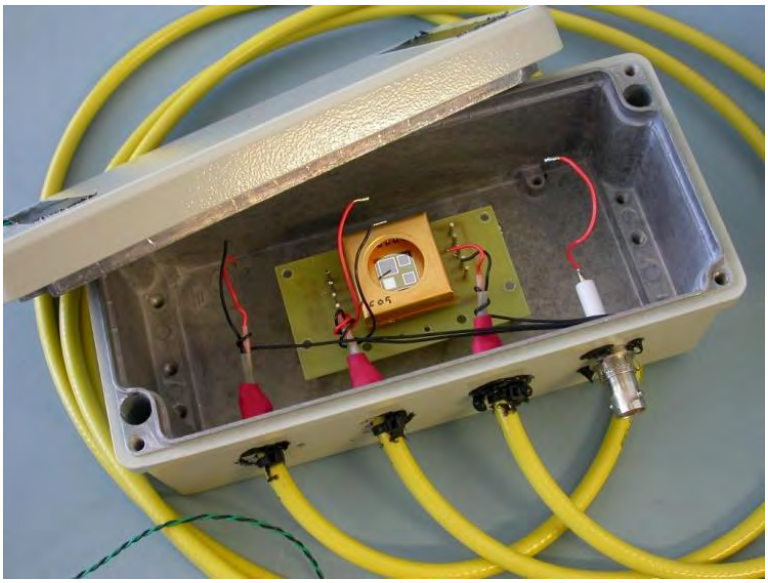

Figure 2.8 The test sample mounted inside the die-cast box used for dark current measurements

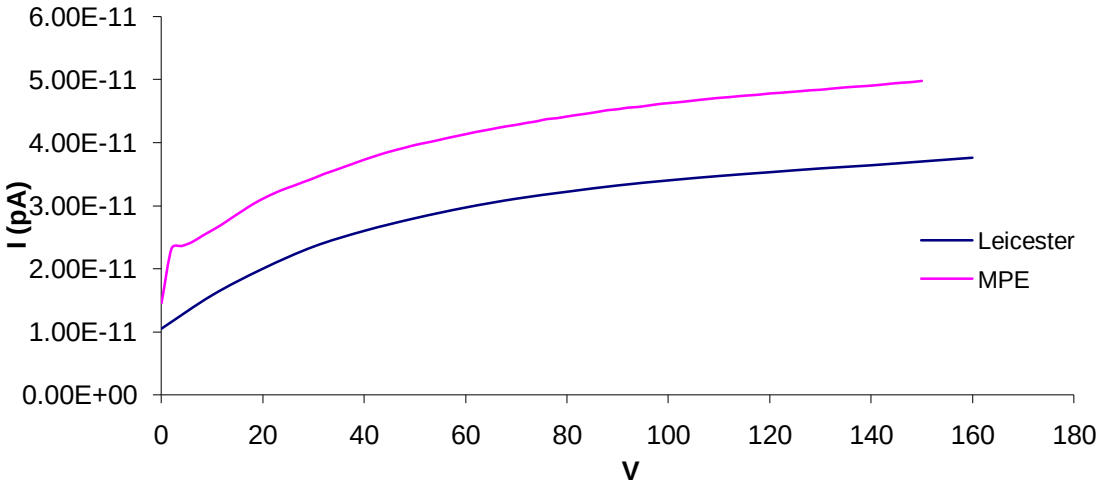

Figure 2.9 An example set of I-V curves for one of the diodes tested. Comparison is made between the results achieved at Leicester and MPE-HLL

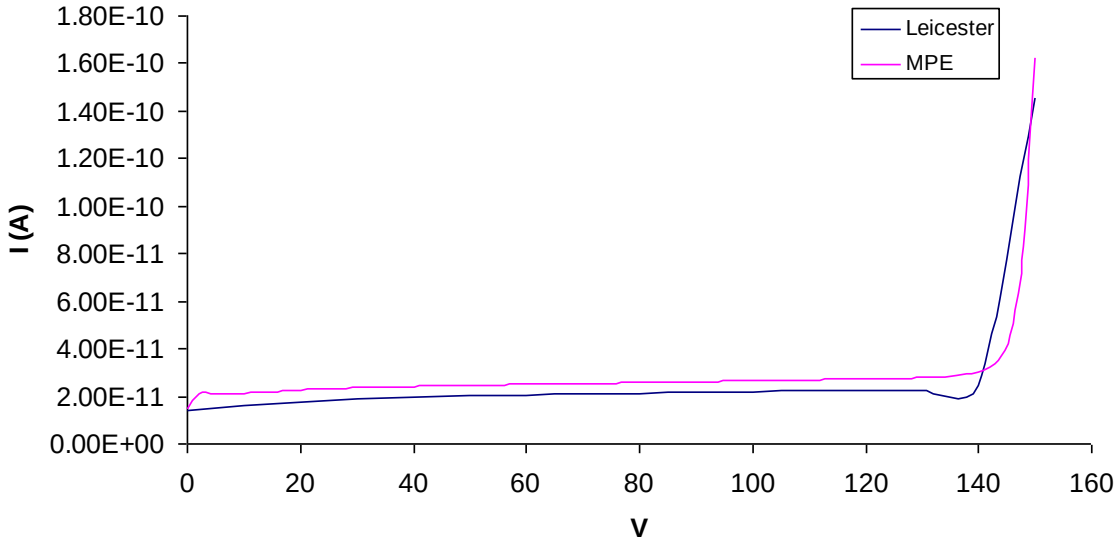

Figure 2.10 I-V curve for diode D1, sample C07, showing breakdown in the device

Pre-irradiation dark current measurements were made also. The dark current on these devices were so small (30-100 pA at 0-160 V and 20±2°C) prior to damage that for the purpose of this experiment it is considered negligible.

2.2.6 THE PROTON IRRADIATION

The diodes were irradiated at the University of Birmingham Cyclotron facility. This section considers the irradiation of the DEPFET diodes and discusses the key parameters of the experiment: proton energy, beam uniformity, flux measurement, dosimetry and the mounting of the test samples.

2.2.6.1 PROTON ENERGY

The BepiColombo proton spectrum is normalised to NIEL 10MeV equivalence (Figure 2.2) so the protons used in this experiment should be mono-energetic 10MeV protons. Due to restrictions in the Cyclotron test facility, however, it was not possible to set the beam energy to 10MeV. The proton energy was set to an energy (~14MeV) such that is was degraded to 10 MeV by the radiochromic film used for uniformity measurement, GAFCHROMIC HD-810 [ispcorp, 2007] (Section 2.2.7), a thin 200 µm aluminium foil placed between the beam exit window and the diode sample and a ~5cm column of air (Figure 2.11). The energy of the protons as they exit the beam

window of the facility is calculated using the Stopping Range of Ions in Matter (SRIM) tables [Ziegler et al, 2010] to establish Figure 2.12 to Figure 2.14.

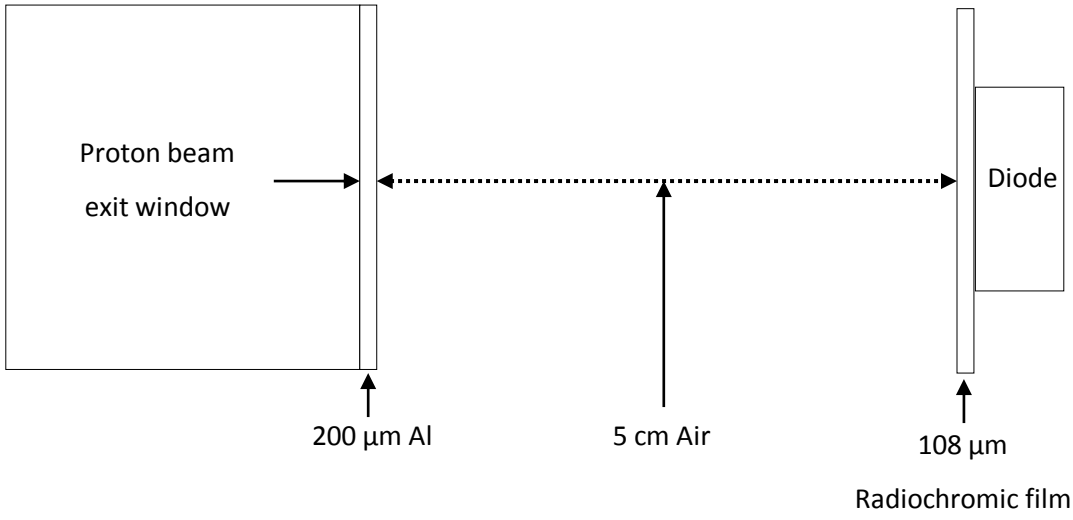

Figure 2.11 Schematic diagram of the test setup, showing the path of the protons from beam exit window to target. This information is required in order to calculate the energy degradation of the protons from exit to target

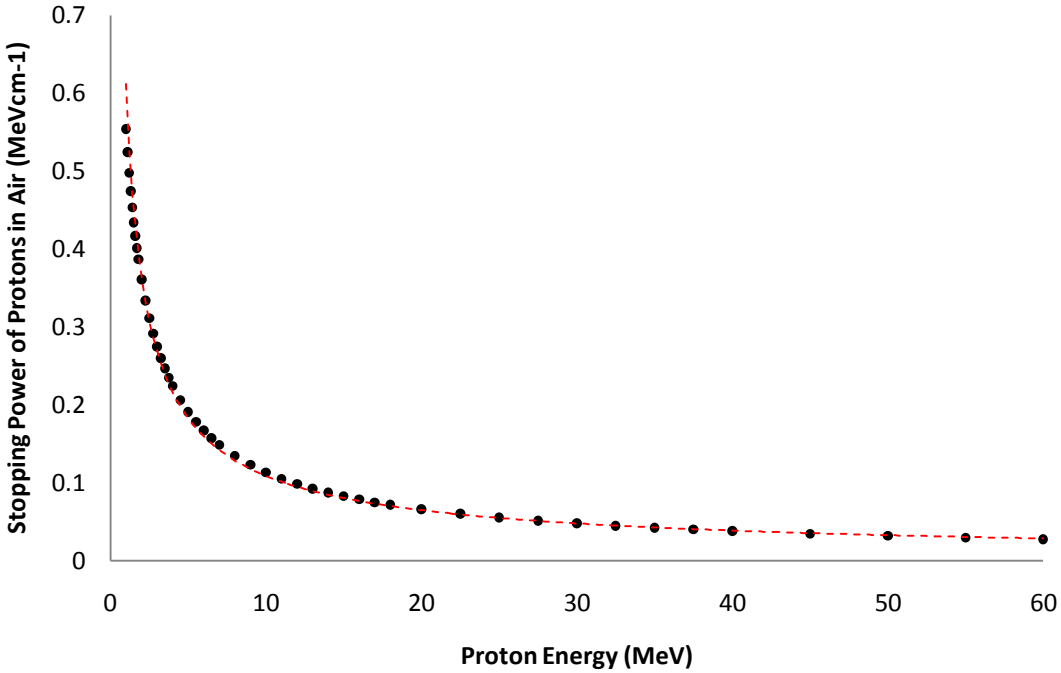

Figure 2.12 Stopping power of air for high energy protons, calculated using SRIM [Ziegler et al, 2010]

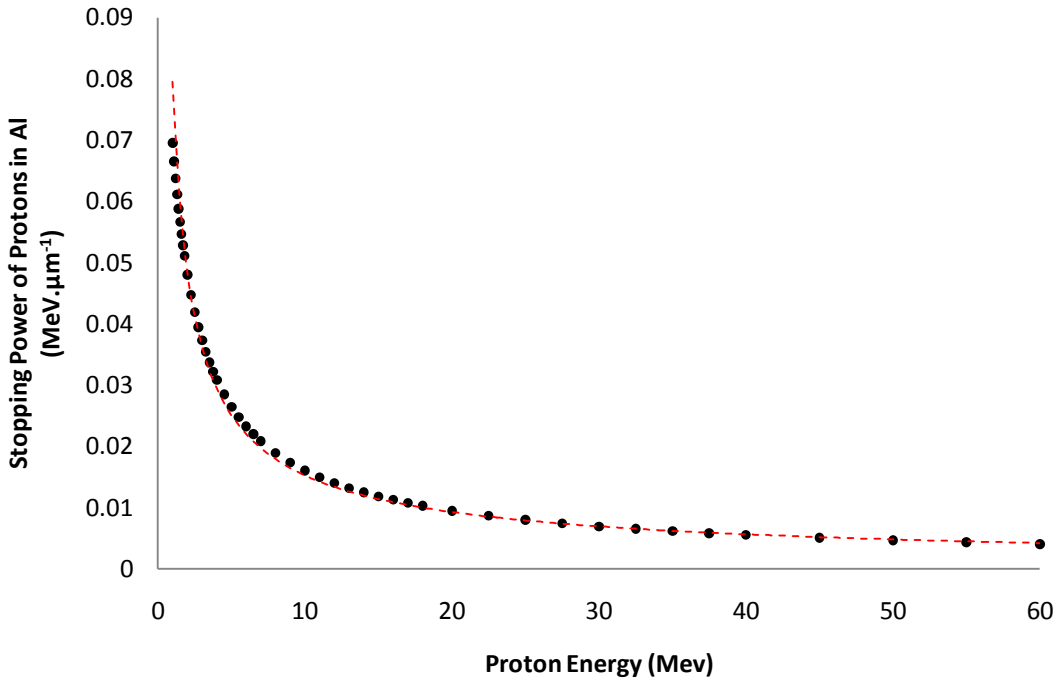

Figure 2.13 Stopping power of Aluminium for high energy protons, calculated using SRIM [Ziegler et al, 2010]

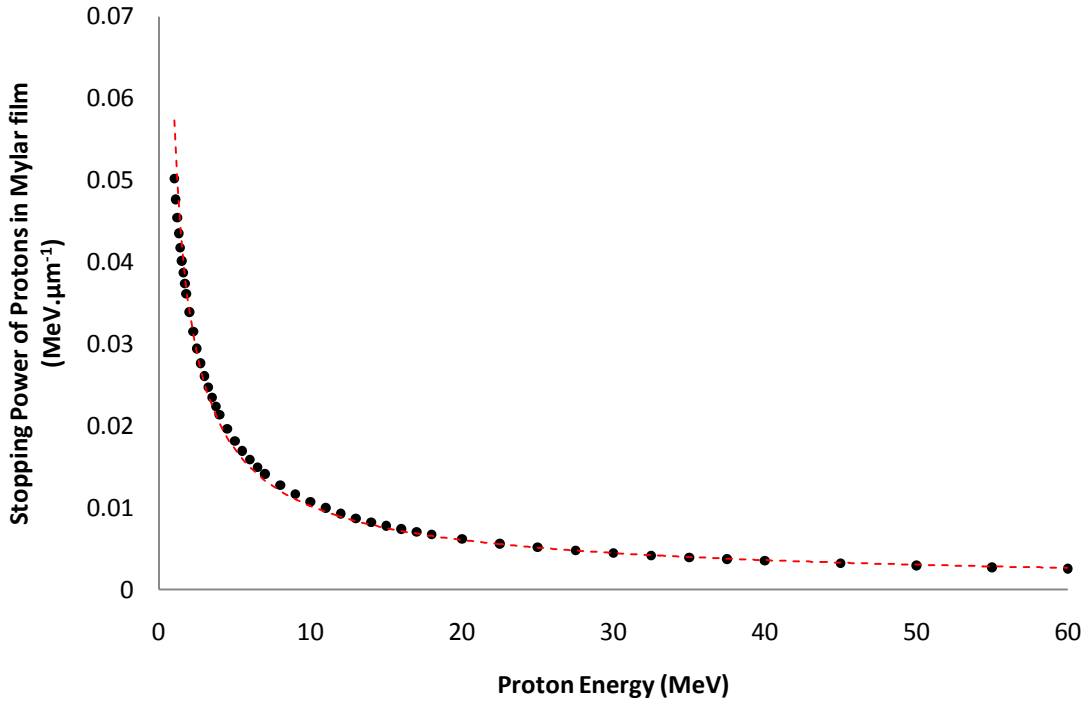

Figure 2.14 Stopping power of Mylar for high energy protons, calculated using SRIM [Ziegler et al, 2010]. Radiochromic film is made of polyester, plus an unknown active agent which is the self developing component of the material

Figure 2.12, Figure 2.13 and Figure 2.14 were used to calculate the degradation of proton energy per unit distance for the aluminium foil, the column of air and the radiochromic film in order to ensure that the protons hitting the diode had an energy of 10 MeV. The active layer of the radiochromic film is only 7 µm thick in a 100 µm + 1 µm polyester sandwich. As the chemical composition of the active layer is unknown, it was assumed that the radiochromic film is 108 µm of polyester. Table 2.2 shows the proton energies as they enter and exit the materials of various thickness in the proton beam line.

	200 µm Aluminium	5 cm Air	108 µm Polyester film
Proton Energy In (MeV)	13.9	11.5	11.0
Proton Energy Out (MeV)	11.5	11.0	10.0
Energy lost in transmission (MeV)	2.4	0.5	1.0

Table 2.2 Table showing the proton energy required to achieve 10 MeV protons at the test diodes. The protons leave the exit beam and travel through aluminium, air and a polyester-based radiochromic film

The operators at the Birmingham Cyclotron Facility set the energy of the cyclotron to 13.9 MeV, where the error on the exit energy of the protons is ±10% [BU, 2007]

2.2.6.2 BEAM UNIFORMITY

With three diodes per sample, knowledge of the proton beam's uniformity is needed if a correct dose measurement is to be made. The proton beam exit window was circular and 2 cm in diameter. The beam was expected by the facility operators to be sufficiently uniform over this aperture, allowing the whole sample containing 3 diodes to be irradiated. Beam uniformity was measured using GAFCHROMIC HD-810 radiochromic film [ispcorp, 2007] during irradiation of the devices, and analysed using a flatbed scanner. Analysis of the film, however, showed non-uniformity of the beam. This is discussed in Section 2.2.7, including more details about the use of this film as a potential dosimeter. In order to increase the beam size and improve uniformity, the beam was raster scanned and defocused. The raster scan and defocusing of the proton beam was achieved using magnets within the facility, controlled by the cyclotron operators.

2.2.6.3 FLUX MEASUREMENT

To establish the dose administered to the sample, the proton flux needed to be measured. This was done using a Faraday Cup [Holmes-Seidle & Adams, 1993]. A Faraday Cup is a shaped, solid

metal barrier which stops all incident protons and creates a flow of charge. This current can be measured, providing the flux of protons hitting the cup.

The beam current was set to approximately 10pA but, when measured, had a fluctuation of approximately 10% over 1 minute. This fluctuation appeared to be an oscillation rather than a random fluctuation based on Faraday Cup current measurements taken over approximately 15 minutes after cyclotron setup. The beam current was measured before and after each irradiation, allowing an average flux to be determined for each sample.

2.2.6.4 DOSIMETRY

Measuring the dose of protons administered to each diode is important when analysing the NIEL damage and drawing conclusions from the data. There were two methods of dosimetry attempted in this experiment; a coarse dosimetry based on Faraday Cup measurements prior and after each sample irradiation, and spatially accurate dosimetry based on radiochromic film images taken during each sample exposure. Measuring the current produced in the Faraday Cup prior to and after each irradiation allows an estimate of the number of protons hitting the cup before and after the diode samples are irradiated. The Faraday Cup does not provide any spatial information as to where the protons hit the sample, however, and as there are three diodes per sample, knowledge of the spatial distribution of protons hitting the sample is desirable.

Taking an image of the proton beam using radiochromic film while irradiating the diode samples allows, in principle, for this spatial information to be determined. As the optical density or opacity of the film is related to the radiation dose absorbed in the film, this should also provide a measure of the proton fluence hitting each diode on the sample. Optical density is defined as:

$$OD = log_{10}\left(\frac{S_0}{S}\right) \tag{2.3}$$

Where *OD* is optical density, S_0 is the gray-level value for the non irradiated film and *S* is the gray value for the film post irradiation. In order to establish the relationship between proton exposure and film opacity, a number of calibration images were made prior to the irradiation experiments. Faraday Cup measurements were used in this calibration in order to determine the fluence of protons for each film exposure. Section 2.2.7 discusses the use of radiochromic film as a spatially sensitive dosimetry device in more detail.

2.2.6.5 TEST FIXTURE

A test jig was fabricated at the University of Leicester which was used to interface to the cyclotron beam line. Figure 2.15 shows the beamline interface to which our test devices were mounted and Figure 2.16, the PCB and diode sample mounted on the test jig. An Aluminium collimator was also placed in front of the sample. A collimator current measurement was initially planned to aid dosimetry, but ultimately this was not used. It was felt that it was sufficient to have two methods of dosimetry and that an additional current measurement would unnecessarily complicate the experiment.

Figure 2.15 The beamline interface mount at the Birmingham Cyclotron Facility

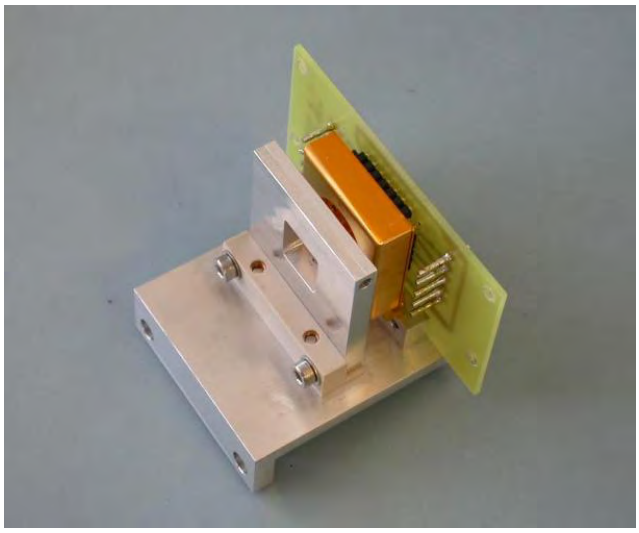

Figure 2.16 The test sample mounted on the PCB and irradiation test jig

2.2.7 RADIOCHROMIC FILM CALIBRATION

The film used in this test is the GAFCHROMIC HD-810 radiochromic film [ispcorp, 2007], used extensively in the biomedical industry for X-ray and electron detection. This film is self developing; when the active ingredient in the film is exposed to radiation it reacts to create a blue polymer. The optical density or opacity of the film is related to the dose of exposure. The higher the dose, the more opaque the film becomes.

As the film is self developing, it is ideal for fast, on-site uniformity measurements. In principle, this film could be used to provide accurate dose measurements for this test, as suggested by the literature and used in high energy photon dosimetry [Niroomand-Rad, 1998][Butson, 2003][Mercado-Uribe, 2009]. Unfortunately, there are no contrast-vs.-dose data available for this film from the manufacturers for proton based radiation. It is therefore necessary to calibrate the film against proton dose if we are to use the film to infer dose measurements based on film opacity.

A sheet of radiochromic HD-810 film was cut into small samples. Each sample was labelled and notched in such a way as to know the active side of each film piece. The test jig was attached to the cyclotron beam line *without* a diode sample in place. A Faraday cup was placed in the position of the diode sample in order to measure the proton beam current. Initially, a current measurement from the Faraday cup was attempted while a radiochromic sample was in place. This resulted in a large current (~200pA as opposed to the expected 15pA beam current as set by the technician) due to electron emission from the film during irradiation. A subsequent beam current measurement was made with no film sample present with a current measurement of ~11pA.

A piece of radiochromic film was placed behind the collimator on a purpose-built holder after an initial beam current measurement. It was assumed that the beam current would be stable during the course of the calibration exposure. The first film sample was exposed to the proton beam for 3 minutes ± 1s, the second for 9 minutes ± 1s, the fourth for 15 minutes ± 1s and the last for 30 minutes ± 1s. Finally, a beam current measurement was taken after the last film exposure. A drop in beam current was observed from 11pA to 9pA over the course of the film exposures. An estimate in exposed dose for each film was made by assuming a linear decrease in current over the ~1 hour of beam time. A film was then placed in front of the diode sample during each of the irradiations, with a Faraday cup measurement taken prior to, and following, each exposure.

The film used in the calibration was scanned using an Epsom flatbed scanner immediately after proton exposure in order to establish the beam uniformity. Figure 2.17 shows one of the radiochromic film exposures and a three-dimensional profile of the image constructed using ImageJ [Rasband, 1997-2010]. It is clear from the analysis of the image that the proton beam was non-uniform over the exposed area. The vertical direction displayed very little non-uniformity, whereas the horizontal non-uniformity was significant. The vertical direction is defined as the direction from floor to ceiling and the horizontal, perpendicular to that.

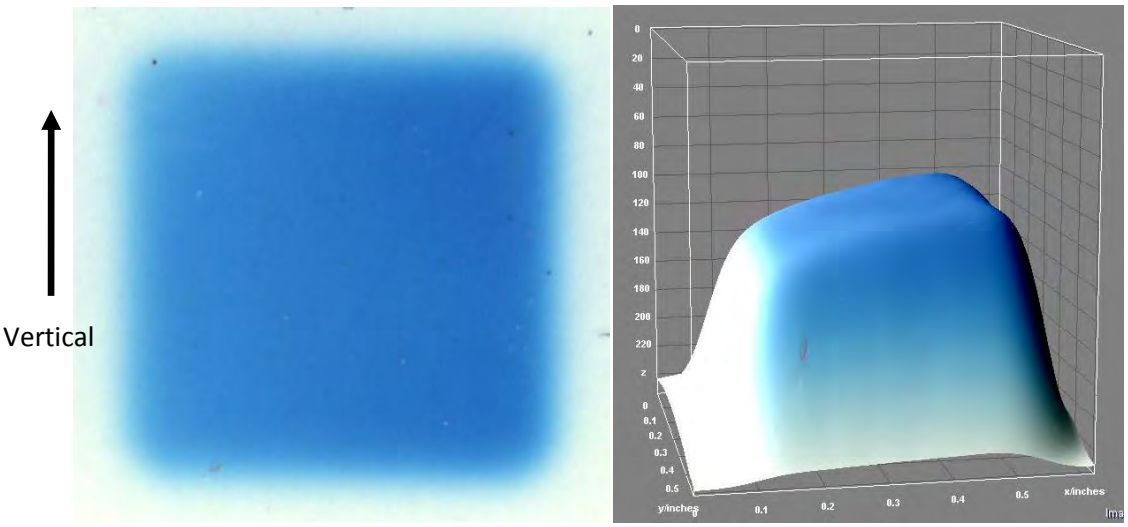

Figure 2.17 Left, radiochromic film exposed to approximately 1x10^{10} 10MeV Protons and right, a 3D profile of the film exposure, showing the non-uniformity of the proton beam. The exposed area is ~1.5x1.5cm^2. The vertical axis in the 3D plot is grey-scale, from 0-254 where 0 is black and 254 is white.

The films were scanned using a flatbed scanner following the procedure reported in [Alva, 2002] and analysed using ImageJ [Rasband, 1997-2010]. They were scanned in two batches, with the calibration samples on both scans. This allowed two separate calibration curves to be made, removing any effects and errors introduced when scanning the images. All automatic colour and contrast corrections were disabled during the scan. The films were placed on the scanner in a column down the centre of the platen, ensuring that any variability across the scanner lamp was negated. A black-white step function was also scanned next to the films in order to set the black and white levels of the scanned image. Figure 2.18 shows the scanned films and step wedge as analysed in this experiment.

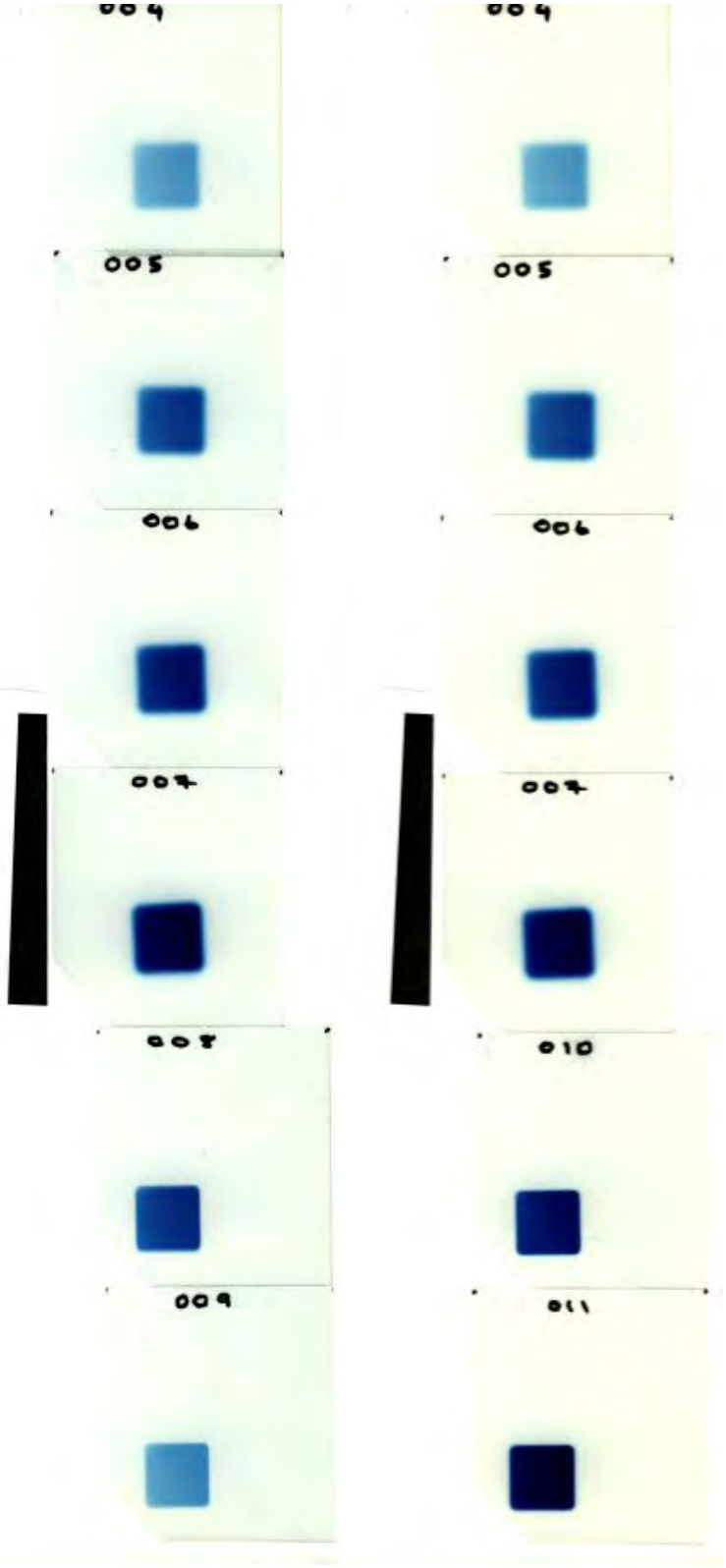

Figure 2.18 The two scanned images showing calibration films 004-007, the exposures taken during the diode irradiations, 008-011 and the black-white step function used to establish the contrast level

Extracting a dose calibration from the radiochromic film, however, has proved to be very difficult. The film is inherently non-linear; the optical density of the film saturates with high doses of radiation, differing depending on the type of radiation. No data exist to determine the proton dose at which the HD-810 film used saturates. When coupled with the non-uniformity of the beam, the uncertainty in the beam energy and the error in the current measurements, the resultant calibration curve is ineffective.

One of the key problems is trying to extract dose information about a small region of interest *within* the irradiated area – there are three separate diodes of two different sizes being irradiated within the square shown in Figure 2.17. Knowing that the fluence is higher towards the right hand side of the sample, we know that the two smaller diodes D2 and D3 receive a higher fluence. Using the calibration curve created from the calibration experiment shows otherwise, with D1 apparently receiving the higher fluence. This is clearly false; D1, according to the uniformity images taken while irradiating the samples, received a lower dose than D2 and D3. This suggests that there were too many variables with large errors in this method of calibration to result in a meaningful dose measure from the use of radiochromic film in this instance. In order to derive proton dose information from radiochromic film in the future, a more careful measurement of fluence would be required, as well as a more uniform proton irradiation, during calibration. A reference detector would also be desirable for comparison during the calibration procedure.

David Smith from Brunel University has since demonstrated that for much lower proton fluence (~$1x10^8$ protons cm^{-2}) the radiochromic film is capable of providing dose information to ~10% accuracy [Smith, 2008]. In the Brunel experiment, the film was found to be linear at this lower fluence and was calibrated using a number of other reference detectors. This experiment used the same proton energy of 10 MeV and was also conducted at the University of Birmingham Cyclotron Facility.

Other experiments that have used radiochromic film have demonstrated similar accuracies in dose measurement. Jones et. al 1999, conducted an experiment at the Indiana University Cyclotron Facility where radiochromic film dose measurements were compared to those made with a Faraday Cup, calorimeter and a calibrated Ion Chamber. This experiment differed greatly to the one reported here as it used protons of higher energy (193MeV) and a more accurate densitometer rather than a flatbed scanner. The use of a flatbed scanner in place of the more expensive densitometer has been studied by M. Bazioglou and J. Kalef-Ezra, 2001. A comparison

of film opacity analyses using both methods was made. It was found that there was '*no variation of statistical significance'* between the optical density as measured using a densitometer and a flat bed scanner for films exposed to fast and thermal neutrons.

In principle, radiochromic film can be used to establish the dose of protons administered to a sample accurately and with spatial resolution down to the micrometer level [Bazioglou and Kalef-Ezra, 2001]. This could be very useful for samples such as those used in this experiment which contain more than one item being irradiated in the area. Unfortunately, the calibration conducted here had too many variables and this information could not be extracted.

2.2.8 PROTON IRRADIATION EXPERIMENT RESULTS

2.2.8.1 COARSE DOSIMETRY

The proton beam current was measured before and after each irradiation in order to provide a coarse dosimetry for the whole sample when coupled with the irradiation time. It was observed that the proton beam fluctuated in a sinusoidal manner, ±15% peak-to-peak, over a period of 1 minute ± 30 seconds. The following table shows the measured current before and after each irradiation, the time of irradiation and the total approximate dose. Note: 1pA = 6.24×10^6 protons per second. The irradiation time was measured using a stopwatch.

Sample	Beam Current (pA)			Irradiation Time	Approximate Dose
	Before	After	Mean	(mins ± 1 second)	(Protons ± 15%)
C03	9.5	10.5	10.0	3.5	1.31×10^{10}
C07	9.5	10.5	10.0	10.5	3.98×10^{10}
E05	10.5	8.0	9.25	17.5	6.06×10^{10}
G03	8.0	11.0	9.5	35	1.24×10^{11}

Table 2.3 Coarse dosimetry for each of the irradiated diode samples based on beam current measurements prior to and after irradiation

2.2.8.2 THE CURRENT RELATED DAMAGE RATE (α) EXPERIMENT

The Damage Rate, α, is the proportionality factor used to relate the current per unit volume of damaged silicon to the fluence used to irradiate the material. The experiment method used to establish α for the BepiColombo MIXS diodes is reported in [ROSE, 1999] and is described here.

DATA ACQUISITION

All devices, once irradiated, were placed into dry ice, preventing room temperature annealing taking place between the irradiation and current measurements.

Each of the damage factor test samples, C03, E05 and G03, were mounted in the test box in turn and an I-V curve was taken, firstly at -40°C and then at 20°C. The time spent at room temperature was kept at a minimum (no more than an hour for each diode from irradiation until test), again to limit the amount of thermal annealing. Some time at room temperature was unavoidable, however, as trying to solder the diode into the die cast box at a cold temperature would result in condensation on the diode.

The damage factor curves are plotted using the diode leakage currents measured at the over-depletion voltage of 190V [ROSE, 2004]. Plotting $I/\kappa V$ against fluence results in a straight line curve with a gradient equal to the damage rate, α (see equation (2.2). The conversion factor used to equate 1 MeV neutrons to 10 MeV protons, κ, is taken to be 3.8 for silicon [Treis et al, 2006].

RESULTS

The room temperature I-V curves taken using samples G03, E05 and C03 were used to establish the current related damage rate, α. Figure 2.19 shows the I-V curve taken using diode D2 from sample C03 prior to and after irradiation with ~1.3×10^{10} protons. Note that the pre-irradiation data was only collected up to 160V rather than 200V.

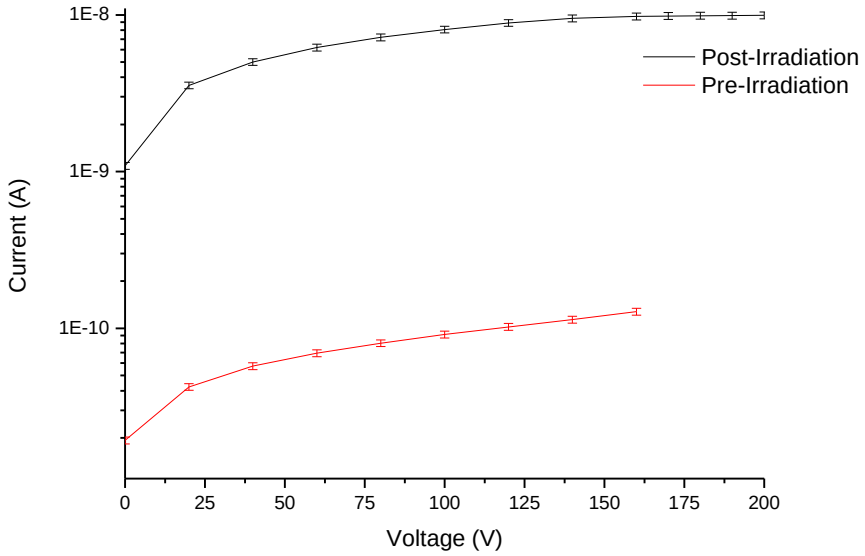

Figure 2.19 I-V curves for D2 on sample C03 taken at 20°C before and after irradiation

Table 2.4 shows the leakage current at 20°C at the depletion voltage, 190V. The proton fluence administered to each of the diodes is also shown.

Sample	Diode	I_{190V} @ 20°C x (10^{-9}A)	Fluence (x10^{-9}protons.cm^{-2})
C03	D1	18.39	9.1
	D2	9.91	9.1
	D3	9.30	9.1
E05	D1	101.30	4.2
	D2	56.47	4.2
	D3	51.19	4.2
G03	D1	199.60	8.6
	D2	105.01	8.6
	D3	100.13	8.6

Table 2.4 The measured leakage current of diodes irradiated in the current related damage rate (α) experiment. The proton fluence used to irradiate each diode is also shown

Figure 2.20 shows the plot of *I/κV* versus proton fluence used to establish the value of *α* for the diodes. The gradient of the line of best fit gives the value of *α* and is measured to be $(6.4\pm0.96)\times10^{-17}Acm^{-1}$.

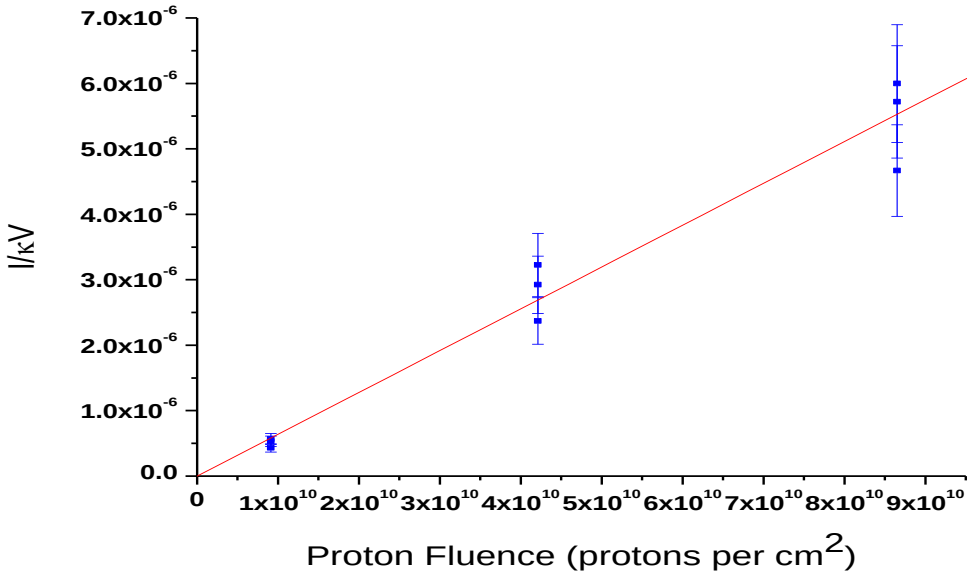

Figure 2.20 Plot of I/κV versus proton fluence, used to establish the value of α

2.2.8.3 THE THERMAL ANNEALING EXPERIMENT

An isothermal anneal, where the temperature is kept constant for the duration of the anneal, was carried out in order to establish the use of thermal annealing in the recovery of device performance for the BepiColombo MIXS instrument. Sample C07 was used in this test. As with the other diode samples, C07 was kept cold using dry ice and the time spent at room temperature was kept at a minimum in order to reduce the effects of room temperature annealing. Each diode sample spent less than an hour at room temperature after irradiation, prior to the I-V curves being taken. This time at room temperature was necessary to mount the diodes into the test box. If the diodes were removed from their dry environment while still cold then the danger of the devices developing condensation and becoming damaged was significant.

An I-V curve was taken at -40°C and at 20°C before commencing the thermal annealing experiment. All I-V curves are reported in Appendix I. The device was warmed to 60°C in an environmental control chamber and a current measurement was taken on each of the diodes. Based on initial I-V curves, it was decided to focus this test on diode D3. D1 on sample C07 was the diode seen to break down prior to reaching full depletion. As this test was automated using a Visual Basic programme written for the Keithley electrometer and the setup requires a manual lead change to measure the leakage current from different diodes, it was necessary to use one primary diode for this test while using the other to take periodic single measurements as a check on the primary.

The diode was held at 60°C ± 0.5°C for ~9 days (7.77×10^5 seconds) in a computer-controlled environmental chamber. The sample annealed at 60°C following the procedure in the RD-48 report which outlines a standard methodology for this experiment [ROSE, 1999]. A current measurement was taken on the D3 diode automatically every 10 minutes using a programme written for the Keithley electrometer, automatically logging the data to a PC. The results were subsequently analysed.

THERMAL ANNEALING RESULTS

Figure 2.21 shows the results of the thermal annealing test, performed on D3 of sample C07. The leakage current prior to irradiation was, in some cases, too small to measure. The leakage current range was from ~0.005 pA to 0.10 pA when measured at -40°C and ~5 pA to 130 pA at 20°C. The leakage current increases with increased bias voltage.

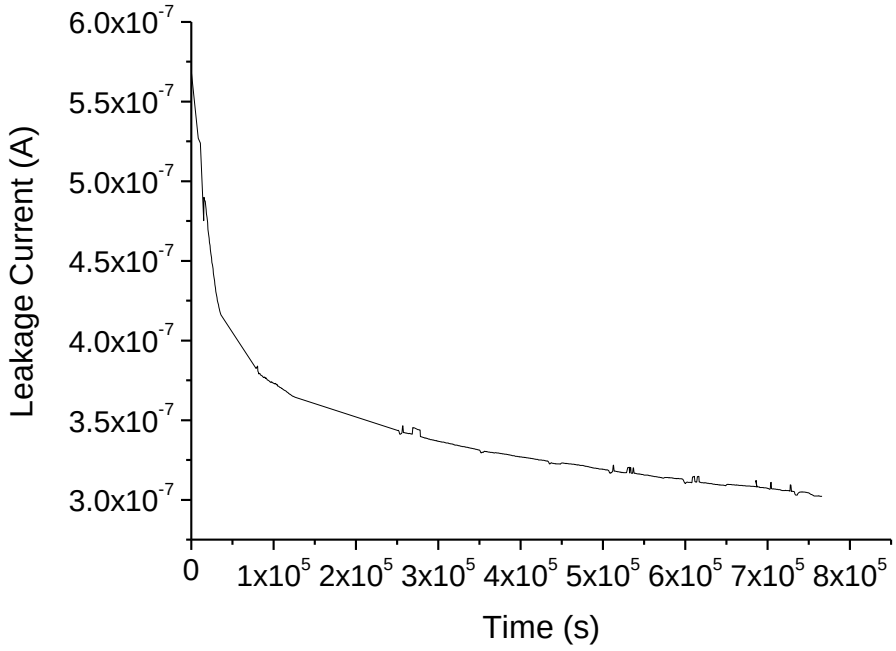

Figure 2.21 Isothermal annealing results from diode D3 on sample C07. The diode was kept at 60 ± 0.5°C for the duration of the experiment

2.2.9 DISCUSSION

2.2.9.1 THE CURRENT RELATED DAMAGE RATE, (α)

Figure 2.20 shows the shows the plot of *I/κV* versus proton fluence for 20°C. Standard α measurements are always quoted at this temperature [ROSE, 1999]. The gradient of the line is the value for α, and in this case is (6.4±0.96)x10^{-17} Acm^{-1}. It is also evident from Figure 2.20 however, that there is a significant spread in the plotted points. Figure 2.22 shows this more clearly, separating the points from the different diodes, D1, 2 and 3.

The α measurement of 6.4 x 10^{-17} Acm^{-1} assumes a uniform illumination of the diodes during irradiation: however we know from Figure 2.17 that this is not so. D1 lies in the region of the device that receives a lesser dose whereas D2 and D3 sit in the most intense part of the proton beam during irradiation. The two separate trends in Figure 2.22 show the significance of this dose discrepancy.

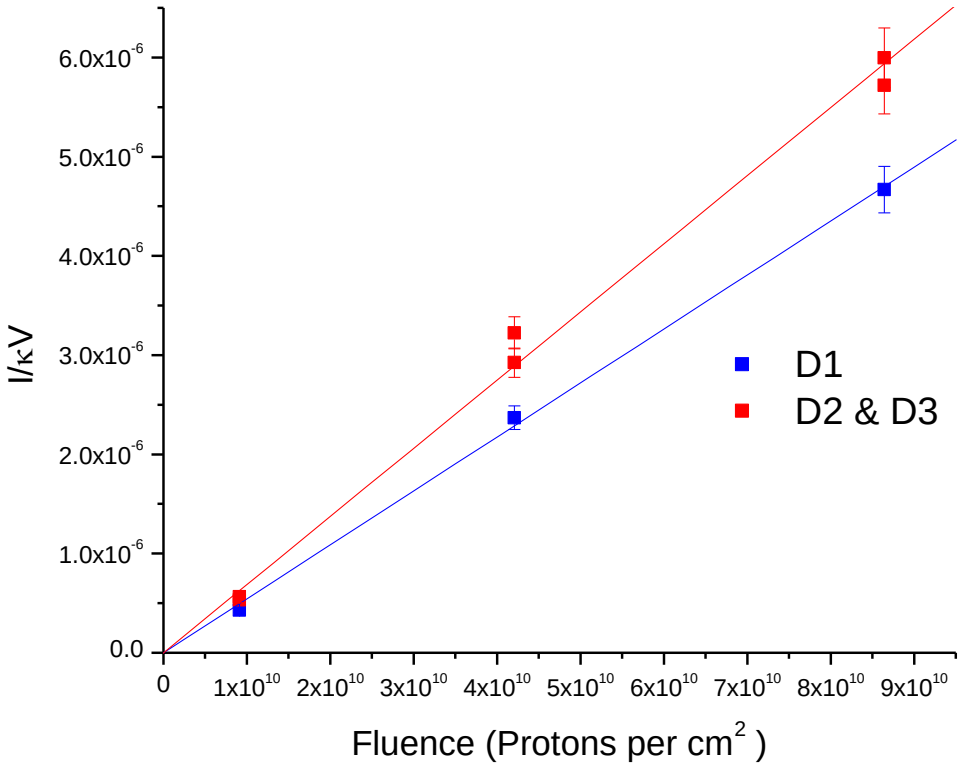

Figure 2.22 Separate α curves for D1 and D2 & D3

The α value for D1 is (5.44 ± 0.27) x 10^{-17} Acm^{-1}, whereas for D2 and D3 α = (6.87 ± 0.34) x 10^{-17} Acm^{-1}. These values differ as they do not use the correct dose value when calculating the value of α. The dose of each diode on the sample is unknown as the information could not be extracted from the radiochromic film, as discussed in Section 2.2.7. The only dose measurement available is the one taken from total beam measurements using the Faraday Cup. The two values of α calculated when assuming a uniform irradiation, as shown in Figure 2.22, represent upper and lower limits for α using the measured fluence in this experiment.

The α value calculated in Section 2.2.8.2, (6.4±0.96) x 10^{-17} Acm^{-1}, is in effect an average value of α as calculated from D1, D2 and D3, and is therefore a meaningful value of α for diodes of 450µm silicon. For comparison, using 350µm silicon, the measured value of α is (3.99 ± 0.03) x 10^{-17} Acm^{-1} [ROSE, 2004].

The error in the average value of α (6.4±0.96) x 10^{-17} Acm^{-1} is 15%, as shown by the error bars in Figure 2.20. The error in this value can be attributed to the following factors

1) The fluctuation in beam current during irradiation

2) The error in time measurement during irradiation

3) The proton beam non-uniformity

The beam current fluctuation and non-uniformity are the largest contributing factors to this error. Solving the non-uniformity of the proton beam would be the most useful improvement to this experiment as a uniform beam would allow a calibration of the radiochromic film and thus allow an accurate measure of proton dose. The error due to beam non-uniformity is removed somewhat when considering D1, 2 and 3 separately in Figure 2.22, reducing the size of the error bars required to match the data to the line of best fit to ~5%.

The α of (6.4±0.96) x 10^{-17} Acm^{-1} is comparable to a recent measurement performed by MPI-HLL on similar silicon strip devices [Treis, 2007], where a value of 7.3 x 10^{-17} Acm^{-1} was obtained. The error in this measurement was not reported.

2.2.9.2 THERMAL ANNEALING

Figure 2.21 shows that annealing a silicon device based on this 450µm substrate can significantly reduce excess dark current produced by non-ionizing proton damage. A 1x10^5 second anneal at 60°C reduced the leakage current of the diode by ~33%, while a 3x10^5 second anneal at 60°C shows a reduction in dark current of ~40%. A reduction of this magnitude could mean recovery of performance that would otherwise render the mission a failure in the extreme case of massive radiation damage to the detector systems onboard MIXS. Table 2.5 shows the probability of different flare types during 2018, 2019 and 2020 [Carpenter & Fraser, 2006]. It can be seen from this table that the probability of seeing a large flare event is very dependent on the year of operation at Mercury. The design of the instrument needs to take a large flare into account, however, and such a flare could potentially provide a dose of 5000 protons per second lasting up to ~3 days [Carpenter & Fraser, 2007]. This is equivalent to approximately 4% of the total mission dose over the course of 3 days.

Flare State	Fraction of year in state		
	1996	1997	1998
	(2018)	(2019)	(2020)
X	0.00001	0.00007	0.0004
M	0.0001	0.0007	0.006
C	0.0045	0.017	0.014
B	0.07	0.3	0.9
Quiet Sun	0.93	0.68	0.08

Table 2.5 Fraction of time measured in various flare states during years analogous to possible years of operation for BepiColombo at Mercury [Carpenter and Fraser, 2006]

DEPFET ENERGY RESOLUTION DEGRADATION CALCULATION

After irradiating the diode D3 on sample C07 with 1.3×10^{10} protons per cm^2, a measure of the leakage current was taken at -40°C. This was 37.5pA. The diode has an area of 3.2 mm x 3.2 mm = $10.24 mm^2$. The error in the current measurement was ±0.05 pA.

The area of a MIXS DEPFET pixel is 300 µm x 300 µm = 90000 μm^2 = 0.09 mm^2.

Assuming that the diode measured provides a good estimate of the dark current of the DEPFET, after an equivalent dose of radiation, this gives 0.3296 pA per pixel.

The time taken to read out one pixel is 6 µs. The readout of the detector is such that the 64 rows of the detector are read out in two parts, so the total readout time for the detector is 6 x 32 µs = 192 µs.

The total charge accumulated over this time is therefore;

0.3296×10^{-12} A x 192×10^{-6} s = 6.328×10^{-17} C = 395 electrons or 19.9 electrons RMS.

The average electron-hole creation energy in silicon is ~3.68eV (-90 °C value, McCarthy et.al, 1995) so 19.9 electrons = 73.23 eV. Expressed as a FWHM value, 73.23 x 2.36 = 172.83 eV FWHM.

$$\Delta E = 2.36w\left(\frac{FE}{w} + R^2 + A^2\right)^{\frac{1}{2}} \quad (2.4)$$

ΔE = FWHM Energy of a line at energy *E* in eV (assumed to be 1 keV in this calculation)

w = average electron-hole creation energy = 3.68eV [Janesick, 2001]

F = Fano factor of silicon = 0.117 (McCarthy et al, 1995)

R= The read noise (which includes the dark current contribution)

A = Amplifier noise

The amplifier noise, *A*, is given as 3.2 electrons [Treis et al, 2005] for the DEPFET. 3.2 electrons = 11.776 eV. Expressed as a FWHM value, 11.776 x 2.36 = 27.79 eV FWHM.

$$\Delta E = \left[\left((2.36w)^2 \times \frac{FE}{W}\right) + R^2 + A^2\right]^{\frac{1}{2}} \quad (2.5)$$

Equation (2.4) was rearranged to give Equation (2.5), for use when *R* and *A* are already in terms of the FWHM contribution to *ΔE.* From this:

ΔE = 182 ± 17% eV FWHM @ 1keV

After annealing the diode D3 on sample C07, a measure of the leakage current was taken at -40°C. This was 9.87pA. Repeating the above calculation for this value:

ΔE = 105 ± 17% eV FWHM @ 1keV

Note the largest source of error in this calculation is the time to read out each pixel (~6μs ± 1 μs). This contributes ~16.7% to the error. The current measurement error was just ±0.05 pA, or ~0.13%. The error in the calculated *ΔE* values is therefore ~ ± 17%.

THERMAL ANNEALING DISCUSSION

Sample C07 was irradiated with a total 3.93×10^{10} protons. The exit window of the beam line is circular with a 2cm diameter. This gives an exit window area of $3.14 cm^2$. Therefore, the dose per cm^2 is 1.3×10^{10} protons. This value is similar to the accumulated dose expected by the time BepiColombo reaches Mercury and is representative of the dose when MIXS begins taking data.

It was shown that after a dose of 1.3×10^{10} ± 15% protons per cm^2 the energy resolution of the MIXS DEPFET detectors will be ~182 ± 17% eV FWHM @ 1keV @ -40 °C. The 15% error is inferred from the curve of best fit in Figure 2.20.

After the annealing experiment, a total of 7.6 x 10^5 seconds @ 60°C, the energy resolution improves to ~105 ± 17% eV FWHM @ 1keV @ -40 °C. The 17% error was calculated from the error in current and time measurements made in the experiment.

The science requirement for the end of life energy resolution for the MIXS detectors is 200eV @ 1keV. From this analysis, it is recommended that the MIXS detectors be annealed immediately after the transit from Earth to Mercury before observations begin.

Calculating ΔE for the detector before launch gives a value of 56.3 eV FWHM @ 1keV. A dose of 1.3x10^{10} protons per cm^2 decreases the detector energy resolution by a factor of 3.2. Based on this value, and the total mission dose estimate of 3x10^{10} protons per cm^2, it is also envisaged that a further anneal will be required after approximately 1 year of observations in order to meet the end-of-life energy resolution requirement of the mission.

Alternatively, decreasing the temperature of the detector will improve the energy resolution. For every reduction of 7°C, the dark current of a silicon detector is halved [Treis et al, 2006]. If the temperature of the diodes were reduced from -40°C to -47°C, the before and after irradiation values result in energy resolutions of 103 eV FWHM @ 1keV @ -47 °C and 72 eV FWHM @ 1keV @ -47°C respectively.

2.3 THE MPI-HLL MIXS DIODE TEST

MPI-HLL, aided by Craig Brown (the author) and Dr James Carpenter from University of Leicester, conducted a proton irradiation test of MIXS diodes similar to those used in the test discussed in the chapter. The tests were conducted at the Garching Tandem Accelerator of the Maier-Leibnitz-Laboratory of the Technical University and the Ludwig Maximilian University of Munich. The devices, having been characterised prior to irradiation, were subjected to different proton doses at an energy of 10MeV, achievable with high accuracy (±2 keV) at this facility [Segneri et al, 2008]. The devices were irradiated while cooled to -50°C rather than at room temperature, differing from the experiment conducted at the Birmingham Cyclotron Facility. This experiment is more representative of the BepiColombo mission as the MIXS detectors will be ~-40°C during operation and, therefore, during irradiation in space.

During the irradiation campaign, an image was taken of the beam using the GAFCHROMIC HD-810 radiochromic film [ispcorp, 2007] described in section 2.2.7. Figure 2.23 shows the image of the proton beam. Prior to this image being taken, it was assumed by the facility operator and the

researchers involved in the experiment that the beam profile would be approximately Gaussian over a 6cm diameter region. This is clearly not the case, with the majority of protons being concentrated in a small area of a 1.5cm diameter circle.

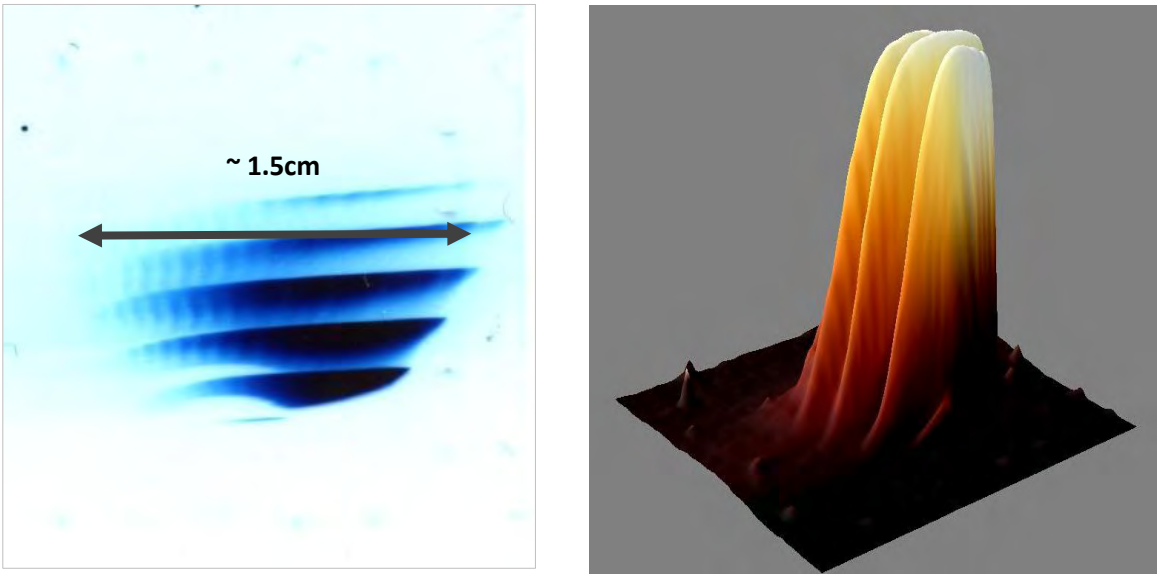

Figure 2.23 Image of the 10MeV proton beam used in the Munich Proton Irradiation experiment. Image was taken using the GAFCHROMIC HD-810 radiochromic film. Right: Intensity beam profile in arbitrary units obtained from the film analysis

There is also a series of 'slats' apparent in the image. These lines are caused by the introduction of thin, opaque wires introduced across the beam to reduce the flux without degrading the beam energy.

The non-Gaussian beam profile, although unexpected, did not overly impede the experiment. Three or four diodes were present on each of the samples irradiated in the proton beam: however each of the diodes was used to measure the fluence of protons received during each irradiation. Dosimetry was not conducted using a Faraday Cup as in the experiment discussed earlier. The dose administered to each diode on the sample was measured by taking a current reading and, after accounting for the dead-time due to pileup in the diodes, the proton fluence is calculated.

After each irradiation, a leakage current measurement was performed while still cold and under vacuum, preventing any room temperature annealing. Details of the experimental method can be found in [Segneri et al, 2009].

Table 2.6 shows the result of this experiment [Segneri et al, 2009], as well as the RD 48 and University of Leicester experiments reported in the chapter. A thickness correction was applied to the Munich result based on a lower hardness factor, κ, although the result using the same κ value as the University of Leicester experiment also results in an α value greater than that reported by RD 48. The thickness correction was implemented as the standard κ_0 value is applicable for thin-layer approximations.

Experiment	α Measurement (Acm^{-1})
RD 48 (300µm Si)	3.99 ± 0.03
University of Leicester (450 µm Si)	6.4 ± 0.96
MPI Silicon Strip Detector (300 µm Si)	7.3*
Munich (450 µm Si, without a thickness correction)	4.57 ±0.06
Munich (450 µm Si, with a thickness correction)	3.66 ±0.05

Table 2.6 Summary of the Current Related Damage Rate Experiments Mentioned in the chapter. *This result was not published but communicated in person by J. Treis

The main conclusion of this experiment was also that the BepiColombo MIXS instrument should be annealed during the mission in order to achieve the end-of-life performance requirements. This agrees with the findings in the experiment reported in Section 2.2.9.

2.4 CONCLUSIONS

The radiation damage tests presented in the chapter show that the devices based on 450µm thick silicon are capable of meeting the end-of-life spectral resolution requirement (200eV @ 1keV) for BepiColombo MIXS if they are annealed. The annealing test carried out also showed that, should the dose exceed mission expectations and cause damage degrading the X-ray spectra beyond mission requirements, then a significant fraction of performance can be recovered with a relatively short (~24 hour) anneal at 60°C. As a result of the findings in this experiment, the MIXS instrument has had annealing capability built into the detector focal plane assembly. At least two anneals will be necessary: one immediately after transit from Earth to Mercury and another after a year of observation. Alternatively, running the detector cooler will reduce the need for annealing, with a 7° reduction halving the dark current contribution to the noise. The possibility of running the detector colder is unlikely, however, due to mission constraints and limited radiator area on the BepiColombo mission.

The diodes used in this test were representative of the MIXS devices in that they are of comparable thickness to the MIXS DEPFET detectors. They have also undergone a similar processing regime. However, these devices may vary to the final DEPFET pixel arrays; the diodes are a great deal simpler than the DEPFET detectors which consist of many pixels which may behave differently to the diodes. For example, they may incur trapping within the macropixel volume. It is therefore necessary to undertake similar proton damage and annealing tests on the MIXS DEPFET detectors as soon as devices become available from the Max Plank Institute.

It has also been shown in these experiments that the devices based on thicker silicon have a similar current related damage rate, α, to devices based on thinner silicon. This should allow good estimates of damage to the BepiColombo devices based on data obtained using thinner silicon devices.

The following Chapter discusses a radiation damage experiment called the XMM-Newton Life Test. This experiment attempts to recreate the damage seen on-orbit in the MOS-1 CCD22 by focussing X-rays onto a small patch of an XMM-Newton flight spare detector. The results of this work are currently being used as an input into the XMM Detector Calibration Team's CCD response modelling as they also investigate this device degradation.

CHAPTER 3

THE XMM-NEWTON LIFE TEST

3.1. THE XMM-NEWTON LIFE TEST

The XMM-Newton Life Test uses a Microchannel Plate Optic to replicate the X-ray radiation dose experienced by the EPIC MOS CCDs over the course of the mission lifetime. The X-rays are focussed in one area on the device allowing localized radiation effects to be studied, as well as greatly decreasing the time required to accumulate the lifetime XMM-Newton X-ray dose. This work was supported by the STFC Rolling Grant.

3.2 XMM-NEWTON AND THE EPIC MOS CAMERA

The XMM (X-ray Multi-Mirror)-Newton X-ray observatory (Figure 3.1) has been in orbit since the 10th December 1999 and is the biggest scientific satellite ever built in Europe, with a launch mass of 3800kg [Jansen, 2001]. The spacecraft houses three separate X-ray cameras, each with a set of 56 nested nickel shells in a Wolter-I configuration focussing X-rays onto the focal plane – also called the European Photon Imaging Camera, or EPIC. The three EPIC cameras are two metal oxide semiconductor (MOS) charge coupled device (CCD) cameras [Turner, 2001] and one PN detector [Struder et al, 2001]. This work is concerned only with the MOS CCD cameras on EPIC.

The EPIC-MOS cameras consist of seven tiled CCD22 chips, each chip with 600 x 600 pixels of 40µm square [Short et al, 1998] (Figure 3.2). The CCDs are epitaxial, 3-phase, front illuminated devices made with high resistivity silicon and have an open electrode structure; a large fraction of the oxide layer of each pixel is etched away to improve low energy quantum efficiency (QE) [Short et al, [Short et al, 2002].

The CCD utilises a buried channel [Ambrosi, 2003] to improve the radiation hardness of the device. The buried channel confines charge collected to a small volume of silicon during charge transfer, reducing the effect of trap sites caused by non-ionizing radiation damage from high energy protons.

Figure 3.1 The XMM-Newton Spacecraft (Credit: NASA)

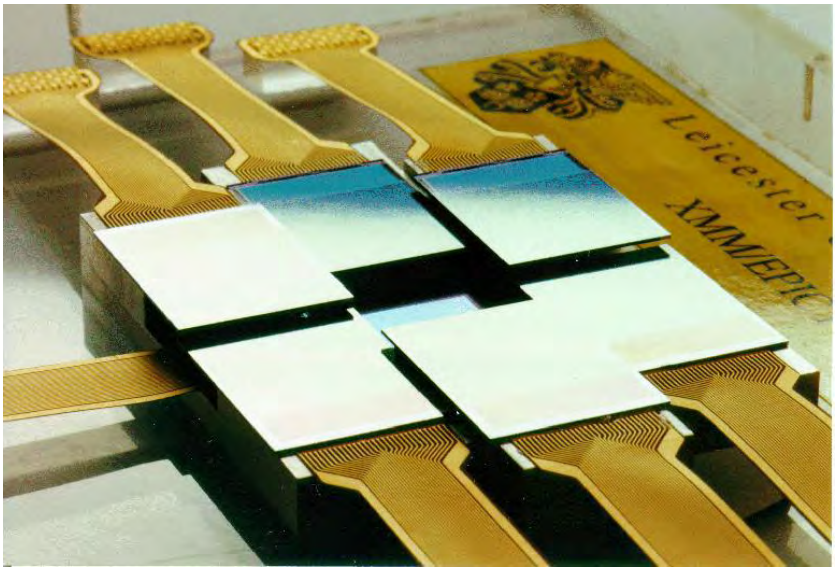

Figure 3.2 Photograph of an EPIC MOS focal plane camera. The camera consists of seven distinct MOS CCDs

The science performed by XMM is extremely diverse, ranging from observations of comets and planets to quasars, galaxy clusters and active galactic nuclei. Since its launch, XMM-Newton has demonstrated its role as one of the most successful space missions ever with more than 2000 peer-reviewed publications in scientific journals based on XMM data. XMM papers are cited more

than four times the average refereed paper in astronomical literature and each call for observing time is consistently oversubscribed [ESA, 2010]. The CCD22 enables this science and its continued good performance is crucial to the extension of XMM-Newton beyond its expected lifetime.

3.3 BACKGROUND TO THE XMM-NEWTON LIFE TEST

It is well known that silicon devices such as CCDs are sensitive to radiation damage. Non-ionizing radiation [Holmes-Seidle & Adams, 1993] in the form of high energy protons are known to be the major contributor to in-orbit damage, generating trap sites within the silicon material, hampering charge transfer during CCD readout. The EPIC-MOS CCDs underwent a rigorous radiation test campaign during XMM instrumentation development [Short, 1998] and a 3cm thick aluminium shield was used on the spacecraft to minimise non-ionizing damage to the devices [Ambrosi, 2003].

After a few years of operation, an unexpected effect in the central region of the EPIC MOS cameras was noted. While revisiting sources previously imaged by XMM-Newton, it was found that a significant amount of spectral redistribution had occurred. This effect was localised to the central region of the camera where the majority of X-ray sources are focussed; approximately 30 x 30 pixels. Figure 3.3 shows a pair of spectra, accumulated using the central area of the CCD camera, taken 2.5 years apart and of the same X-ray source. The second spectrum shows a significant energy redistribution of approximately 100 eV below 500 eV, and gives some clues as to the possible radiation process behind this phenomenon. Notably, the X-rays affected by this damage are soft X-rays which interact in the top surface of the device.

The most recent XMM-Newton calibration status document [Guainazzi, 2009] recognises this issue as an extremely important, yet little-understood, problem and states:

> ***MOS redistribution:*** *The MOS cameras are suffering strong spatial dependent redistribution effects due to a patch in the focal position of the CCD. The current understanding of the extension of the patch is still crude and only modelled with 3 circular 2-D regions (1: on patch, 2: patch wings, 3: off patch). The detailed determination and remodelling of the patch spatial structures is a medium and long term goal for EPIC targeted for the calibration efforts of 2008-2010.*

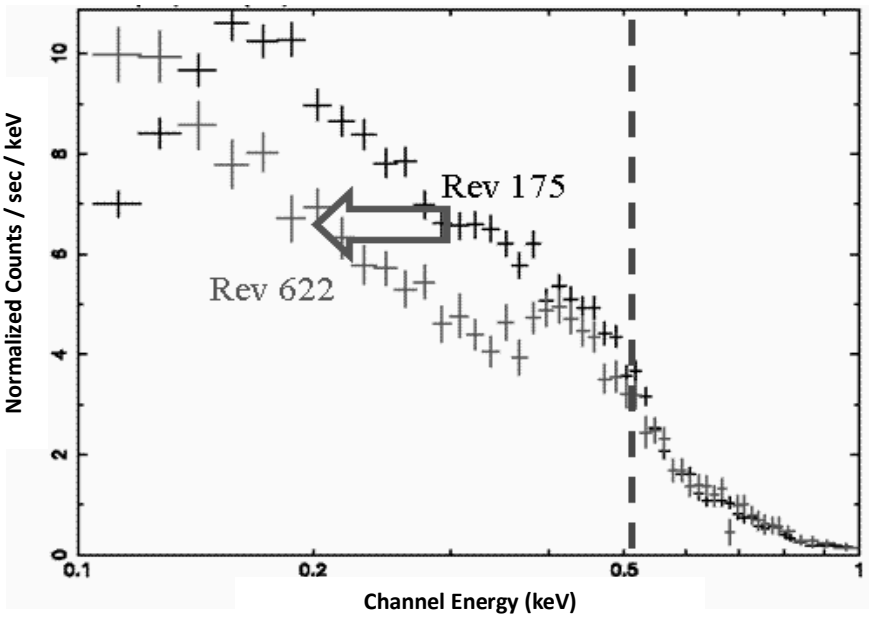

Figure 3.3 Two observations of a typical X-ray Source, 2.5 years apart, using the central region of the XMM-Newton EPIC-MOS camera [Read and Abbey, 2007]. Note the spectral redistribution in the more recent data set

Figure 3.4 shows a series of X-ray spectra at different energies, taken at a synchrotron source using a CCD22 EPIC MOS CCD. These data indicate a region in the CCD silicon material that absorbs charge generated when a soft X-ray photon interacts close to the CCD surface. This effect is measured on an un-irradiated device.

This redistribution of charge close to the CCD surface is well understood and is explained fully by Janesick (2001) and is demonstrated in Figure 3.5. Janesick showed that the potential inside a CCD drops as it approaches the oxide layer at the surface of the device. This drop in potential results in charge being collected at the surface rather than at the buried channel within the device. Softer X-ray photons interact close to the surface of the device in this region of reduced potential, resulting in the spectral redistribution shown in Figure 3.4. What was unexpected in the XMM-Newton mission was for this effect to change so greatly with time.

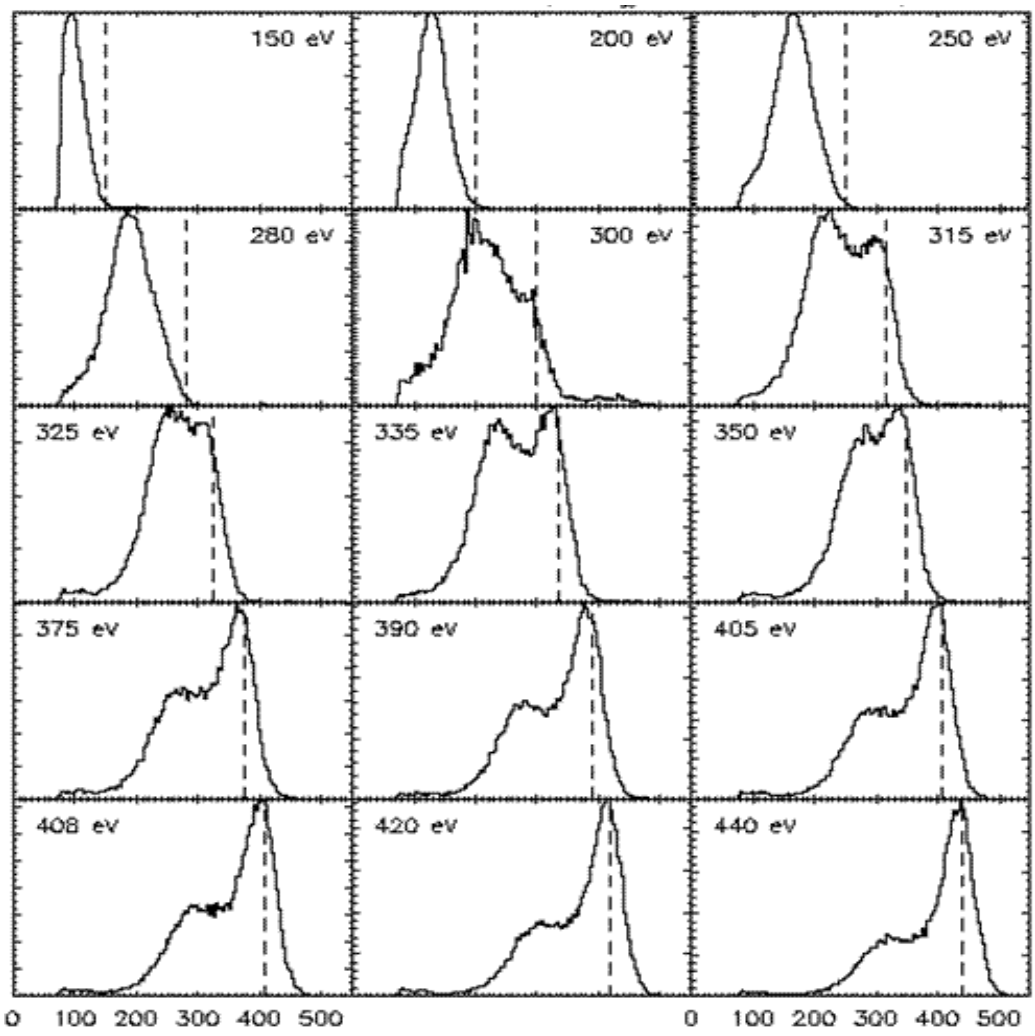

Figure 3.4 Spectra taken at a synchrotron radiation source [Read and Abbey, 2007] demonstrating the low energy spectral redistribution which the XMM Life Test attempts to recreate. Each 'snapshot' is taken using a different X-ray photon energy.

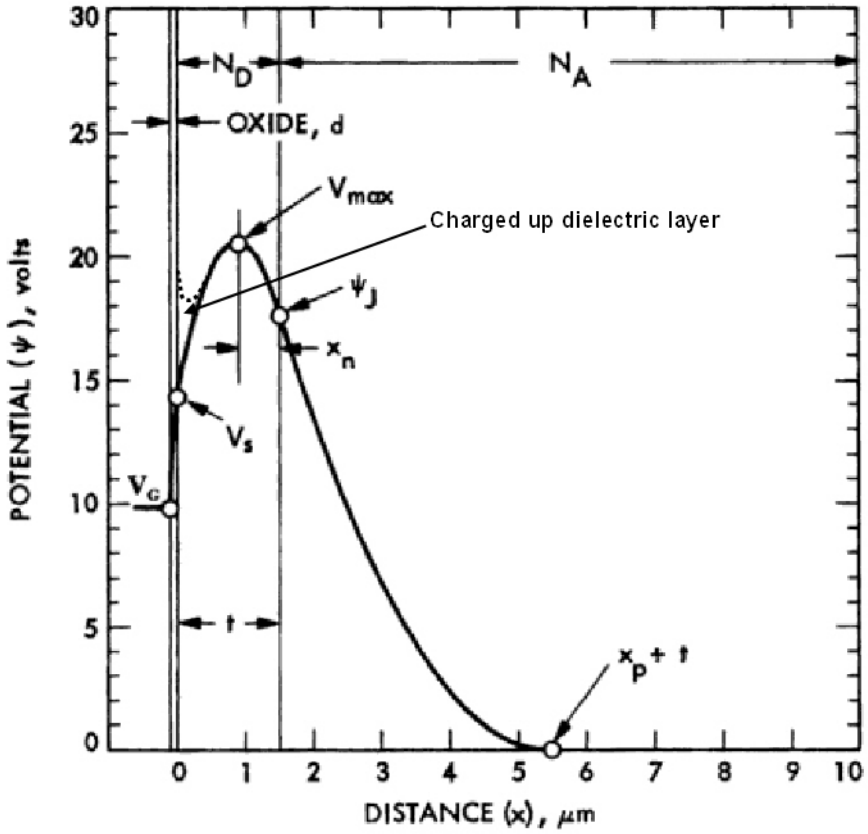

Figure 3.5 Modelled potential within a CCD showing the variation of potential with depth. Charge generated in the CCD will be swept to the buried channel (V_{max}) [Janesick, 2001]. When the dielectric layer is charged then X-ray generated charge can be lost to this layer rather than being swept to the buried channel.

The XMM Life Test experiment aims to reproduce this effect in the laboratory by using an MCP optic to focus X-rays, equivalent to the dose accumulated over the XMM-Newton mission, as shown in Figure 3.6 [Read and Abbey, 2007], onto a localised region of a CCD22 device. This Chapter introduces the test setup, reports the initial results and discusses the future direction of this experiment.

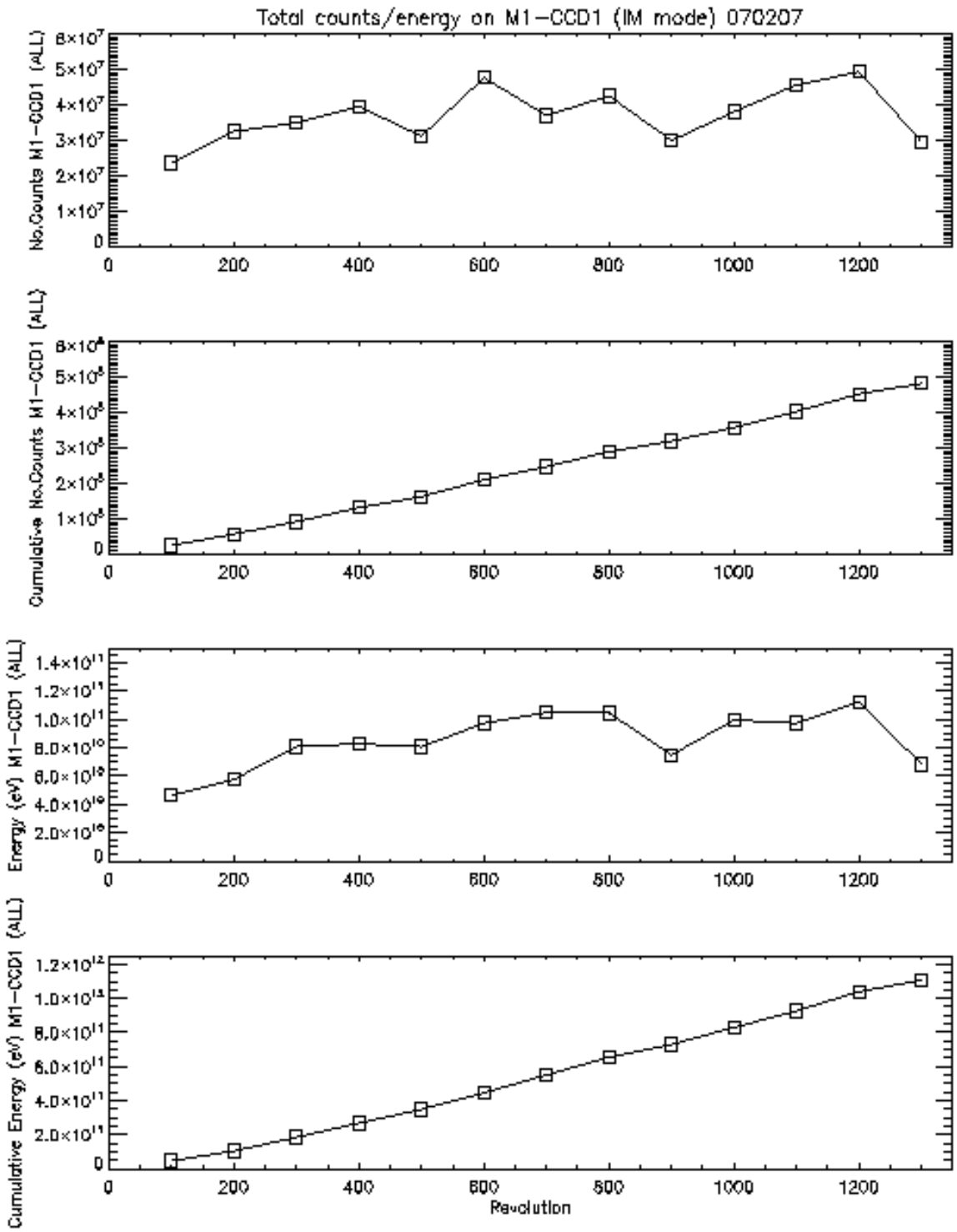

Figure 3.6 Plots, courtesy of A. Read, showing the energy deposited and X-ray counts accumulated over the XMM-Newton mission from launch to 2007. Note that 1 revolution, or orbit, takes 2 days.

3.4 EXPERIMENTAL SET-UP

The XMM Life Test facility consists of a CCD22 mounted in a vacuum test facility which is rotary-pumped to < 10^{-6} mbar and cooled to -100°C using a copper cold finger connected to a liquid nitrogen reservoir. An electron gun and copper anode are used to produce bremsstrahlung X-rays which are passed through a crystal monochromator that is used to select a specific energy of X-ray to be passed through a microchannel plate optic mid-way down the test facility (for point-to-point focusing). The MCP optic mounted in the facility is the flat ME001-8 square-pore square-packed optic discussed previously and is used to concentrate X-rays on the CCD22 at the end of the X-ray facility. It is possible to move the MCP optic in and out of the X-ray path without opening up the chamber, with fine adjustment to the positioning of the optic achieved using a mounted micrometer on the optic arm. Figure 3.7 and Figure 3.8 show a series of photographs depicting the main components to the XMM Life Test Facility.

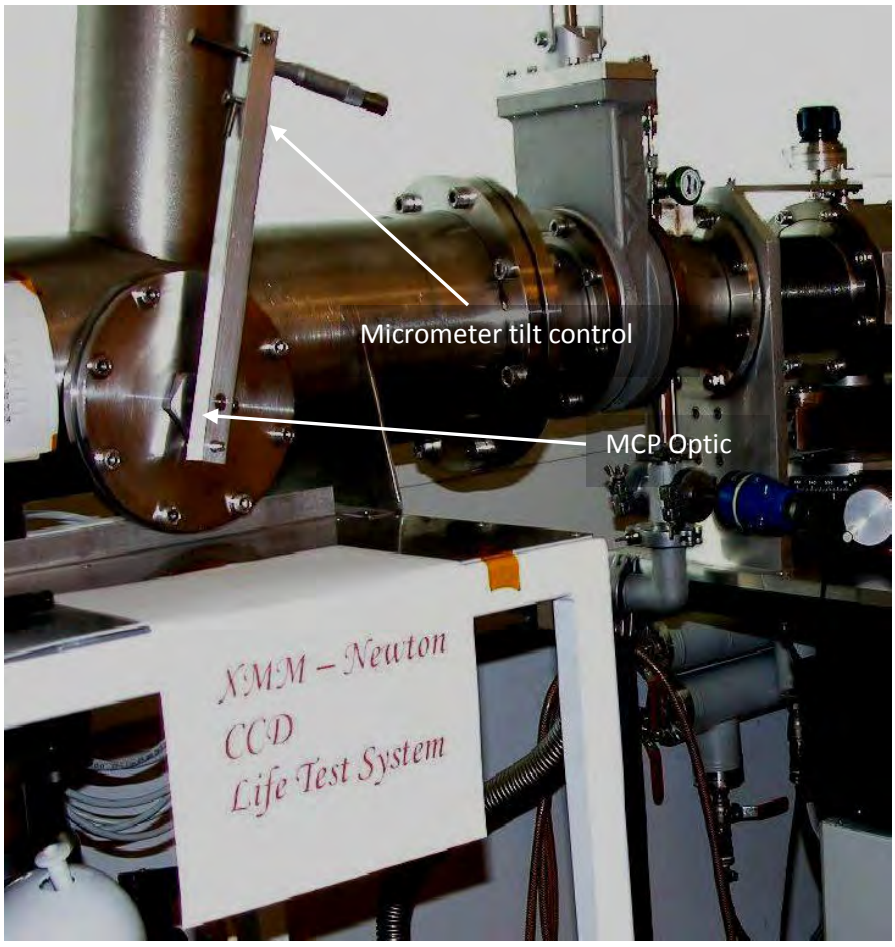

Figure 3.7 The XMM-Newton Life Test Facility

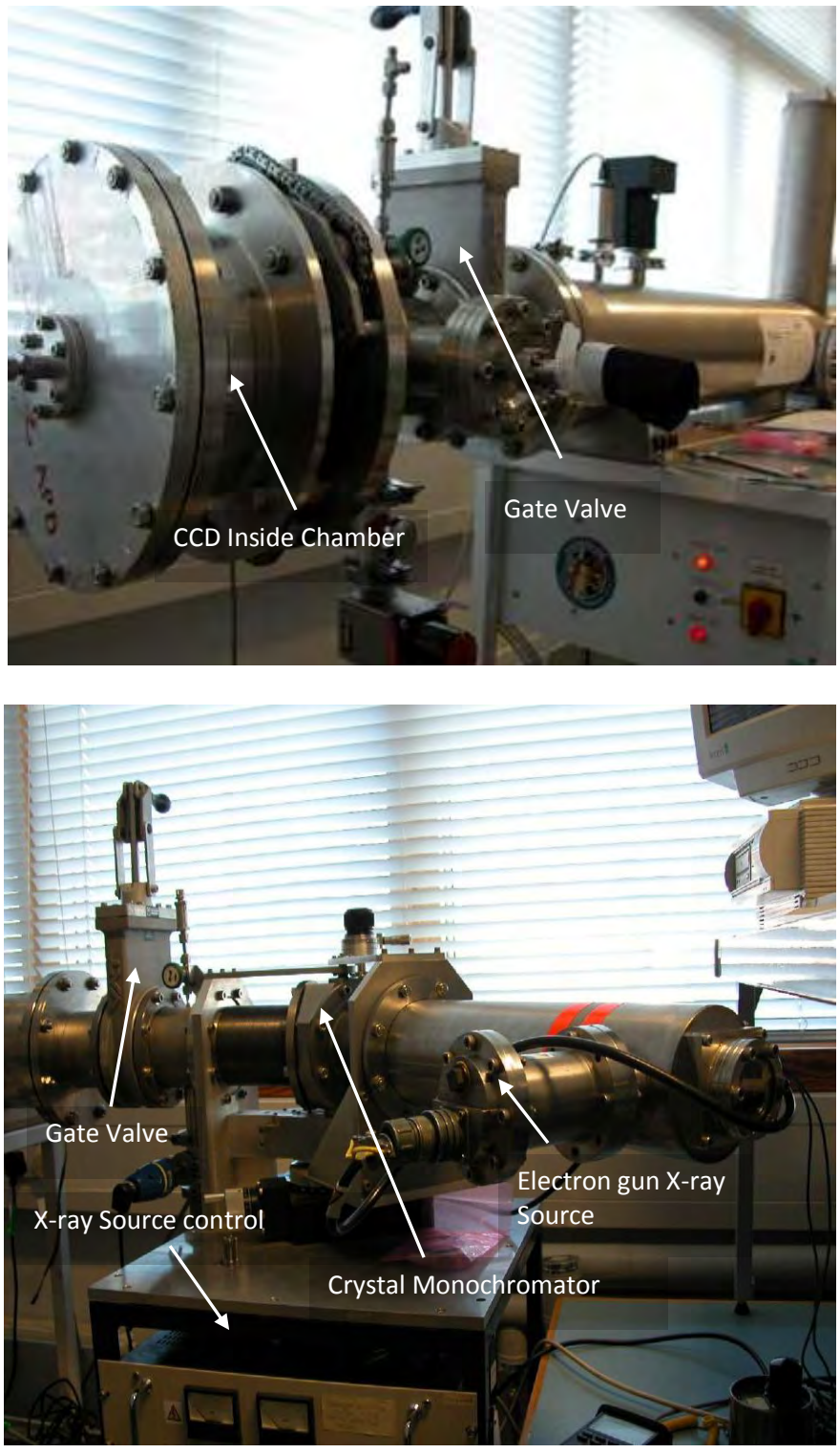

Figure 3.8 The XMM-Life Test facility – comprising an electron gun X-ray source, crystal monochromator, MCP optic and a CCD22 detector

3.5 THE EXPERIMENT

3.5.1 TEST AIMS

The primary aim of the experiment was to create localised damage on a CCD using X-rays of similar energy and dose to that experienced on XMM-Newton and to propose an explanation for the cause of this damage. A secondary aim of the experiment was to attempt to reverse the damage through annealing. If this damage is reversible then an in-flight solution could potentially be found to improve the current detector response of XMM-Newton.

The purpose of the MCP optic in this experiment is to localise the X-rays incident on the device, as well as to also locally analyse the post-irradiation damage to the CCD by directing X-rays to different regions of interest during data acquisition.

The total accumulated energy on the MOS-1 EPIC device was $1x10^{12}$ eV (Figure 3.6). The X-ray dose used in the Life Test was to be administered in 4 steps of $2.5x10^{11}$ eV, with any damage to the CCD examined between each irradiation. Measurement of the dose during each phase was to be done by establishing the average energy deposited on the device per CCD frame. As the length of time per frame is known, an estimated time of total dose accumulation could be calculated.

In order to analyse the damage of the device, X-ray data were taken in different regions of interest across the CCD and the X-ray spectra analysed and compared to the spectra accumulated on the device before irradiation. The spectra were analysed using curve fitting functions in OriginPro 7.5 (OriginLab, Northampton, MA) software to measure redistribution of the X-ray energy.

3.5.2 PRE-IRRADIATION TESTS

Prior to X-ray irradiation, X-ray spectra were taken using the CCD at various energies from Carbon (284eV) to Copper L (928eV). It was found that an uneven dark current pattern was present across the CCD and, from looking at the device history, it was found that the CCD had been previously subjected to a very long ^{55}Fe exposure. Figure 3.9 shows a dark current image taken at -100°C prior to any X-ray irradiation and clearly shows the elevated dark current level seen on the right hand side of the CCD22 used in the test.

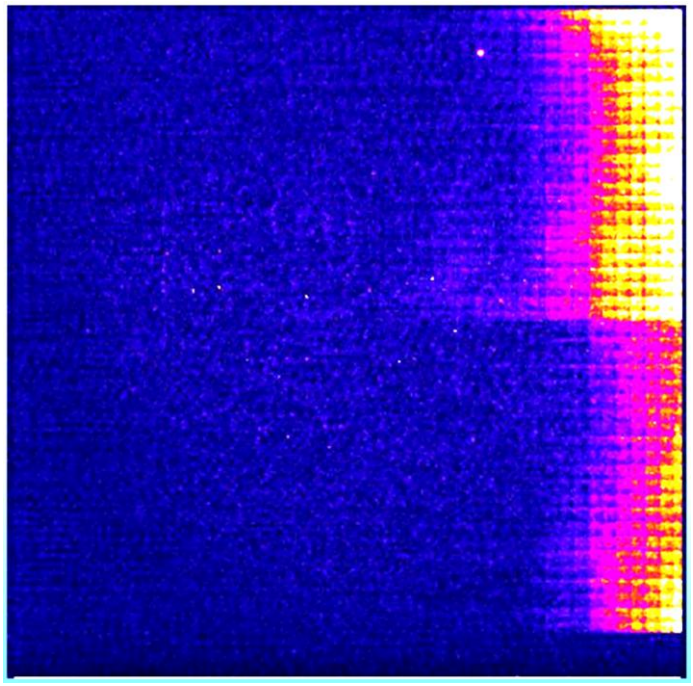

Figure 3.9 CCD22 Dark Current Image taken at -100°C prior to any X-ray Irradiation. Image is 2.5x2.5cm^2.

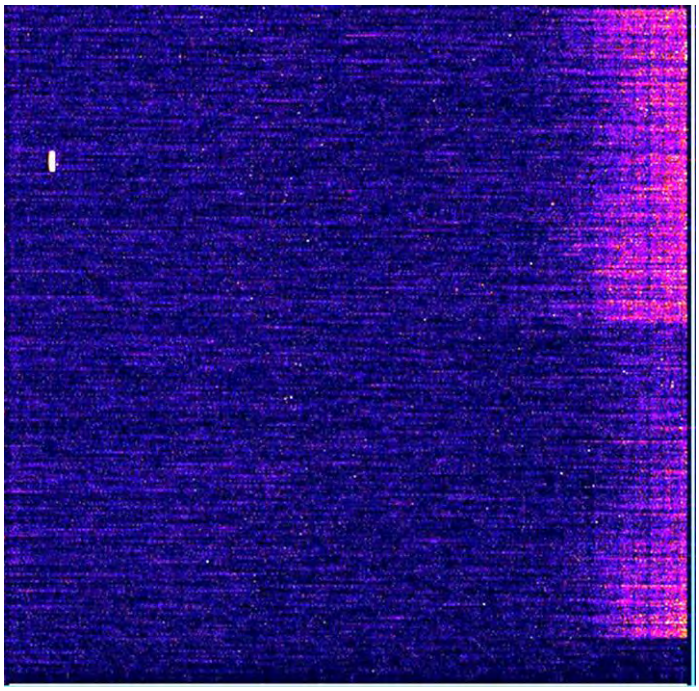

Figure 3.10 CCD22 Dark Current Image taken at -100°C after 24 hours of annealing at +100°C. This image was taken at twice the gain and twice the exposure time of Figure 3.9. Image is 2.5x2.5cm^2.

It was decided to perform a thermal anneal of the device in an attempt to improve the performance of the CCD. Also, performing a high temperature anneal prior to irradiation ensures that improvements seen in subsequent anneals, post-X-ray irradiation, can be attributed to removal of the newly created damage rather than that which incurred prior to the XMM Life-Test experiment. The device was heated to 100°C for 24 hours.

Figure 3.9 and Figure 3.10 show before and after images of the CCD and clearly demonstrate the improvement achieved by annealing this device. A further anneal of 85 hours at 100°C was performed resulting in further improvement in the dark current problem, as well as a slight improvement of the CCD energy response.

3.5.3 X-RAY IRRADIATION

The flat MCP optic focuses X-rays onto the CCD in the characteristic cruciform shape (Figure 3.11). In order to measure the X-ray energy deposited in the focal spot of the MCP optic image, X-rays were produced using a current of 80µA and 5kV on the anode (~3.5keV X-ray spectrum peak). Higher beam currents resulted in saturation of the device and an inability to measure the energy deposited in the 7.3s frame time. At 80µA, the MCP optic focussed ~85keV into the focal spot during the accumulation of 1 frame. Increasing the beam current to 4mA therefore produces a flux of approximately 500KeVs^{-1} in the focal region, or 150 photons per pixel per second.

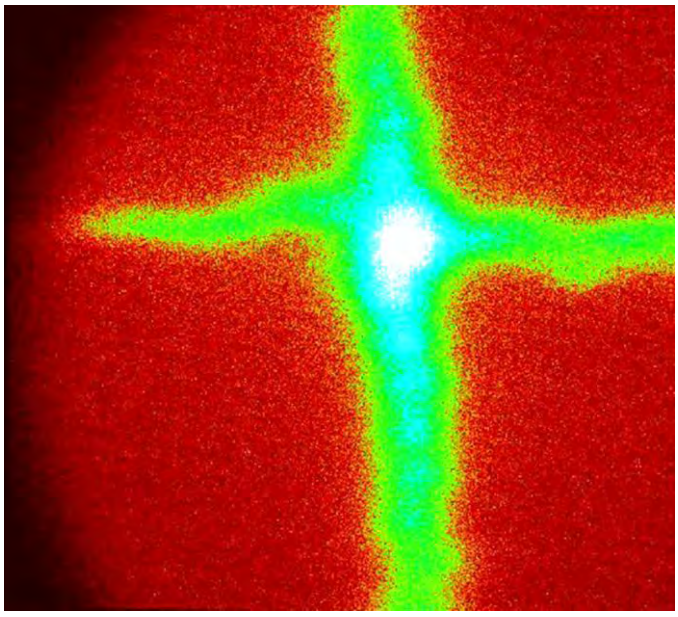

Figure 3.11 The MCP Optic is used to focus X-rays onto the CCD. This image is 2.5cm x 2.5cm.

The XMM-Newton dose of $1x10^{12}$ eV was the total dose experienced by the whole CCD, most of which is concentrated to the centre of the device. Unfortunately, there was an error in the dose administered to the CCD22 during this experiment as the pre-damage calculation assumed a dose of $1x10^{12}$ eV per pixel. The device was given ~8000 times the required dose in just 28 hours!

Figure 3.12 shows the first dark current image taken after the irradiation. Heightened dark current is evident in the cross shape of the MCP optic focus, clearly showing the damage caused to the device by the overdose of X-rays. A series of dead columns is also evident in the image towards the centre of the device. These columns were later found to be a result of a flat-band voltage shift often seen in semiconductor devices irradiated by ionizing radiation [Janesick, 2001].

Figure 3.13 shows an image captured with CuL X-rays incident on the CCD immediately after the irradiation. Significant smearing of the X-rays indicates charge transfer efficiency problems.

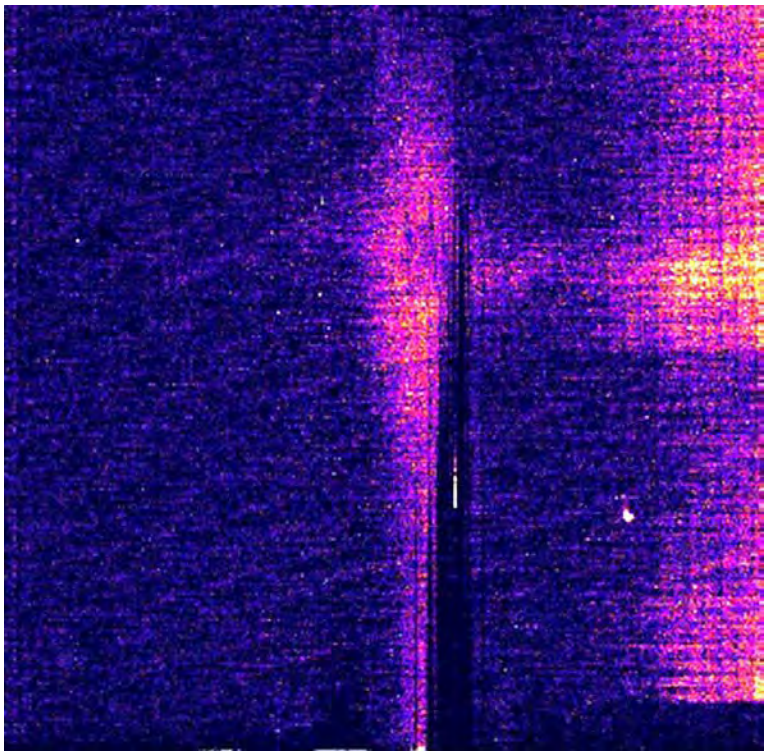

Figure 3.12 The first dark frame taken without X-rays incident on the CCD22 after the first irradiation. Note the high dark current and dead columns towards the centre of the CCD. Image is 2.5x2.5cm^2.

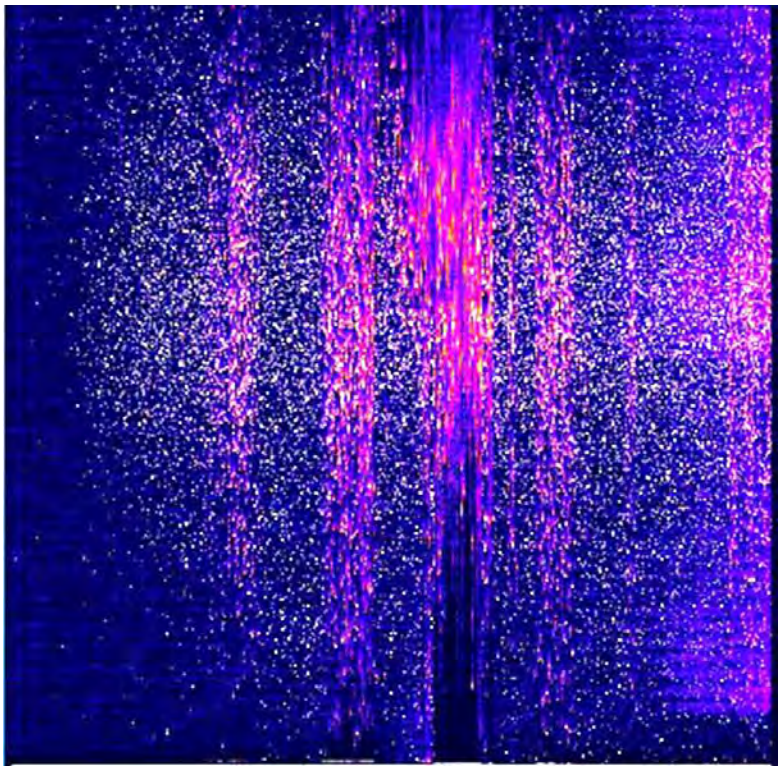

Figure 3.13 CuL X-ray image taken with the CCD22 after the first irradiation. Image is 2.5x2.5cm^2.

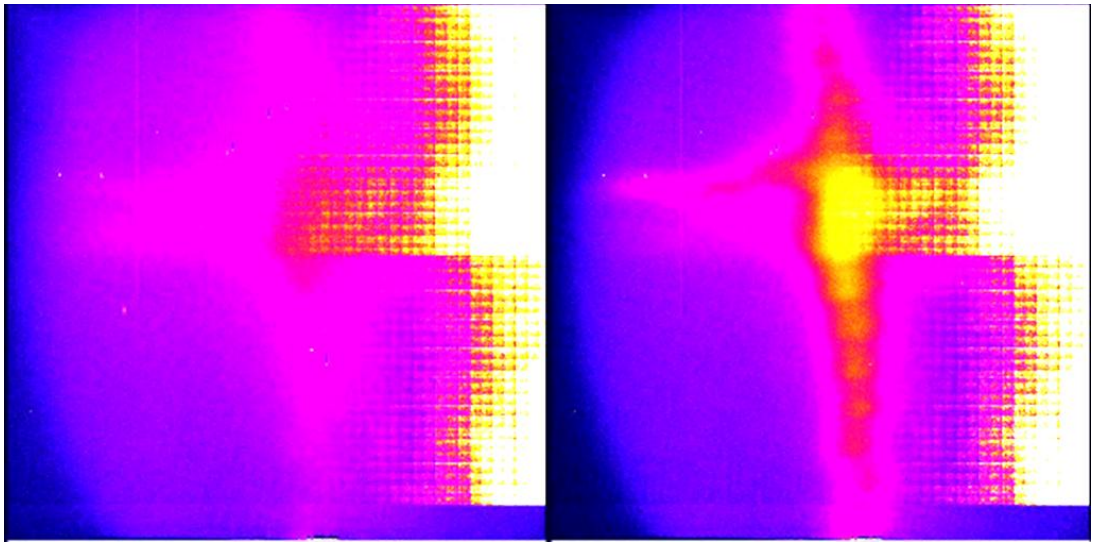

Figure 3.14 'Warm' dark images taken at -50°C. The image on the left was taken as the CCD was warmed up from -100° while the image on the right was taken when cooling the device down after a 13-hour room temperature anneal. Each image is Image is 2.5x2.5cm^2.

Dark images taken at -50°C during the heating up of the device to room temperature and then while cooling down to -100°C after 13 hours at room temperature, show the cruciform image of the MCP optic in elevated dark current (Figure 3.14). Note, however, that certain regions of the device remain unaffected relative to the focal region of the optic, such as the top and bottom left of the CCD. These areas offer an opportunity to continue using this particular device to a) investigate the damage caused by this irradiation and b) to conduct further, more controlled damage experiments in currently unaffected areas of the CCD.

In order to recover some of the functionality of the device a second high temperature anneal was performed, with the device spending 85 hours at 100°C.

Figure 3.15 shows a histogram constructed using three data sets taken using 450eV X-rays in a region of interest in the centre of the CCD: the first data set prior to irradiation, the second after the irradiation and the third post high-temperature anneal. The histogram shows the percentage of total counts registered in the ROI that are isolated (that is, those that consist of just one pixel), bi-pixel, tri-pixel, quad-pixel and events consisting of 5 pixels. Very few photon interactions at this low X-ray energy result in events consisting of >5 pixels.

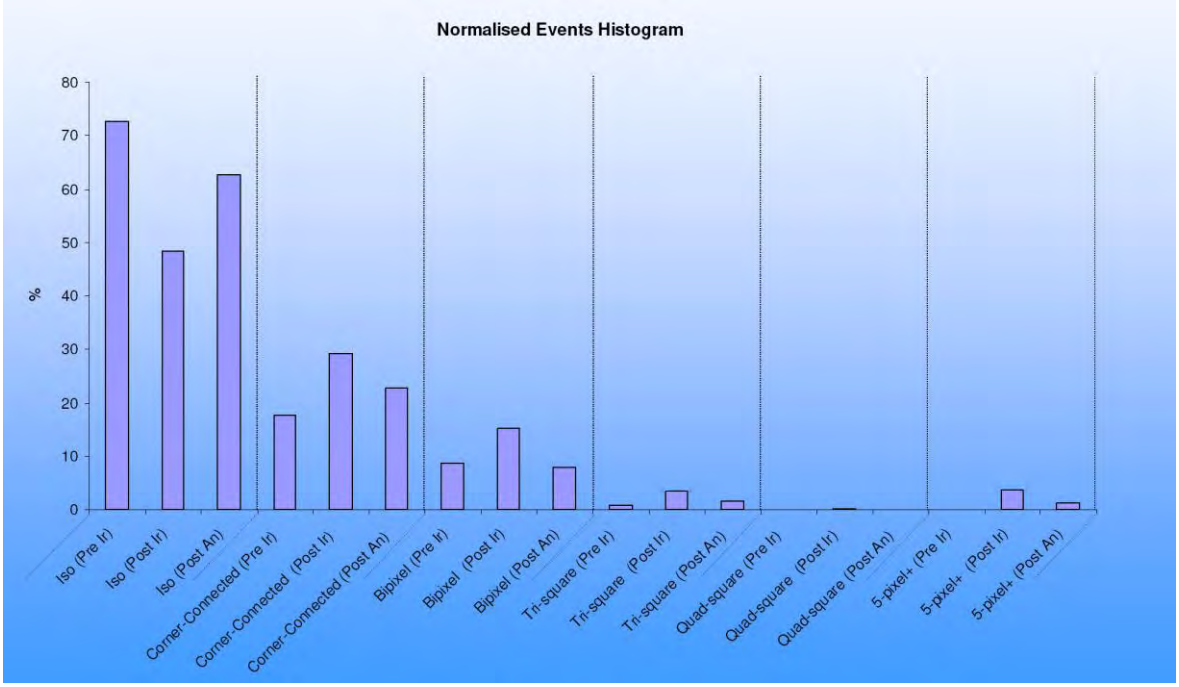

Figure 3.15 Histogram showing the normalised events measured before irradiation, after irradiation and after the high temperature anneal. The more damaged a device, the more multipixel events will be registered.

What is clear from this figure is that, after the irradiation, the number of single pixel events, as a fraction of the total, decreases significantly. This is coupled with an increase in the larger-scale events showing that the damage has resulted in many of the interactions spreading out over numerous pixels. This is an indication of charge transfer problems in the CCD. A significant improvement, however, is also evident after the CCD is annealed at high temperature. A shift is seen in the opposite direction as the larger events are reduced and isolated pixel events increase in proportion.

Ultraviolet (UV) light is known to recover some CCD performance after a device has suffered ionizing damage. This works by neutralizing trapped charge in the gate dielectric [Ristic, 2009][Janesick, 2001] and has been employed in-orbit onboard the Solar X-ray Telescope on the SOLAR-A mission to reverse a negative flat band shift [Tsuneta et al, 1991]. This UV flood technique was applied to the Life Test CCD22 and further improvement was seen. With the UV flood and a re-optimisation of the CCD voltages, the dead region at the centre of the CCD was recovered. The average noise of the CCD was measured to be approximately 5.5 electrons after the thermal anneal and UV flood.

3.5.4 LIFE TEST DAMAGE ANALYSIS

Using the MCP optic, it is possible to concentrate X-rays into regions on the CCD of little damage such as the top left hand corner. This allows data to be taken with statistical significance in a short period of time in a small region of interest. The damage experienced on XMM-Newton results in significant redistribution at low X-ray energies. In order to compare the damage done to different regions of interest, a figure of merit based on redistribution is defined: the redistribution factor, R.

Figure 3.16 shows an isolated event spectrum taken with the damaged CCD22 device in the XMM Life Test facility. The Nitrogen k_α x-ray energy (0.39keV) was chosen using the crystal monochromator[1], although a significant Carbon k_α line is also present in the spectrum due to system contamination. Carbon X-rays were seen in all observations using this test facility.

[1] The crystal monochromator was used to select a narrow 'line' energy of 0.39keV from the broad bremsstrahlung X-rays generated by the X-ray source. The bremsstrahlung spectrum can be set to peak at the energy of interest by adjusting the voltage of the X-ray source.

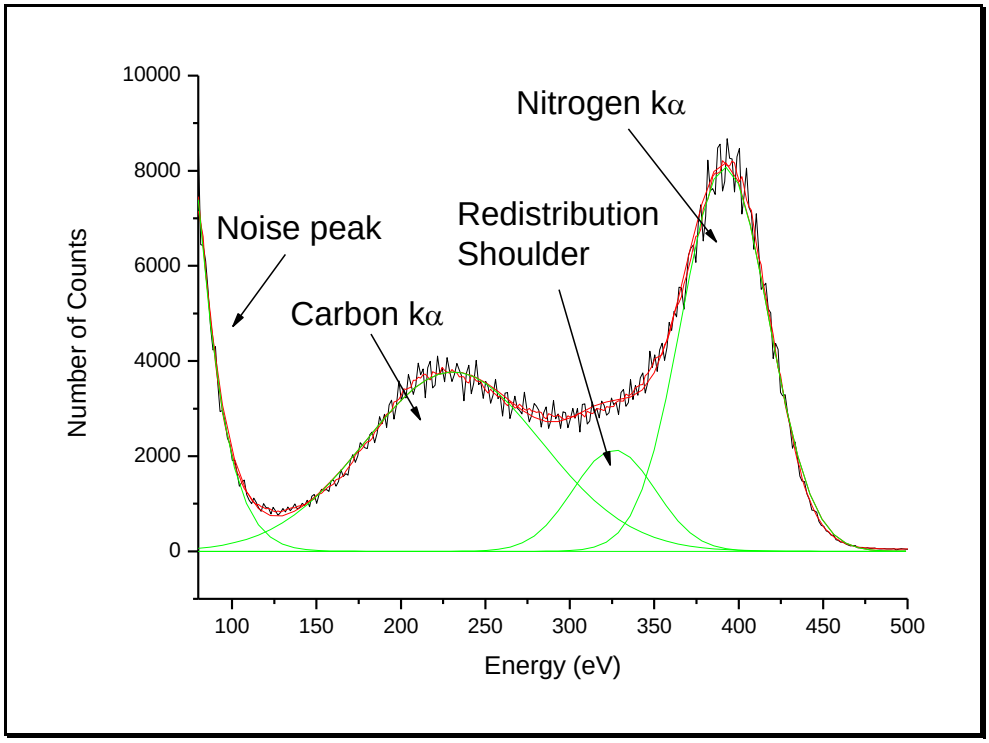

Figure 3.16 Isolated Event Spectrum taken using the damaged CCD22 and the XMM-Life Test facility. The monochromator is used to select the Nitrogen line (0.39keV). A series of Gaussian curves is used to approximate the main components of the spectrum. The X-ray lines have been redistributed to lower energies.

Energy redistribution in a damaged device results in a significant portion of events moving from the main Nitrogen peak into lower energies. The redistribution factor, R, is defined as:

$$R = \frac{Total\ counts\ in\ main\ peak}{(Total\ counts\ in\ redistribution\ peak + Carbon\ peak + Noise\ Peak)} \qquad \textbf{(3.1)}$$

and is normalised to the whole device for comparison. Note that R is larger for areas which result in less redistribution (corresponding to less damage) whereas smaller values of R represent regions of the device which experience large redistribution effects and, hence, have greater damage.

The CCD was split into different regions of interest and a spectrum taken in each from an exposure consisting of 1000 frames. A series of Gaussian curves were fit to each ROI spectrum as in Figure 3.17 and the redistribution factor, R, calculated for each region.

Table 3.1 and Table 3.2 summarise the results.

When these R values are mapped onto the CCD image (Figure 3.18) it is clear that the central damaged area and regions of previous signs of damage suffer the highest levels of redistribution.

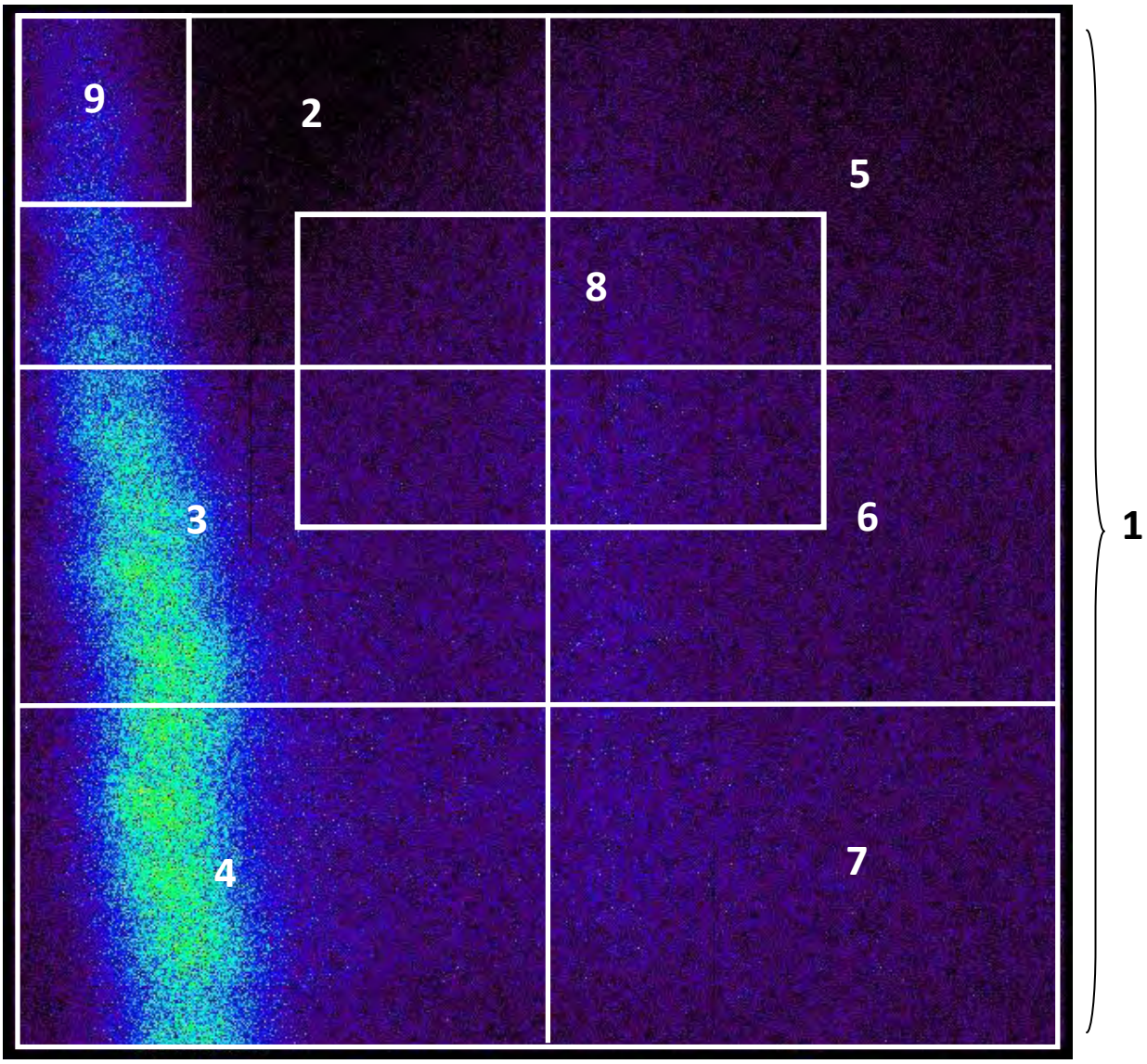

Figure 3.17 CCD22 Image showing the Regions of Interest (ROIs) investigated on the damaged CCD22. Note the X-rays directed by the MCP Optic to the areas less exposed during the irradiation.

Table 3.2 also shows that these areas have the largest shift in peak position, another indicator of damage.

ROI	Counts, Noise	Counts, Ck_{α}	Counts, Redist.	Counts, Nk_{α}	R	$R_{Normalised}$
1	7371727	497486	130188	521557	0.06519956	1
2	234395	55180	21454	61405	0.19742495	3.02801
3	314654	123600	44957	145048	0.30017601	4.603957
4	201937	136496	42086	158562	0.41669779	6.391113
5	3622848	23192	31976	25050	0.0068106	0.104458
6	2395167	31281	54985	49279	0.01985896	0.304587
7	1357009	35005	52337	51416	0.03559791	0.545984
8	2548031	27734	50826	45115	0.01717621	0.263441
9	14849	9610	4494	10511	0.36303413	5.568045

Table 3.1 Summary of counts in each spectrum peak and the calculated value of R for each region of interest

ROI	X, Ck_{α} (eV)	X, Redist. (eV)	X, Nk_{α} (eV)	W, Noise (eV)	W, Ck_{α} (eV)	W, Redist. (eV)	W, Nk_{α} (eV)
1	230.99944	326.28323	392	73.35293	105.23488	48.73843	51.50187
2	226.87131	323.40952	392	88.02941	91.59272	57.98265	51.20775
3	230.50564	322.70426	392	94.07991	90.53803	53.59946	51.91087
4	238.56707	326.79875	392	114.26274	90.98245	47.67143	50.6319
5	184.84997	315.71978	392	65.84379	84.8264	136.29746	48.38214
6	192.56839	303.71275	392	69.50324	76.66063	144.82779	50.32058
7	202.20543	311.67846	392	73.79636	81.65907	131.64085	50.09785
8	196.99365	302.36601	392	69.71745	74.67798	140.64384	50.66741
9	229.36795	326.41997	392	123.4409	87.60027	62.48592	49.5597

Table 3.2 Summary of peak positions on the x-axis and the FWHM values of the main peaks for each ROI. The position of Nk_{α} was fixed and the position of the other peaks allowed to vary.

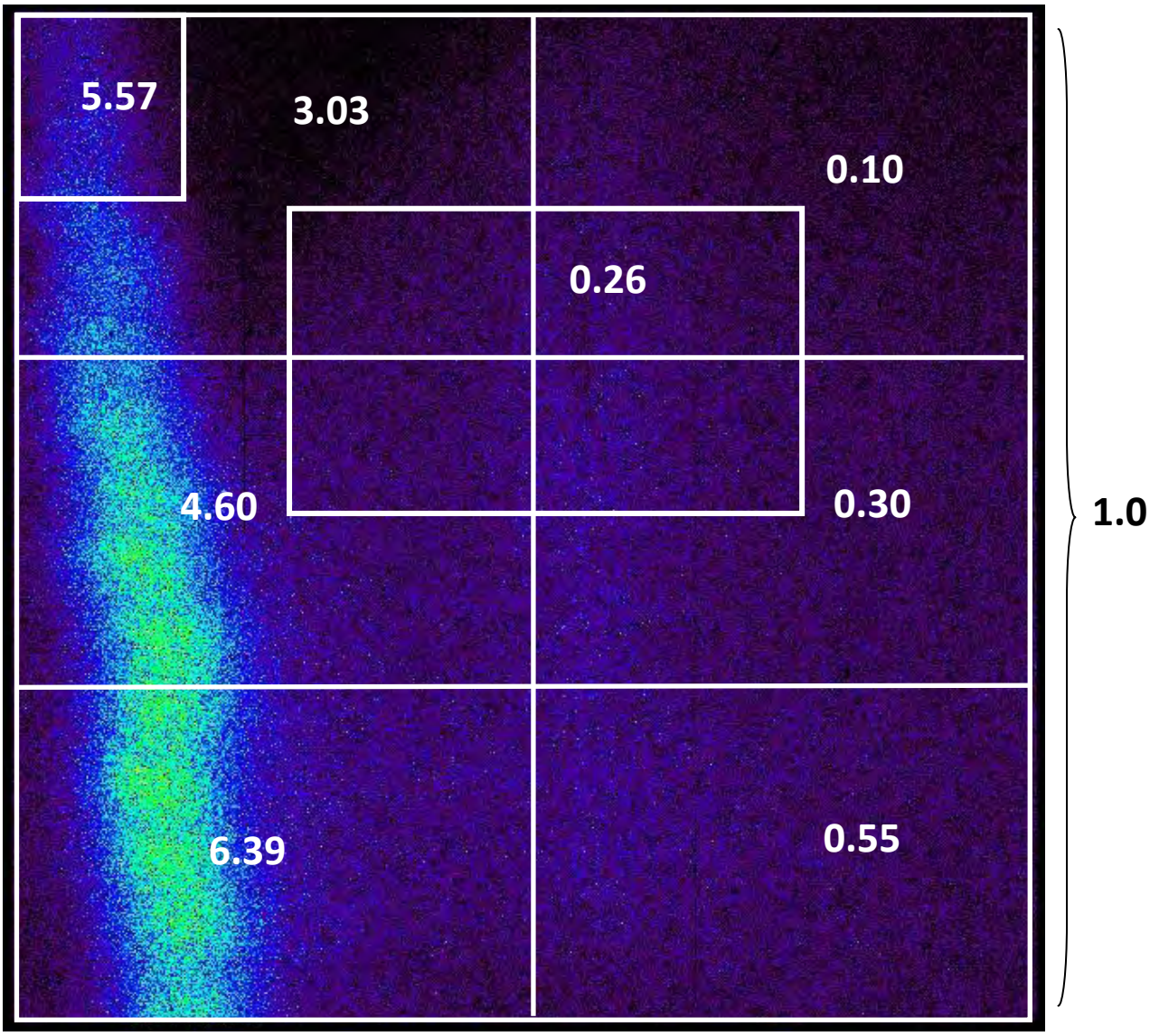

Figure 3.18 CCD image split into Region of Interests with the associated redistribution factor, R. The greater the value of R, the less redistribution and therefore the less damage has occurred.

It can be seen from Figure 3.18 that the central region and right-hand-side of the device has the smallest R values and therefore demonstrates the greatest redistribution. It is these regions that experienced the largest amount of damage during the X-ray irradiation experiment (Figure 3.14) and also exhibited damage effects from previous prolonged exposure to ^{55}Fe X-rays (Figure 3.10).

The CCD22 has an open electrode structure, meaning that a significant area of oxide in each pixel is etched away to increase the device sensitivity to lower energy X-rays. It has been noted that

vertical bi-pixel events *must* interact within this open electrode region [Hiraga et al, 2001]. Horizontal bi-pixel events, conversely, *must* interact with the thicker electrode structure. Figure 3.19 and Figure 3.20 show CCD images composed of horizontal and vertical bi-pixel events, respectively. It can be seen that the horizontal events, those photons interacting through the electrode, produce a fairly homogeneous image with X-rays showing across the whole area of the CCD. The vertical bi-pixel image, however, clearly shows sign of significant damage. The MCP cross feature is clearly visible on the CCD due to the absence of X-rays in this region.

Clearly the open electrode portion of the pixel is much more susceptible to ionizing damage caused by the X-ray radiation than the closed electrode part.

From the preliminary evidence presented in the chapter, a hypothesis regarding the variable CCD22 ionizing damage can be made. The low energy redistribution effect, coupled with the evidence that the damage is specific to the open electrode structure, suggests that the thin, insulating, dielectric oxide layer is charged up over time by incoming low-energy X-rays interacting close to the CCD surface. Also, thermal annealing of the device post-damage resulted in very little improvement in the CCD response. If the damage is the result of charge locked within the CCD dielectric, thermal annealing would not be able to remove this.

The charging up of the dielectric layer would change the electric field within the device (Figure 3.5) such that a portion of the charge generated by photon interactions close to the CCD surface would likely be lost. The inability of the insulating dielectric to release this charge would mean this effect is cumulative and, therefore, changes with time. The amount of charge held in this insulating layer would eventually reach maximum capacity, suggesting that after a time the degradation of the CCD due to this effect ceases. Recent XMM-Newton observations support this hypothesis as the degradation effect appears to have halted [Sembay, 2009].

This result has significant implications to the manufacture and use of open electrode devices where large ionizing doses are expected; either through large X-ray flux or operation over an extended time. The benefits in low energy response of such devices must be traded off with the expected degradation of the devices with X-ray dose.

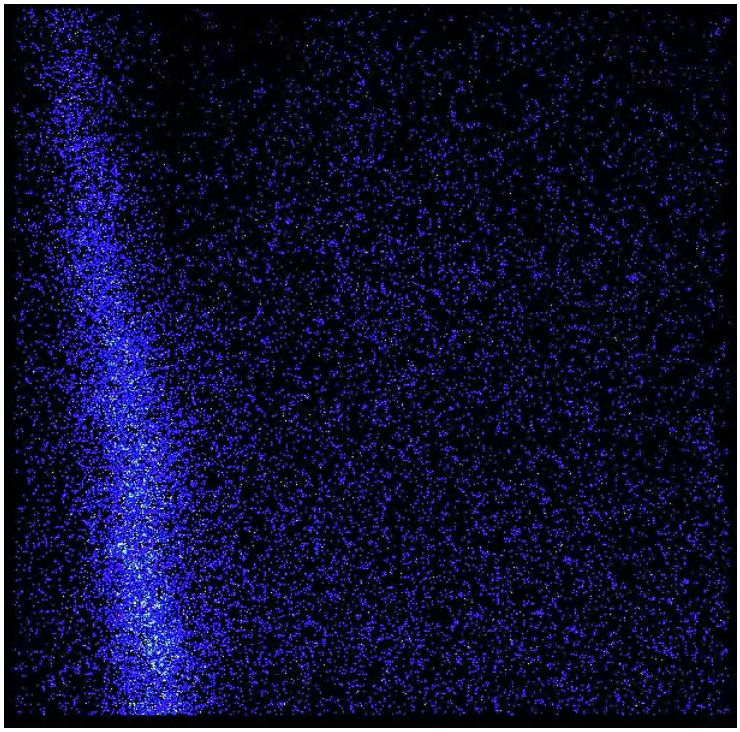

Figure 3.19 Horizontal Bi-pixel X-ray Event Image

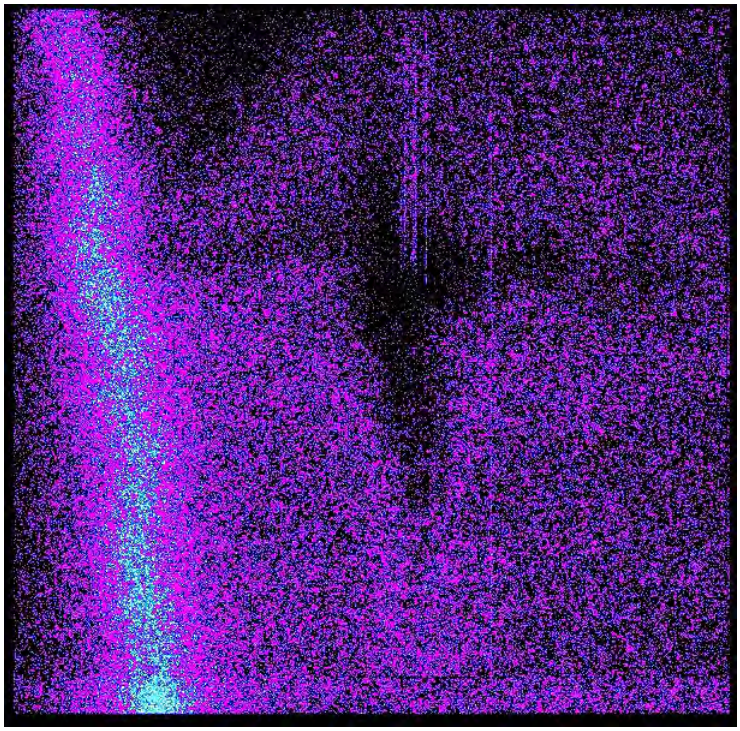

Figure 3.20 Vertical Bi-Pixel X-ray Events. These events MUST occur in the open electrode part of the pixel.

3.6 XMM-LIFE TEST FUTURE WORK

The XMM-Life Test experiment is ongoing and there are a number of activities, beyond the scope of this PhD, which will be undertaken. It would be desirable to irradiate a previously undamaged CCD22 device with systematic, controlled doses of X-rays up to the XMM-Newton dose. The results of this should then be compared to a similar irradiation experiment on a CCD which doesn't have an open electrode component. The damage done to the CCD22 tested here was far in excess of that seen on XMM-Newton and is therefore not truly representative of the mission.

The investigation into reversing the cumulative ionizing damage should continue, possibly focussing on the use of UV radiation of different wavelengths to neutralize trapped charge in the open electrode dielectric [Ristic, 2009].

Current CCD22 modelling uses correctional terms representing damage to match flight data rather than an understanding of the principle damage mechanisms. Steve Sembay at the University of Leicester is leading a research project that complements the work done in the XMM Life Test. A predictive model of ionizing and non-ionizing damage to XMM CCDs is being made, using both in-flight data from XMM and data from damaged laboratory CCDs – including the data presented in the chapter. This future work should allow better prediction of the performance of damaged CCDs – particularly important for the SWIFT and AstroSat missions which both use the CCD22 in the focal plane of their X-ray telescopes.

3.7 SUMMARY

Microchannel Plate Optics have been shown to be useful in the laboratory when performing X-ray damage experiments in the XMM Life Test facility. The ability to focus X-rays onto a small area enabled the X-ray damage (albeit excessive) of a localised region of the CCD22 and proved to be crucial for the timely acquisition of X-ray data in undamaged areas of the device.

It was shown in this experiment that damage resulting from very high doses of ionizing radiation in the form of X-rays can indeed result in localised damage to a CCD22 such as that flown onboard XMM. This effect had not been seen using the CCD22 on ground prior to this experiment. It was also shown that this sort of damage is device specific, with the damage occurring solely in the open electrode structure of the CCD22. This localised damage results in large redistribution effects in generated X-ray spectra. Future devices wishing to avoid this sort of long-term damage

should avoid using an open electrode to achieve low-energy quantum efficiency improvements. Instead, back illuminated devices under full depletion should be baselined as a viable alternative detector capable of avoiding this type of radiation damage.

The next chapter investigates the effect of depletion on CCD performance, with the aim to improve spectral resolution and quantum efficiency.

CHAPTER 4

IMPROVING THE PERFORMANCE OF X-RAY SENSITIVE CCDS: DIRECT DEPLETION REGION MANIPULATION

4.1 DEVELOPMENT OF THE CCD66 FOR FUTURE X-RAY MISSIONS

Charged-coupled devices (CCDs) for future X-ray astronomy, such as the International X-ray Observatory (IXO) and planetary missions, such as ExoMars, require improved quantum efficiency (QE) and spectral resolution at higher energies (>10 keV) if science requirements are to be met [Kaastra, 2005][Griffiths, 2005]. Quantum efficiency is the measurement of charge conversion efficiency in X-ray sensitive detectors such as semiconductor devices, describing the fraction of incident X-rays converted to signal at a given energy. Silicon based CCDs for astronomy have traditionally had useful QE from 0.6-10keV although developments such as back illumination (e.g. the EPIC p-n Camera) [Struder, 2001], open electrode structures and electrode etching (e.g. the EPIC CCD22) [Turner, 2001] have been used to very good effect in order to increase the useful energy response to lower (~0.2 keV) energies. The limited 10-20% QE of standard CCDs up to ~15keV is also of use, although longer observation times are required to produce spectra with similar statistics as those covering lower X-ray energies. Figure 4.1 shows the QE curves for the XMM-Newton EPIC MOS and p-n CCDs prior to launch [Turner et al, 2001][Struder et al, 2001].

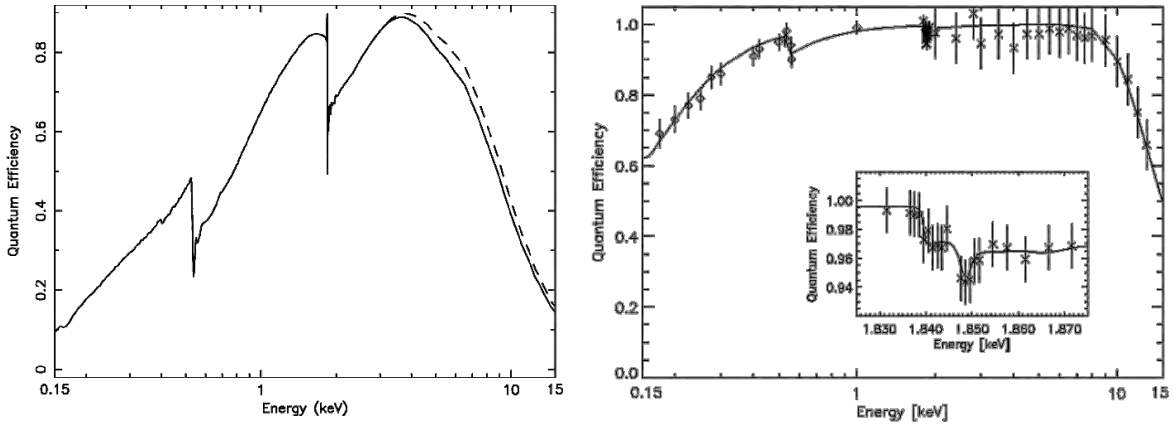

Figure 4.1 The XXM-Newton EPIC MOS 1(left) and p-n camera (right) Quantum Efficiency Curves

The development of many X-ray instruments for Astronomy in recent times has been geared towards the International X-ray Observatory (IXO) [IXO Payload Definition Document, 2009]. Annex 1 of this thesis describes in detail the spacecraft and diverse payload elements of IXO.

The University of Leicester and e2v Technologies produced a series of prototype CCDs [Keay, 1999], aimed at meeting the IXO Wide Field Imager requirement of large detector focal plane at a long focal length, and a broad energy response (i.e. ~100% QE up to 10keV, ~60% QE at Carbon K and Fano-limited resolution up to 10keV). The CCD development programme resulted in the production, by e2v, of a test device designated the CCD66, described in Section 4.2. CCDs are also the baseline detector for the IXO X-ray Grating Spectrometer, with e2v providing the CCDs for the Off-Axis Grating Spectrometer instrument option. The type of CCD detectors used for the Off-Axis Grating Spectrometer is still yet to be determined. The work presented in the chapter describes the experimental framework and test campaign aimed at increasing the high energy response of the detector and highlights the key results obtained including QE and spectral resolution.

In addition to the CCD experimental work reported in the chapter, the CCD modelling work carried out as part of this thesis is also presented. A model was created by modifying the CCD22 Monte Carlo code developed for the XMM-Newton EPIC CCD camera and the Swift XRT detector [Short 2002], and was used to model the CCD66 event spectra for different depletion depths. This code is discussed in detail in Section 4.5.1. In addition, the model code was used to establish the depletion depth induced by the applied negative substrate voltage in the CCD66 experimental work. These results are also presented.

4.2 THE CCD66

The CCD66 is a prototype, large pixel CCD produced by e2v for the University of Leicester, primarily with the X-ray Evolving Universe Spectrometer (XEUS) observatory in mind [Parmar, 2005]. The aim of the device design is to use large pixels while constraining the signal charge within a small volume of silicon. The interaction of the charge with any bulk traps within the device is minimised and the CCD becomes more radiation hard as increased radiation dose has a lesser effect on charge transfer. Confining charge to a thin channel in the silicon is achieved using the supplementary buried channel approach [Ambrosi, 2003]. The design of the CCD66 element is similar to that of the CCD22, described in Chapter 2, but with improved serial charge transfer due to an additional supplementary channel being incorporated into the device. The supplementary

channel in parallel direction is also subtly modified in its shape from the CCD22, driven by the large pixel size and the need to rapidly and efficiently move charge from the point of X-ray interaction to the buried channel for device readout. Unlike the CCD22, however, there is no open electrode structure, leading to poorer low-energy response. Both the CCD66 and the CCD22 are epitaxial devices on a silicon substrate. The CCD66 is manufactured using 1500 Ω cm high resistivity silicon, which implies deep depletion.

The CCD66 is a full-frame array [Janesick, 2001]. Figure 4.2 shows a photograph of the CCD66, showing the two different pixel regions on the device. The chip is comprised of 40 x 140 elements, each with a 70 µm horizontal pitch. The device is split into two sections, the right section containing 40 rows of 100 µm vertical pitch, and the left section 100 rows of 70 µm vertical pitch. The CCD66 also uses a supplementary channel in the serial transfer of charge in order to minimise charge transfer loss from traps during readout. This is shown in the pixel structure diagram in Figure 4.3.

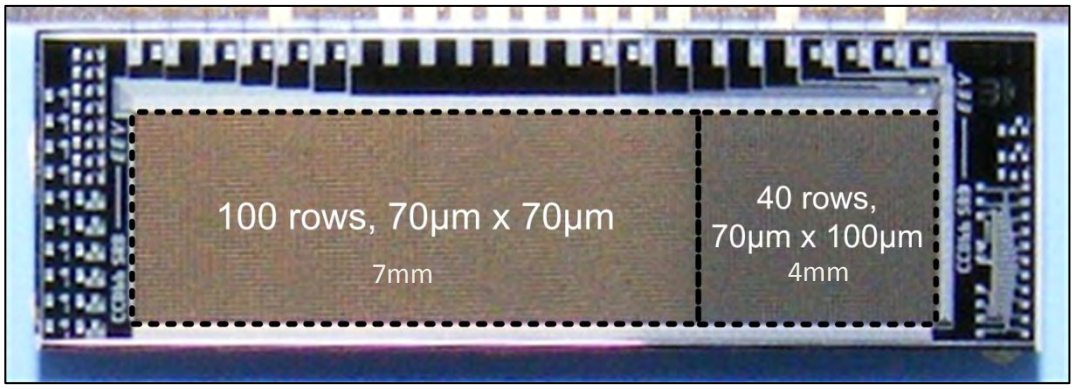

Figure 4.2 Photograph of the CCD66 chip. The two different pixel regions are labelled and marked using a dashed line

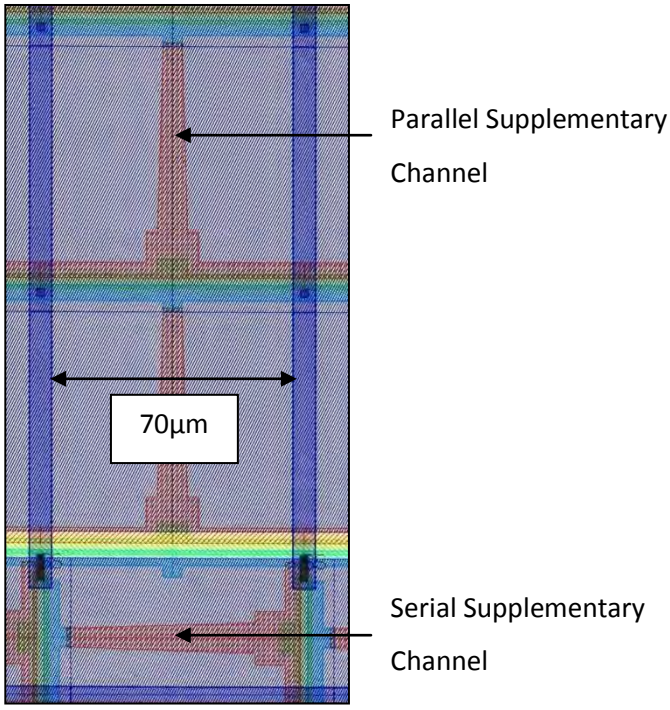

Figure 4.3 Diagram of the CCD66 pixel layout, showing the supplementary channel in the serial direction

4.3 DEPLETION DEPTH

4.3.1 DEPLETION IN SEMICONDUCTORS

Depletion is the name given to the effect of removing all charge carriers within a region of a doped semi-conducting material by either natural diffusion or by the application of an electric field. Due to the absence of charge carriers, the depleted region in a semiconductor is insulating rather than conducting, with the only elements left within the region being ionized donor or acceptor impurities [Ayers, 2004].

Under zero bias, a depletion region is naturally created when a p-n junction is formed. An n-type semiconductor has an excess of free electrons, whereas a p-type semiconductor has an excess of holes, or positive charge carriers. When a junction of these materials is formed, the electrons from the n-type semiconductor and holes in the p-type diffuse across the junction. When an electron meets a hole, recombination occurs [Ayers, 2004].

The net result is that free electrons and holes are removed from the depletion region, leaving behind charged ions adjacent to the interface region with no mobile carriers. The ions are positive on the N side due to the removal of an electron and negative on the P side due to the removal of a

hole. This, in turn, creates an electric field, referred to as the built-in field, which provides a force which opposes further recombination of holes and electrons across the junction gap by diffusion, thus limiting the depth of depletion of a given junction under zero bias. The built-in electric field for silicon is ~0.7V [Janesick, 2001].

Under forward bias, where the p-type anode has a positive voltage with respect to the n-type cathode, resulting in a field in the opposite direction of the built-in field, the depletion region becomes smaller. Once the field exceeds the ~0.7V built-in field, a current can flow; this current increases exponentially with the applied bias. The device, in this situation, no longer has a depletion region and is fully conductive.

Application of a reverse bias to the material, when the p-type anode has a negative voltage with respect to the n-type cathode, will result in the voltage increasing across the depletion region. This widens the depletion region. X-rays which are absorbed in a CCD's depletion region create a cloud of electrons and holes. The charge carriers are separated by the electric field present, the majority carriers being swept to the electrode whereas the minority carriers drift towards the substrate. As the number of electron-hole pairs is proportional to the energy of the X-ray incident with the device, measuring the charge generated by the X-ray is a direct measure of its energy [Janesick, 2001].

The greater the depletion depth, the better the CCD works as an X-ray detector at higher energies as there is a larger volume within which a constrained charge cloud can be created by an X-ray interaction. The depletion depth is limited, however, by an effect known as device breakdown. There are two mechanisms by which a semiconductor breaks down when under reverse bias: Firstly, a process known as avalanche breakdown and secondly, Zener breakdown, an effect related to quantum tunnelling of the charge carriers through the silicon. At low doping levels and higher voltages, the avalanche mechanism dominates while at high doping levels and lower voltages, the Zener mechanism is dominant. For CCDs, where a large built-in field is desired and therefore doping levels are lower the dominant effect is avalanche breakdown [Janesick, 2001].

Avalanche breakdown occurs as the result of the applied reverse bias becoming great enough to cause an electron to gain enough kinetic energy to free electrons bound to silicon atoms in crystal lattice due to kinetic impact. This is known as impact ionization. This results in a large cascade of electrons which then, in turn, also gain enough kinetic energy to break more bonds. The huge

number of electron-hole pairs created result in a large current and the CCD is said to have broken down and can no longer be operated as an X-ray detector [Janesick, 2001].

4.3.2 MANIPULATION OF DEPLETION DEPTH

The depletion depth is a measure of the active volume within a CCD. Events that occur in the depletion region only spread over a small number of pixels (1-4 pixels), whereas events occurring in the field free region below the depletion layer result in large-scale multipixel events of >4 pixels [Tsunemi, 2002]. A deeper depletion depth allows more penetrative, higher energy X-rays to be detected and a reduction in event splitting. The one dimensional depletion depth, d, is then given by (5.1) from the solution of Poisson's equation [Sze, 1985].

$$d = \sqrt{\frac{2\varepsilon_{\mathrm{Si}}}{qN_B}(V_{\mathrm{bi}} - V_{ss})} \tag{4.1}$$

N_B is the lightly doped bulk concentration, q is the electronic charge, ε_{Si} is the permittivity of silicon (~11.9±1 [Yang et al, 2006]) and V_{bi} is the built-in potential at the p-n junction. V_{ss} is the potential difference between the gate and device substrate, and is positive for forward bias and negative for reversed bias. Note that this is a one dimensional solution to a two-dimensional problem and, in reality, the depletion depth is limited by the physical thickness of the device and device breakdown. Device breakdown is described in Section 4.3.1. A high resistivity material helps to mitigate this by increasing the achievable ΔV before avalanche breakdown occurs [Sze, 1985].

It can be seen from equation (4.1) that a negative substrate voltage will result in an increased depletion depth (hereafter, V_{ss} refers to negative substrate voltages unless stated). Also, decreasing N_B will have a similar result. This is achieved by lowering the substrate doping concentration i.e. using higher resistivity silicon. For example, Figure 4.4 shows the depletion depth as a function of $(V_{bi}-V_{ss})$, or ΔV, for a resistivity of 1500 Ω.cm and a channel potential, V_{bi}, of 5.5 V.

In reality, an asymptote will exist for a semiconductor at the point where full depletion is achieved. Often, device break-down occurs before full depletion is reached and the semiconductor material in the CCD becomes conducting and cannot function as an X-ray detector. Based on the work presented in Section 4.4.2, for example, the CCD66 undergoes device breakdown at a V_{ss} of approximately 20V, significantly limiting the achievable depletion depth of

the device. Breakdown is non-destructive as no damage occurs to the silicon crystal lattice in this condition. However, the heat generated by the increased current flow can cause damage, particularly for diodes, so either the current must be limited or adequate heat sinking must be supplied [Ayers, 2004].

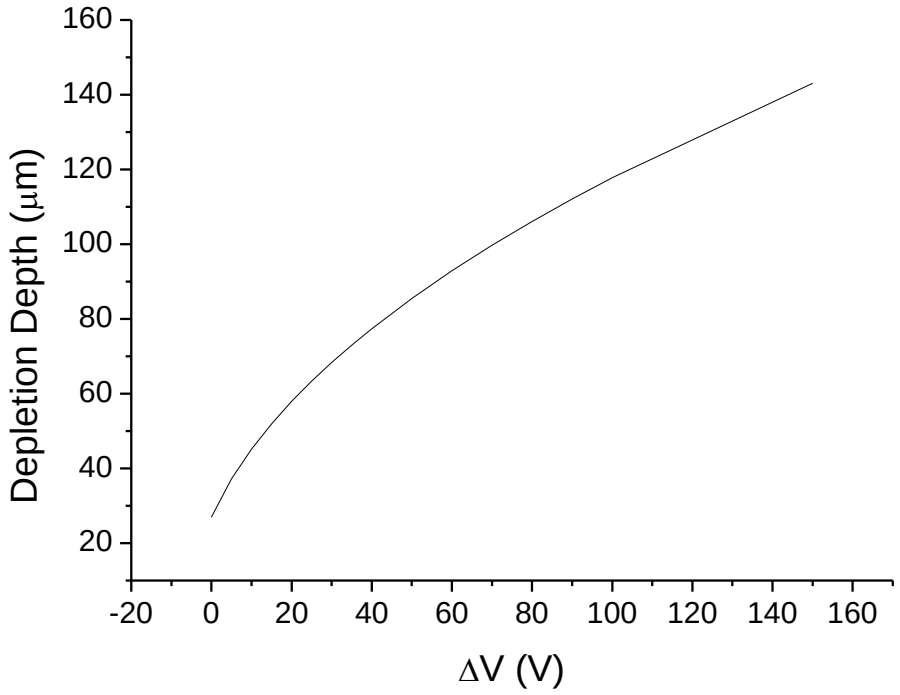

Figure 4.4 The 1-D depletion depth, as calculated using equation (4.1), versus ΔV (V_{bi}-V). The resistivity used is 1500 Ω.cm and the channel potential, V_{bi}, is 5.5V

An experiment was conducted in order to demonstrate how an externally applied negative substrate voltage could be used to increase the depletion depth of the CCD66, prior to device breakdown, and is reported in Section 4.4.

4.4 INVESTIGATING EXTERNALLY APPLIED NEGATIVE V_{ss} AND DEPLETION DEPTH

The experiment outlined in this section was conducted to establish how applying a negative substrate voltage externally to a CCD66 device affects the depletion depth and, hence, device performance. The results presented in this section, and in Section 4.5, have been published in SPIE, 2008 in a paper entitled 'Improving Quantum Efficiency and Spectral Resolution of a CCD through Direct Manipulation of the Depletion Region' [Brown et al, 2008].

4.4.1 EXPERIMENTAL METHODOLOGY

Figure 4.5 and Figure 4.6 show photographs of the CCD test facility in the experimental setup. The CCD66 was mounted in the EPIC/Swift CCD test facility, rotary pumped to $<10^{-6}$ mbar and cooled to -100°C using a copper cold finger attached to a liquid nitrogen reservoir (seen in Figure 4.6). The CCD voltages were optimised for noise and gain at negative substrate voltages (V_{ss}) of 0V, 5V, 10V, 15V and 20V. The V_{ss} was applied by an external power supply unit. Table 4.1 summarises the optimised CCD66 voltages, showing the voltages used when performing the noise calibration and data collection.

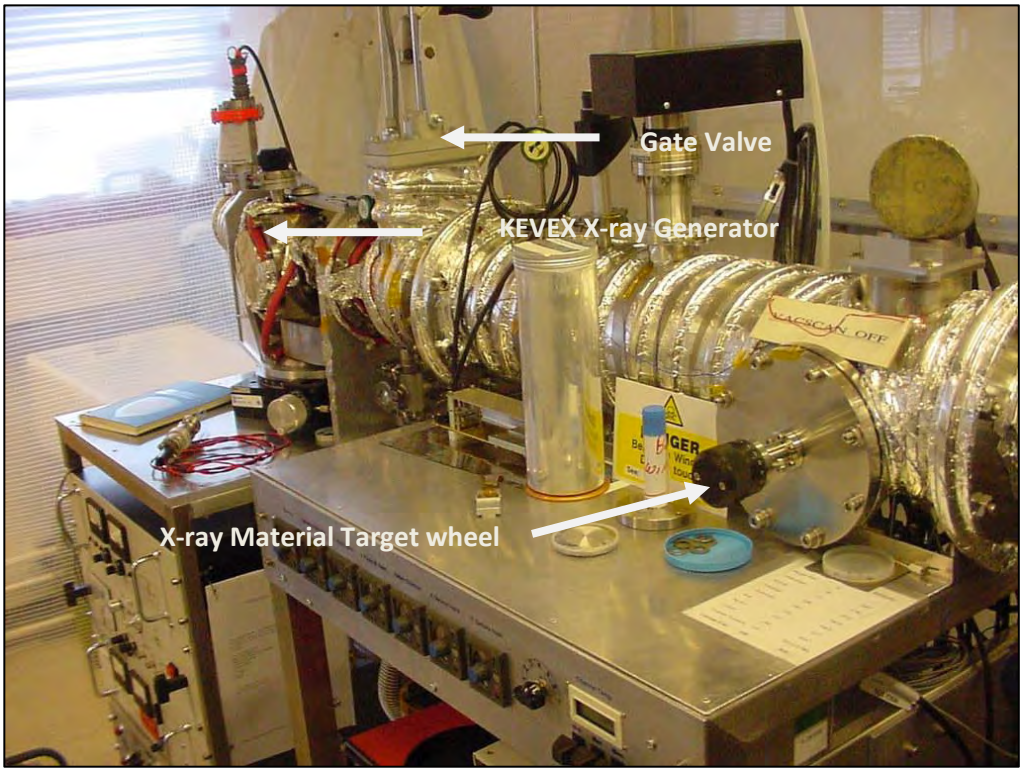

Figure 4.5 Photographs of the EPIC/Swift CCD Test facility, showing the experimental setup used to test the CCD66 device. This picture shows the X-ray generating equipment and material target wheel

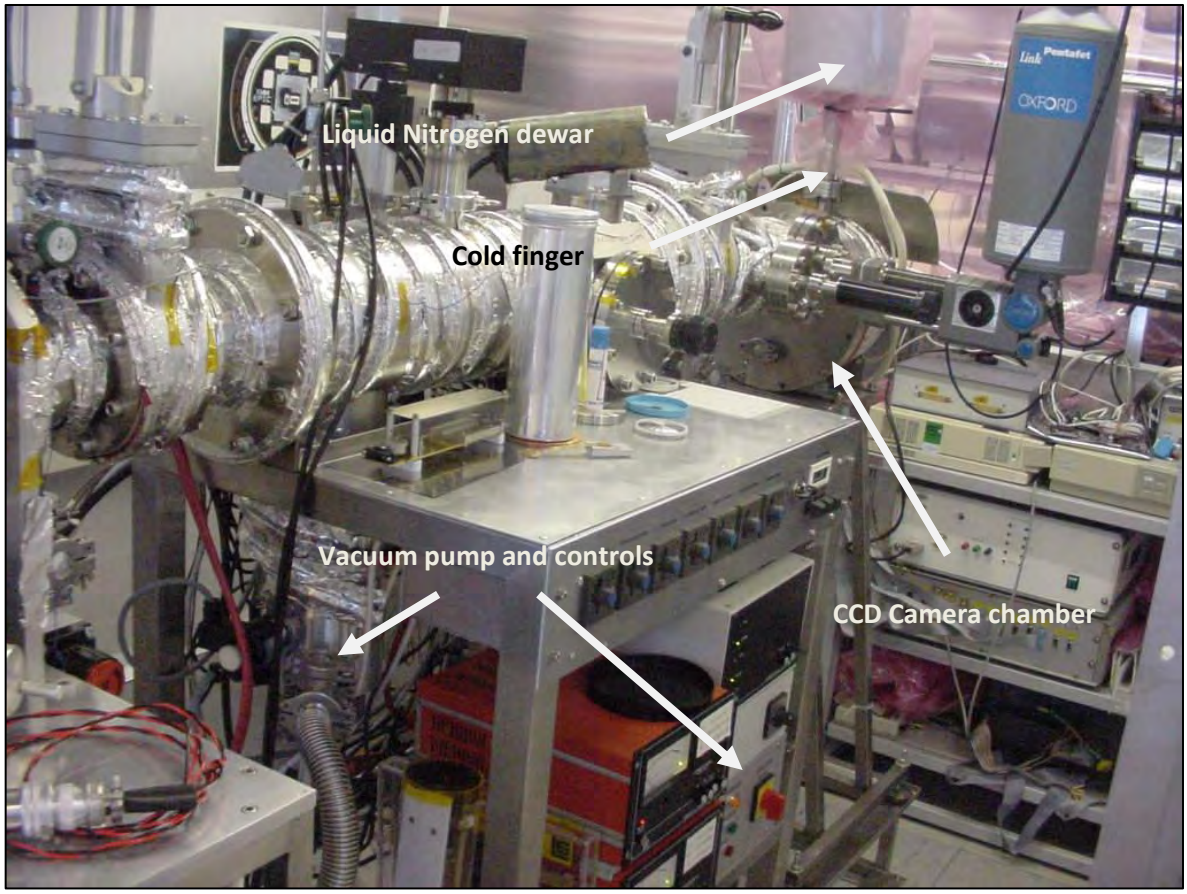

Figure 4.6 Photograph of the EPIC/Swift CCD Test facility, showing the experimental setup used to test the CCD66 device. This picture shows the camera chamber end of the facility

The CCD noise peak was calibrated using Ti Kα X-rays (4.51 keV) prior to taking data, consisting of 7500 frames, using Cu Kα X-rays at 8.05 keV. This process was repeated for negative substrate values of 0 V to 20 V in 5 V steps. The resultant spectra are all presented in Appendix III.

Parameter	Symbol	Values				
Substrate Voltage (V)	V_{ss}	0	5	10	15	20
Output Drain (V)	V_{od}	26.8	29	30	30	31
Reset Drain (V)	V_{rd}	17.1	22	22	23	17
Output Gate (V)	V_{og}	1.5	5	4	3	2.5
Current Output Source (V)	V_{ios}	3.4	3.5	3.5	3	2
Diode Drain (V)	V_{dd}	27	27	27	27	27
Reset Clock (V)	φR	14	13	12.5	13	9
Register Clock (V)	R	10.5	10.5	10.5	10.5	10
Bias Gate (V)	$I\varphi 4$	1.2	2.5	2	1.5	1
Image Clock (V)	I	7.2	8	8	8.5	8.5
Gain^{-1}	-	2.8355	2.8755	2.6973	2.6701	2.5568
Noise (e^-)	-	6.16	7.51	8.89	10.6	7.97

Table 4.1 Summary of the CCD66 Voltage optimisation used when collecting data and during noise calibration

4.4.2 EXPERIMENTAL RESULTS

Device breakdown began to occur at 20 V and the device broke down completely at voltages greater than this (V_{ss} of ~21 V). The spectra obtained from 0-20 V were analysed, comparing isolated (single pixel event) spectra, summed (1-4 pixel event) spectra, and all event spectra. Figure 4.7 shows an example isolated event spectrum taken using the CCD66 while no external negative substrate voltage was applied. A FWHM resolution of 136.5 eV was obtained at the Cu Kα peak. A very good separation between the Kα and Kβ peaks is evident. The measured noise levels varied from 6-10 electrons when experimenting with this device. As expected, Figure 4.8, which shows an equivalent isolated spectrum for an applied negative substrate voltage of 15 V, is no different to the spectrum at 0 V; the 15 V produces a peak with a FWHM resolution of 135.0 eV. Increasing the negative substrate voltage will increase the size of the depletion volume of the device, resulting in fewer multipixel events. Isolated event spectra do not contain any multipixel events and, as such, do not show improvement when the depletion region is increased. The significant improvement in resolution occurs in the summed event spectra as reported in Section 4.4.3.

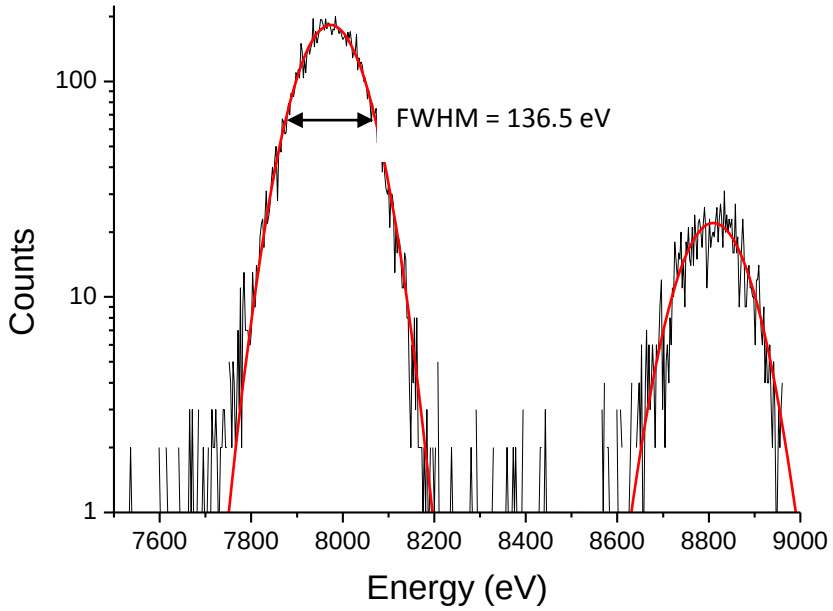

Figure 4.7 Isolated Cu K spectrum taken with the CCD66 with no additional external negative substrate voltage. The Cu Kα and Kβ peaks are well separated

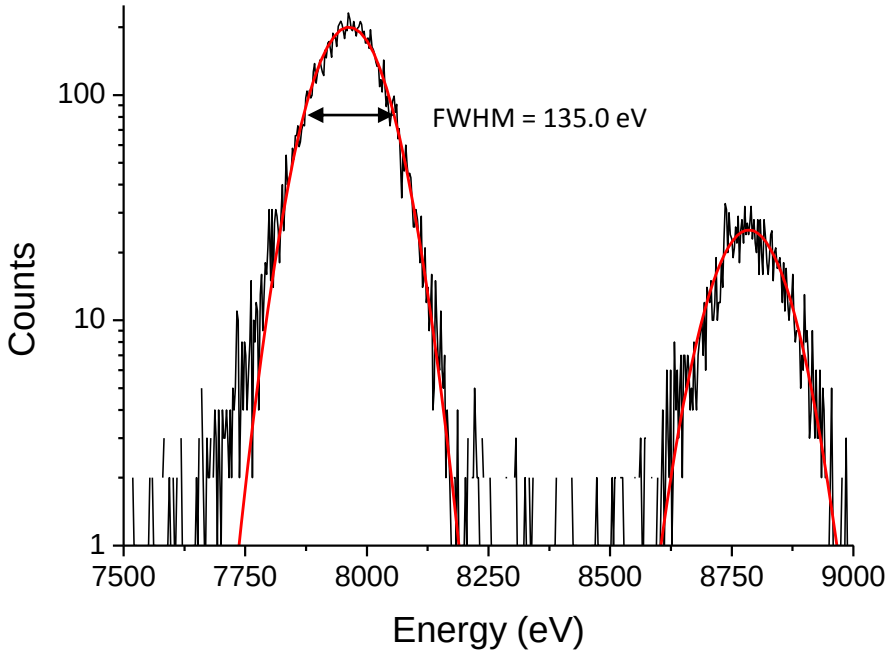

Figure 4.8 Isolated Cu K spectrum taken with the CCD66 with 15V external negative substrate voltage

4.4.3 CCD66 DATA ANALYSIS

The data were analysed to determine the effect of V_{ss} on the multipixel event distribution of the CCD66 for increasing negative substrate voltages and, as such, increasing depletion depth. An event size histogram was produced in order to compare the populations of multipixel events for varying negative substrate voltages. Figure 4.9 shows the event size histograms obtained from this experiment. The figure shows that a larger depletion depth results in a large reduction of split events, particularly those involving 12 or more pixels, while simultaneously increasing the detection efficiency of events within the depletion region (1-4 pixel events). In order to compare the effectiveness of increasing substrate voltage on detection efficiency, the percentage of total events interacting in the depletion region of a device for a given negative substrate voltage should be compared.

Figure 4.10 considers only events that interact within the depletion region; that is, only 1-4 pixel events. The percentage of 1-4 pixel events is plotted versus the applied negative substrate voltage, V_{ss}. As predicted, a greater proportion of events occur within the depletion region as the negative substrate voltage is increased.

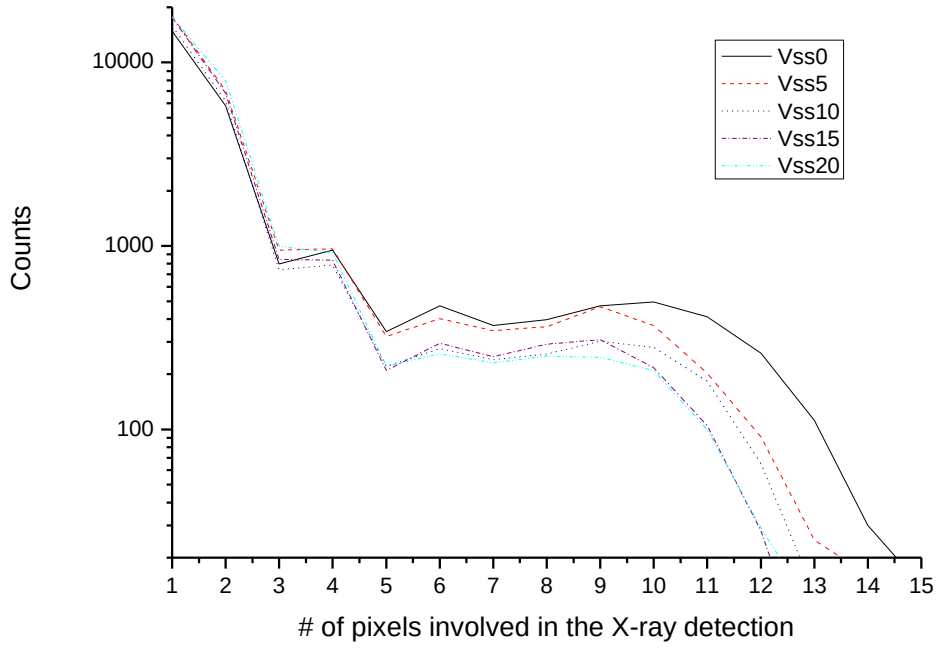

Figure 4.9 Event size histograms showing how multipixel events are effected by increasing negative substrate voltage. Increased negative substrate voltage increases the percentage of total counts interacting within the depletion region (1-4 pixels)

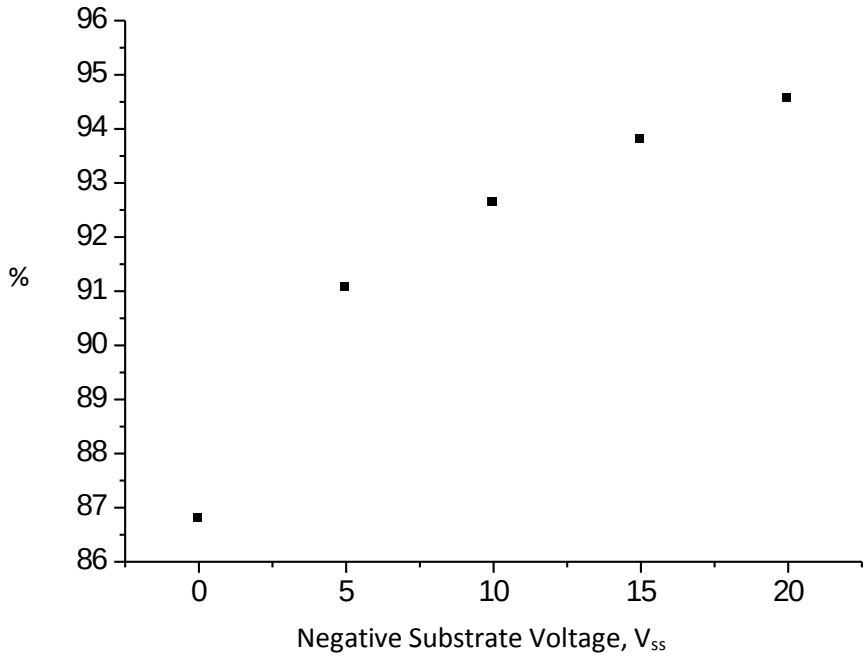

Figure 4.10 Percentage of Cu Kα X-rays interacting within the depletion region (1-4 pixel events) versus negative substrate voltage

The data plotted in Figure 4.10 were obtained by summing all of the events occurring at a given substrate voltage, and then calculating the percentage of 1-4 pixel events occurring within each value. No error bars are shown as the data present the number of events registered in the depletion region by the CCD as a percentage of total events detected.

The summed (1-4 pixels) spectra were also analysed in order to establish the spectral resolution of the CCD66 at the applied negative substrate voltages. Each Cu Kα peak was fitted with a Gaussian curve and the FWHM energy resolution was determined. Table 4.3 shows the FWHM summed event spectral resolution measured for each of the V_{ss} values used.

An improvement in spectral resolution is seen for increased depletion depths when the summed spectra are analysed. An improvement of 10.9 eV is seen when the V_{ss} goes from 0V to 15V. Note, however, that at V_{ss} = 20V a poorer spectral resolution is observed. This is likely to be the result of device breakdown beginning to occur.

Figure 4.11 shows a summed event spectrum taken at V_{ss} of 20V.

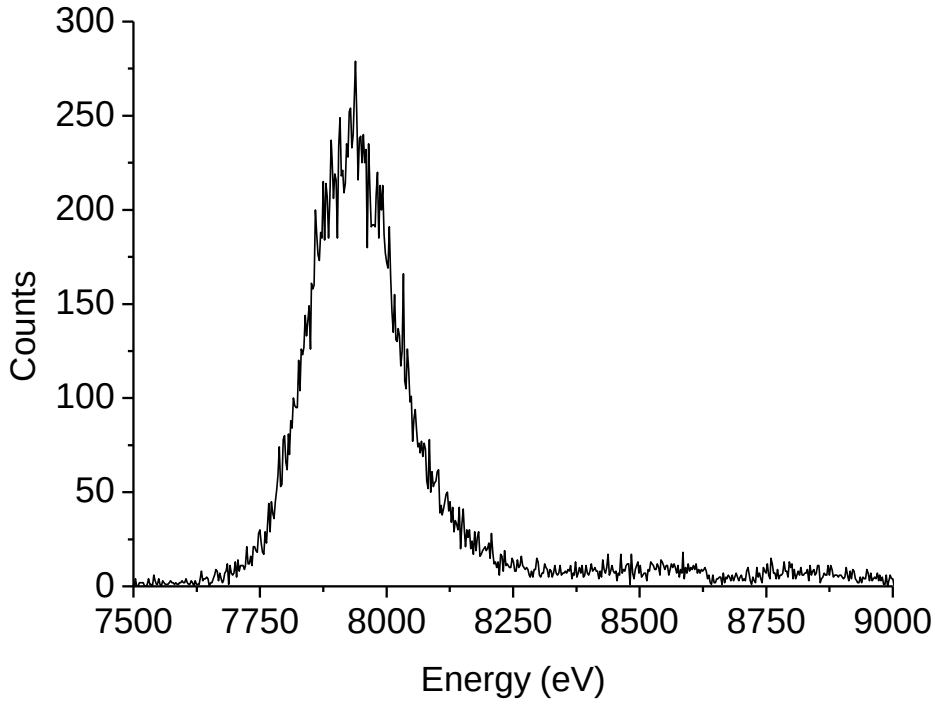

Figure 4.11 Summed (1-4 events) Cu Kα spectrum taken with the CCD66 with 20V external negative substrate voltage

The Cu Kβ line is not evident in this spectrum, possibly having been redistributed to lower energies and contributing to the main peak. These redistributed events would result in an increased width in the Cu Kα line and would explain the shoulder in the spectrum towards the upper energy of the main Gaussian peak. Comparing the number of X-ray counts in the main peak of the 15V spectrum and the 20V spectrum shows an increased number of counts in the 20V spectrum, roughly equivalent to the number of counts missing from the Kβ peak . Summing the total counts in each of the spectra shows, however, that the counts are roughly equal in both This suggests that redistribution has occurred. As the V_{ss} approached 20V, the range of gate voltages used to operate the CCD became more restrictive, also. Exceeding a V_{ss} of 20V resulted in complete device breakdown.

Table 4.2 shows the percentage of counts in the Kα and Kβ peaks of spectra taken with a V_{ss} of 15 V and 20 V. It can be seen that, indeed, the number of counts as a percentage of the total which register in the main peak increases in the 20 V case, suggesting that redistribution has occurred.

V_{ss} (Volts)	% Counts in Kα (7500-8300eV)	% Counts in Kβ and shoulder (8300-9000eV)
15	87.8	12.2
20	91.7	8.3

Table 4.2 Analysis of the Cu Kα and Cu Kβ lines for 15 V and 20 V negative substrate voltage and redistribution of counts

The reported improvement in spectral resolution of 10.9 eV is small, although the improvement is still greater than can be accounted for by curve fitting errors. The error in the curve fit is 1.2 to 1.6 eV for each curve, so the improvement seen as negative substrate is increased is not due to statistical error in the curve fitting process.

The modelling work presented in Section 4.5.2 uses the modelled CCD66 response to infer the depletion depth induced by varying the negative substrate voltage from 0V to 20V.

V_{ss} (Volts)	FWHM Spectral Resolution (eV)	Error in Curve Fit (eV)
0	159.7	± 1.6
5	159.3	± 1.2
10	151.4	± 1.2
15	148.8	± 1.2
20	164.5	± 1.6

Table 4.3 The FWHM Spectral Resolution of Cu Kα summed (1-4 pixel) spectra taken at negative substrate voltages (V_{ss}) of 0V-20V in 5V steps

4.5 MONTE CARLO CCD SIMULATION

In order to establish the depletion depth increase when a negative substrate voltage is applied to the CCD66, the Monte Carlo CCD22 Model [Short, 2002] used by the Swift XRT team was modified for the CCD66. The modelling work is discussed in this section.

4.5.1 THE CCD22 SWIFT-XRT AND THE CCD66 MODELS

The Swift Gamma Ray Burst Mission [Gehrels, 2004] incorporates three instruments: the gamma ray Burst Alert Telescope (BAT), the UV/Optical Telescope (UVOT) and the X-ray Telescope (XRT). The XRT uses the CCD22 as the focal plane detector, the same device used in the EPIC MOS cameras on XMM-Newton (see Chapter 2). A Monte Carlo CCD response model was created for the XMM-Newton EPIC MOS camera in order to develop a response function for the detectors. The need for the model was driven by the lack of calibration data prior to launch of the spacecraft. This model was subsequently developed for the Swift telescope XRT detectors [Short, 2002][Osborne, 2005][Godet, 2007][Godet, 2009] in order to model the redistribution effects seen in the CCD22.

There are a number of key differences between the CCD22 and CCD66 which lead to modifications of the original code. For example, the pixel dimensions of the CCD66 are different. The CCD66 also has a closed electrode structure with no etched area of the pixel, as present in the CCD22. The model allows the charge transfer efficiency in the parallel and serial directions to be varied as well as the different CCD layer thicknesses (silicon, silicon dioxide and silicon nitride). The modified code neglects surface loss effects as the majority of X-ray energies used in the experiment will not interact near the surface of the device.

The architecture of the modified CCD66 model, and how it computes the output spectra, is shown in Figure 4.12. The key variables were extracted from the original CCD22 code and incorporated into an input file, creating a very useful tool for modelling CCDs of differing structure, layer thickness and material. The option for also investigating back illumination and different angle of X-ray incidence was also incorporated into the model. The work presented in the chapter uses a normal angle of incidence, although the work presented in the following Chapter makes use of this new angle function in order to investigate the effect of varying X-ray angle of incidence on a CCD22.

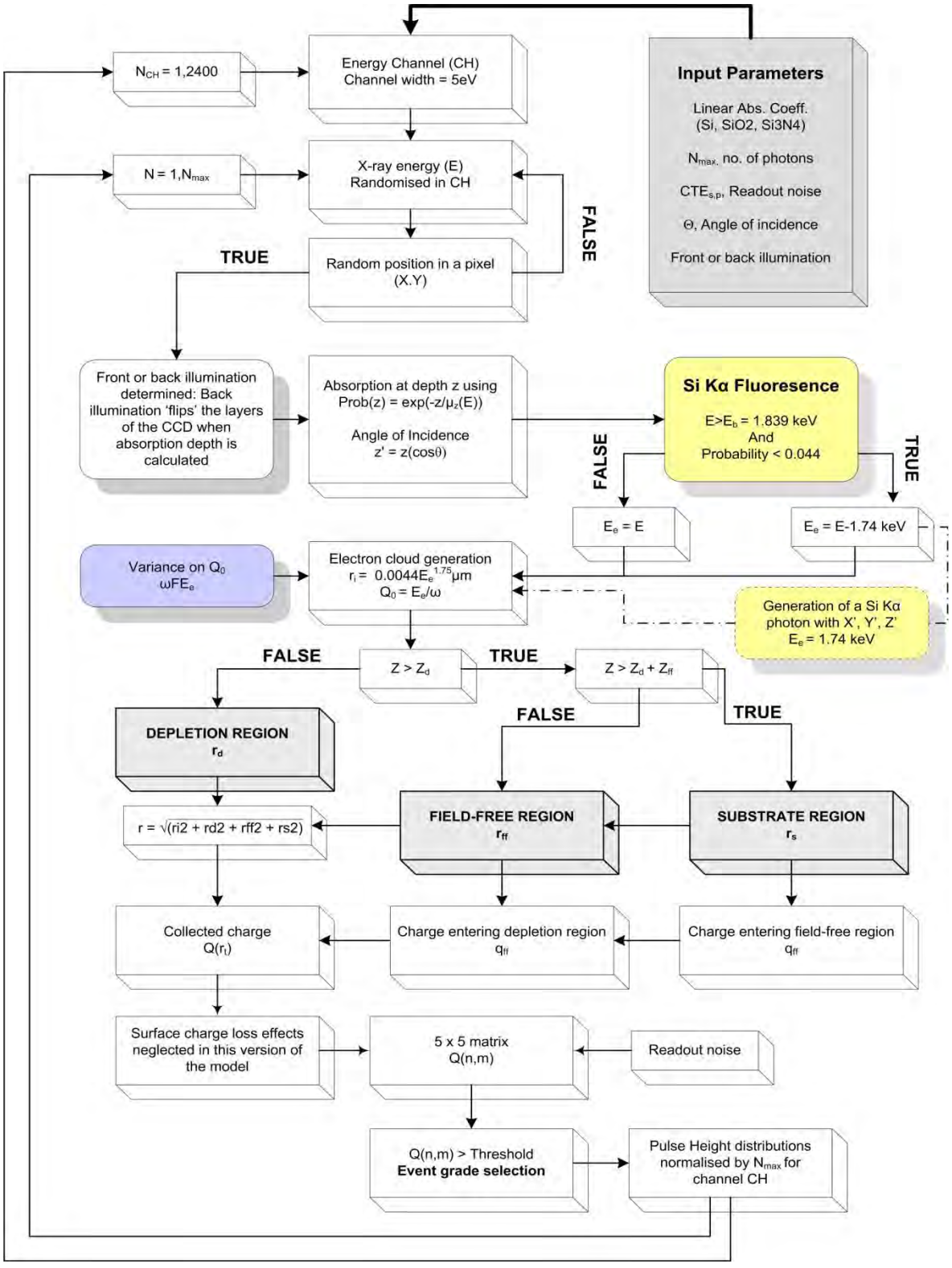

Figure 4.12 A flow diagram summarising the CCD Monte Carlo model architecture that was used to investigate the CCD66. This has been modified from the CCD22 Swift XRT model architecture from [Godet, 2009] and details the changes made from the original code to make the new model

The CCD pixel dimensions were measured using a microscope image in order to determine the geometry to be used in the model. Figure 4.13 shows an image of the smaller of the two different pixels, superimposed with the sizes measured. The dimensions of the two different pixels, as used in the model, are shown in Figure 4.14.

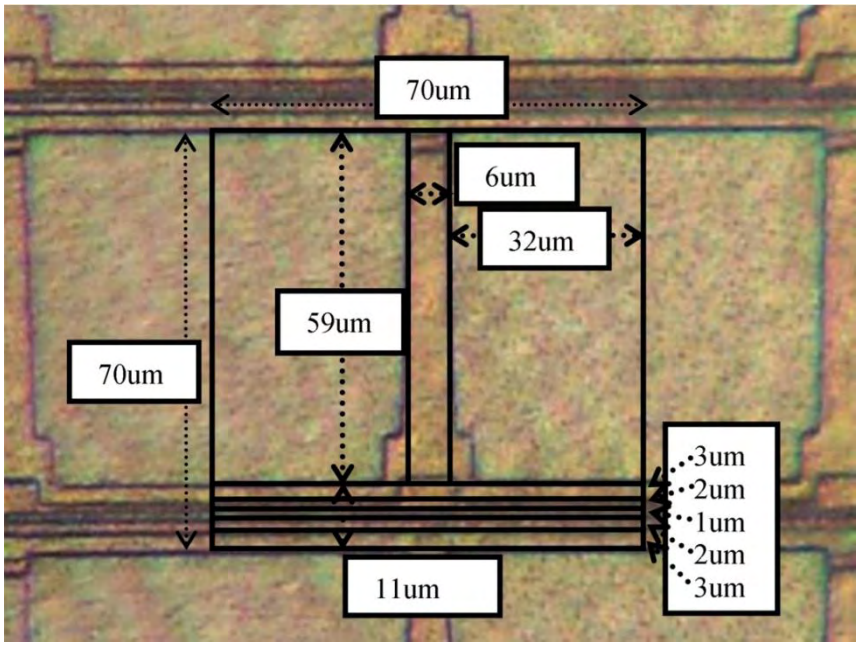

Figure 4.13 Microscope photograph of the CCD66 pixel structure, overlaid with the pixel dimensions. Note that the central CCD finger has been simplified as a regular column when, in fact, the actual finger is tapered

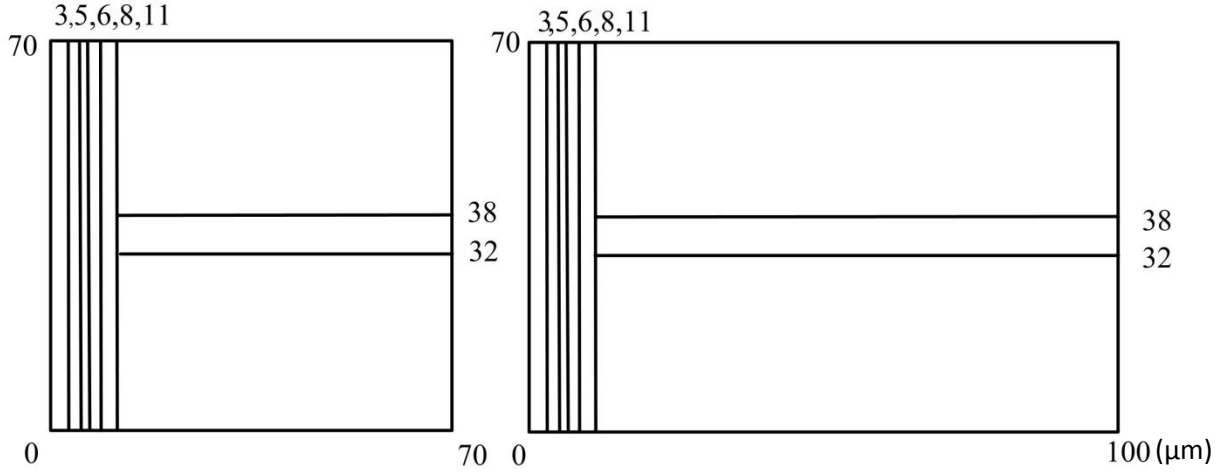

Figure 4.14 A schematic showing the two different sized pixels used on the CCD66 and their dimensions (in microns) as used in the model

4.5.2 CCD66 Depletion Depth Modelling Results

The physical model of V_{ss} shown in Figure 4.4 is limited, as equation (4.1) is a one dimensional solution to a two-dimensional problem. In reality, the depletion depth is restricted by the physical thickness of the device and device breakdown [Sze, 1985]. In order to establish the actual depletion depths induced by the changes in V_{ss}, Monte Carlo simulations were conducted using the Monte Carlo code. The model was used to simulate Cu K X-rays in order to compare the model output with the data taken using the CCD66. Figure 4.15 shows a simulated spectrum compared to data taken with the CCD66 at V_{ss} = 0V. Excellent agreement is found between the two, verifying the model for the new CCD66 pixel structure.

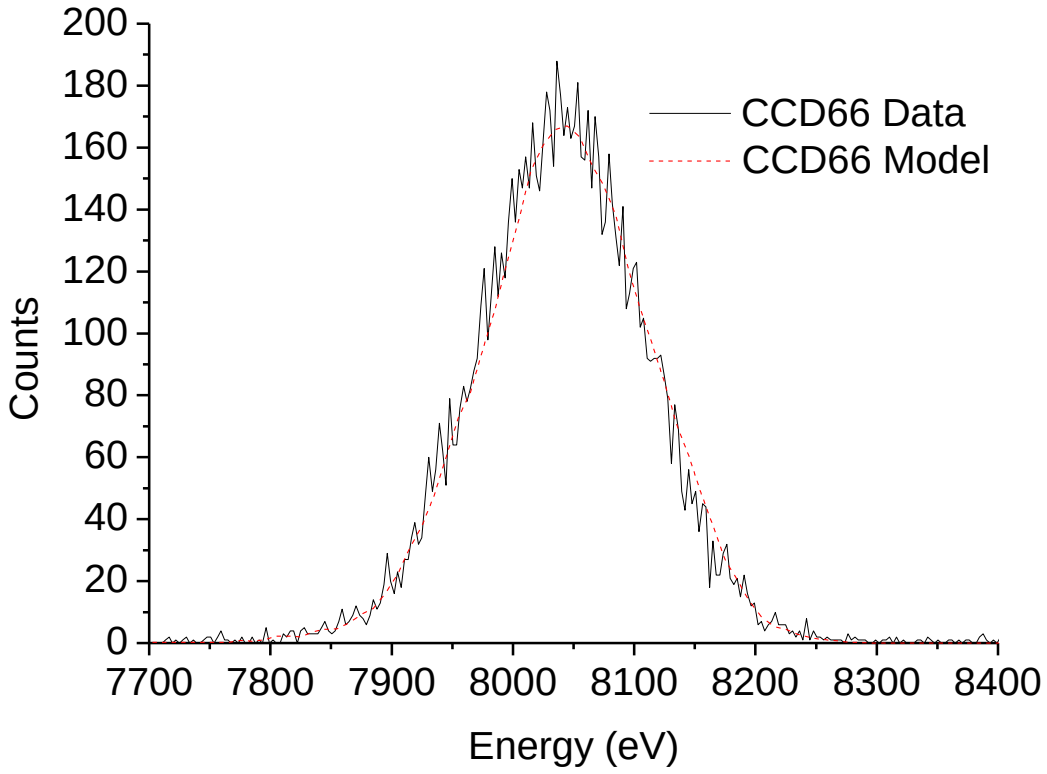

Figure 4.15 Comparison between Cu Kα data taken with V_{ss} = 0V and simulated data using the CCD66 model

The model was used to determine the resultant depletion depths achieved with the application of a negative substrate voltage on the CCD. A series of spectra at 1μm intervals of depletion depth were simulated using parameters established in the CCD66 lab experiment (Figure 4.16). The percentage of events occurring within the depletion region (1-4 pixels) out of all events (1-9 pixels) was calculated and compared with the data shown in Figure 4.10. Table 4.4 shows the resultant depletion depths inferred from the simulation work.

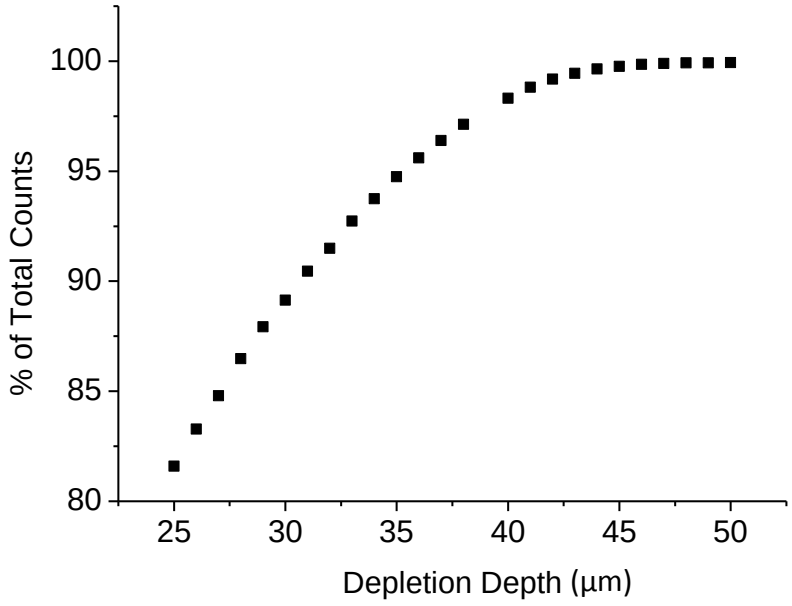

Figure 4.16 Depletion depth versus the percentage of all counts interacting within the depletion layer of the device, as simulated using the CCD66 model

% of (summed/all) events	Associated V_{ss} (V) from experiment	Inferred Depletion Depth (μm)
86.8	**0**	28.4
91.1	**5**	31.6
92.6	**10**	32.9
93.8	**15**	33.9
94.6	**20**	34.7

Table 4.4 The depletion depths inferred from the comparison of CCD66 data and the CCD Monte Carlo modelling results

Plotting the values shown in Table 4.4 and fitting a curve to the data, it is possible to estimate the depletion depth for a given V_{ss} value. Figure 4.17 shows these data. It was found that an empirical logistic curve, of the form $y = A_2 + (A_1 - A_2)/(1 + (\frac{x}{x_0})^p$, fits both the physical model and the Monte Carlo data very well. A logistic curve is a sigmoid function which shows saturation at a certain value. The curves were fit using the analysis software Origin 7.5, finding A_1 = 28.4, A_2 = 98.05, x_0 = 1634.01 and p = 0.52 for the CCD66 Monte Carlo model data.

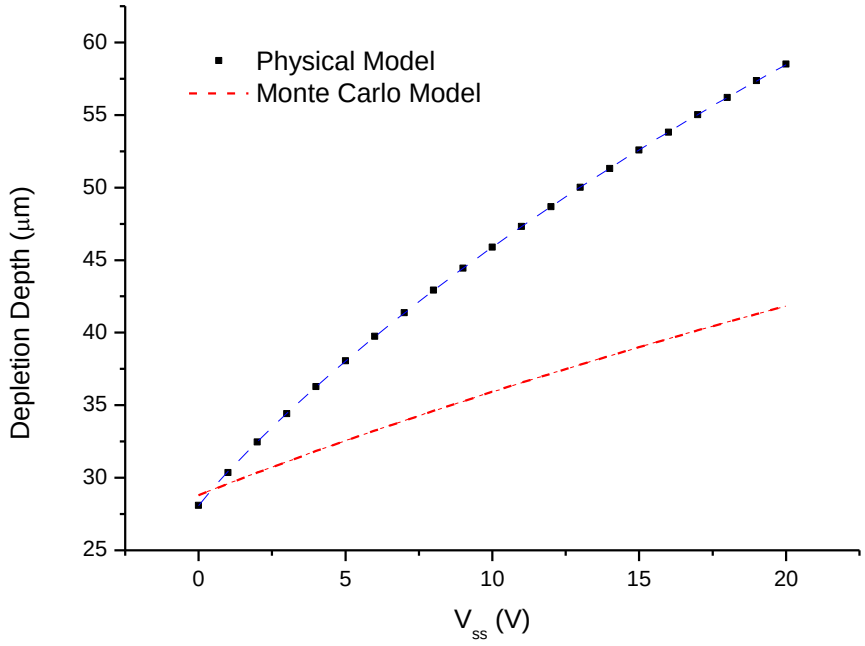

Figure 4.17 Plot of the CCD66 depletion depth versus negative substrate voltage, showing both the physical model and the Monte Carlo model results. A logistic curve was found to fit the data very well and is used to establish the depletion depth for a given V_{ss}

Comparing the modelling results with the 1D physical model demonstrated by equation (4.1) and in Figure 4.4 shows the significant difference between the 1D and 2D solution. Estimating the depletion depth of CCDs using equation (4.1) will result in a large overestimate of the depletion depth if a negative substrate voltage is employed.

The modelling has shown that a relatively small increase in negative substrate voltage (20V) results in a 6.3μm increase in depletion depth. This, in turn, results in a 7.8% increase in the number of events registering in the depletion region of the device.

4.5.3 CCD66 Quantum Efficiency Modelling Results

The model can be used to establish the quantum efficiency of a CCD by calculating the percentage of events which interact within the depletion region (or within a single pixel), out of the total number of input X-rays at a given energy. Through building up a number of these percentages at a range of energies from 0.1-10 keV, a quantum efficiency curve can be created.

The model was used to investigate the change in quantum efficiency of the CCD66 when the depletion depth is increased. A QE curve was created for a negative substrate voltage of 0V, corresponding to 28.4µm depletion, and 20V corresponding to a depletion depth of 34.7µm. In addition, the hypothetical case where the depletion depth could be extended to 80µm was also investigated for comparison. Figure 4.18 shows the result of the QE modelling for isolated events.

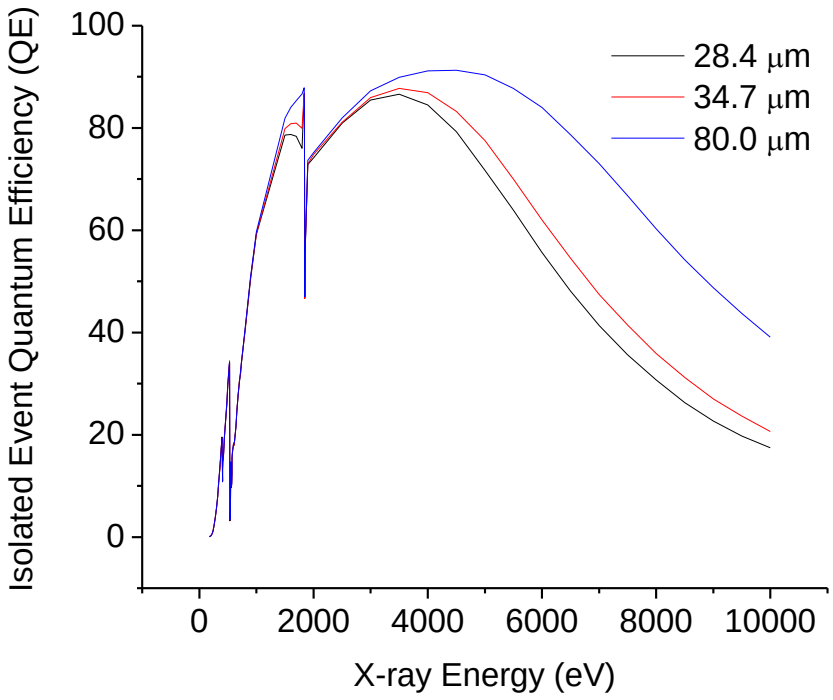

Figure 4.18 Modelled QE curves for CCD66 isolated events corresponding to a V_{ss} of 0V, 20V and a hypothetical 80µm depletion depth

Clearly, a significant increase in QE at higher X-ray energies can be expected for isolated events when the depletion depth is increased. The QE at 10keV increases from 17.5% to 20.6% for an

increase in V_{ss} from 0V to 20V. Should the CCD66 support an 80µm depletion, a QE of 39.1% at 10keV could be expected.

4.6 CONCLUSIONS

It has been shown experimentally that by increasing substrate voltage on the CCD66, the number of high multipixel X-ray detections is greatly reduced due to an increase in depletion depth. A greater number of 1-4 pixel events are also observed and, as a result, better spectral resolution is achieved.

The CCD22 model, developed for the XMM-Newton and Swift telescopes, has been modified to investigate the pixel structure and composition of the CCD66. Having verified the model using the laboratory data taken with the CCD66, the model was used to infer the depletion depths achieved by applying an external negative substrate voltage, V_{ss} to the CCD. It was found that the depletion depth increased by 6.3µm for a V_{ss} of 20V, resulting in a significant increase in quantum efficiency. Quantum efficiency curves were also constructed using the model, demonstrating that, as expected, high energy QE is greatly improved for large depletion depths.

Device breakdown occurred through applying a negative voltage >20V to the substrate, however, demonstrating that the current CCD66 design cannot achieve complete depletion. A new p+ channel, bulk CCD66 design is currently being produced by e2v with improved features such as much higher resistivity silicon and improved implantation to allow much deeper depletion depths. The new CCD66 also uses an ultra-thin electrode that will also significantly improve the QE at low X-ray energies. This device should improve, yet again, on the performance of the current CCD66.

Another situation where direct manipulation of the depletion region has been used is on the Swift-XRT to improve the performance of the CCD22 detectors [Godet, 2009]. The XRT was designed to operate the CCD22 at -100°C. Soon after launch, however, the thermo-electric cooler used to achieve this temperature failed. The XRT has subsequently relied on passive cooling to achieve an operational temperature between -75°C and -52°C. This marked increase in temperature results in an increase of dark current generated noise. Experiments performed on the Swift flight spare devices showed that raising the substrate voltage to +6V reduces the dark current produced [Osborne, 2005][Godet, 2007]. This reduction is due to the thinner depletion layer in the CCD. Of course, the reduction of depletion depth also resulted in lower QE at higher X-ray energies and a re-optimisation of CCD voltages and gain were needed.

Direct manipulation of a CCD's depletion region can be used to good effect when tailoring the performance of a device, be it decreasing the dark current noise contribution as seen with Swift, or by increasing QE at high energies. Future missions requiring high QE at greater X-ray energies, as well as good X-ray response at low energies should use fully depleted, back illuminated devices such as the DEPFET APS detector (Chapter 2 and Annex 1). The next generation CCD66, with its deep depletion and ultra-thin electrode, may prove to be a viable, front-illuminated, CCD alternative to the DEPFET APS.

The following Chapter investigates the effect of X-ray angle of incidence on CCD performance using the CCD66 Model introduced here.

CHAPTER 5

IMPROVING THE PERFORMANCE OF X-RAY SENSITIVE CCDS: INVESTIGATING THE X-RAY ANGLE OF INCIDENCE

5.1 X-RAY ANGLE OF INCIDENCE

The majority of laboratory experiments testing X-ray detectors use X-rays that are impingent approximately normal to the CCD surface. Some space applications of CCDs, such as the X-ray Diffractometer (XRD) proposed for ExoMars [Marinangeli, 2007], however, are designed such that the X-rays incident on the devices are not normal to the CCD surface. The performance of detectors in these circumstances differ to those measured when the X-rays are normal to the surface. In fact, X-rays focussed from X-ray mirrors (such as those proposed for the International X-ray Observatory [Parmar, 2009]) will also enter the detector at a slight angle; only X-rays entering a CCD from an on-axis infinite source, where the X-rays are approximately parallel, in a non-imaging system, enter the device normal to the CCD surface. Figure 5.1 shows the geometry of the IXO mission as an example of this.

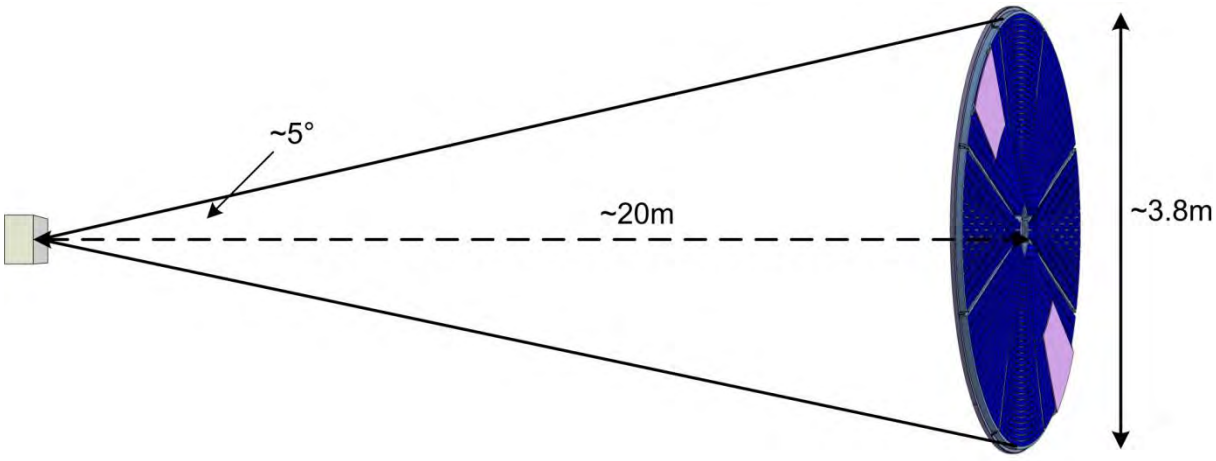

Figure 5.1 The geometry of the International X-ray Observatory, showing that X-rays entering the CCD are not normal to the CCD surface when entering the detector. A range of angles can be expected dependant on the X-ray energy and the radius of interaction with the X-ray mirror

The large 3.8m diameter mirror and long >20m focal length mean that X-rays up to ~5.4° from the normal will enter the detectors at the focal plane.

Another example of an instrument where X-rays enter the detector at an angle from the normal is the XRD (X-ray Diffractometer) instrument on ExoMars. The XRD detectors are arranged in a curved configuration, as can be seen in Figure 5.2.

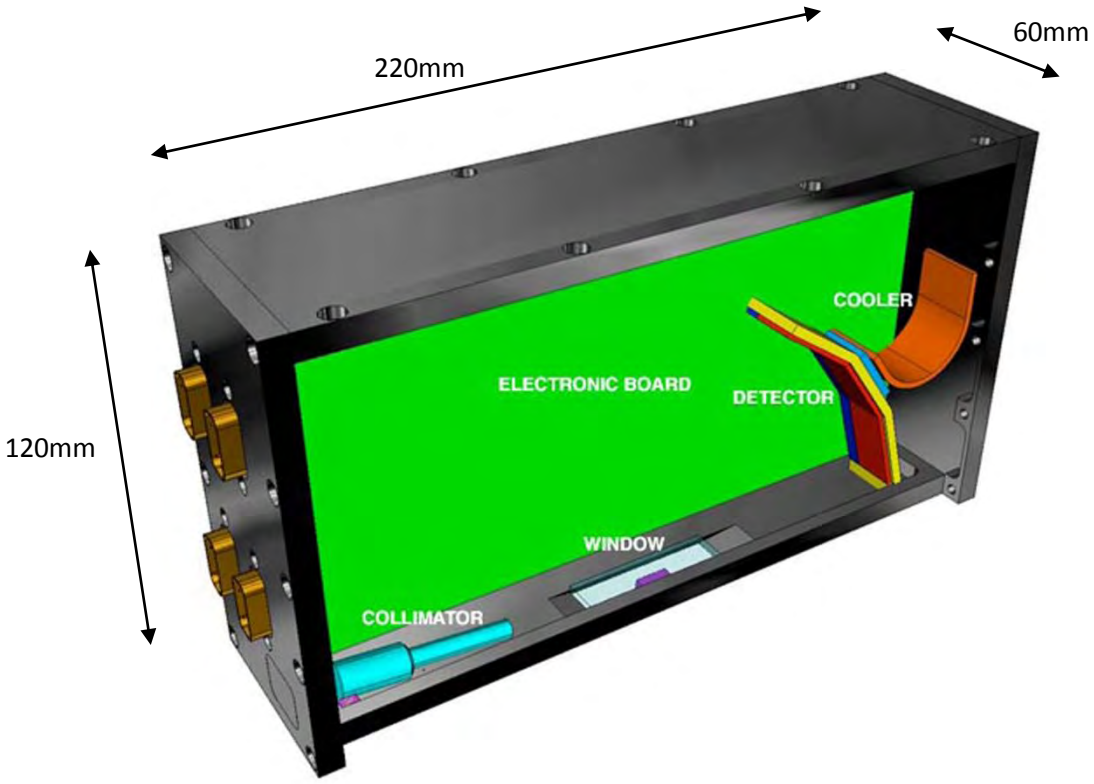

Figure 5.2 Early CAD model of the X-ray Diffractometer (XRD) ExoMars Instrument. Note that the detector plane is curved rather than flat

Changing the depletion depth of a CCD has a significant effect on detector performance, with greater depletion depths resulting in much improved QE at higher energies, as well as an improved spectral resolution due to a reduction in large-scale multipixel events [Brown et al, 2008], as can be seen in Chapter 4. Changing the X-ray angle of incidence is, in effect, similar to a change in the CCD depletion depth. As the incident angle ϑ_i increases from 0° from the normal to 90°, the incident photons have to travel through thicker regions of depleted silicon, increasing the likelihood of a depletion region interaction. In addition to this effect, the useful area of the pixels

on a position sensitive detector is different , with the effective pitch of each pixel being reduced by $cos\vartheta_i$ of the actual pixel length, where again θ_i is the angle from the normal.

This Chapter investigates the effect of the X-ray angle of incidence on CCD performance using the modified Swift-XRT Monte Carlo model described in Chapter 4. The work detailed in the chapter was presented at the Position Sensitive Detectors 8 Conference in Glasgow, 2008.

The Monte Carlo model, based on the CCD22 Swift-XRT code [McCarthy et al, 1995][Godet et al, 2007][Short, et al, 2002], was modified such that it is possible to model the effect of varying X-ray angle of incidence on a CCD. The aim of the modelling work shown here is to establish the change in quantum efficiency (QE) at higher energies when increasing the X-ray incidence angle from the CCD normal.

5.2 EFFECTIVE DEPLETION DEPTH

The active region of a CCD is determined by the depletion depth, with events occurring in the depleted region result in a 1-4 pixel event. Events occurring in the field free region result in larger multipixel events [Tsunemi et al, 2002]. The energy threshold of the device, determined by the noise level, will lead to some electrons from true events being lost from these large multipixel events, and the registered energy being redistributed from the photo peak to lower values. This redistribution manifests itself in a low energy shoulder [Osborne et al, 2005] to the peak, subsequently resulting in degraded FWHM energy resolution.

In addition, the greater the number of pixels contributing to an event, the greater the noise which contributes to the X-ray spectra. Each pixel contributes a near-equivalent amount of noise to the event so the larger the number of pixels, the lower the signal-to-noise.

Greater depletion depth results in better high-energy QE and fewer multi-pixel events, leading to improved energy resolution. Depletion depth is determined by two things; firstly, the resistivity/impurity concentration of the silicon, N_B, and secondly, the difference between built-in voltage and substrate voltage, V_{bi} - V_{ss}. ε_{si} is the permittivity in Silicon. The 1-D equation for depletion depth, d, [Sze, 1985] is :

$$d = \sqrt{\frac{2\varepsilon_{Si}}{qN_B}(V_{bi} - V_{ss}} \tag{5.1}$$

This 1-D equation is discussed in more detail in Chapter 4. An additional factor which leads to a change in QE is the angle of X-ray interaction with the device. An X-ray entering a sensor at a shallow angle travels through a greater region of depleted silicon and is therefore much more likely to interact in the depletion region. To account for angle of interaction, ϑ_i, in equation (5.1), an expression for the effective depletion depth, d_{eff}, can be written (equation (5.2)). ϑ_i is defined as the angle of X-ray interaction from the axis perpendicular to the surface of the CCD and d is the actual depth of depletion. This is shown in Figure 5.3.

$$d_{eff} = {}^{d}/_{cos\theta_i} \tag{5.2}$$

The Monte Carlo model uses the principle shown here to enable the investigation of CCD response to varying incidence angle. The model was modified to allow fixed values of ϑ_i, as well as a randomly variable ϑ_i for investigation of isotropic X-ray sources.

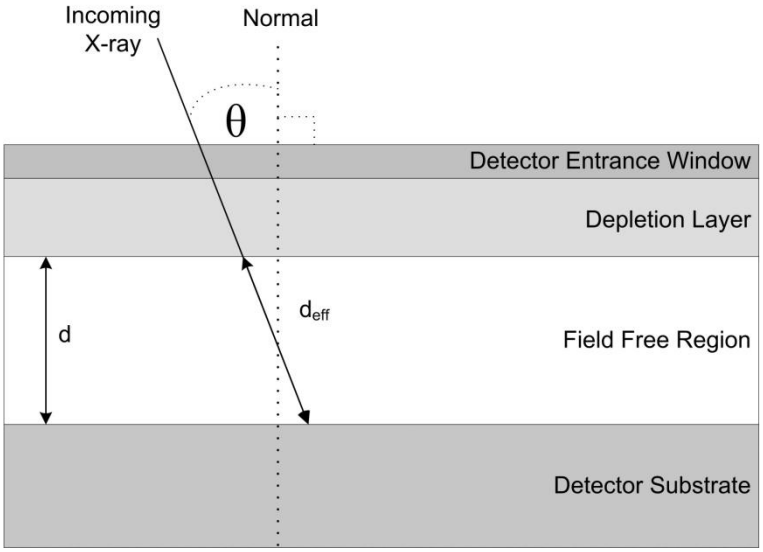

Figure 5.3 A diagram showing the effective depletion depth, d_{eff}, due to an X-ray incident at an angle ϑ_i from the CCD normal

Figure 5.4 shows a schematic of an X-ray interaction with a CCD pixel, the primary charge cloud generation and how electron diffusion in the CCD can result in isolated and split-pixel events. Energy redistribution will result if the energy deposited into a neighbouring pixel is below the set threshold. The threshold is determined by the system noise and is such that the signal-to-noise ratio is acceptable. As the number of electrons created in the primary charge cloud is

proportional to the energy of the incident X-ray, when a fraction of the electrons produced are discounted due to thresholding, the X-ray incident on the CCD is calculated to have less energy.

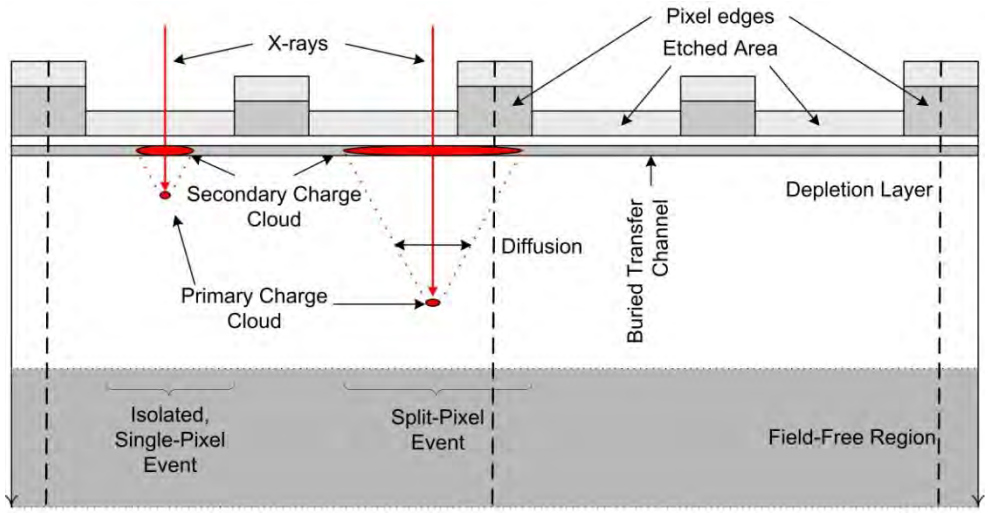

Figure 5.4 Schematic diagram of electron diffusion within a CCD pixel, resulting in a split-pixel event

5.3 SPATIAL RESOLUTION

The spatial resolution of an X-ray CCD is mostly determined by its pixel size although it has also been shown [Tsunemi et al, 2001] that it is possible to obtain sub-pixel resolution by considering split events occurring at the edge of pixels. Tsunemi showed that the knowledge of the primary and diffuse charge cloud geometries derived from the diffusion of electrons within the device and the X-ray penetration depth, can be used to determine the X-ray point of interaction on a CCD to distances smaller than the pixel size if the event is split over a number of pixels. This method was shown to be most useful when considering corner events, where the charge is split between three or four pixels. The drawback of using such a system is that only 4-10% of events will result in this splitting pattern [Tsunemi et al, 2001] so large collecting areas or long exposures are required to achieve good statistics. Also, thresholding due to CCD noise levels will result in some charge loss and increased noise, which in turn will lead to energy redistribution and poorer energy resolution.

For X-rays entering a CCD at an angle, it is expected that there will be an improvement in energy resolution in the direction of tilt as the CCD pixel size, from the perspective on the incoming photon, will be reduced by a factor of $cos\vartheta_i$ and, thus, will have a smaller sampling aperture. This effect could be particularly useful for the ExoMars XRD instrument as improved spatial resolution as a result of incidence angle will aid in better resolving the resultant diffraction patterns.

There is also the possibility, however, that an X-ray could enter one pixel at an angle and result in an isolated event in the adjacent pixel if it passes through the region in which a split event would result, as seen in Figure 5.5. This could result in image blur, particularly if the pixel size is small.

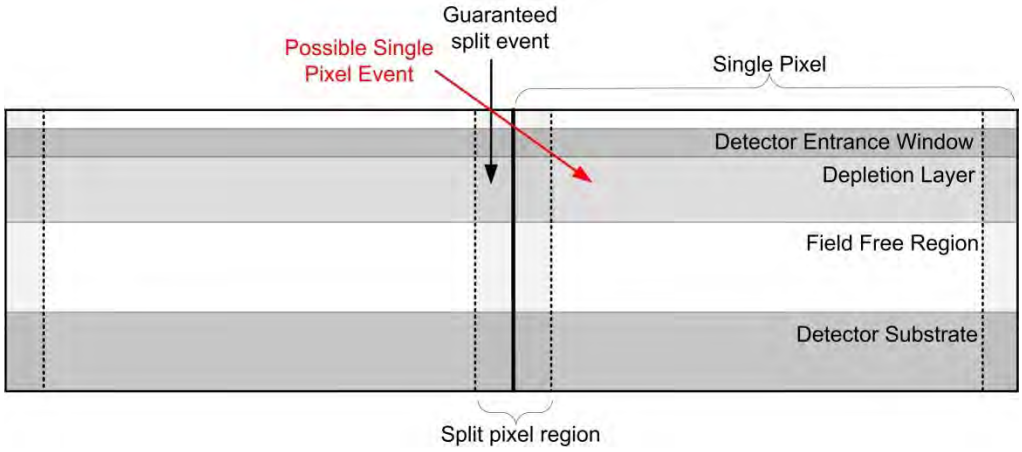

Figure 5.5 A schematic showing how an event can enter one pixel at an angle, yet still register as an isolated event in the adjacent pixel. This can result in image blur.

5.4 CCD MODEL ASSUMPTIONS

The Epic-Swift Monte Carlo model was modified to include ϑ_i, as in equation (5.2), to investigate changing ϑ_i from the Z axis (0º to 90º). Here, the Z-axis is defined as that perpendicular to the surface of the CCD. A number of assumptions were made and are summarised below.

- CCD type; CCD22
  - Pixel dimensions are 40µm x 40µm
  - Open electrode structure
- Operating temperature = -100°C
- CCD Noise = 20 electrons
- Depletion Depth = 29µm
- Parallel Charge Transfer Efficiency = 0.999967
- Serial Charge Transfer Efficiency = 0.99978
- $2x10^6$ photons used to model ^{55}Fe (5.9 keV)
- $2x10^8$ photons used to model ^{109}Cd (22.2 keV)

The assumptions are based on CCD22 experiments conducted in the X-ray diffraction test facility at Leicester University's Solid State Device Laboratory, designed to test the effect of varying the

angle of incidence, conducted by another PhD researcher, Huawei Su. The methodology and results of this initial experiment are summarised in section 5.7.

The CCD22 pixel structure is different to the CCD66 modelled in Chapter 4; the CCD22 has an open electrode structure where a portion of the pixel is etched away in order to improve low energy QE. Figure 5.6 shows the simplified CCD22 pixel structure as modelled using the Monte Carlo code. The dimensions of the pixel are shown, showing the different regions of the pixel such as the etched area and the central CCD22 finger. The equations used to calculate the X-ray transmission through the different device regions in the model are shown with the figure, also.

Figure 5.7 shows a microscope image of the CCD22 surface and an electron microscope image of the interface between etched area and un-etched region of the CCD22. It can be seen that the central finger is slightly tapered as opposed to straight as in the CCD model. Also, the model does not take into account the etched residue material between the etched region and the un-etched regions of the device. The model was verified using CCD22 data obtained in the laboratory. Section 5.5 details the verification of the code.

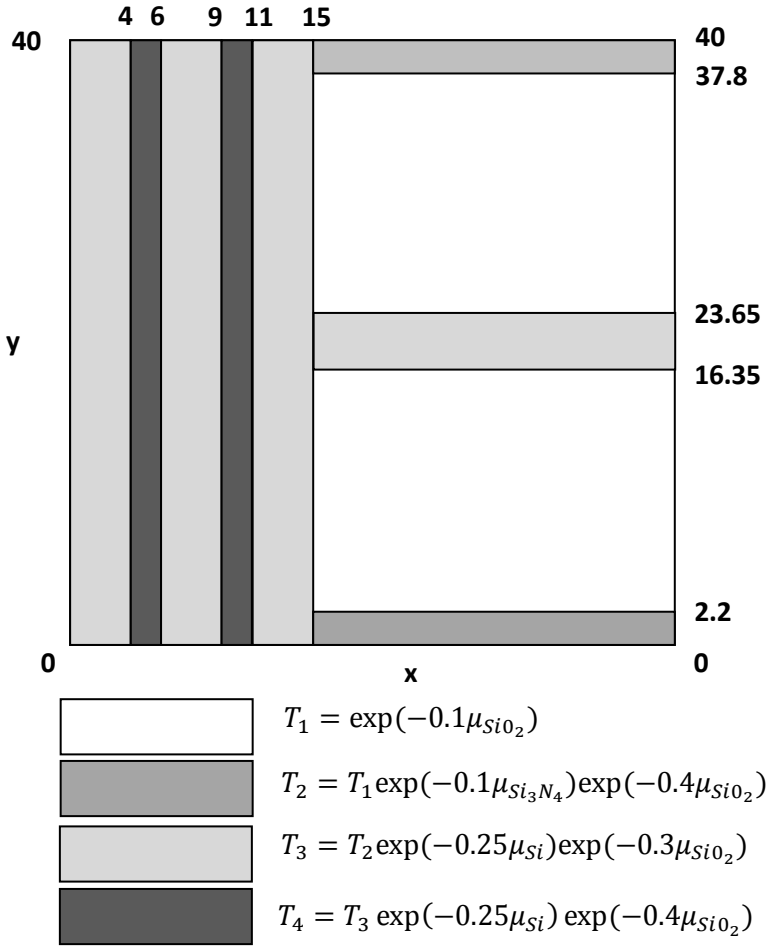

Figure 5.6 Dimensions and transmission coefficients of the various regions of the CCD22 pixel, as used in the Monte Carlo model. From [Godet, 2009]

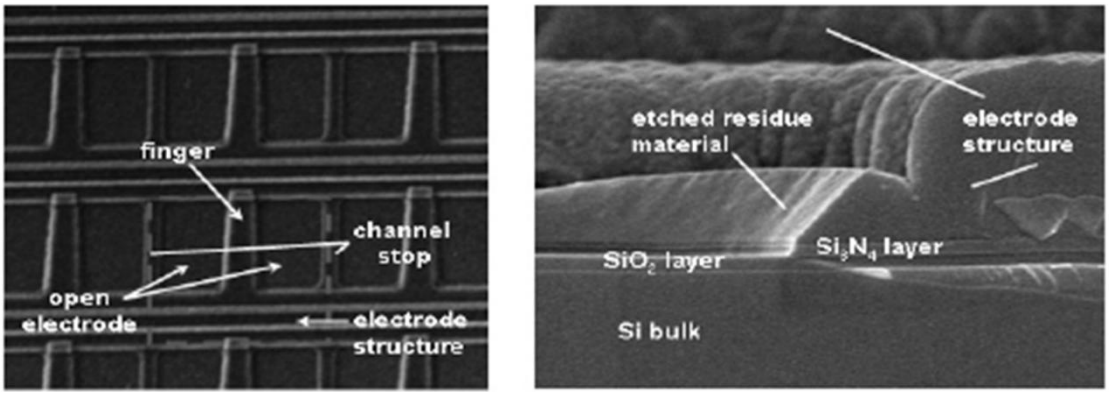

Figure 5.7 Left: Microscope image of the CCD22 electrodes, showing the main elements. Right: Electron microscope image of the CCD22 etched pixel showing the different pixel constituents at the etched interface. Images provided by e2v. From [Godet, 2009]

5.5 VERIFICATION OF THE MODEL

The updated Monte Carlo code, modified to include the effect of changing θ_i and higher X-ray energies, was verified using both the original, unmodified code used for the Swift XRT [Mukerjee et al, 2002] and experiment. Figure 5.8 shows a modelled CCD22 response to CuKα X-rays, generated using the modified code, and a CuKα spectrum taken in the lab. It can be seen that an excellent agreement is achieved between the two different spectra, providing confidence that the model is representative of the CCD22 response.

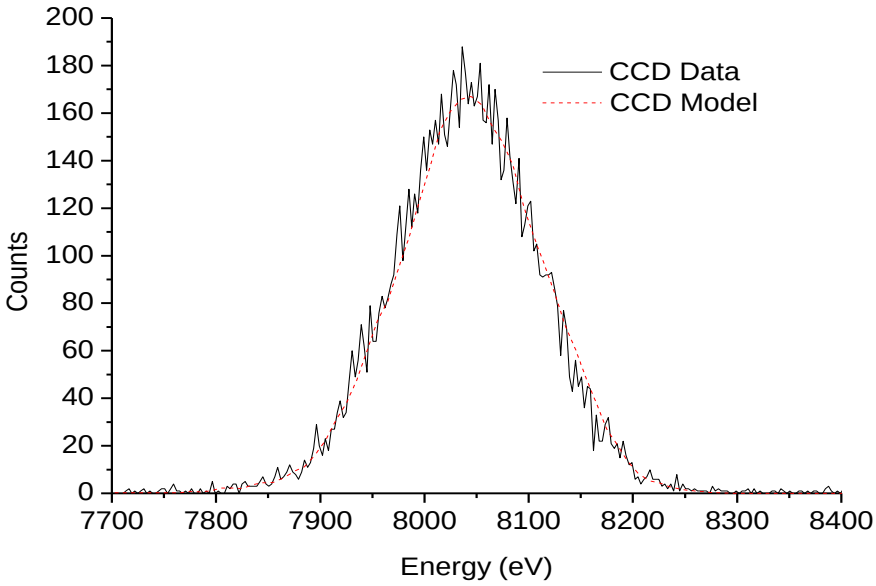

Figure 5.8 Comparing the Monte Carlo model results to experimental data, using CuKα X-rays (8.05 KeV)

5.6 MODELLING RESULTS AND DISCUSSION

5.6.1 QUANTUM EFFICIENCY (QE)

Figure 5.9 shows the modelled QE versus θ_i for isolated events (single pixel) and summed events (1-4 pixels) for ^{55}Fe (MnKα) X-rays at 5.90keV. An improvement of ~30% in QE is achieved for isolated events from 0º to 80º from the Z-axis. A 20% increase in QE is seen in summed events. Figure 5.10 shows a series of isolated event QE curves for a range of energies, demonstrating the QE improvement with increasing angle.

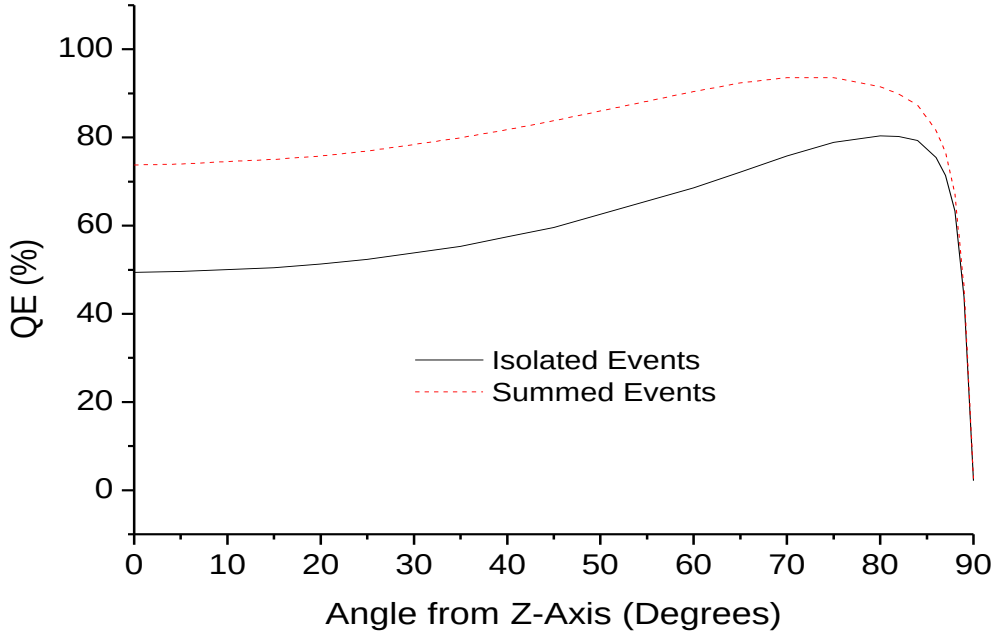

Figure 5.9 Modelled CCD22 ^{55}Fe (MnKα) X-ray quantum efficiency (QE) curves for isolated and summed events with varying incident angle, ϑ_i, from the Z-axis which is normal to the CCD surface

Note that in Figure 5.10 that a decrease in QE is observed at low energies as the incident angle is increased from the Z-axis. As θ_i increases, the effective thickness of the silicon oxide and silicon nitride layers at the CCD entrance window increases by the same factor as the depletion depth, $\cos\theta_i$. The effectively thicker oxide and nitride layers prevent lower energy X-rays from entering the depletion layer and being registered as events by the CCD.

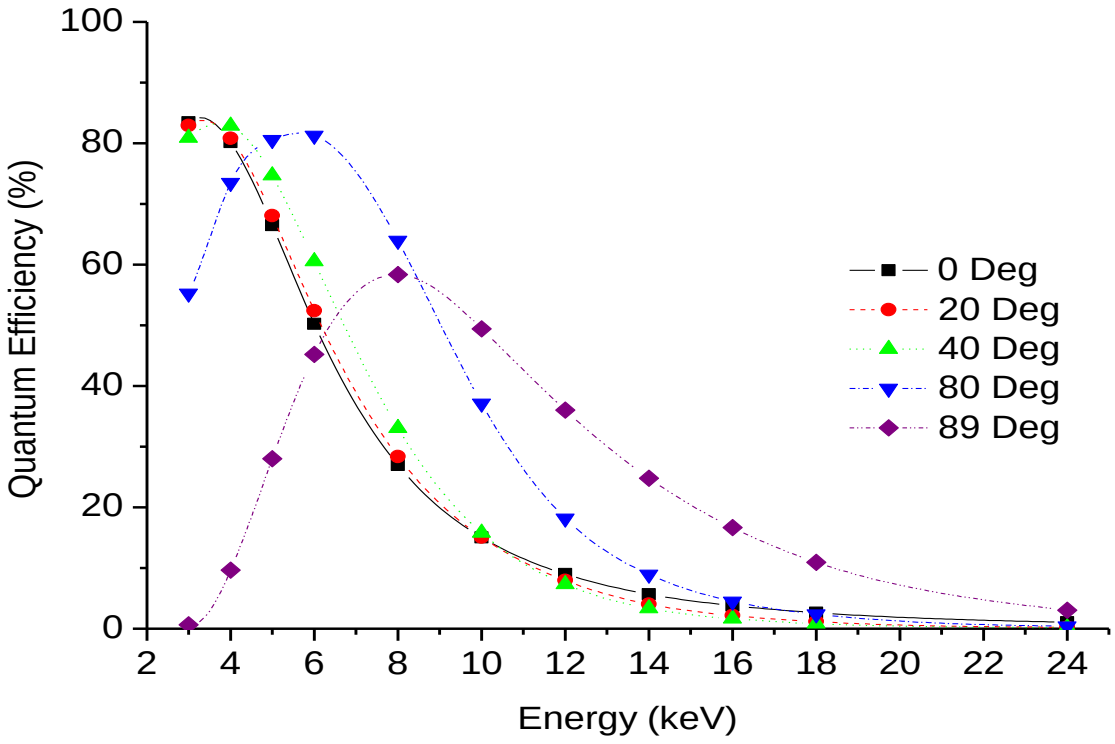

Figure 5.10 Isolated event quantum efficiency curves modelled for the CCD22 at 0°, 20°, 40°, 80° and 89° for energies ranging from 3keV to 24keV

This curve shows the promise of using X-ray CCDs at energies that would otherwise be inaccessible, particularly at angles approaching 90°. Tilting a device with respect to the incident X-rays can in principle provide an improvement in the standard QE at a given energy. A device tilted by 80° to the incoming X-rays, for example, would have >60% QE at 8keV whereas the same device normal to these X-rays would just see ~18% of events.

5.6.2 Energy Resolution and Multi-pixel Events

Higher energy X-rays entering a CCD at shallow grazing angles are more likely to interact in the depletion region closer to the electrode, creating a more constrained charge cloud and, as such, are less likely to spread over many pixels. Improved spectral resolution results as less charge is lost through thresholding split events, reducing redistribution, and less noise is integrated per event improving signal-to-noise. Three modelled ^{55}Fe summed-event spectra are shown in Figure 5.11 for 0°, 50° and 86°. A large reduction in redistribution is evident with increased θ_i. 33% of all counts are redistributed from the peak into the shoulder at 0° whereas at 86° only 3.2% of events appear in the shoulder. Figure 5.12 shows the fraction of events which occur in the main photo peak clearly showing a large reduction in redistribution at shallower grazing angles. Improvement

of ~6eV FWHM energy resolution (ΔE) is achieved as a result, the photo peaks having a FWHM ΔE of ~190.7±0.6 eV at 0° and ~184.6±0.2 eV at 86°. Significant improvement of energy resolution is also achieved with a 50° tilt, with a ΔE of ~184.8±0.9 eV. A major drawback of the large 86° tilt at ^{55}Fe energies is that a large number of photons are absorbed in the oxide and nitride layers of the CCD electrode, as seen in Figure 5.10.

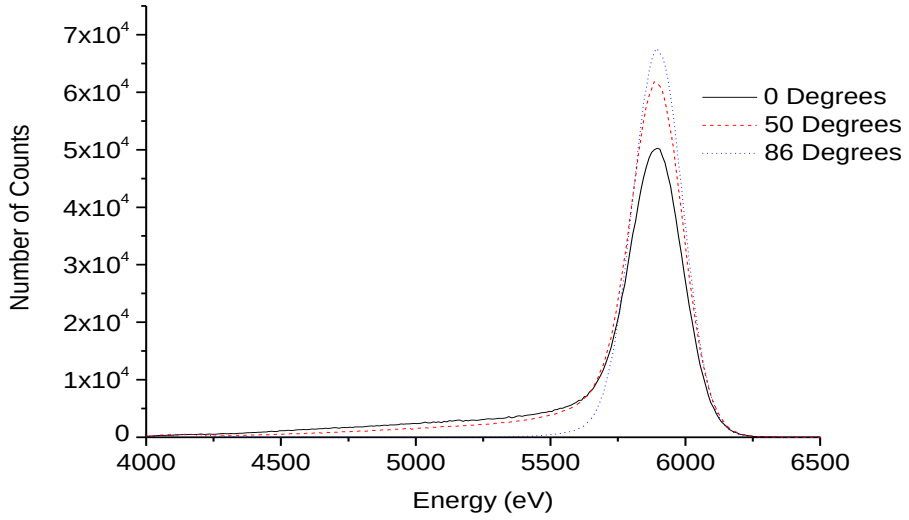

Figure 5.11 Modelled ^{55}Fe (MnKα) summed event spectra for 0°, 50° and 86°. A large reduction in spectral redistribution is observed as the incident angle approaches 90° from the z-axis

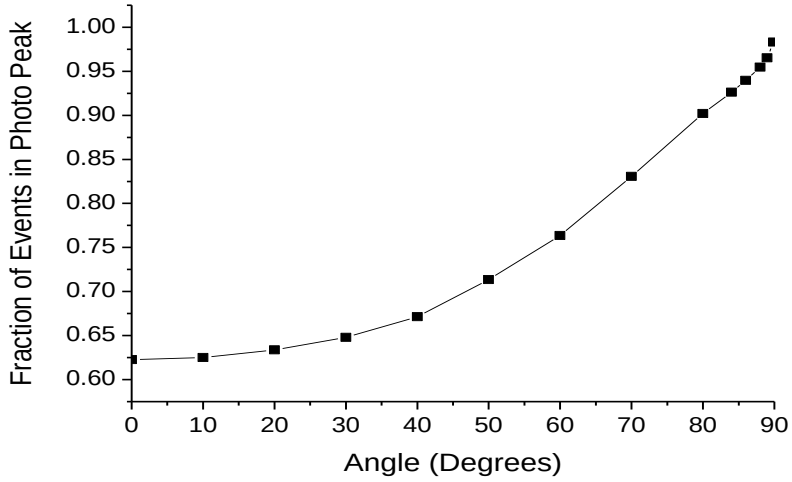

Figure 5.12 The fraction of summed events occurring in the photo peak as a function of angle

5.7 EXPERIMENTAL WORK

This section summarises the laboratory work carried out with Huawei Su, conducted in parallel with the modelling work presented in section 5.6. A series of experiments were carried out in order to establish the effect of incidence angle on the response of a CCD22, while also comparing the results with those shown in the model.

5.7.1 THE EXPERIMENT SETUP

5.7.1.1 THE CCD22

The EPIC-MOS CCD22 detector [Short & Turner, 1998] was developed by e2v Technology with the University of Leicester for the XMM-Newton X-ray Observatory. This device is discussed in more detail in Section 3.1. The device is a high resistivity, epitaxial silicon, buried channel, frame transfer array consisting of 600 x 600 pixels, each pixel 40µm x 40µm in size. A typical noise value for the CCD22 is <5 electrons, however due to the high noise electronics used in this experiment, a typical noise level of 15-20 electrons was achieved. The CCD has an assumed depletion depth of ~29µm. The CCD was cooled to -100°C using liquid nitrogen in a cryostat, with the chamber evacuated to $<1x10^{-6}$ mbar.

5.7.1.2 THE X-RAY SOURCE

The experiments were conducted with ^{55}Fe (5.9keV) and ^{109}Cd (22.2keV) sources, both measured to be approximately isotropic in output over the range of angles required using a Geiger counter. A number of source mounts were custom made to attach to the CCD frame, sitting at different angles, allowing a range of X-ray incidence angles of ~38° to 75°. Figure 5.13 shows a photograph of the ^{55}Fe source mounted on the angled source mount alongside the CCD22 device.

5.7.2 THE EXPERIMENTAL METHOD

The source was mounted at a distance of ~90mm from the CCD, with the X-ray incidence angle set by the choice of one of two source holder arms. X-rays will enter the CCD at angles between 40°-50° and 56°-64°. Shallower angles were not possible due to the geometry of the CCD holder.

The CCD22 is a large area CCD, about 2.5cm square. X-rays hitting one end of the device enter the CCD at a different angle to X-rays hitting the opposite end. Selection of different regions of

interest (ROI) across the CCD allowed a small range of incidence angles to be investigated for each of the holder arm positions.

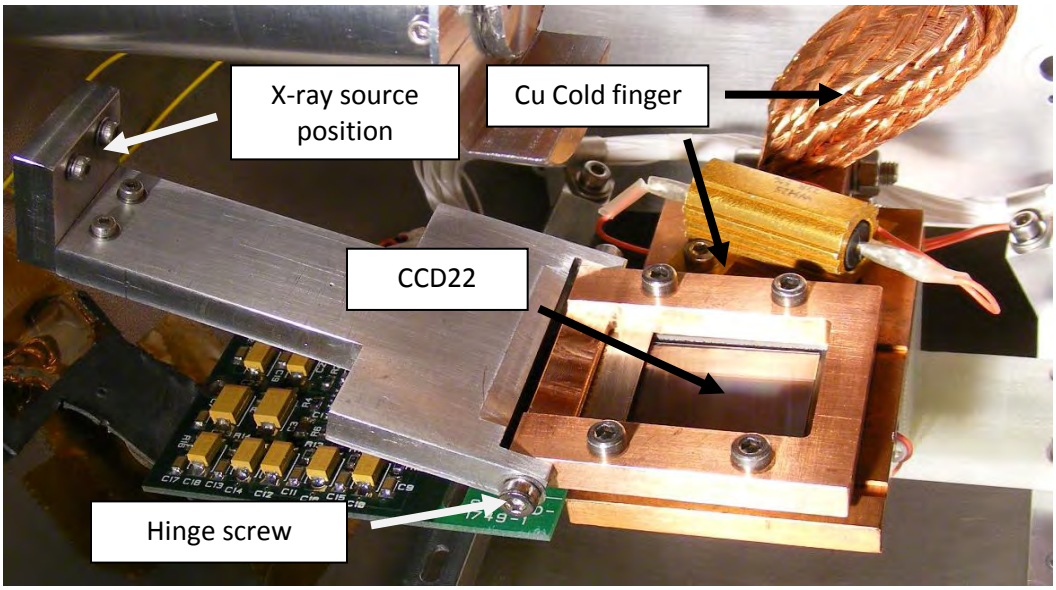

Figure 5.13 Photograph of the experimental setup, showing the radioactive source mounted at an angle to the CCD22

5.7.3 RESULTS

Figure 5.14 shows ^{109}Cd spectrum for an incident angle of 47° normalised to the peak count value. The modelled spectrum for this energy and angle is shown for comparison. Figure 5.15 shows ^{109}Cd QE, normalised to the modelled QE at 45°, compared with the QE curve modelled for this energy. The data were normalised to the 45° value as no absolute QE calibration was conducted for this CCD. The normalisation allows the relative shapes of the QE curves to be compared, rather than absolute QE.

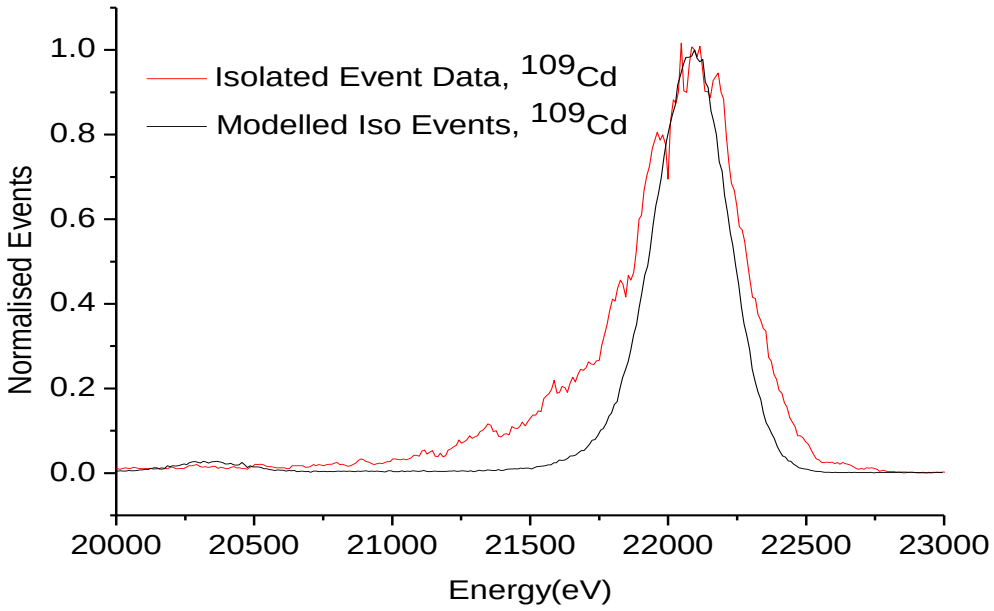

Figure 5.14 ^{109}Cd data compared with the equivalent model outputs. The spectra were normalised to the peak counts in both cases

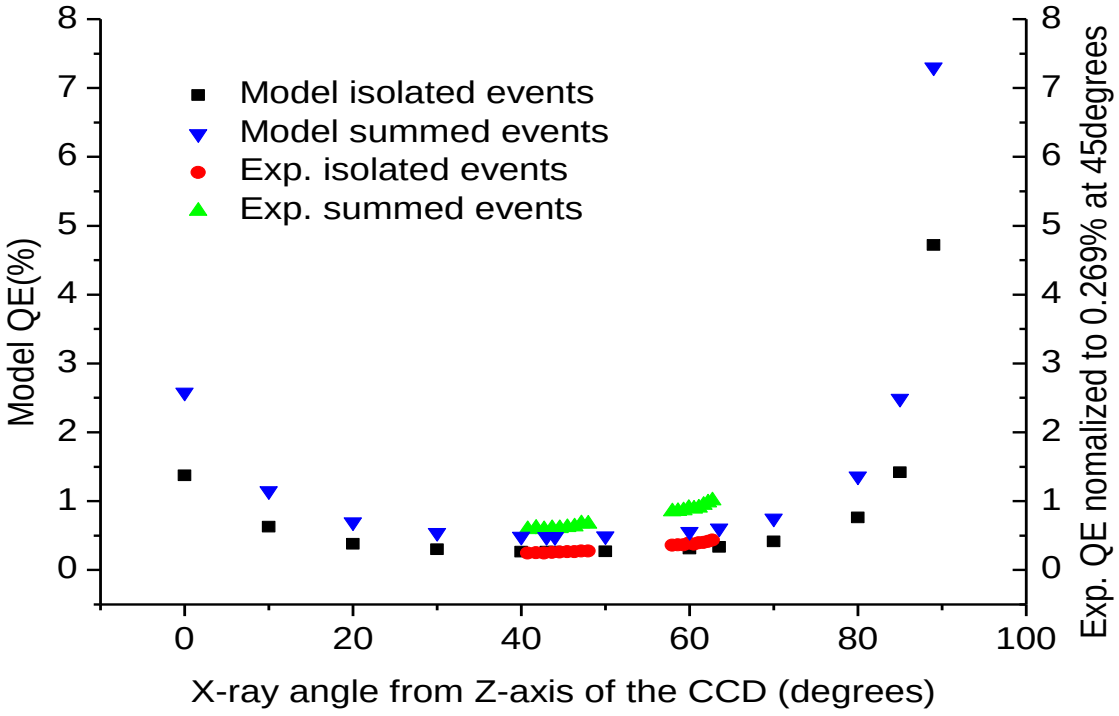

Figure 5.15 Modelled ^{109}Cd spectrum compared with experimental data. Experimental data are normalised to the modelled value at 45°

The ^{55}Fe source used in this experiment was found to be of insufficient activity to provide adequate statistics, leading the analysis to be conducted on the higher-energy ^{109}Cd X-ray source data.

5.7.4 EXPERIMENT DISCUSSION

The laboratory data and modelled data show a significant difference in spectral resolution due to a large amount of redistribution in the experimental data (

Figure 5.14). Figure 5.16 shows a pair of Gaussian curves fit to the experimental data. The two curves fit well to the data (99.3% fit using Origin 7.5) and give a FWHM ΔE of the main photo peak of 327.6 eV. The Gaussian fit to the redistributed shoulder has a FWHM of 674.2 eV. The modelled data was fit with a single Gaussian curve, showing a FWHM ΔE of 276.6 eV, a 51 eV difference between the two photopeak measurements.

This significant difference is likely to be caused by one or more of three factors;

1) Surface loss effects, where X-rays interacting near the surface of the CCD cause electrons to migrate toward the Si-SiO interface. These electrons are not registered as signal and subsequently redistribution occurs [Janesick, 2001].
2) The source of greater redistribution in the experimental data could be due to an error in the assumption that the CCD22 depletion depth is 29µm. This value was calculated using the CCD Monte Carlo model, comparing it to event distributions in CCD22 data as was done for the CCD66 in Chapter 4. Should the depletion depth of the device be smaller in reality, then more X-rays will interact in the field-free region, spread out to encompass a greater number of pixels and, through thresholding, charge will be lost. Again, redistribution will occur.
3) The threshold level of the system is high (~280eV), due to the high noise of the system, resulting in significant redistribution. Large packets of charge will be discounted from the spectrum when events are split over a number of pixels. A smaller system noise level would allow a lower threshold, which would, in turn, result in much less charge loss.

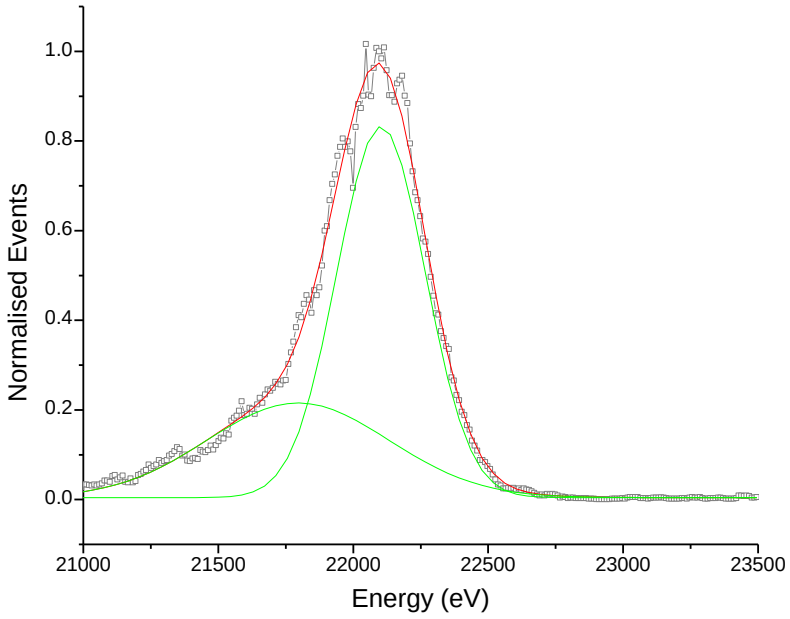

Figure 5.16 The spectral redistribution of the ^{109}Cd peak can be fit with two Gaussian curves

^{109}Cd X-rays (22.1 keV) have a long attenuation length through silicon, silicon oxide and silicon nitride [CXRO, 2009]; 1.37mm, 2.56mm and 1.42mm respectively. This suggests the first explanation, although potentially significant for values of θ_i >80°, is not the likely reason for the discrepancy between experiment and model here. The second explanation, although possible, is also not likely as this method of establishing depletion depth was shown to match very well with data obtained in the CCD66 experiment detailed in Chapter 4. The most likely reason for this redistribution is the third explanation; that the redistribution has resulted largely due to a high (~280eV) threshold. The threshold of the experiment setup was set high due to the very noisy electronics used to run the CCD and in the data acquisition system. Even with such a large threshold applied, the CCD noise was still 20 electrons, 15 electrons higher than is usually achieved when using a CCD22 device.

It is also worth noting from Figure 5.15 that the higher θ_i values deviate from the modelled distribution greater than lower values of θ_i. This is possibly due to surface charge loss effects which were not included in the modified CCD Monte Carlo code.

The figure also shows that the range of angles considered in the experiment was very limited, with data collected at θ_i = 40° to 50° and 56° to 64°. The experimental setup for this work was,

unfortunately, constrained by the vacuum chamber design which is optimised for use in X-ray fluorescence experiments and could not easily be modified in the short time available. It can be seen in Figure 5.13 that the copper CCD mount and aluminium holder prevent shallower angles from being exposed to X-rays due to shadowing of the device. The most significant angle effects were expected at much shallower angles than this (approaching θ_i = 90°) where any improvements in QE would be more significant and certainly more apparent.

Due to limitations on the availability of the test facility, it was not possible to design a more appropriate experiment to test the incident angle effect at shallower angles within the scope of this thesis.

5.7.5 CONCLUSION

The Monte Carlo model was used to investigate the effect of changing the X-ray angle of incidence on QE and spectral resolution. The model showed that a large reduction in multipixel events is expected to occur with increased angle from the CCD normal, resulting in an improvement of high energy QE. Spectral resolution is also improved due to reduced energy redistribution, as well as improved signal-to-noise ratio from a reduction in the number of large scale multi-pixel events.

The experiment conducted by Huawei Su to test this effect using ^{55}Fe and ^{109}Cd X-ray sources was unfortunately unable to adequately verify the results of the modelling work due to limitations in the set-up. The absolute QE for the CCD22 used in this experiment is yet to be established. Factors which could be responsible for the difference between laboratory and modelled data include assumptions made for the depth of depletion and device noise in the model, as well as a high threshold set on the device during data acquisition. The most likely cause of this discrepancy, however, is the very high threshold which was required due to the very noisy CCD electronics used. Unfortunately, due to limitations with the experimental setup and the availability of the test facility, further experiments designed to investigate shallower angles of incidence were outside the scope of this thesis.

5.8 SUMMARY

The modelling work presented both here and in Chapter 4 demonstrate the usefulness of the new CCD Monte Carlo model for investigating changes in depletion depth on CCD response, as well as a useful tool for indirectly establishing the depletion depth of a CCD by modelling the 1-4 pixel event proportion as a function of depletion and comparing these modelling results with laboratory data. The ability to modify the pixel size, thickness and material of the different CCD layers, as well as the angle of X-ray incidence and the direction of illumination, make this model a very powerful tool for modelling different types of CCD for different applications.

The following Chapter concludes this thesis.

CHAPTER 6

CONCLUDING REMARKS

Radiation damage is a serious challenge for scientific payloads for future space missions. Radiation effects reduce science performance, cuts short the lifetime of instruments and also results in increased cost of mission resources as shielding mass is used to mitigate the damage. This thesis has presented the challenge of radiation damage to future missions, as well as investigates some of the methods that can be employed to reverse some of the degradation.

The BepiColombo mission to Mercury will experience one of the harshest solar system environments due to its proximity to the Sun. The work presented in this thesis was vital in ensuring that the Mercury Imaging X-ray Spectrometer (MIXS) will have the capability to anneal its focal plane instrumentation in order to reverse the non-ionizing damage that it will suffer from high energy proton interactions. The experimentation conducted at the University of Birmingham Cyclotron Facility showed that the expected mission dose results in a dark current increase that will prevent the end-of-life spectral resolution requirement being met, but also that a thermal anneal will recover this performance.

The XMM-Newton spacecraft is the longest operating European X-ray telescope and, as such, its detectors have been exposed to unprecedented levels of focussed X-ray radiation. The unexpected degradation of the devices associated with this large dose of ionizing radiation has been shown in this thesis to be a direct result of the detector configuration. The open-electrode structure, necessary for enabling the CCD low energy response, is also responsible for the low energy redistribution effects seen over time. The X-ray damage replicated in the laboratory was present in data taken where events which only occur in the open electrode portion of each pixel were accounted for yet no damage was visible when events occurring in the closed structure were displayed. This provides a key bit of evidence that will allow the XMM-Newton Detector Calibration Group to better model the CCD response matrices, a vital task in the coming months as XMM-Newton is again due to have its life extended by the European Space Agency.

Radiation damage of detectors reduces the scientific performance CCDs. This thesis also investigates the ability to improve scientific performance of such devices by directly manipulating

the CCD substrate voltage. The work showed that for devices specifically designed to have such a voltage applied, for example the CCD66 designed for the IXO Wide Field Imager, characteristics such as high energy quantum efficiency and spectral resolution can be improved. The improved depletion depth achieved was inferred from the results achieved using a modified version of the EPIC XMM-Swift Monte Carlo code. The modifications made to this code have resulted in a very useful tool for investigating the spectral response and QE of CCDs with different pixel structures.

The modified CDD code was also used to investigate the effect of X-ray angle of incidence, showing the geometric effect of apparent increased depletion depth when X-rays enter a CCD away from the surface normal. The angle of X-ray incidence was shown in the model to result in increased high-energy response as well as a small improvement in spectral resolution. The experiment designed to verify these effects in the laboratory were unfortunately inconclusive due to complications related to the experimental setup.

Following this thesis summary are two annexes containing additional information and work carried out by the author. Annex 1 contains a case study detailing the International X-ray Observatory (IXO) and its instrumentation. IXO utilises many different types of X-ray detector which cover a diverse range of application from polarimetry with a gas-based device, to high spectral resolution using cryogenic detectors. IXO's instruments will all be subject to radiation damage over the course of the mission lifetime so the work presented in this thesis will be applicable to the IXO payload.

Annex 2 details work carried out by the author in the field of X-ray optics. An experiment is presented which characterises a microchannel plate optic, demonstrating for the first time an intrinsic angular resolution which meets the needs of future mission concepts such as the BepiColombo mission. In addition, the appendices attached to this thesis present the data obtained during the PhD in various experiments.

The understanding of radiation damage mechanisms and how to mitigate the resultant damage is essential for future space missions. The need for ever-more performant instruments will mean that protecting against damage which degrades performance is increasingly important. The work carried out as part of this thesis adds to the understanding of this problem and will hopefully aid BepiColombo and the International X-ray Observatory to achieve their science goals.

ANNEX 1

MISSION CASE STUDY: THE INTERNATIONAL X-RAY OBSERVATORY

The International X-ray Observatory (IXO) [Bavdaz et al, 2009][ESA, 2009] is a large X-ray telescope mission currently being assessed by the European Space Agency and NASA as a potential future mission concept. The author of this thesis is currently employed by Astrium Ltd in the UK as the System Engineer for the ESA IXO Assessment Study, with particular responsibility for the payload complement. IXO is an ideal case study for investigating the current state-of-the-art optics and detector technologies. The telescope utilizes a complement of six focal plane detectors, each using a different detector technology. The large range of science goals of the mission requires an extremely diverse capability from the detectors, which are each described in this section.

A1.1 IXO SCIENCE OBJECTIVES

The IXO mission has three broad science themes; matter under extreme conditions, formation of structure and life cycles of matter and energy [IXO Mission Requirements Document, 2010]. These themes are described below. The IXO payload, discussed in this appendix, is designed to meet these objectives.

A1.3.1 MATTER UNDER EXTREME CONDITIONS

This theme requires the investigation of supermassive black holes (SMBH) and neutron stars. IXO will be used to establish the growth of SMBHs and their link to the formation of the first galaxies in the universe by observing SMBHs at high red shift. These objects are rare (<1 source per arcmins^2) [Schleicher, Spaans and Klessen, 2010][Nandra et al, 2010], so a combination of large field of view (>15 arcminutes) and good angular resolution (< 8'') is required, as well as a large effective area (≥2.5m^2 @ 1.25keV) in order to capture enough photons from these faint objects. IXO will measure X-ray spectral slopes and luminosities which will provide constraints on accretion rates and, therefore, SMBH growth rate. In particular, IXO will be able to use its large throughput to measure Fe Kα lines, generally too faint to provide useful physical insights on SMBHs [NASA IXO flight Mirrors, 2010].

The investigation of matter accreting onto black holes is also of interest, and will help the investigation of black hole spin. Both accretion and black hole collisions can change spin rates. Measuring the spin rate of a large number of black holes will enable the determination of the spin mechanism over cosmic time [Nandra et al, 2010].

An objective of the IXO mission is to establish the equation of state of neutron stars. This will be achieved through measuring the size and mass of a number of neutron stars, constraining the equation of state. Neutron stars consist of some of the densest matter in the Universe, and are dominated by the Strong Force. Neutron stars also provide an ideal means to investigate high density, low temperature physics. There is no current consensus on the emission of electromagnetic radiation from pulsars, so one of IXO's goals is to further investigate this emission using X-ray polarimetry and high resolution (2.5eV @ <6keV) spectroscopy in order to constrain current models [Paerels et al, 2010].

A1.3.2 FORMATION OF STRUCTURE

This theme is concerned with dark matter, dark energy and its distribution throughout the Universe. IXO will be used to constrain current models of dark energy and dark matter by investigating galaxy cluster evolution and the chemical properties of the Intergalactic Medium (IGM). IXO will be unique in its ability to probe X-ray emission from clusters deeper in space and hence further back in time, enabling the investigation of cluster evolution. A large collecting area is essential to do this.

Cosmic Feedback is the process by which gas is heated by black hole emission, both radiatively and mechanically (through winds and jets). IXO should have the ability to distinguish between the two different types of heating mechanism using its high resolution spectral capability.

IXO will also be used to answer the mystery of the missing baryons in the Universe. Less than 10% of the baryons in the local universe are accounted for in stars and galaxies. It is hypothesised [Bregman et al, 2010] that the remainder of this material exists in a 'Cosmic Web' of dilute gaseous material. IXO will map the hot gas in and around the Milky Way and local group of galaxies. This gas emits radiation in the X-ray regime. Measuring the distribution of this gas around the Milky Way will allow astronomers to establish the location of the 'missing stellar baryons'. It is predicted that the Cosmic Web is, in parts, heated to temperatures of 10^7 K and chemically enriched by galactic winds. IXO should be capable of detecting these missing baryons and is required to characterise their velocity distribution along 30 lines of sight over the course of the mission [NASA IXO Science Objectives, 2010].

A1.3.3 LIFE CYCLES OF MATTER AND ENERGY

This theme investigates the origin and dispersion of the elements, particle acceleration, stellar magnetic fields and planet formation. IXO will be used to investigate the ejection of element-rich gases from supernovae using high throughput imaging. Investigation of explosive nucleosynthesis by measuring the absorption lines in hundreds of lines of sight will allow IXO to map the distribution of metals throughout the Milky Way [Lee et al, 2010].

Evidence of cosmic ray proton acceleration has been hard to obtain, so IXO will be used to investigate this high energy process. Understanding how high speed shock processes heat electrons and ions will require polarimetric and spectroscopic observations of many supernova remnants of varying ages [Strickland et al, 2010].

The effect of X-rays on planetary formation and habitability is of interest, and IXO will be used to observe the emission of X-rays from host stars and their energy input into proto-planetary disks and planetary atmospheres. The effect of X-rays on the thermodynamics, chemistry and dynamics of proto-planetary disk formation will be investigated, as well as the effect of host star X-ray emission on the habitable zone [Feigelson et al, 2010]. IXO will also be used to investigate stellar X-ray emission from magnetic reconnection events.

A1.2 THE IXO PAYLOAD COMPLIMENT

The information presented in this section summarises the key science requirements [IXO Payload Definition Document, 2009] of the IXO payload and demonstrates the very diverse set of detector types, including CCDs, active pixel sensors, strip detectors, cryogenic detectors and gas pixel detectors. Each of the instruments will be used to meet the many science goals of the IXO mission.

The IXO payload consists of six separate instruments which will be used to achieve the mission science goals. These are the Wide Field Imager (WFI), the Hard X-ray Imager (HXI), the X-ray Microcalorimeter Spectrometer (XMS), the High Time Resolution Spectrometer (HTRS), the X-ray Polarimeter (XPOL) and the X-ray Grating Spectrometer (XGS). The requirements for each of these instruments are summarised in Table A1.1 [IXO Payload Definition Document, 2009].

Instrument	WFI & HXI Combined		XMS	HTRS	XPOL	XGS[1]
Characteristic	WFI	HXI				
Detector type	Si APS (DEPFET)	CdTe + Si strip detectors	Micro-calorimeter TES	Silicon Drift Diodes	Gas Pixel Detector	CCD
Mass (kg) excluding baffles and radiators	83 116	33	389[2] 352[3]	30	11	6.7 + 43.8[4]
Peak power (W)	283 344	61	1221[2] 1080[3]	165	61	115
Operating temperature	210K	233K	50mK	253K	283K	183K
Cooling	Radiator	Radiator	Closed cycle coolers/ADR	Radiator	Peltier	Radiator
Detector size (mm)	102.4 x 102.4	70 x 70	31.2 x 31.2	16.1 (Hexagonal)	15 x 15	786 x 24
Energy range (keV)	0.1-15	10-40	0.3-10	0.3-10	2-10	0.3-1
FWHM energy resolution	50eV @ 282eV 125eV @ 6keV	1keV @ 40keV	2.5eV @ 6keV	200eV @ 6keV	1200eV @ 6keV	E/ΔE >3000
Pixel size (μm)	100	220	300 (& 600)	4000	50	24
Number of pixels in one dimension	1024	320 strips	40 (+32)	7	300	32768
Field of view (arcmin square)	17.6	12	2 (& 5.4)	2.8 (Hexagonal)	2.6	N/A
Unvignetted FOV (arcmin)	17.6 (diam)	12	5.4 (diam)	2.8 (diam)	2.6	N/A

[1]Assuming the NASA Critical Angle Transmission grating option
[2]JAXA redundant cooler option
[3]ESA CDF baseline cooler option
[4]6.7kg for both grating boxes and 43.8kg for the camera

Table A1.1 A summary of the International X-ray Observatory detector requirements taken from the ESA IXO Statement of Work Payload Definition Document [IXO Payload Definition Document, 2009]

A1.3.1 THE WIDE FIELD IMAGER (WFI)

The purpose of the WFI is to proved images of X-ray sources in the energy band of 0.1 to 15 keV with spectral and time-resolved photon counting, and establishing the location in the sky of faint X-ray sources to be followed up in later observations using the higher energy resolution X-ray Microcalorimeter detector. The WFI instrument has the largest area of IXO's detectors, being 10 x 10 cm^2, with a field of view of 17.6 x 17.6 arcminutes square. The detector is a Depleted Field Effect Transistor (DEPFET) Active Pixel Sensor (APS) [Treis, 2009], very similar to those used on the MIXS instrument on BepiColombo [Treis, 2008], the main subject of Chapter 2 of this thesis. The primary difference between the WFI and the MIXS detectors is the size of the DEPFET sensor. The IXO WFI is 1024 x 1024 pixels, with each pixel 100 x 100 μm^2. The large field of view requirement of the WFI is one of the primary reasons for using the DEPFET APS, as this type of detector can, in principle, be made as large as a commercial silicon wafer. In comparison, the BepiColombo MIXS detectors have 64x64 pixels, each pixel 300 μm x 300 μm.

The detector energy response has shown, in the laboratory, to be 'Fano limited' [Treis, 2008]. The Fano limit is the theoretical best spectral resolution achievable by a semiconductor detector and results from statistical variation of the electron-hole pairs created when an X-ray interacts with the material. [Janesick, 2001]. If the number of electrons in a charge cloud created by an X-ray interaction with a material is *N,* the variance (σ^2_N) is given by $\sigma^2_N = F_a N$ where F_a is the Fano factor [Fraser, 1989]. The Fano factor can be used to relate the measured FWHM of an X-ray line and the average energy expended to produce an electron-hole pair by equation A1.1.

$$FWHM(eV) = 2.355[E(eV)F_a E_{e-h}]^{1/2} \quad \text{(A1.1)}$$

E (eV) is the photon energy in electron Volts and F_a is the Fano factor. $E_{e\text{-}h}$ is the energy required to create an electron-hole pair in the detector material. Experimentally, the Fano factor has been determined to be 0.118±0.004 for silicon [Fraser et al, 1994][Lowe and Sareen, 2007].

The DEPFET is a combined detector-amplifier structure, every pixel consisting of a p-channel MOSFET integrated onto a fully depleted silicon bulk (Figure A1.1), where depletion is achieved by the sideways depletion principle [Gatti and Rehak, 1983]. An internal gate is generated in the device using a deep n-channel implant, constrained to the region below the transistor channel. X-rays interacting in the bulk silicon create electron-hole pairs, the holes drifting to the nearby p-contact and the electrons swept to, and collected by, the internal gate. The conductivity of the MOSFET channel is affected by this charge collection, and measuring the change in conductivity is therefore a direct measure of the charge generated by the incident X-ray.

The DEPFET establishes the energy of an incoming X-ray as follows. To begin, the charge in the device is removed by using the ClearFET, a nearby n-channel MOSFET, and the conductivity of the pixel is determined. Charge is then integrated for a certain length of time before the conductivity is, again, measured; this second measurement now includes any charge generated by incoming X-rays during the integration period. The difference between the cleared conductivity and the conductivity of the integrated pixel is a measure of the accumulated charge. The pixel is then cleared once more and the process is repeated. Figure A1.1 shows a schematic diagram of the DEPFET pixel and its various doped regions.

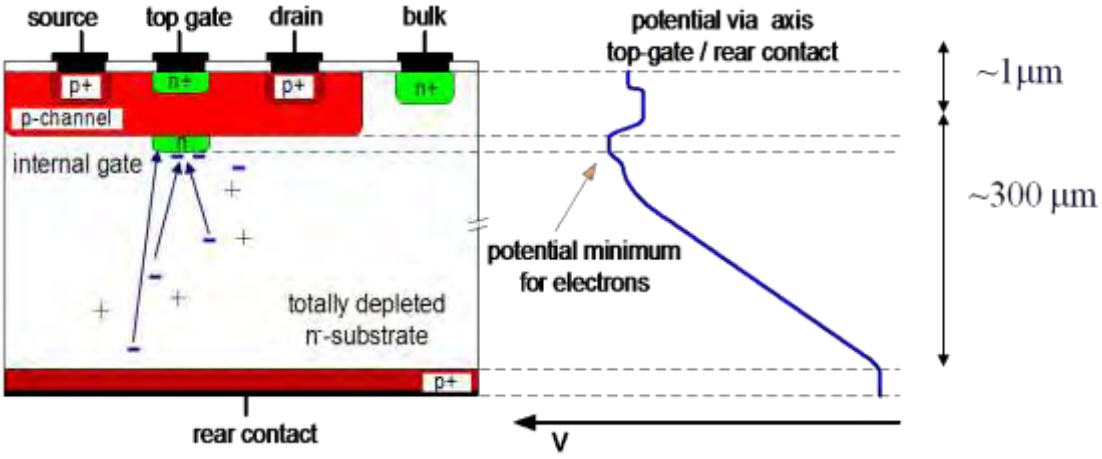

Figure A1.1 Schematic diagram of a DEPFET pixel

Requirement	Specification	Comments
Device Dimensions		
Area	10 x 10 cm^2	Integrated on monolithic 6'' wafer
Thickness	450 µm	For good QE at high energies
Pixel Size	100 x 100 µm	PSF size incl. Oversampling
Array Dimensions	1024 x 1024 pixels	Largest array dimension suitable for monolithic integration
Spectroscopy		
Energy Resolution		
@ Mn Kα (5.9 keV)	125 eV FWHM	
@ C Kα (282 eV)	50 eV FWHM	
Readout Noise	3-5 e^- ENC	
Readout Timing		
Readout time/frame	1.28 – 2.56 ms	Depends on FE performance
Processing time/row	2.5 – 4 µs	
Raw data rate	1.6 GByte/s	Final data rate depends on pre-processing
Quantum Efficiency		
Fill factor	100%	
QE @ C Kα (282 eV)	33%	
QE @ Si Kα (1.74 keV)	93%	Depends on implementation of filter (70nm Al filter and dielectric layer system assumed)
QE @ Cu Kα (8.05 keV)	100%	
QE @ 10 keV	96%	
QE @ 20 keV	35%	

Table A1.2 Table showing the preliminary IXO-WFI performance requirements, as presented in the ESA IXO Statement of Work Payload Definition Document [IXO Payload Definition Document, 2009]

The large field of view and the DEPFET's susceptibility to stray light, both visible and X-ray, results in the need for both a baffle and filter to ensure that the incident photons on the detector are X-rays from the objects of interest being focused by the spacecraft mirrors. Each of IXO's instruments has similar stray light requirements; however the large field of view of the WFI drives the size of the baffle, which is shared by all instruments. The WFI filters can be removed from the instrument by a filter wheel in order to maximise the low energy QE (33% at 282 eV) when ambient light levels are low enough at the focal plane to maintain the required signal to noise ratio. When the filter is in place the QE at 282 eV is reduced to

approximately 6%, below the required QE at Carbon Kα, but often necessary to reduce the optical light to acceptable levels.

The detector must be operated at 210K ±0.1K and is passively cooled using a cold finger attached to a dedicated radiator to cold space. The total power requirement of the instrument is expected to be 283.1 W, including a 20% margin. The WFI and Hard X-ray Imager (HXI) share a position at the focal plane, with the HXI mounted behind the WFI, allowing simultaneous measurements by both instruments; X-rays with an energy >10 keV are likely to pass through the WFI DEPFET detector where they will be absorbed and detected by the HXI instrument.

A1.3.2 THE HARD X-RAY IMAGER (HXI)

The Hard X-ray Imager (HXI), positioned behind the WFI, allows simultaneous measurements at both soft (0.1-15keV using the WFI) and hard (up to 40keV using the HXI) X-rays. The HXI consists of three detector layers; two silicon strip detectors [Aono et al, 2008] and one Cadmium Telluride (CdTe) detector. The first two silicon layers are sensitive to X-rays <30keV that pass through the WFI. The third CdTe layer detects X-rays <40keV which pass through the first two silicon strip detectors. The baseline detectors are each 7cm x 7cm in area, although an option to make the HXI detectors with an area of 10.5cm x 10.5cm, with an equivalent field of view to the WFI, is under investigation [IXO Payload Definition Document, 2009].

As the WFI is placed at the optimum focal point, the HXI detectors are slightly out of focus, with the three layers sitting 20, 22.5 and 25mm behind the WFI. The point spread function (PSF) of the IXO mirrors is ~1.55mm larger in diameter at the HXI due to the out of focus position of the detectors.

The energy resolution requirement for the HXI is >1keV FWHM at 40keV and the field of view should be 12 x 12 arcmins^2. The HXI silicon detectors become essentially transparent above 30keV so the CdTe detectors are crucial to extending the detector response to 40keV due to their high mass absorption coefficient. There are currently two options for the CdTe detector types: a double-sided strip detector and a pixellated detector configuration. The double sided strip detector offers a better spatial resolution than the pixel detector, 220µm as opposed to <600µm. All three detectors will be 0.5mm thick. An anticoincidence shield (ACS) is also used to suppress the background generated from high energy photons, particles and secondary X-rays which will enter the detector from outside the field of view. This ACS will be made of 2cm

thick BGO ($Bi_4Ge_3O_{12}$) crystals, a scintillating material, and read out using avalanche photo diodes.

The two silicon detectors placed above the CdTe detector in the HXI are also strip detectors [Aono et al, 2008]. A strip detector uses long one-dimensional electrodes laid across the surface of a semiconductor material in strips. Double-sided strip detectors have a second layer of electrodes perpendicular to those on the front side. When charge generated in the bulk of the material by a particle or photon interaction is collected at the electrodes at either surface of the detector, the position of photon interaction in the device can be determined by measuring the charge. Figure A1.2 shows a diagram of a double sided strip detector.

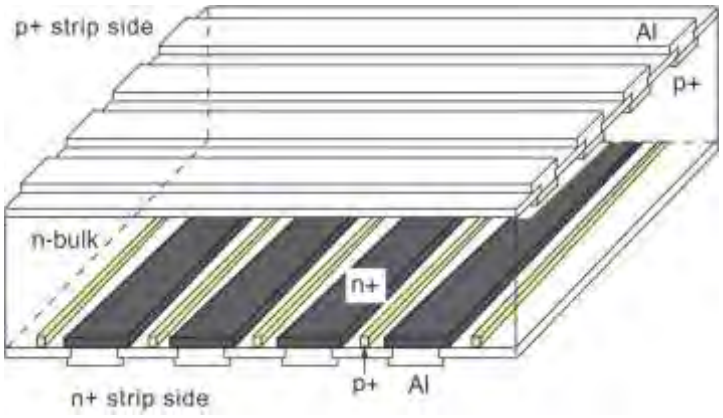

Figure A1.2 Diagram showing the configuration of a double-sided strip detector

The CdTe detector will, with time, become activated by cosmic ray and particle irradiation due to its stopping power. This will increase the noise of the detector above the maximum level allowed if the spectral resolution requirement at the end of the mission is to be met. This is another justification for introducing the two silicon strip detectors to the instrument. The silicon strip detectors are useful in the 10keV to 30keV range and will not become activated in the same way as the CdTe detector. This ensures that only the 30keV-40keV energy band is adversely affect by this activation effect over time. The detector will be heated to 278K once a month in order to minimise this degradation.

The QE of the combined silicon and CdTe strip detectors is shown in Figure A1.3, with 100% QE expected up to 40keV [IXO Payload Definition Document, 2009].

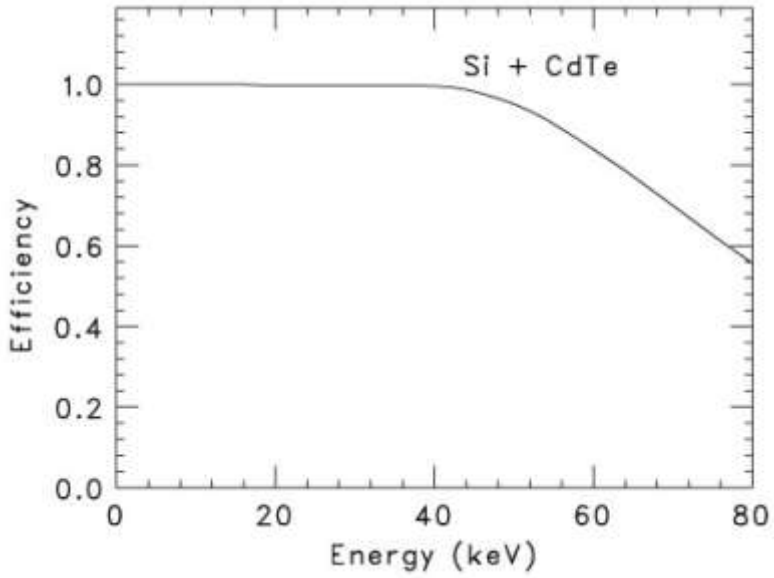

Figure A1.3 The expected QE of the combined silicon and CdTe strip detectors used in the HXI instrument. Graph taken from the ESA IXO Payload Definition Document [IXO Payload Definition Document, 2009]

Table A1.3 summarises the two possible HXI detector configurations; the option of choice, using a double-sided CdTe strip detector and two silicon strip detectors, and the backup option of using a CdTe pixellated detector. The HXI spectra obtained using the CdTe strip detector are expected to be similar to those shown in Figure A1.4, obtained using a large pixel CdTe detector [IXO Payload Definition Document, 2009].

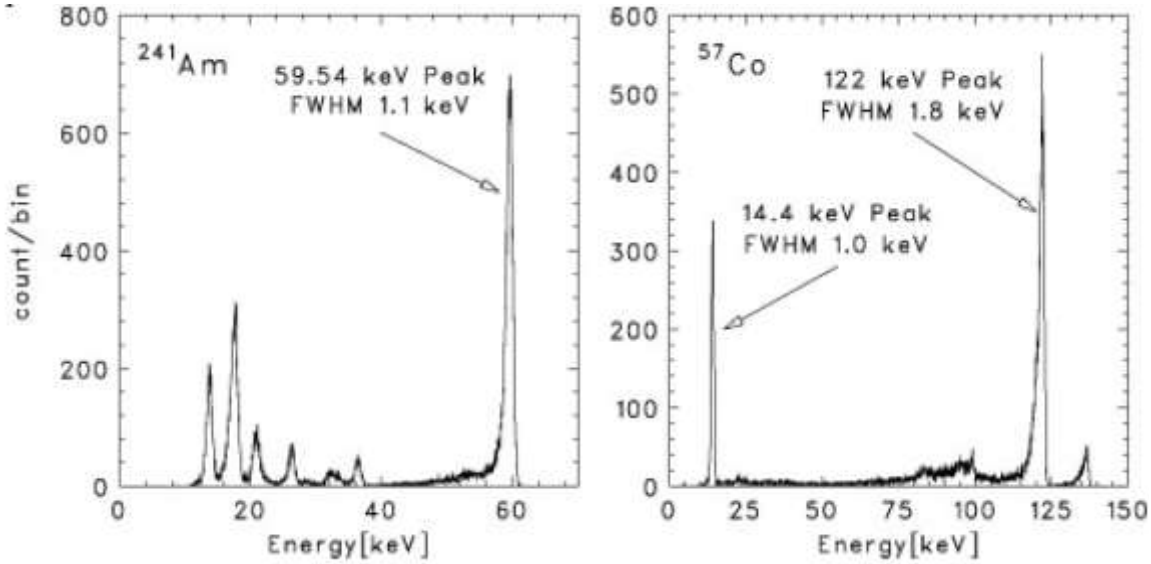

Figure A1.4 Spectra obtained from a large area CdTe pixel detector [IXO Payload Definition Document, 2009]. Left: Using an ^{241}Am source and Right: Using a ^{57}Co source.

Characteristic	Strip Design	2-D Pixel Array Design
Detector type	Si and CdTe Schottky Diode double sided strip	Double sided Si strip and CdTe Schottky Diode pixel devices
Strip pitch	220µm for both sides	<600 µm for CdTe pixel
Number of strips	320 (for both sides) total 1280 strips for CdTe. Two layers of double-sided silicon strip detectors are placed in from of the CdTe, with a total of 2560 strips	>13k/>31k+ channels for 70mm wide CdTe pixel detector, and 2 layers of Silicon Strip detectors, in total 2560 strips
Array size	70mm x 70mm	70mm x 70mm
Field of view	12 x 12 $arcmin^2$	12 x 12 $arcmin^2$
Energy range	10-80keV	10-80keV
Energy resolution	ΔE<1keV FWHM at 40keV	Similar or better
Non-X-ray detector background	$5x10^{-4}$ counts $keV^{-1}cm^{-2}s^{-1}$ roughly flat	$5x10^{-4}$ counts $keV^{-1}cm^{-2}s^{-1}$ roughly flat
Count rate/pixel with 10% pile-up	20000 counts s^{-1} independent of the position	20000 counts s^{-1} independent of the position
Count rate/source with 10% pile-up	20000 counts s^{-1} independent of the position (note Crab is expected to generate 100-500 counts s^{-1} only	20000 counts s^{-1} independent of the position
Timing accuracy	10µs	10µs
Typical/Max telemetry	10 $kbit.s^{-1}$ (1$Mbit.s^{-1}$ max for ground calibration)	10 $kbit.s^{-1}$ (1$Mbit.s^{-1}$ max for ground calibration)
Operating temperature	Detector, -40 or -30 ± 2°C (TBC), Electronics, 20 ± 20°C	Detector, -40 or -30 ± 2°C (TBC), Electronics, 20 ± 20°C
Instrument power, excl temp control	41W	41W
Total mass	25kg	25kg
Total power	46W, with an additional 50W needed to heat the detector to 5°C for annealing	46W, with an additional 50W needed to heat the detector to 5°C for annealing

Table A1.3 Comparison between the two possible HXI detector configurations: CdTe strip detector or CdTe pixellated detector plus 2 silicon strip detectors [IXO Payload Definition Document, 2009]

A1.3.3 THE X-RAY MICROCALORIMETER SPECTROMETER (XMS)

The X-ray Microcalorimeter Spectrometer is the IXO cryogenic detector used to conduct very high resolution spectroscopy. The XMS has a narrow field of view of 5.4 arcminutes and will, therefore rely, on the WFI to locate new sources of interest for XMS observations. A microcalorimeter measures the change in temperature of an absorbing material when the material absorbs the energy of an X-ray. The ability to accurately measure this tiny change in temperature allows very precise determination of the incident X-ray's energy. High energy resolutions (~10eV @ <6keV), unobtainable with semiconductor detectors which are limited by the Fano factor of the material [Fraser, 1994], are therefore possible with cryogenic detectors such as the XMS. One of the main factors limiting the energy resolution of these detectors is baseline temperature stability.

There are two competing technologies for this instrument: the Superconducting Tunnel Junction (STJ) detector [Verhoeve et al, 2004] and the Transition Edge Sensor (TES) [Macculi, 2009]. The current IXO baseline payload assumes the use of an array of absorbers read out by TES for the microcalorimeter so this section focuses on this technology.

The aim of the XMS is to provide spectra with extremely high energy resolution of typically 2.5eV from 0.2-10 keV for the central detector, and 10eV for the wider field outer section of the instrument.

In order to achieve the extremely good energy resolution of the XMS, the device needs to be cooled to a temperature of 50mK. This is done using a cryogenic cooling chain which is, as yet, largely undefined. The cryogenic system will be extremely resource hungry and, as such, the XMS instrument drives many of the IXO payload requirements. Figure A1.5 shows a schematic of the XMS detector.

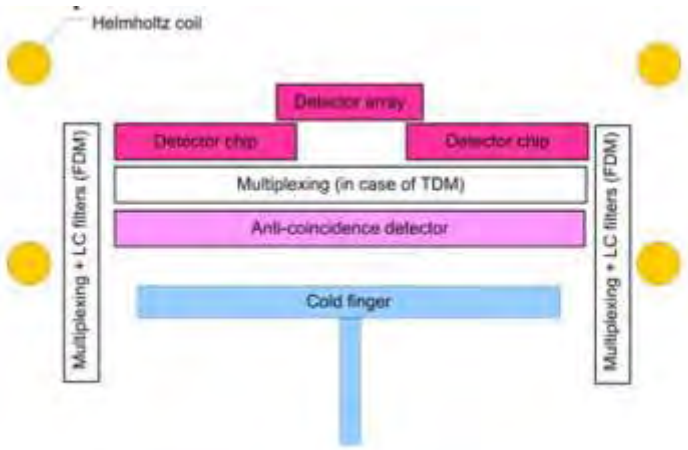

Figure A1.5 Schematic diagram of the XMS detector [IXO Payload Definition Document, 2009]

The TES consists of a bi-layer which is biased in its transition between super conducting and normal resistance. The temperature change in the absorber is established by measuring the resistance change in the TES. The resulting current change is read out by a Superconducting Quantum Interference Device (SQUID), which acts as a current amplifier.

The XMS detector consists of the following components;

- An array of absorbers read out by TESs. The array has an inner section with a resolution of 2.5eV and an outer section capable of 10eV resolution. Four outer array pixels are connected to one TES and this is known as a super pixel.
- Multiplex electronics for the read-out
- The anticoincidence detector mounted underneath the detector
- A set of Helmholtz coils to control the magnetic field in the detectors

The XMS requirements are summarised in Table A1.4. A possible XMS camera design is also shown in Figure A1.6. This is the concept proposed by SRON, the Netherlands Centre for Space Research, and is based on frequency domain multiplexing.

It should be noted that the XMS instrument uses a microchannel plate in its optical chain to diffuse the incoming X-rays to a manageable level when observing bright sources, preventing signal pile-up in the TES. Microchannel plate optics, their applications to astronomy and planetary science instruments, and the research conducted by the author in this technology are discussed in more detail in Annex 2 of this thesis.

An additional option which is currently under investigation for the XMS instrument is the inclusion of dichroic filters for the purpose of measuring X-ray polarization [Martin, 2010].

Dichroism is an effect in optics where a material absorbs photons of different polarization by different amounts. This method of X-ray polarimetry is currently under investigation by A. Martindale and N. Bannister in the Space Research Centre of the University of Leicester [Martindale et al, 2009].

Parameter	Requirement	Comment
Inner array		
Energy range	0.3-10 keV	Goal: 0.1-12 keV
Energy resolution (E<6keV)	2.5 eV	
Field of view	2 arcmin	Corresponds to 40x40 pixels
Pixel size	300 µm	Pixel size is a compromise between FoV and undersampling the PSF (500µm)
Outer array		
Energy range	0.3-10keV	Goal: 0.1-12 keV
Energy resolution (E<6keV)	10 eV	15eV may be more realistic for the FoV
Field of view	5.4 arcmin	Corresponds to 31.2 x 31.2 mm^2
Pixel size	600 µm	4 pixels per TES
Full array		
Time resolution	10 µs	
Max count rate input on instrument	120000 counts/s	Based on observing the Crab
Typical count rate	500 counts/s	Typical observation, 4mCrab
QE at 1keV	>60%	
QE at 7keV	>80%	Defines absorber thickness
Detector dead area	<5%	
Non-X-ray background	$2x10^{-2}$ counts/cm^2/keV/s	4 times background measured by Suzaku. Needs an Anti-Coincidence Shield.

Table A1.4 Summary of the XMS detector requirements from the IXO PDD [IXO Payload Definition Document, 2009]

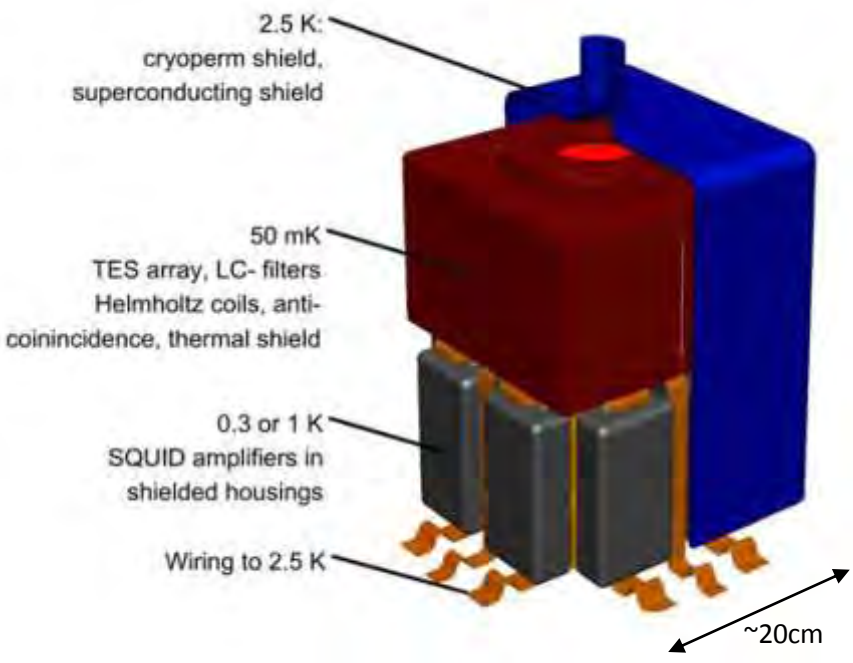

Figure A1.6 A possible XMS detector head design based on the SRON (Netherlands Institute for Space Research) configuration, taken from the IXO PDD [IXO Payload Definition Document, 2009]

X-ray dichroism occurs in some materials as a result of the material's X-ray absorption coefficient within a few tens of eV of an absorption edge, known as the X-ray absorption fine structure (XAFS) [Owens et al, 1997]. The highly ordered materials which make up the proposed Leicester University X-ray dichroic filters have an XAFS polarization dependence. The main advantage of using such filters to perform polarization measurements compared to, for example, the X-ray Polarization Instrument (XPOL) on IXO, is that a filter can be used in conjunction with another instrument such as the XMS rather than requiring a dedicated separate instrument with all the associated demands on spacecraft resources such as mass, power and volume.

A1.3.4 THE HIGH TIME RESOLUTION SPECTROMETER (HTRS)

The purpose of the High Time Resolution Spectrometer (HTRS) is to give IXO the ability to observe very bright galactic X-ray sources, such as X-ray binaries and magnetars, which can generate up to 1 million counts per second (~5 Crab). As such, the device must be capable of working at a very high count rate of up to >1MHz; the current instrument requirement [IXO Payload Definition Document, 2009] is 2MHz read out. Also, the instrument must provide spectroscopy with a very high time resolution of 10μs, with a resolving power E/ΔE of 5 to 50 in the energy band of 0.5 to 10keV. The HTRS will provide better than 200eV resolution at 6keV. The detector best suited to meet these requirements is an array of silicon drift diodes (SDD) [Lechner et al, 2004].

A hexagonal array of 37 SDDs will make up the focal plane detector of the HTRS. Figure A1.7 shows a schematic diagram of a single SDD pixel and the layout of the HTRS hexagonal-packed array. To limit the amount of dead time and X-ray pile-up in the detector, the HTRS will be placed slightly out of focus, such that the PSF is spread over a number of SDDs. The number in each hexagonal pixel in Figure A1.7 represents the percentage of 1keV X-rays hitting the pixel from the PSF. The PSF is not even across the device while it is out of focus, as is seen by the variation of these percentages from pixel to pixel. The percentages were calculated assuming the device is 12cm out of focus, with a telescope focal length of 20m [IXO Payload Definition Document, 2009]. As the primary function of this detector is spectroscopy rather than imaging, the unfocussed image on the HTRS is not important. Table A1.5 and Table A1.6 summarise the HTRS requirements and baseline detector characteristics, respectively.

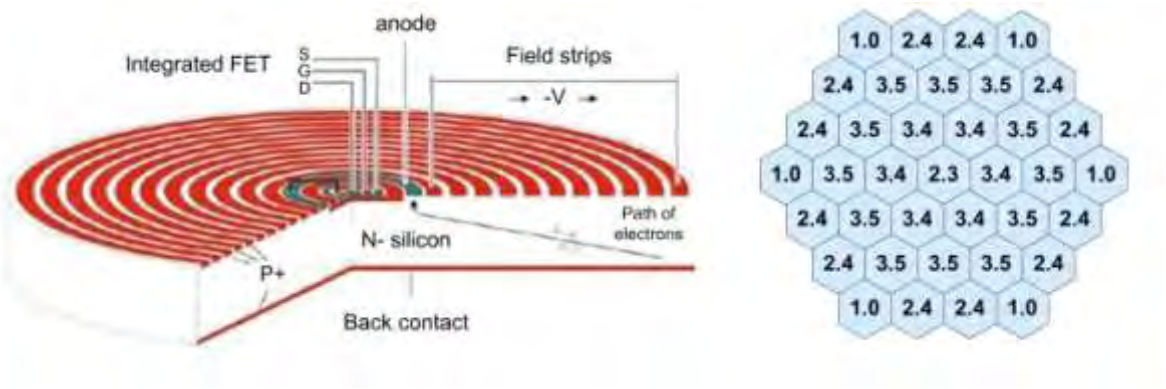

Figure A1.7 Left: A diagram of a single Silicon Drift Diode (SDD) X-ray spectrometer. S, G and D refer to the source, gate and drain terminals of the Field Effect Transistor used to read out the charge generated in the silicon bulk. Right: the HTRS array consisting of 37 hexagonal SDDs, showing the percentage of 1keV X-rays from the PSF hitting each SSD pixel (calculated by ESA) [IXO Payload Definition Document, 2009]

Maximum Count Rate	2 Mcounts/s (~10 Crab)
Energy Range	0.3 – 10keV
Time Resolution	10μs
Energy Resolution	<200 eV @ 6keV (150eV goal)
Deadtime @ 1 Crab	<1%
Pile-up @ 1 Crab	<1%
Data rate @ 1 Crab (full resolution)	~6.6 Mbits/s

Table A1.5 Table summarising the HTRS requirements

Detector type	37 silicon drift diodes
Diode dimension	Hexagon of 4 mm
Diode thickness	450 microns of silicon
Diode sensitive area	13.9 mm^2
Total sensitive area	5.13 cm^2
Detector dimensions	28.7 mm x 21.9 mm
Operating temperature	-20°C
Cooler	Radiator
Bias voltage	150V

Table A1.6 Summary of the current HTRS baseline detector characteristics

A1.3.5 THE X-RAY POLARIMETER (XPOL)

The X-ray Polarimeter (XPOL) is a Micropattern Gas Detector [Bellazzini et al, 2003] providing polarization measurements with angular measurement (5 arcseconds), spectral measurements (E/ΔE of ~5 @ 6keV) and timing resolution in the order of 5 μs. The detector is sensitive to X-rays in the range of 2-10keV.

XPOL is a polarimeter which uses the photoelectric effect to determine the polarization of incident X-rays. The photoelectric effect is very sensitive to polarization [Bellazini and Spandre, 2005]: the differential cross section for linearly polarized photons has a maximum in the plane orthogonal to the direction of the incoming photon and varies with the polar angle ϑ and the azimuth angle φ. Photoelectrons are therefore preferentially emitted in the plane orthogonal to the incident X-ray photon direction and have a $cos^2\varphi$ modulation around the direction of the Electric Field, or Polarization vector.

This method of determining the polarization of an incident X-ray is much more efficient, with nearly two orders of magnitude improvement of sensitivity on more traditional X-ray polarization detectors which use Bragg diffraction at 45° or Compton scattering around 90° [Latronico, 2004].

The information on the degree and angle of polarization of the incoming X-rays can be determined by reconstructing the photoelectron tracks projected onto the finely segmented collection plane of the Gas Pixel Detector. Figure A1.8 shows this schematically: the angular distribution of the ejected photoelectrons as projected onto the detector plane (XY).

Polarization measurements are made with XPOL by reconstructing the track of photoelectrons within the gas and by determining the ejection direction of the primary photoelectron. Figure A1.9 shows the principle of operation of a Micropattern Gas Detector such as XPOL [Bellazzini et al, 2006].

The IXO PDD [IXO Payload Definition Document, 2009] outlines the XPOL detector requirements. These are summarised in Table A1.7. The expected XPOL quantum efficiency at different X-ray energies is shown in Figure A1.10. The detector will be most efficient at ~2.5 keV. The low QE below 2 keV is due to a 50µm Beryllium entrance window used in the XPOL instrument. The QE of the gas drops dramatically after 3keV.

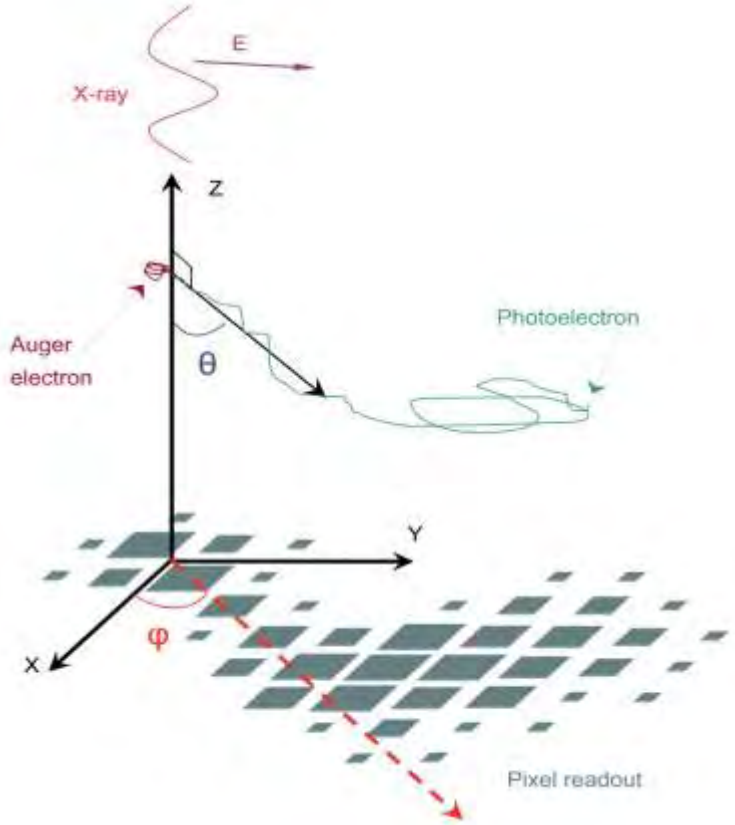

Figure A1.8 Angular distribution on the detector plane (XY) of the ejected photoelectrons [Attie, 2009]

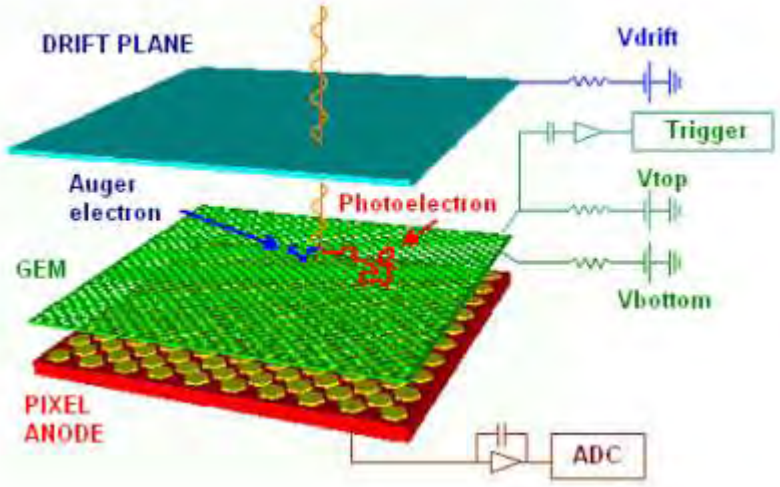

Figure A1.9 Diagram showing a Micropattern Gas Detector. The read-out plane is grounded while both sides of the Gas Electron Multiplier (GEM) and the drift plane are at increasingly negative high voltage.

Polarization sensitivity	1 % MDP (3σ) for a 1mCrab source
Detector size	15 x 15 mm^2
Energy range	2 – 10 keV
Energy resolution	20% at 6 keV
Angular resolution	7''
Pixel size	50 µm
FOV	2.6 x 2.6 arcmin square
Timing resolution	5 µs
Efficiency	See Figure A1.10
Polarization angle resolution	~1 degree

Table A1.7 The summary of XPOL Instrument Requirements as given in the IXO PDD [IXO Payload Definition Document, 2009]

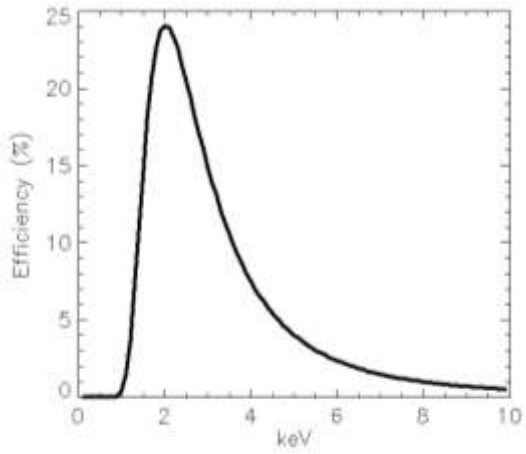

Figure A1.10 The modelled quantum efficiency of the XPOL detector [IXO Payload Definition Document, 2009]

The XPOL Micropattern Gas Chamber has a fully pixellated multi-anode readout. An X-ray photon enters the detector through a thin entrance window and then enters a detection/drift gap where it is absorbed in a Helium-Dimethylether gas mixture. On absorption, a primary photoelectron is ejected which then produces an electron-ion track. The electrons and ions are separated by the applied electric field, and the electrons drift towards the Gas Electron Multiplier (GEM), a thin 50µm insulating foil which is metalized on each side and etched with a regular pattern of 60µm diameter holes.

The track charge is amplified by the GEM, although the shape of the track is unmodified. The amplified charge is then collected by read-out pixels on a CMOS analogue chip which is a matrix of 105,600 hexagonal pixels with a 50 µm pitch. The image of the track is analysed to reconstruct the point of impact of the X-ray, as well as the direction of the primary photoelectron. Despite the large number of pixels, only sub-frames of 400 to 600 pixels which

completely include the electron-ion track are extracted in real time at each event. Figure A1.11 shows a photoelectron track image taken with a Micropattern Gas Detector, showing how the direction of emission is derived. The larger the hexagonal pixel in the image, the more charge collected in that pixel.

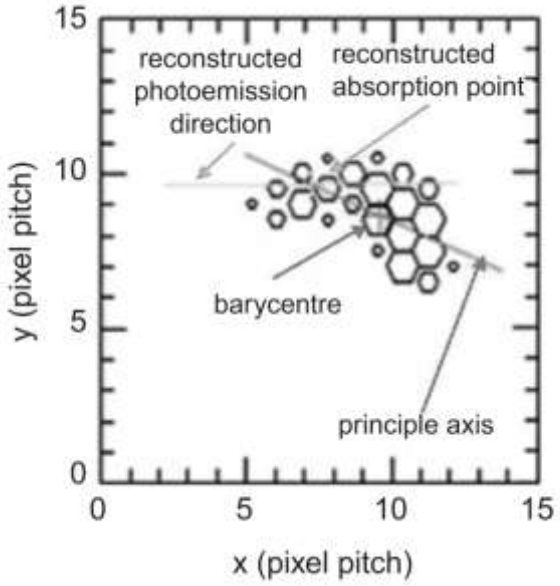

Figure A1.11 Real photoelectron track, as published by Bellazzini et al, 2003. Reconstruction of the photoemission direction is done with identification of the absorption point and the removal of the final part of the track.

A1.3.6 THE X-RAY GRATING SPECTROMETER (XGS)

There are currently two candidate instruments for the IXO X-ray Grating Spectrometer (XGS); a Critical Angle Transmission Grating Spectrometer (CAT-GS) and the Off Plane Grating Spectrometer (OP-GS). The current IXO baseline assumes CAT-GS as the instrument. The CAT-GS will be used to conduct high resolution spectroscopy (~5eV in the 0.3 – 1.0 keV region for the complete duration of the missions, as the XGS instrument is not mounted and moved in and out of the main focus at the focal plane but is in use at all times during observations, mounted at the first order position of diffraction from the X-ray grating. Figure A1.12 shows the difference between a transmission grating, like the one used in the CAT-GS and an off-plane grating like the one used in OP-XGS.

It is desirable that the X-ray gratings mounted behind the main IXO mirrors can also be removed from the X-ray path for observations requiring the maximum number of photons at the primary focal plane instrument. This requires an additional mechanism at the grating.

Table A1.8 summarises the key features of the CAT-GS.

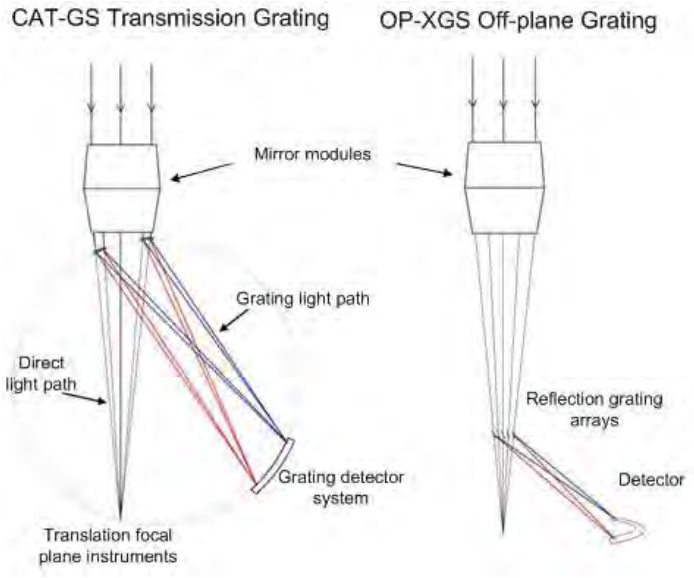

Figure A1.12 Schematic diagrams showing the CAT-GS and OP-XGS candidates for the IXO XGS Instrument [IXO Payload Definition Document, 2009]

Initially, the CCD was a contender for the focal plane detector on the IXO WFI detector [Holland, 2003]. The current WFI baseline is to use the DEPFET detector [Holland et al, 2003], however. The XGS instrument, however, does use a number of CCDs in the instrument focal plane. Figure A1.13 shows a diagram of the CAT-GS focal plane assembly. The CAT-GS has 32 CCDs in a line configuration. The instrument baseline uses the Massachusetts Institute of Technology (MIT) CCID41 device, each with 1024 x 1024 pixels, each pixel 24µm x 24 µm in size. The total focal plane assembly is ~45cm long and sits at the 1st order diffraction position of the XGS gratings, away from the main IXO focal position of the X-ray mirror assembly.

CAT-GS Key Features	Description
Mass	The gratings are very lightweight, being only a few microns thick.
Alignment	Alignment of the grating is in the order of a few arcminutes due to the insensitivity of the optic alignment.
Diffraction Efficiency	Summed diffraction efficiency ~50% which leads to a high effective area (~50% of the geometrical area of the optic).
Spectral Resolution	Due to the blazing of the grating optics, shorter wavelengths also contribute to higher orders of diffraction, leading to higher spectral resolution.
Transparency and synergy with other instruments	The very thin X-ray gratings become transparent at higher energies, allowing simultaneous observations with XGS and other focal plane instruments, most of which have a good energy response between 1 and 5 keV.
Polarization and modelling	Negligible polarization sensitivity. The behaviour of the gratings is well understood and can be modelled in a straight-forward manner.

Table A1.8 Summary of key features of the CAT-GS Instrument

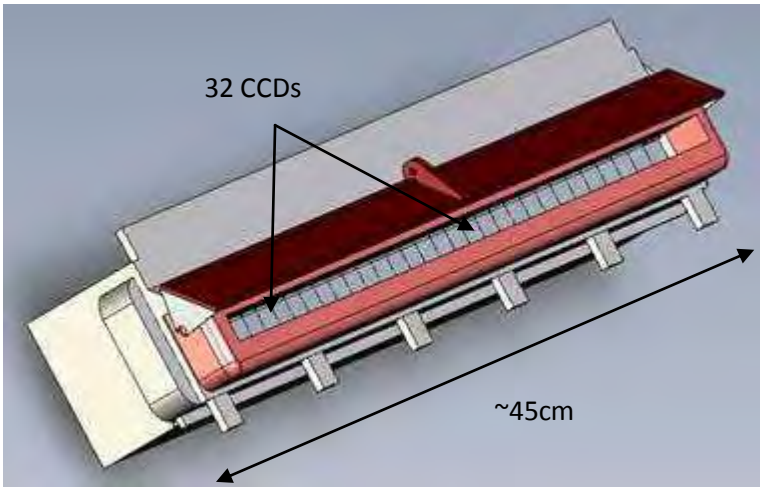

Figure A1.13 The CAT-GS focal plane assembly [IXO Payload Definition Document, 2009]

UK CCDs provided by e2v are currently the baseline CCDs for the Off-Plane X-ray Grating Spectrometer option for this instrument [Holland, 2010] and may well incorporate elements from the CCD66 discussed in Chapter 4.

A1.3 THE IXO MIRRORS

There are two technologies currently being considered for the IXO mirrors; the European Silicon Pore Optics (SPO) [Beijersbergen et al, 2004][Gunther et al, 2006][Ackermann et al, 2009]and the American Slumped Glass Optics (SGO) [Zhang et al, 2009][Reid, 2009]. The IXO mirror technology finally chosen must achieve the requirements shown in Table A1.9.

Requirement	Value
Effective area @1.25keV	≥2.5m^2*
@6keV	≥0.65m^2 (goal, ≥1m^2)
@30keV	≥150cm^2 (goal, ≥350cm^2)
FWHM Angular Resolution	≤5 arcsec (goal, ≤2 arcsec)
Focal Length	20m (goal, 25m)
Field of View	18’

Table A1.9 A summary of the IXO Mirror Requirements.
****The low energy effective area requirement was revised down to 2.5m^2 from 3m^2 in response to findings from the IXO Assessment Study.***

A1.3.1 SILICON PORE OPTICS

Silicon Pore Optics are a new European development in X-ray optics making use of 'cheap and off-the-shelf' (COTS) high-grade silicon wafers produced by the electronic and computer industries. Commercially available Silicon wafers are near perfect, mechanically, and have a much lower density than the nickel shells used in X-ray optics for XMM Newton ($2.3 gcm^{-3}$ instead of $8.9 gcm^{-3}$), resulting in a much lighter mirror assembly for a given effective area. Figure A1.14 summarises the construction of the SPO structure using these wafers.

The mirror modules consist of two blocks of SPOs slumped to a Wolter I conic approximation, (parabolic and hyperbolic slump radii) and mounted back to back as shown in Figure A1.15. These are then mounted into a petal frame, a number of which (yet to be decided) will make up the IXO mirror module (Figure A1.16).

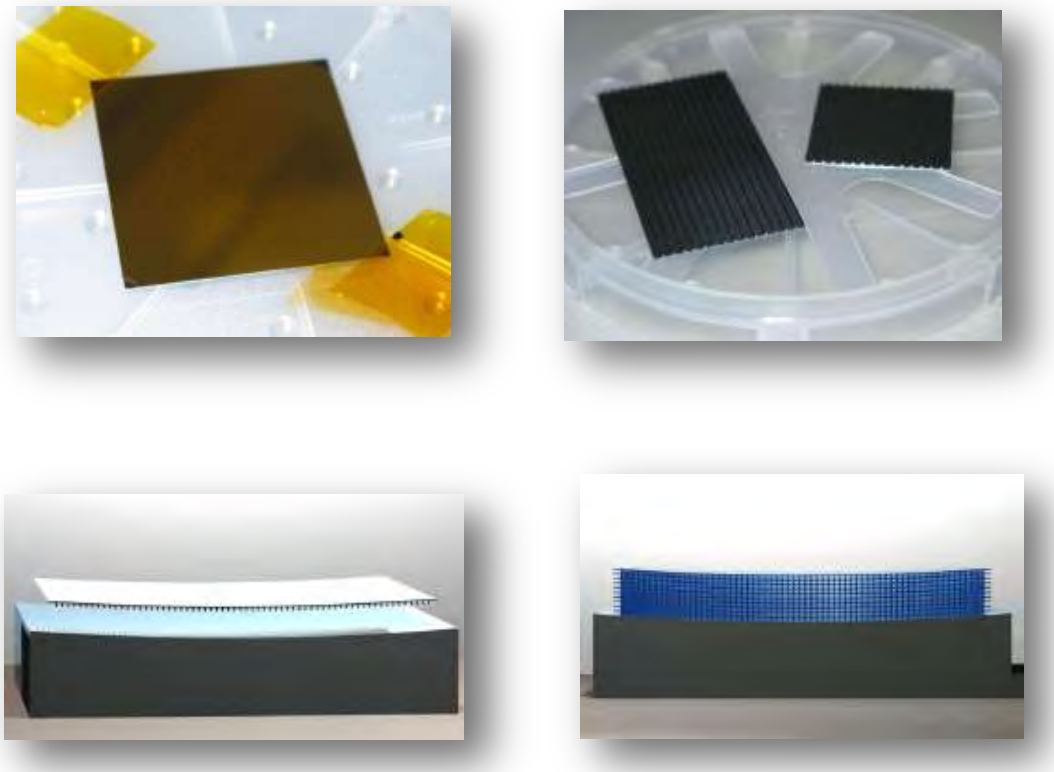

Figure A1.14 The Assembly of a Silicon Pore Optic Mirror Module. (Top left) The process begins with a high-grade, polished silicon wafer. (Top right) The wafers are etched with ribs along the wafer length, creating a series of regular channels. (Bottom left) The ribbed wafer is placed on a precision machined mandrel, slumped to the desired radius for the mirror module. (Bottom right) The process is repeated, stacking ribbed wafers on top of each other with the slump radius maintained, as required, for the correct optic geometry. [Bavdaz et al, 2009]

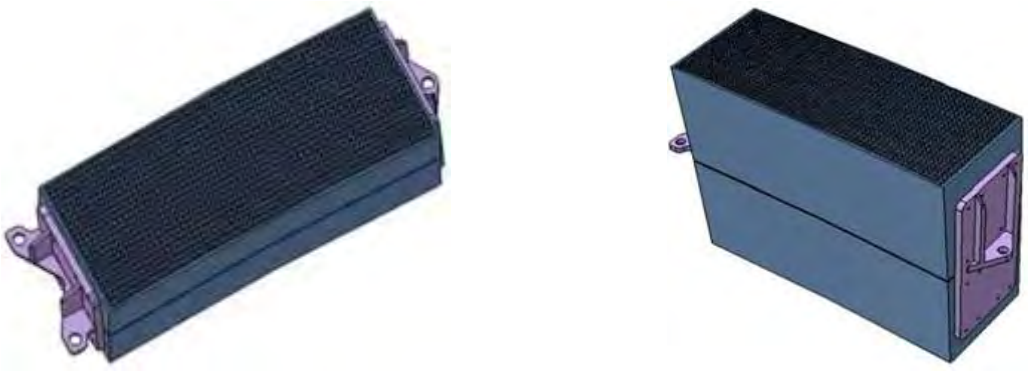

Figure A1.15 X-ray high-precision pore optics mirror section (in two views) consisting of two mirror stacks connected by two brackets. Close inspection of the black top face of the section reveals the apertures of the individual pores. [IXO CDF Study Report, 2009]

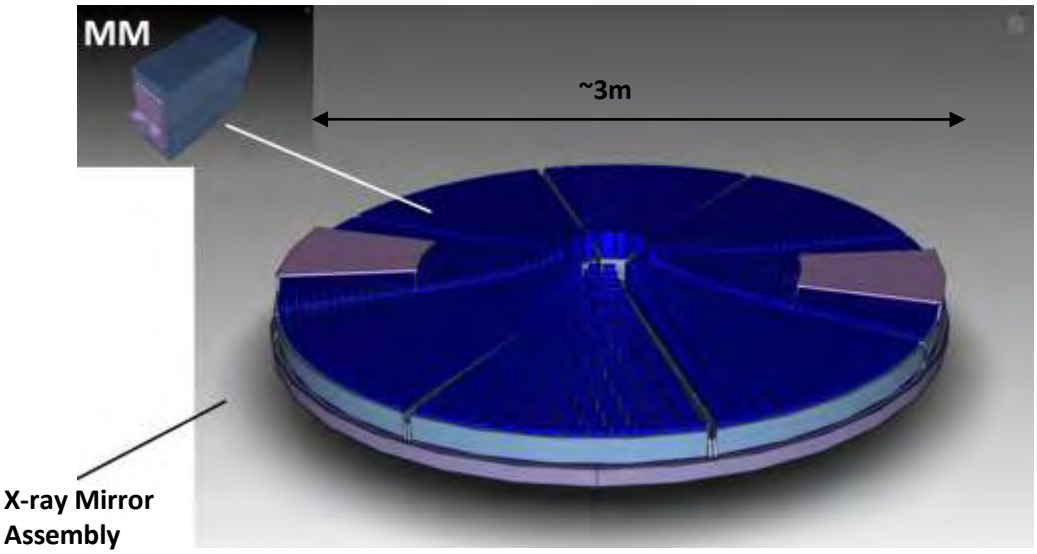

Figure A1.16 (Top Left) An IXO Mirror Module constructed from silicon pore optics and (Above) an 8-petal configuration including the X-ray grating segments, together making the IXO X-ray Mirror Assembly [IXO CDF Report, 2009]

A1.3.2 SLUMPED GLASS OPTICS (SGO)

Slumped Glass Optics (SGO) technology has been investigated extensively in the USA in preparation for the Constellation-X mission[1] and now also for IXO. Research into this technology has also been pursued in Italy, with the European Space Agency currently developing this optics technology in parallel with the Silicon Pore Optics. Similar in principle to the slumped nickel shells used for XMM Newton [Aschenbach, 2000] spacecraft and the ceramic glass optics of Chandra [Zhao, 2004], concentric shells of coated glass are nested in the Wolter I configuration. Unlike both Chandra and XMM Newton, however, the circular

[1] Constellation-X was a NASA X-ray telescope mission concept which was merged in May 2008 with the ESA XEUS telescope to create the International X-ray Observatory. Constellation-X differed from XEUS in that it used an extendable optical bench rather than formation flying. The mission had less emphasis on hard X-ray imaging and spectroscopy in its science goals when compared to the XEUS mission.

shells are constructed in segments, similar to the SPO technology, rather than as monolithic shells.

The first stage of the process is the slumping of the glass over a precision mandrel by heating a glass sheet, which then assumes the slump radius and, importantly, the surface smoothness of the mandrel. Once slumped, the glass section is cut to size and then coated with a layer of reflective material such as Iridium or a multilayer coating consisting of Iridium/Carbon bi-layers, designed to increase X-ray reflectivity. Such bi-layers achieve an increase in reflectivity due to X-rays scattering at the refractive index boundaries and interfering constructively (Tripp 2005). Figure A1.17 shows a schematic diagram demonstrating this principle. The coating is composed of two materials, α and β with two different reflective indices. D is the bi-layer thickness, calculated by summing the thickness of an α and β layer. The angle of reflection, 2ϑ, is calculated using Bragg's lay: $n\lambda=2D\sin\vartheta$: λ is the wavelength of the incoming photon.

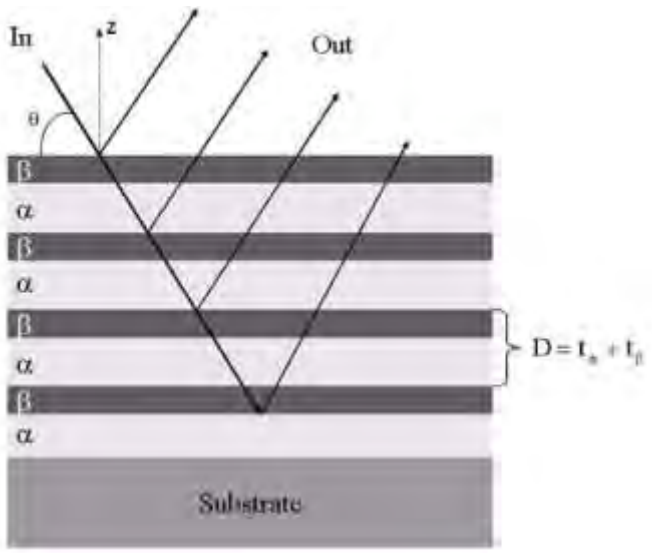

Figure A1.17 Schematic diagram demonstrating the principle of bi-layer X-ray coatings (Tripp et al, 2005)

The coated mirror sections are then mounted and bonded into mirror segments and combined to make the IXO Mirror Module. Figure A1.18 shows one of the NASA Mirror Module concepts for the IXO mission.

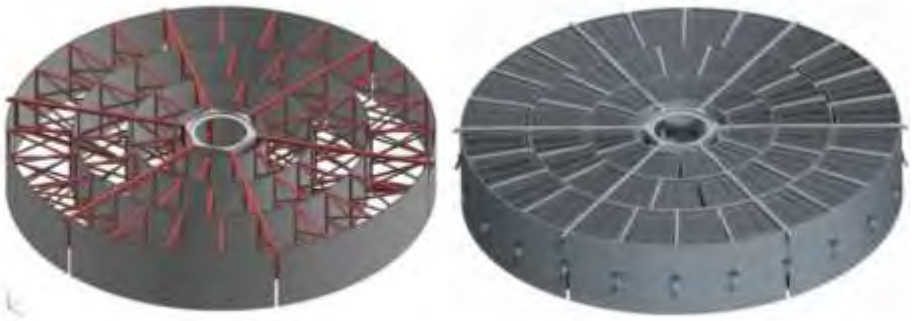

Figure A1.18 (Left) The frame of one of the NASA IXO Mirror Module concepts and (Right) the complete NASA mirror concept mounted with the slumped glass mirror segments (IXO Payload Definition Document, 2009).

ANNEX 2

MICROCHANNEL PLATE OPTICS FOR X-RAY FOCUSING

A2.1. MICROCHANNEL PLATE OPTICS – BACKGROUND AND APPLICATIONS

Microchannel plate (MCP) optics are compact, lightweight optics capable of focusing soft X-rays, ideal for space applications requiring good angular resolution imaging (<8 arcminutes FWHM) over a large field of view [Fraser et al, 2010][Willingale et al, 1998].

This annex summarises some of the space applications of Microchannel Plate Optics to soft X-ray focusing and also documents the MCP laboratory work conducted as part of this PhD. The angular resolution of a flat square-pore, square packed MCP optic was measured and the results presented in this annex demonstrate the best measured resolution of such an MCP optic to date: <2 arcminutes FWHM.

The use of an MCP optic in a laboratory radiation damage campaign is also discussed. The XMM-Newton Life Test used an MCP optic to concentrate soft X-rays onto a CCD in an attempt to reproduce the localized ionizing damage experienced by the XMM-Newton EPIC camera over a period of ~7 years. The results of this campaign are presented and future work is discussed.

Many papers and theses outline the theory and manufacturing process of MCP optics [Price, 2001][Martindale, 2008][Chapman, Nugent and Wilkins, 1991], available in both square-pore, square-packed [Fraser, 1993] and radially packed configurations, the latter capable of being used in a Wolter I geometry for imaging [Price, 2002]. This section introduces some of the current, and future, terrestrial and space applications of MCP optics.

A2.1.1. SPACE APPLICATIONS OF MCP OPTICS

This section of the thesis outlines some of the suggested space applications for Microchannel Plate Optics. Such optics have been subject of an extensive development programme at the University of Leicester in conjunction with the manufacturer of the optics, Photonis S.A.S, Brive, France.

A2.1.1.1. THE WIDE FIELD TELESCOPE

The Wide Field Telescope concept proposes the use of slumped square-pore, square-packed MCP optics to collimate X-rays from a very large portion of sky onto a detector. This type of telescope has been proposed for a satellite-based mission [Priedhorsky et al, 1996] and an instrument based on the International Space Station (ISS) [Fraser et al, 2002]. The ISS-mounted instrument, for example, would be able to view the entire X-ray sky once every 90 minutes, due to the large (~162°x22.5°) field of view of the microchannel plate instrument. The Wide Field Telescope has the capability to produce a survey of the X-ray sky equivalent to the total ROSAT sky survey once per week [Priedhorsky et al, 1996] and, over the course of the whole 3-year mission, establish an unsurpassed catalogue of X-ray sources with the ability to monitor photometric changes on timescales of ~1 second in sources bright enough to be seen by ROSAT. Martindale (2008a) discusses the science of the Wide Field Telescope in more detail.

A2.1.1.2 THE MAGNETOSHEATH EXPLORER IN X-RAYS, MAGEX

Steve Sembay from the University of Leicester is leading a NASA-funded feasibility study of a moon-based X-ray telescope called MagEX, the Magnetosheath Explorer in X-rays [Sembay, 2007]. The telescope will be pointed towards Earth, detecting X-rays emitted from the magnetosheath from the interaction between it and the solar wind. MagEX will be able to view the entire magnetosheath, very different to current methods of investigating this important region of space, where satellites take in-situ particle measurements in very localised regions [Lester, 2007]. The concept uses an MCP telescope, such as that shown in section A2.1.1.3, which would be installed on the Moon by astronauts. There are large benefits of placing such a telescope on the Moon rather than in orbit. Firstly, the telescope will have very good pointing stability, sitting on the Moon's surface rather than in an orbit. No propellant will be required to maintain its attitude and orientation which limits the lifetime of orbiting satellites. Also, the moon maintains a distance from Earth ideal for viewing the complete magnetosheath. The observations will be made during the 14-day lunar night, which can also be used to passively maintain the very cold temperatures (-100°C to -120°C) required by the CCD detectors used by MagEX. Heaters will need to be used for the electronics which will require warmer temperatures. The key parameters of the MagEX telescope are shown in Table A2.1.

Telescope Parameter	Parameter Value
Mass	<40kg
Field of View	30° x 30°
PSF Size	1.5 arcminutes
Energy Resolution	~50eV FWHM @600eV

Table A2.1 Summary of the MagEX Telescope Key Parameters [Sembay, 2007]

A2.1.1.3 THE BEPICOLOMBO MERCURY IMAGING X-RAY SPECTROMETER, MIXS

The Mercury Imaging X-ray Spectrometer (MIXS) [Fraser, 2010] is the UK-led payload onboard the Mercury Polar Orbiter, one of two spacecraft going to Mercury as part of the joint ESA-JAXA Cornerstone mission, BepiColombo. The mission and science case is discussed in detail in [Fraser et al, 2010].

MIXS is comprised of two optical elements which utilize microchannel plate optics: MIXS-C, a collimator using slumped, square-pore, square-packed MCP optics: and MIXS-T, an imaging telescope using radial-packed, square-pore MCPs in a Wolter-I approximation. Both MCP channels concentrate X-rays to identical solid-state Depleted Field Effect Transistor (DEPFET) Active Pixel Sensors (APS) [Treis, 2009]. Chapter 2 has a more detailed discussion of the DEPFET APS detectors. Figure A2.1 shows the MIXS instruments as they will be mounted on the spacecraft. Figure A2.2 show the current engineering models for the MIXS telescopes.

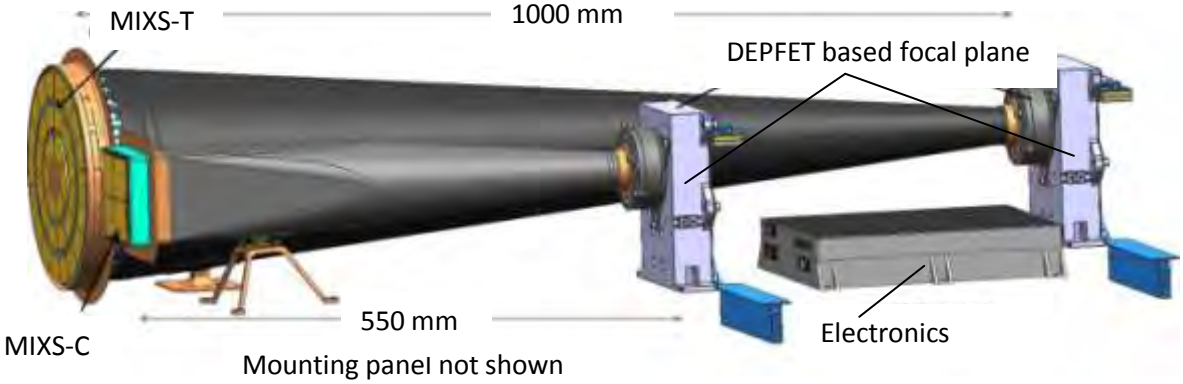

Figure A2.1 MIXS-C and MIXS-T as will be mounted on the spacecraft [Fraser et al, 2010]

Figure A2.2 Full Size Test Models of the BepiColombo MIXS-T (left) and MIXS-C (right) optic frames and telescope tubes. Image courtesy of Magna Parva.

THE MIXS COLLIMATOR, MIXS-C

Table A2.2 summarises the characteristics of the MIXS-C MCP optics [Fraser, 2010] and Figure A2.3 shows a computer aided design (CAD) model of MIXS-C. The DEPFET detector is positioned on the optical axis at the centre of curvature, 550mm from the MCP optic module.

Parameter	Value
Channel Diameter (D)	20 µm
Channel aspect ratio (L/D)	55:1
Format	Square-Pore Square-Packed
Open Area	60%
Slump radius (R_{MCP})	550 mm
Angular resolution	~2 arcminutes
Metallisation for enhanced reflectivity	Iridium Coating
Total field of View	10.4°
Effective Area (@ 1keV)	1.9cm^2
Length of Collimator	55cm

Table A2.2 Characteristics of the MIXS-C MCP Optics

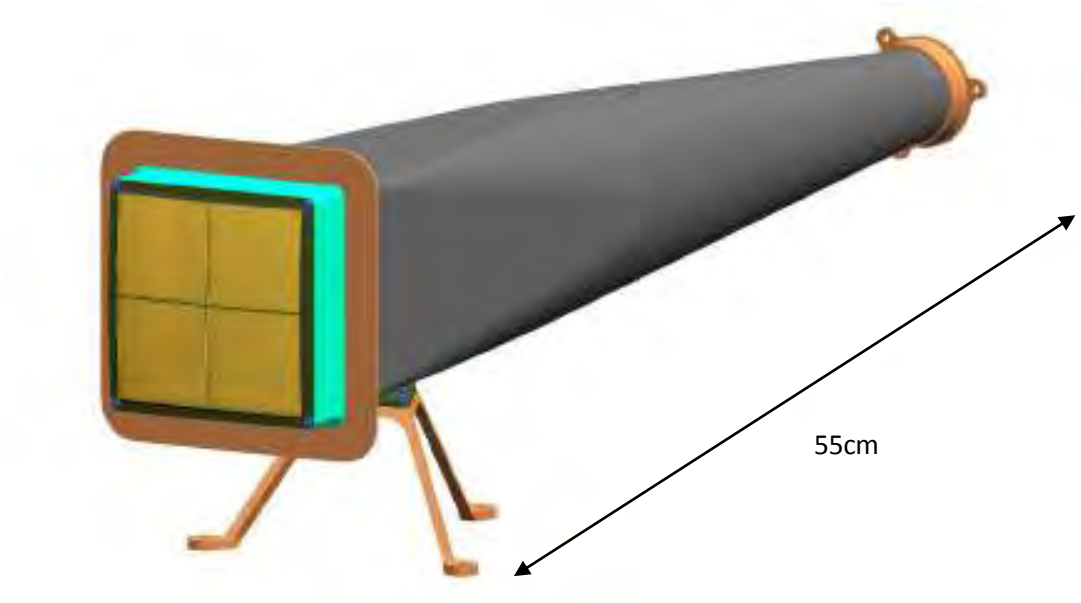

Figure A2.3 CAD Model of MIXS-C showing the four slumped MCP optics and telescope tube

The field of view of the collimator is given by the collimator diameter divided by the slump radius plus the acceptance angle of the channels. The acceptance angle is defined by the aspect ratio, L:d. Carpenter and Fraser (2007) investigated the performance of MIXS-C. Figure A2.4 shows their analysis of the collimator effective area and FOV.

The FOV is approximated as a top-hat function and has two components. The total FOV was determined to be 10° when reflected rays are neglected and 6.5° when considering just the core Field of View component.

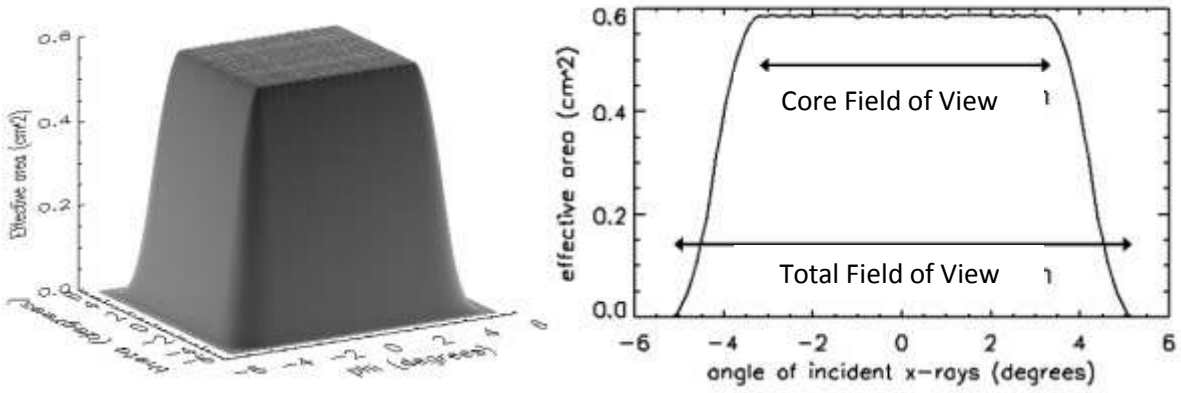

Figure A2.4 MIXS-C effective area as a function of off axis angle. The channel's FOV is 10° (Carpenter and Fraser, 2007)

It was also shown that coating the channel walls with Iridium would improve the soft X-ray reflectivity of the MCP optics, resulting in an improved effective area when compared to bare glass. The grasp, defined as a product of a telescope's field of view and effective area, as modelled by Carpenter and Fraser 2007, is shown in Figure A2.5 as a function of energy.

The calculated grasp for MIXS-C includes the energy dependent quantum efficiency of the DEPFET APS, absorption of the aluminium thermal and optical filters and the reflectivity of the MCP optics. The energy dependent grasp of the optics was determined by Monte-Carlo ray-tracing using the model of Price et al (2001). Grasp, which is the product of telescope effective area and field of view, is a figure of merit often used to compare different telescope systems.

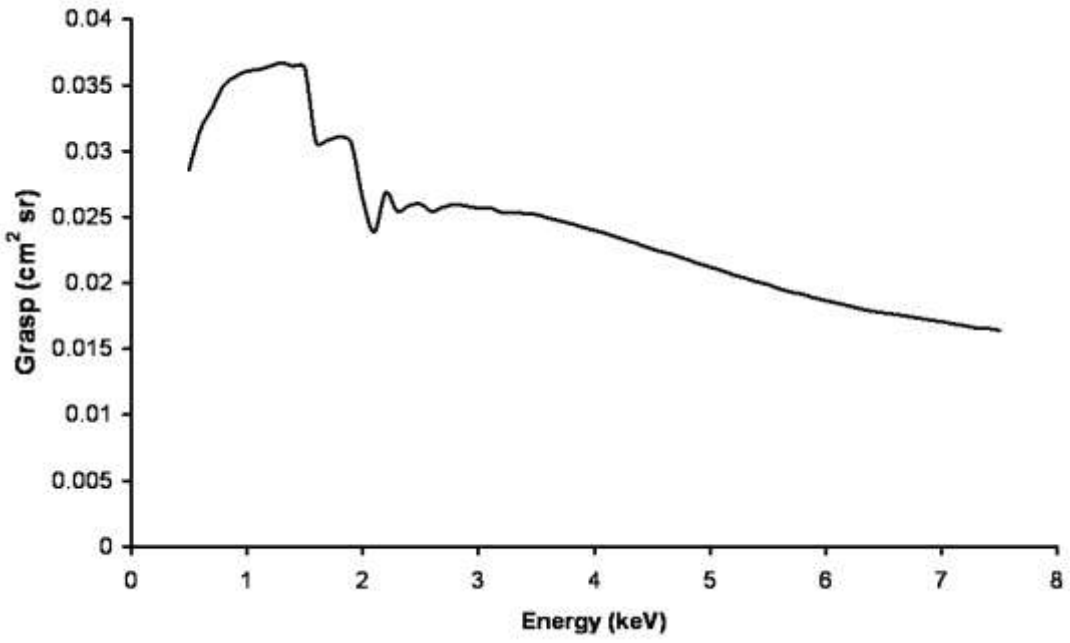

Figure A2.5 Grasp of MIXS-C as a function of energy, as derived by Carpenter and Fraser (2007)

Detailed performance analysis of the MIX-C instrument was conducted by J. Carpenter [Carpenter and Fraser, 2007] and established the expected spectra likely to be seen for various solar flare states (Figure A2.6). From Figure A2.6, MIXS-C will be able to provide good spectra for all but quiescent solar states. SIXS, the Solar Intensity and particle X-ray Spectrometer, another instrument onboard BepiColombo, will be used to provide vital information about the Solar X-rays hitting Mercury [Stankov, 2005]. SIXS will take broadband spectra measurements of solar X-rays (1 - 20keV), proton (0.5 – 30MeV) and electrons (0.1 - 3MeV) in order to establish the high energy photon and particle flux hitting Mercury's surface, resulting in fluorescent X-ray emission [Stankov, 2005]. This information is needed to analyse the data from MIXS-C and MIXS-T. The fluorescent X-ray yield is dependent on the solar proton spectrum so knowledge of this spectrum is required in order to interpret the measured X-ray fluorescence from orbit. The input solar radiation changes with solar activity in an

unpredictable way with time scales from seconds to years. The time resolution of the SIXS detector is 1 second, simultaneously observing both photons and particles [Stankov, 2005].

Carpenter (2007) determined that the MIXS-C instrument will be capable of establishing the surface concentrations of major surface elements at a spatial resolution sufficient to separate the major Hermean terrains [Carpenter and Fraser, 2007], and will therefore meet the science requirements of the mission [Carpenter et al, 2006].

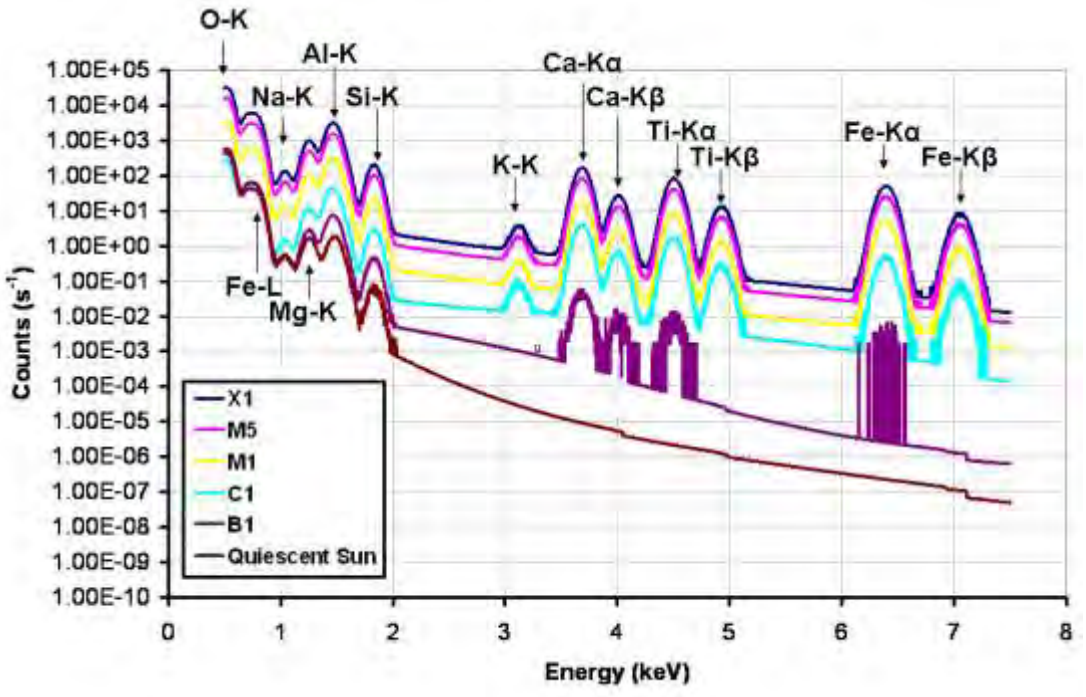

Figure A2.6 Modelled MIXS-C spectral response for different solar states from Carpenter 2007. A surface composition of lunar basalt was assumed for the surface of Mercury and a detector resolution of 100eV @ 1keV and 150eV @7keV,

THE MIXS TELESCOPE, MIXS-T

The MIXS Telescope, or MIXS-T, uses an MCP optic design which uses the Wolter I configuration to provide X-ray imaging capabilities. Due to the large area of the telescope aperture and the limitation of MCP area in the manufacturing process, the optic is made of a large number of tessellating segments. Figure A2.7 shows one such segment mounted on a test frame during adhesive testing conducted by Magna Parva, a Leicestershire-based engineering company providing the MIXS-T and MIXS-C telescope structure and optic frames [Martindale, Pearson and Evans, 2008]. In order to provide the double reflection needed in the Wolter I configuration [Price, 2002], two segments, called a tandem, are placed back-to-back, each slumped to the correct profile (R1 = 4m, R2 = 1.33m) to provide the Wolter I geometry.

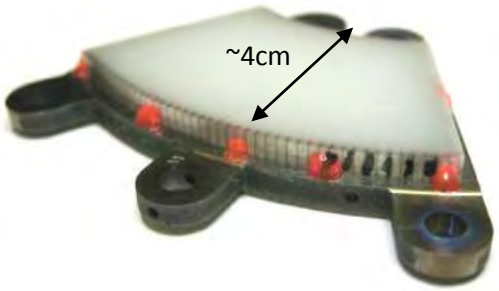

Figure A2.7 A MIXS-T MCP Optic segment mounted on a test frame during adhesive tests [Pearson, 2007].

Each of the MCP tandem pairs is mounted into a Sextant, consisting of one inner, two middle and three outer tandem pairs. Once secured in the Sextant frame, six Sextants are mounted together to form the complete MIXS-T optic. Figure A2.8 shows a Tandem, Sextant and the complete optic.

Figure A2.8 CAD Drawing of a MIXS-T tandem, a Sextant containing 6 tandem pairs and the final Wolter I optic consisting of 6 Sextants [Pearson, 2007].

The MIXS-T optic is mounted on the spacecraft with a telescope tube in order to ensure no stray light hits the DEPFET detector and also provides some structural support to the instrument. Figure A2.9 shows the complete Mirror Optic Module (MOM) with the telescope tube as it will be mounted on the spacecraft. The key characteristics of the MIXS-T MCP optics are shown in Table A2.3.

Parameter	Value
Channel Diameter (D)	20 µm
Channel aspect ratio (L/D)	Graded across the optic diameter
Format	Square-Pore Radially Packed
Open Area	60%
Angular resolution	<9 arcminutes
Metallisation for enhanced reflectivity	Iridium Coating
Total field of View	1.1°
Effective Area (@ 1keV)	~ 70cm^2
Focal Length	1m
Slump radius 1 (1st plate of tandem)	4.0m
Slump radius 2 (2nd plate of tandem)	1.33m

Table A2.3 Characteristics of the MIXS-T MCP Optics

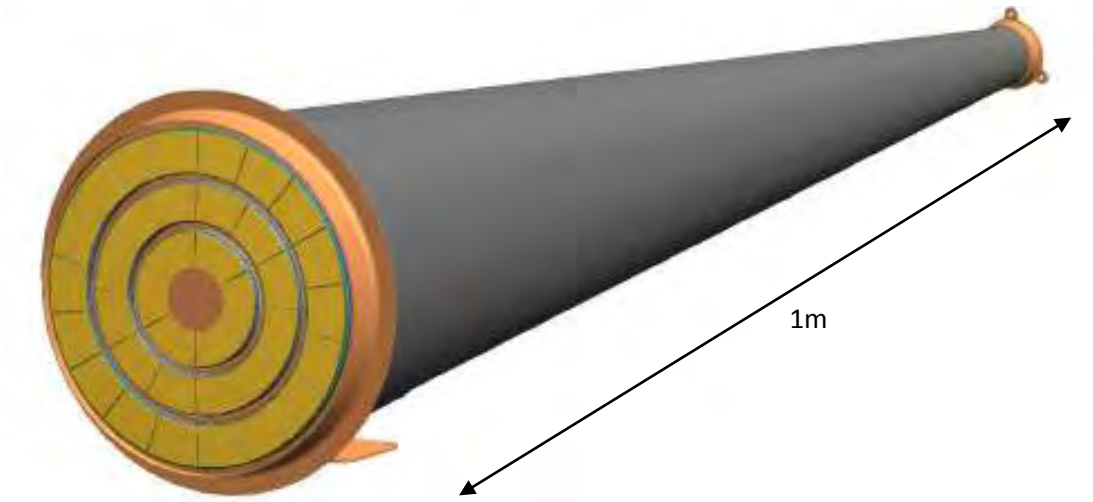

Figure A2.9 The MIXS-T Mirror Optic Module

A great deal of progress has been made in the characterisation of radial packed MCP optic sectors that will be used on MIXS-T, reported in Martindale, Pearson and Evans, 2008. Figure A2.10 shows an image collected using an inner MIXS-T sector in the Tunnel Test Facility (TTF) at the University of Leicester. The TTF is a long baseline (28m) X-ray beamline which has been modified to allow X-ray testing of the full MIXS-T MCP optic as well as individual X-ray plates and tandem pairs. The X-rays used in the TTF tests presented in Figure A2.10 have a bremsstrahlung X-ray spectrum peaking at 1 keV. The FWHM resolutions measured in the horizontal and vertical directions in Figure A2.10 are 8 arcmins and 1.2 arcmins respectively.

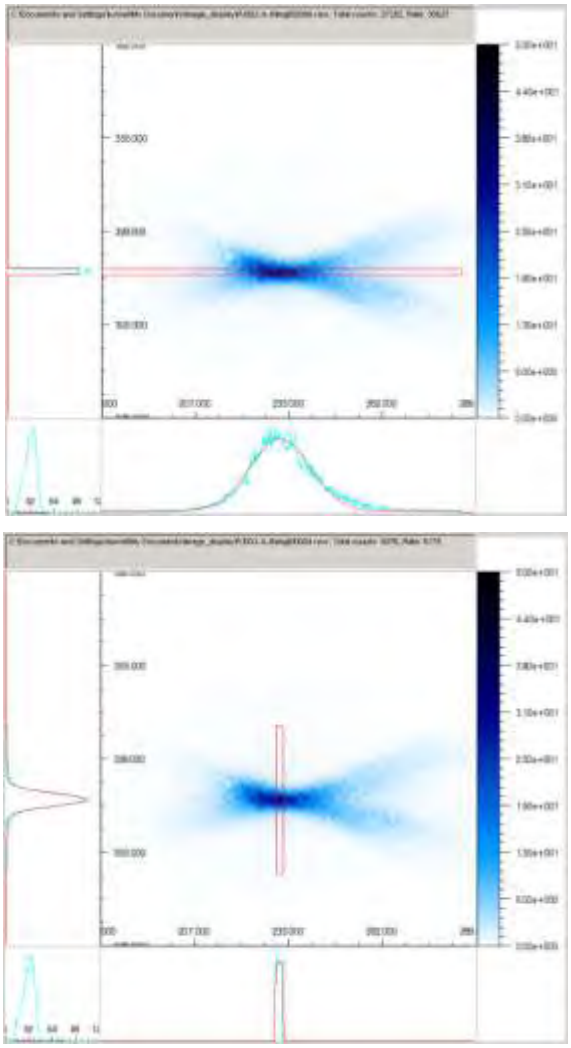

Figure A2.10 MIXS-T MCP Inner sector image taken in the Tunnel Test Facility by Martindale, 2008. Left image shows a horizontal cut through the point spread function and the right shows a vertical cut.

A key parameter of MIXS-T is the effective area of the optic. J. Pearson (2006) used the sequential ray tracing model (Willingale, 2004) to calculate the effective area of the complete MIXS-T optic. The on-axis effective area calculated is shown in Figure A2.11. The diameter of the optic is assumed to be 21cm, radially packed, with 22µm square channels with a 26µm pitch. An Iridium coating is also assumed, increasing the reflectivity at higher energies [Carpenter, 2008].

Using the effective area curve modelled by Pearson, Carpenter [Carpenter, 2007] calculated the expected performance of MIXS-T for differing solar flare events. A 1.1° field of view and a detector background equivalent to that seen on the EPIC MOS CCDs [Read, 2007] were assumed. Figure A2.12 shows the calculated spectral response of the MIXS-T optic [Carpenter, 2007] assuming a Lunar basalt composition and a detector resolution of 100eV @ 1keV.

Carpenter also showed that the detection and quantification of the major elements using MIXS-T, (Na, Mg, Al, Si and Fe), are fully compliant with the values specified in the BepiColombo Science Requirements Document [Carpenter, 2006].

Minor elements of interest, such as Ca and Ti, can be detected and quantified by summing the X-ray spectra over larger areas of the planet's surface. At periods of high X-ray flux, the full imaging capability of MIXS-T can be used, giving a best resolution of 2-4 arcminutes. The science requirement of the MIXS-T optic is ~9 arcminutes [Fraser, 2010]

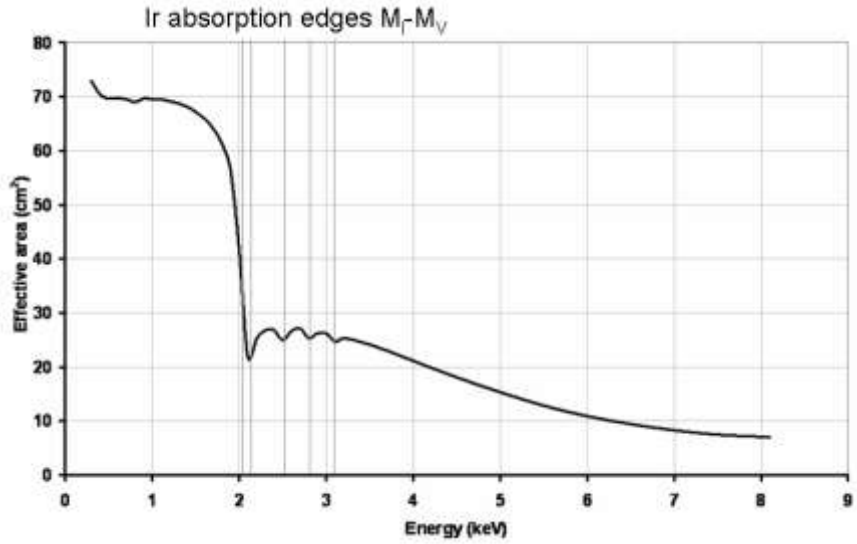

Figure A2.11 Modelled On-axis Effective Area of the MIXS-T optic [Pearson, 2006]

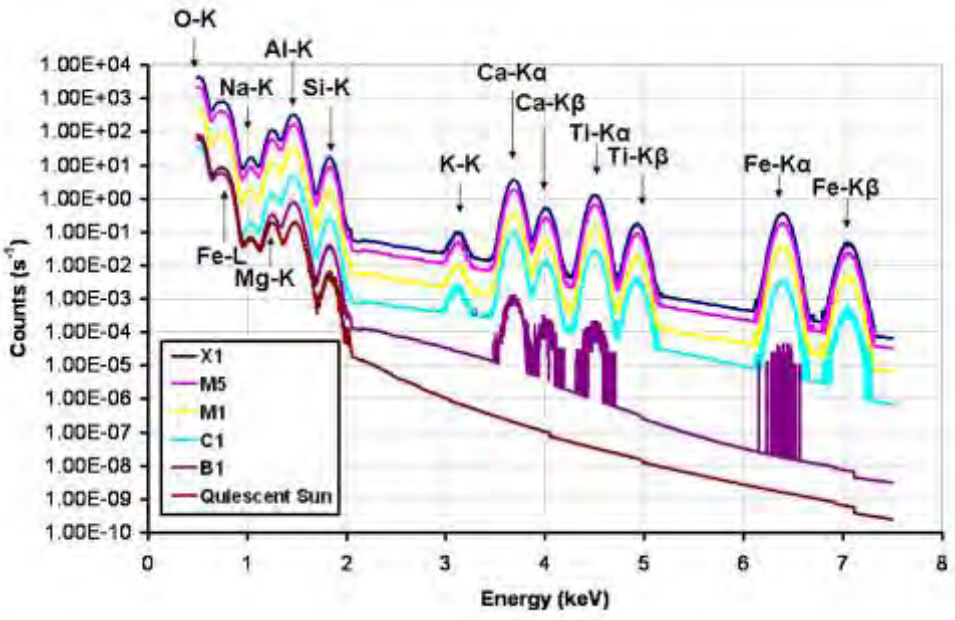

Figure A2.12 Modelled MIXS-T spectral response for different solar states from Carpenter 2007. A surface composition of lunar basalt was assumed for the surface of Mercury and a detector resolution of 100eV @ 1keV and 150eV @7keV,

A2.1.2. LABORATORY APPLICATIONS

The Microchannel Plate Optic can be used as a laboratory tool when focussed X-rays are required. One such example of this is the XMM-Newton Life Test experiment described in detail in Chapter 3. The purpose of the XMM-Newton Life Test was to expose a CCD to the ~7 years worth of ionising X-ray radiation experienced by XMM-Newton in orbit over the course of its mission. The XMM MOS CCDs have experienced unexpected levels of ionizing damage as a result of the unprecedented number of ionizing photons interacting with the devices over the course of the mission lifetime. Using an MCP optic to focus the X-rays allows a large dose to be accumulated in a small area much more quickly than if the device was to be irradiated in a small section (by shielding part of the device) with unfocussed X-rays.

The results of the XMM-Newton Life Test experiment show that an accumulation of charge in the CCD dielectric layer is likely to cause redistribution of low energy X-rays (<600 eV), broadening X-ray lines of interest from 200-600 eV with an exaggerated low-energy shoulder. Interestingly, the ionizing damage was shown to occur primarily in the open electrode structure of the CCD22 [Short, 2002]. The results of this experiment are currently being used by the multinational XMM EPIC Camera Calibration Group in order to establish a model of the low energy redistribution which has developed as a result of focussed X-rays on the focal plane detector.

The ability to move the MCP optic in and out of the X-ray beam without having to open up the test chamber, which is under vacuum, is useful. Being able to move the X-ray focal spot across the face of a detector to accumulate X-ray data in certain regions of interest is also a valuable function that can be implemented.

Flat, square-pore, square-packed MCP optics are also used in the imaging X-ray Fluorescence (IXRF) spectrometer [Martin et al, 2001][Su, in prep.][Price, 2001] experiment. The IXRF uses an MCP Optic to map the elemental composition of samples by measuring fluoresced X-rays that are focused onto a CCD using a MCP optic. [Price 2001] reports that spatial resolution better than 1mm is achieved, using the IXRF, when measuring the emitted X-rays as a function of position across the sample. The technique is much more time-efficient than other XRF methods, which requires rastering X-rays across the object of interest rather than illuminating the whole sample at once.

The laboratory experiments presented here are just a fraction of the possible terrestrial applications of MCP optics. Wherever the focusing of soft X-rays is required, and where size

and mass are a constraint, with a mass-per-unit effective area of ~25kg/m^2 @ 1keV, MCP optics could be of use.

A2.2. MICROCHANNEL PLATE CHARACTERISATION

One of the key drivers in developing MCP optic technology is the improvement of angular resolution. Manufacturing optics with excellent channel alignment and near-perfect channel smoothness is essential to achieving the best possible resolution. X-ray missions such as BepiColombo MIXS [Fraser, 2010] and the Lobster All-Sky Monitor [Fraser, 2002] require compound, slumped MCP optics with angular resolution requirements of at least ~9 arcminutes in order to achieve the mission science goals. Such optics would require the development of flat square-pore square-packed MCP optics with an angular resolution of ~2 arcminutes, a resolution that, until recently, had not been demonstrated in the laboratory. The MIXS angular resolution requirement for the complete telescope, taking into account misalignments between tandem pairs and sextants, is <9 arcminutes overall [Fraser, 2010]. This section presents the work undertaken as part of this thesis to characterise a square-pore square-packed Lobster MCP Optic, designated ME001-8. This characterisation activity resulted in the first image taken with an angular resolution <2 arcminutes, meeting the requirements of future space missions. All MCP images shown in this section were analysed and processed using the University of Leicester's Q image analysis software [Willingale, 2010].

The values presented in Table A2.4 [Martindale, 2008] show the best measured characteristics of flat MCP optics prior to those presented in this annex.

Parameter	Values
Channel Diameter (D)	8.5 - 200µm
Channel aspect ratio (L/D)	50:1 500:1
Format	≤ 54 x 54 mm^2
Channel Surface Roughness	1.1 nm RMS
Angular resolution	7 arcmins FWHM

Table A2.4 Best measured characteristics of an MCP optic prior to the measurements presented in this annex

A2.2.1. MEASURING MCP OPTIC ANGULAR RESOLUTION

A number of factors contribute to the measured MCP optic angular resolution, ϑ_m: the intrinsic resolution of the optic, ϑ_i, the spatial resolution of the detector, ϑ_d, the depth of focus of the MCP, ϑ_x, and the X-ray source size, ϑ_s. These contribute to the measured resolution quadratically, assuming each contribution is Gaussian[1], as in equation (A2.1). ϑ_m is measured by determining the Full-Width Half Maximum (FWHM) of a cut, 76 µm (1-pixel) wide, through the image central focus.

$$\boldsymbol{\theta_m = \sqrt{\theta_i{}^2 + \theta_d{}^2 + \theta_x{}^2 + \theta_s{}^2}} \qquad \textbf{(A2.1)}$$

Figure A2.13 was taken using the ME001-8 MCP optic. The X-rays were generated using an electron beam incident on a copper anode, resulting in both Cu-L X-rays (0.93 keV) and bremsstrahlung X-rays. The *x* and *y* axes are presented in pixels, where 1 pixel = 76 µm = 0.39 arcminutes in this geometry. This image has been normalised using the Q image analysis software for comparison with other images and linearised using a function derived from a pinhole mask, compensating for the non-linear response of the detector. The MCP optic nomenclature used throughout this thesis when referring to the accumulated MCP images is also shown in Figure A2.13.

[1] This assumption is an initial simplification as the response of a MCP optic is not Gaussian but is, in fact, a convolved top-hat and triangle function [Martindale, 2008].

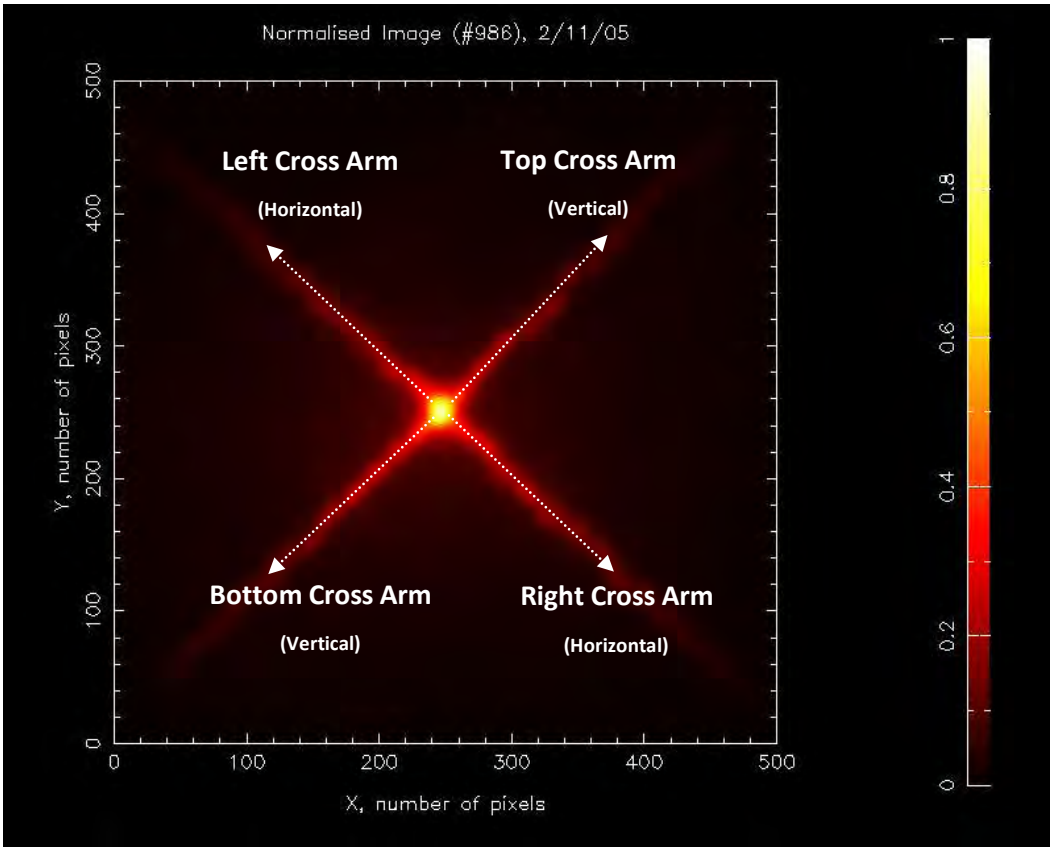

Figure A2.13 Soft X-ray Image (CuL X-rays) taken with the ME001-8 square-pore square-packed MCP optic. Image accumulated prior to any X-ray system optimisations. 1 pixel = 76 µm = 0.39 arcmins.

A2.2.1.1. X-RAY SOURCE SIZE MEASUREMENT

The characterisation tests reported in this section were conducted in the Vacuum Test Facility (VTF) in the University of Leicester's Microchannel Plate Laboratory. A schematic diagram and photograph of the VTF and the characterisation test setup are shown in Section A2.2.2. In order to establish the Microchannel Plate (MCP) Optic's intrinsic resolution, the X-ray source size needs to be measured. A method of performing this measurement is to take an image of the X-ray source using a pinhole mask. The size of the X-ray source can then be derived from measuring the image size and knowing the diameter of the pinhole used. As any image taken with the MCP optic also includes a contribution to the angular resolution from the source size, the source size must also be minimised.

Figure A2.14 shows a schematic of the mask experiment and Figure A2.15 shows a diagram which is used to derive the equation relating X-ray source size, d_s to the pinhole and X-ray image diameters, d_{pin} and d_i respectively. Note that due to the shape of the copper anode, the image on the MCP detector is not circular but is elliptical. When the 'diameter' (d_i) of the image is discussed, this will refer to the length of the minor axis of the elliptical image.

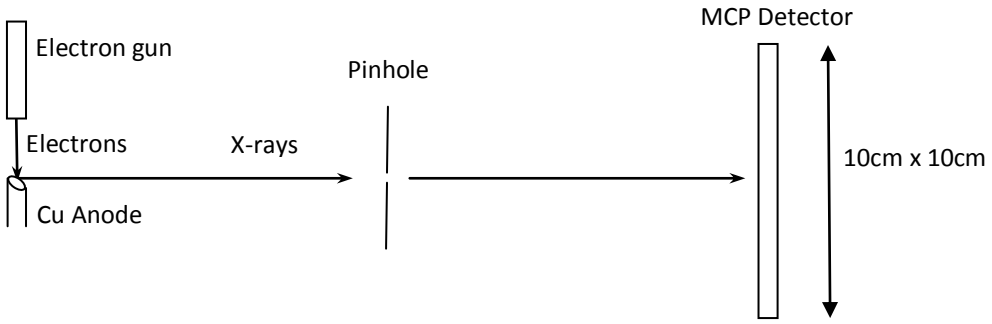

Figure A2.14 Schematic Diagram of the Pinhole Mask Experiment

The MCP optic was removed from the VTF and a pinhole mask was placed into the X-ray path using the filter wheel. In order to minimise the source size, a 'minimum' was found for each of the electron gun settings by taking a number of images. Each image was analysed using the Q image analysis software, where a sample cut was taken through the minor axis of the image and the image size was measured. Once the electron gun settings were optimised to provide the image with the shortest image minor axis, the size of the source was established.

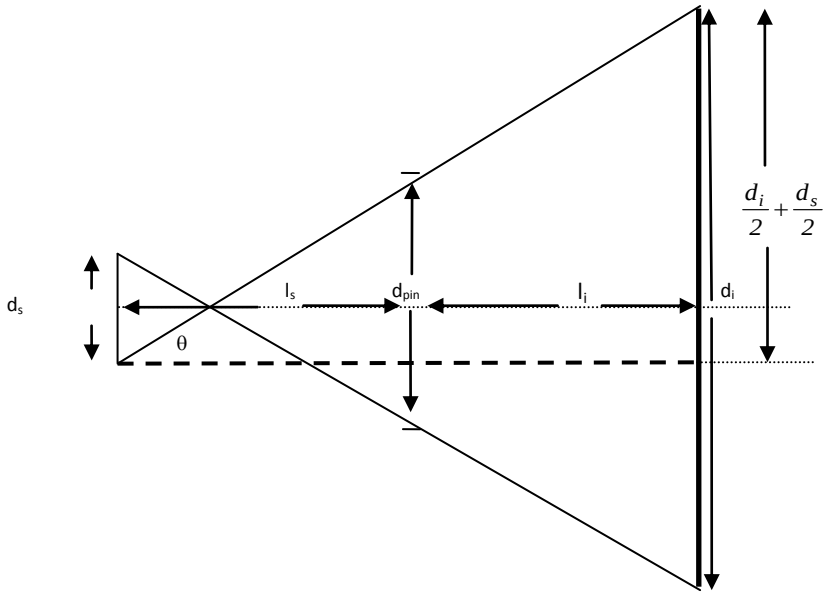

Figure A2.15 Schematic showing the pinhole mask experiment setup, used to derive the equation for X-ray source size measurement

The source size was determined by deriving the relationship between the pinhole size, image size and source size as follows:

Using the ratio of the two similar triangles in Figure A2.15;

$$\frac{d_{pin}+d_s}{l_s}=\frac{d_i+d_s}{l_s+l_i} \qquad \textbf{(A2.2)}$$

Rearranging and expanding (A2.2) gives;

$$\left(d_{pin}+d_s\right)\left(l_s+l_i\right)=l_s\left(d_i+d_s\right) \qquad \textbf{(A2.3)}$$

$$l_s d_{pin}+l_s d_s+l_i d_{pin}+l_i d_s=l_s d_i+l_s d_s \qquad \textbf{(A2.4)}$$

$$l_i d_s=l_s d_i-l_s d_{pin}-l_i d_{pin} \qquad \textbf{(A2.5)}$$

Rearranging for d_s gives equation (A2.6) which can be used to establish the source size based on the measurement of the image size, d_i.

$$d_s=\frac{l_s\left(d_i-d_{pin}\right)}{l_i}-d_{pin} \qquad \textbf{(A2.6)}$$

In order to determine the source size, the dimensions of Vacuum Test Facility were required to be accurately measured. Table A2.5 summarises the measurements made with their associated measurement accuracies.

Dimension	Measurement (mm)	Uncertainty (mm)
Distance from X-ray source to pinhole (l_s)	444.5	1
Distance from pinhole to MCP detector (l_i)	946	1
Diameter of the pinhole (d_{pin})	1	0.1
Diameter of the elliptical image minor axis (d_i)	3.8	0.2

Table A2.5 Summary of the VTF dimension measurements and their measurement accuracies

Inputting the values shown in Table A2.5 into Equation (A2.6) gives a value of d_s = 320µm. The standard error propagation formulae for products and sums were employed to Equation (A2.6) in order to determine the error on the calculated value of source size, d_s. It was found that the error in this measurement is ±145µm.

A sensitivity analysis on the errors and how they propagate through this experiment has shown that the largest contributor to the error in d_s is the error in measuring the size of the image, d_i. The larger the image at the detector, the less the error in its size measurement; the determined resolution in the image analysis is limited by the pixel size of the processed image which is ~100μm. It would have been, therefore, highly beneficial to increase the magnification of the pinhole mask by moving the mask closer to the X-ray source in order to reduce this error. Unfortunately, the distance of pinhole mask to X-ray source is limited by the dimensions of the VTF.

To conclude, the source size was calculated at the optimum electron gun settings and was shown to be approximately 320μm in the minor axis. The error in this value is large (~ ± 145 μm or ~45%) due to the relatively large distance between pinhole and X-ray source.

A2.2.2. MCP OPTIC CHARACTERISATION TEST SET-UP AND OPTIMISATION

Figure A2.16 shows a schematic diagram with distance measurements of the Vacuum Test Facility (VTF) used in the laboratory to measure and characterise the X-ray response of the flat-plate MCP optics. The dimensions of the VTF were measured and are also shown in the diagram. Placing a flat MCP optic in the centre of the beamline allows point-to-point focusing. The detector used in the focal plane to detect the focussed X-rays is a large 10cm x 10cm MCP detector [Lees and Pearson, 1997

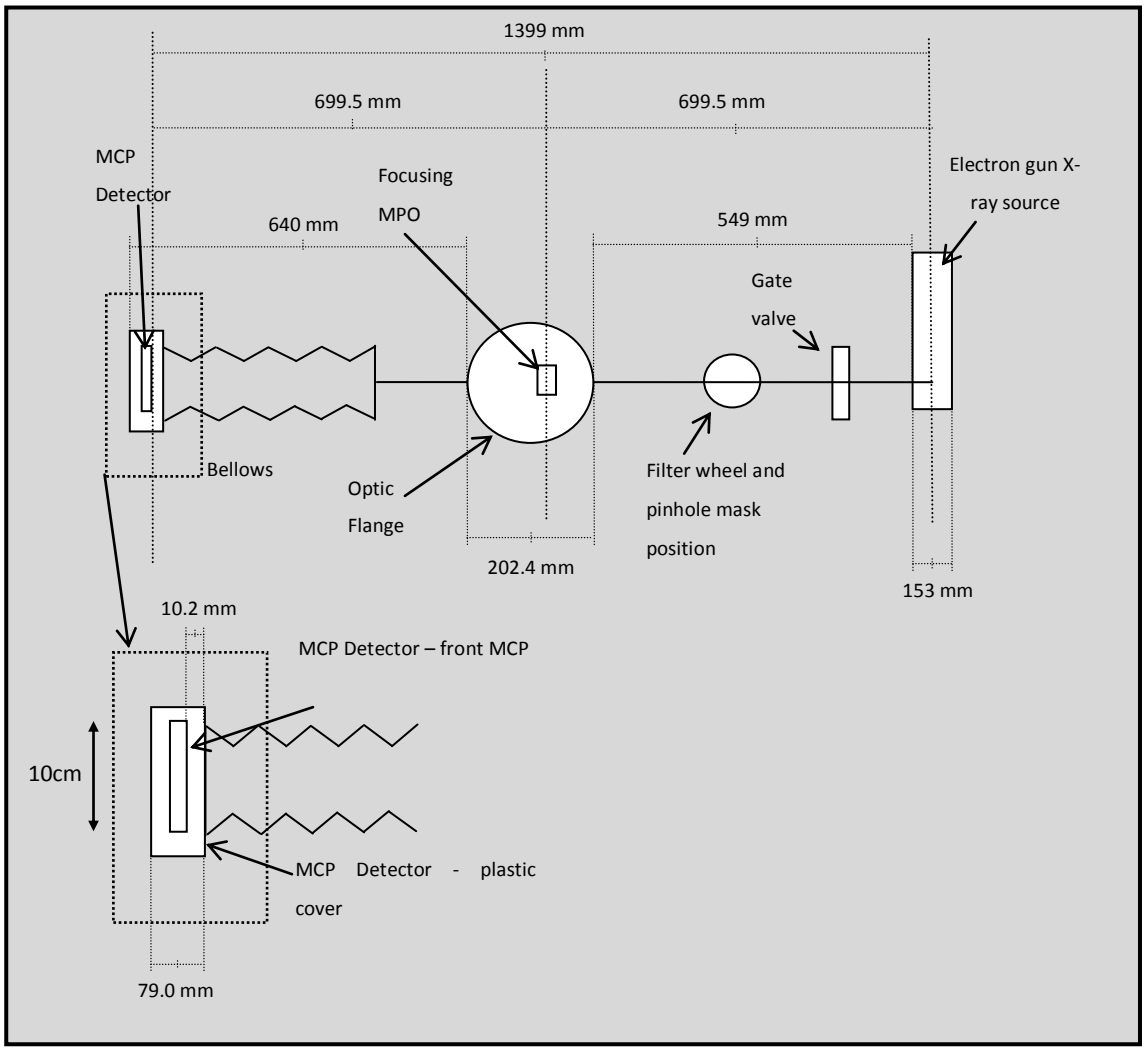

Figure A2.16 Schematic Diagram of the Vacuum Test Facility used in the MCP characterisation presented in this annex

Figure A2.17 and Figure A2.18 are photographs of the VTF and flat-plate MCP optic mounted on the MCP holder.

The MCP is mounted onto the holder and secured in place at the centre of the VTF, with a tight vacuum seal achieved by using a copper gasket. The VTF is then evacuated to a pressure $<10^6$ mbar. The electron gun X-ray source, producing CuL and bremsstrahlung X-rays, is activated and an X-ray image is accumulated on the optimised X9 MCP detector. Depending on photon count rate (~300cps to ~1500cps), an X-ray image is collected over 1-24 hours.

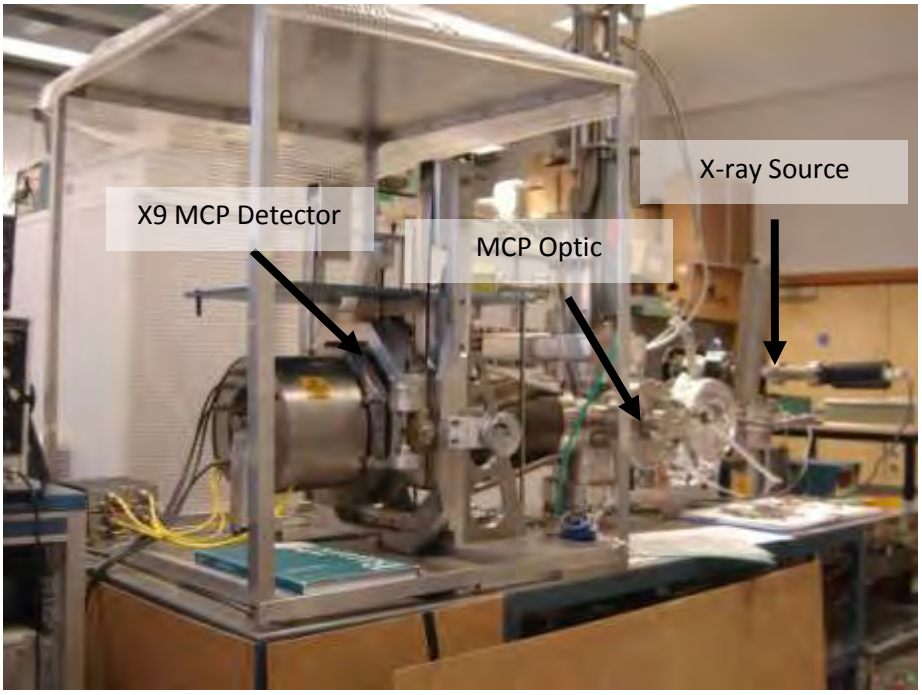

Figure A2.17 Photograph of the Vacuum Test Facility used to test Flat-Plate MCP Optics

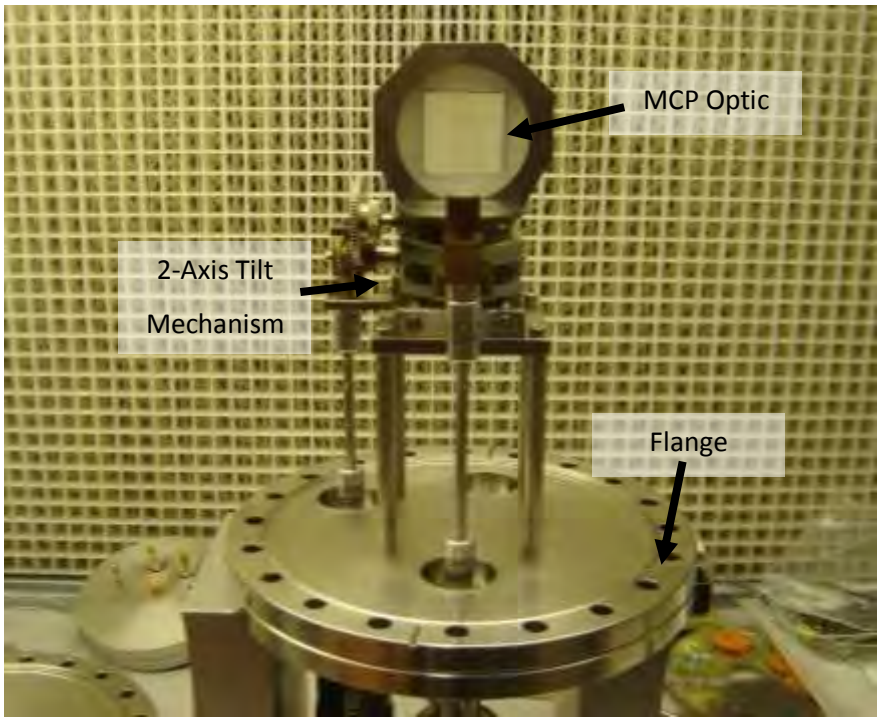

Figure A2.18 The Flat MCP Optic Mounted on the VTF Holder

Figure A2.19 shows the normalised image (designated #986) taken with the ME001-8 flat MCP optic *before* any X-ray source size optimization had been conducted. Different images

normalised to the brightest pixel in each image better allows comparison of these images. Figure A2.19 shows the characteristic cruciform structure of the square-pore square-packed MCP optic [Fraser et al, 1993]. Taking a vertical[2] cut, which is 1 pixel (76 microns) wide, through the central focus of Figure A2.19, gives a histogram showing the X-ray counts in the vertical arm, through the focus (Figure A2.20). The FWHM resolution of this cut shows a resolution of ~10 arcminutes, where each pixel on the processed image is ~0.39 arcminutes.

In order to maintain consistency while analysing the MCP images, an algorithm was written to automatically analyse each image and determine the FWHM resolution. In the programme, the brightest pixel within the central focus region was identified and a cut through this pixel, one pixel wide and 200 pixels long, was made along the vertical arm. This removes any human error while judging the focal spot of the image through which to make the cut. The programme then established the FWHM resolution of the cut and printed the results to screen, including the resolution converted from number of pixels to arcminutes. Using this automated method significantly improved the analysis process by reducing the time taken to analyse each image and ensuring consistency from data set to data set.

Optimisation of the source size was carried out using the pinhole mask method described in Section A2.2.1.1. The settings on the electron gun were systematically changed to achieve the smallest spot size and a low count rate. Figure A2.21 shows the image obtained *after* X-ray source optimisation was carried out and the MCP Optic was placed in the nominal position at the centre of the VTF. The FWHM angular resolution, as determined from a cut through the focus (Figure A2.22) was measured to be approximately 10.4 arcminutes. This is consistent with resolution measurements made of the MCP optic prior to source size optimisation.

However, once the source was optimised, the MCP optic was revealed to produce a double cruciform structure, as shown in Figure A2.21. A double cruciform image is expected if a flat plate is *not* in the correct position for point-to-point focusing, demonstrated with Monte Carlo ray trace modelling by J. Pearson (2005), suggesting that the optic is away from its nominal position at the centre of the VTF.

[2] Note that the nomenclature used to describe these images is explained in Figure A2.13. They are described as vertical and horizontal cross arms in order to distinguish between the two.

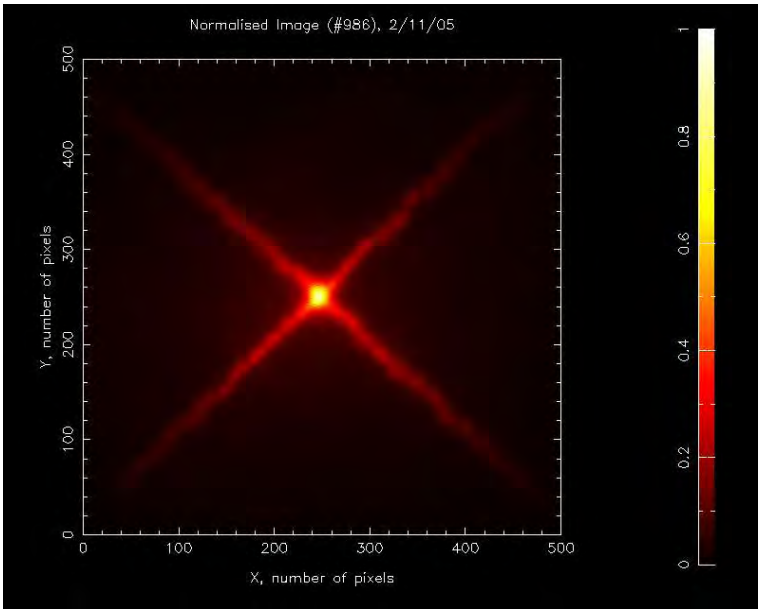

Figure A2.19 Normalised Image 986. No X-ray Source Optimisation has been performed for this image

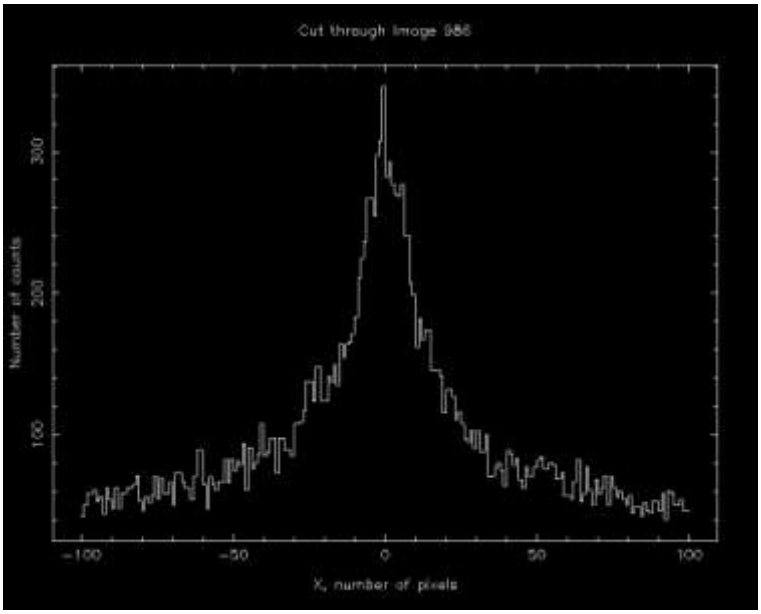

Figure A2.20 Vertical cut, one pixel wide, taken through the central focus of image 986

Measurements of the VTF show that the nominal position at the centre of the facility is correct, therefore suggesting that the plate cannot be as flat as expected.

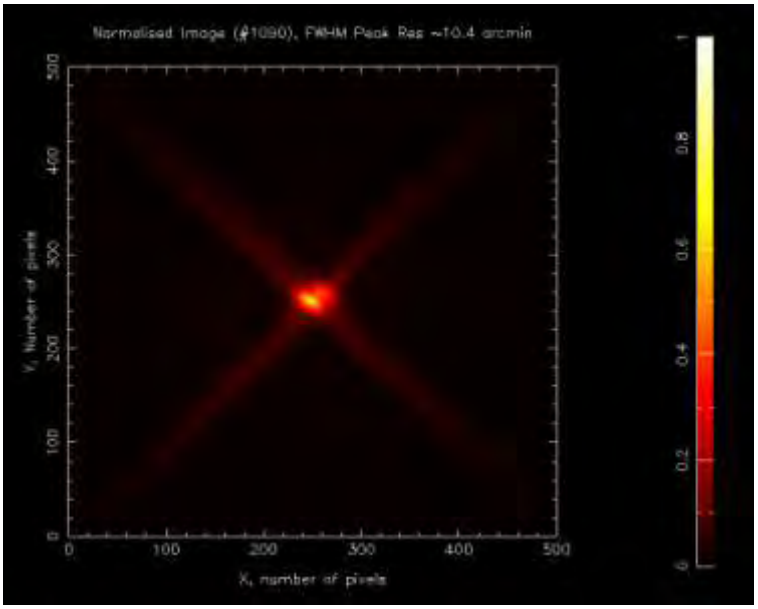

Figure A2.21 Normalised MCP Image 1090 taken with the Flat-Plate optic in the nominal position, at the centre of the VTF, post X-ray Source Optimisation. Note the double cruciform structure.

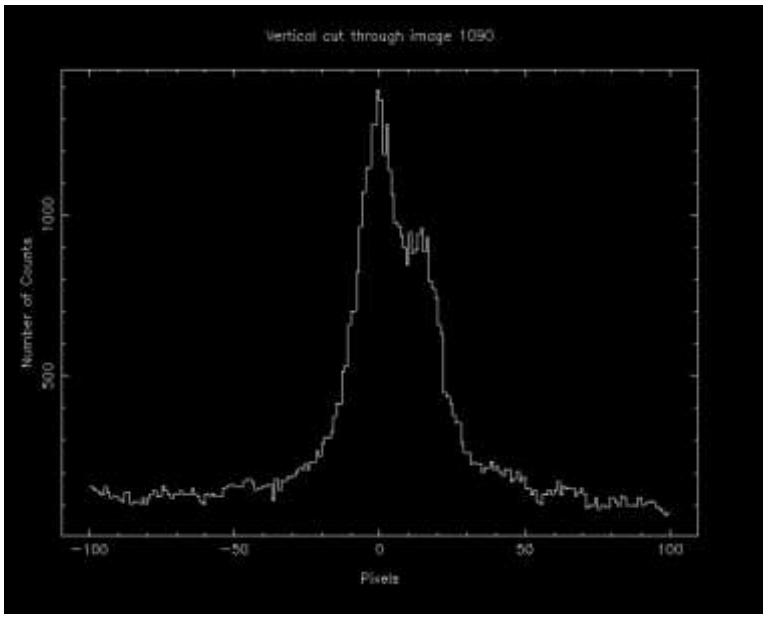

Figure A2.22 Histogram showing the vertical cut through the double foci of image 1090. Two distinct peaks are evident from the analysis. FWHM resolution ~10.4 arcminutes.

Simulation and measurements of the double cross feature image suggested a movement of ~1.4cm towards the detector would result in a greatly improved resolution as the two separate cross features combine. This change was made and images were taken at this new optic position. Figure A2.23 was taken 1.4cm away from the nominal optic position at the centre of the VTF as suggested by the simulation work. The double cruciform feature appears

to have gone due to the recombination of the crosses as expected, resulting in a much improved measurement of the optic resolution: 4.9 arcminutes.

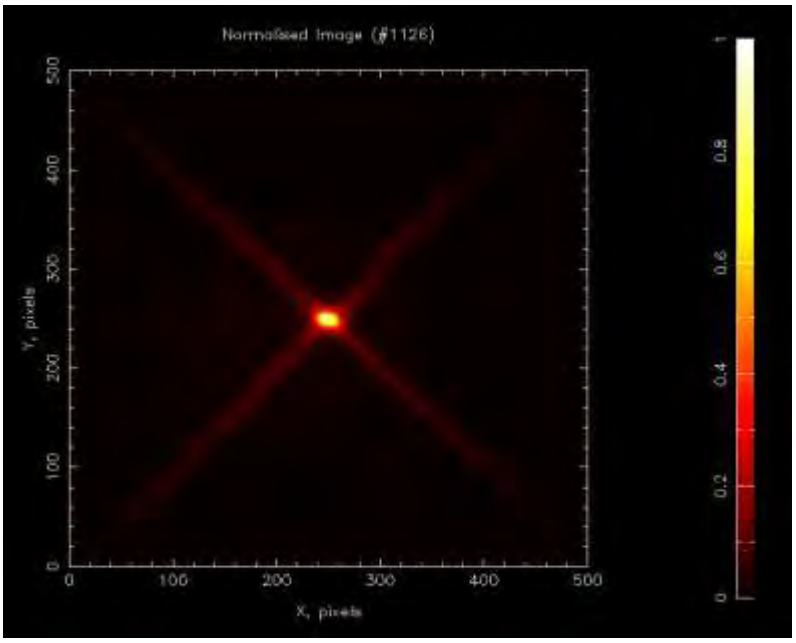

Figure A2.23 Image 1126 taken ~1.4cm towards the detector and away from the original 'nominal' optic position at the centre of the VTF. Note that the double cross feature is no longer evident.

Careful measurement of the VTF showed that the plate was indeed in the correct position for point-to-point focussing. In order for the plate to result in a double cruciform image, the optic must have a slight curvature and the focal length is not, therefore, equivalent to the distance of the plate from the X-ray source.

Further optimisation of the MCP optic position was carried out, scanning the MCP along the optical axis in order to determine the correct focal position for the slightly curved plate. This was done in steps of 2mm; shorter steps would be ineffective due to the 2mm depth of focus of the optic, where the depth of focus is approximately twice the thickness of the MCP optic.

An image was accumulated at each step along the axis and analysed using a cut along the vertical axis to determine the FWHM resolution. Figure A2.25 summarises the results of the focal length optimisation process. The measured resolutions were plotted against the amount the MCP optic was moved away from the nominal position, both toward and away from the X-ray source. Negative values on the x-axis represent optic movement towards the X-ray source while positive numbers show movement towards the detector.

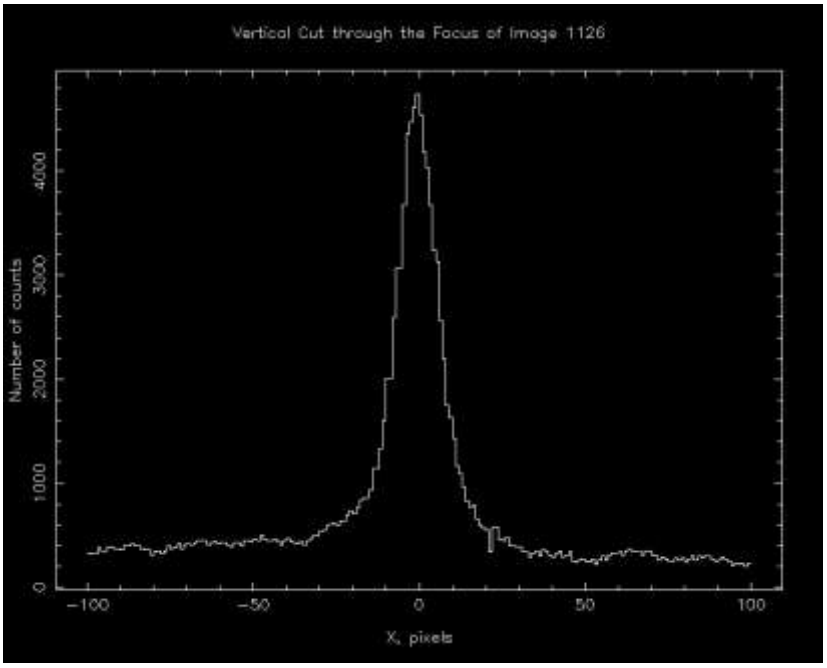

Figure A2.24 Histogram showing the vertical cut through the focus of image 1126. The measured FWHM resolution is 4.9 arcminutes.

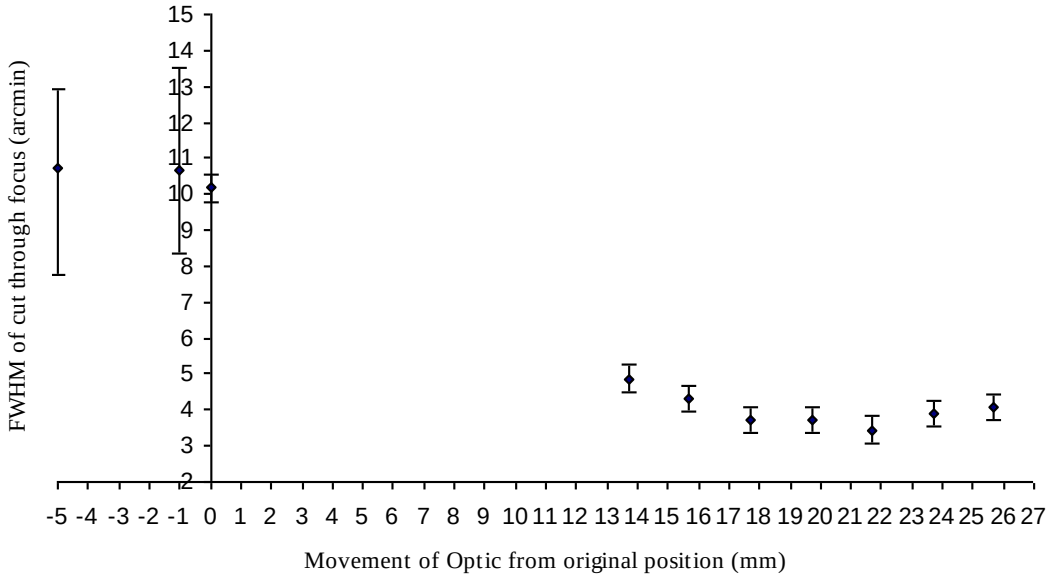

Figure A2.25 Graph showing how the FWHM resolution varies with distance from the 'nominal' optic position at the centre of the VTF. Negative numbers represent the MCP optic being moved towards the X-ray source whereas positive numbers show movement towards the detector.

The optimum focal length for this MCP optic was found to be ~22mm from the centre of the VTF. This is used in Section A2.2.4.2. to calculate the effective radius of curvature of the MCP optic.

A2.2.3. CHARACTERISATION RESULTS

A2.2.3.1. PRIMARY RESULTS

The MCP optic was moved to the optimum focus position, as determined by Figure A2.25, and a 24 hour image, taken with a very low X-ray count rate (~300 counts per second), was accumulated. A low count rate is preferable as the MCP detector is very susceptible to X-ray pile-up. The image will become blurred due to electric charge spreading as it enters the second MCP in the detector chain. Figure A2.26 shows the normalised image obtained, with Figure A2.27 showing the vertical cut taken through the focus spot.

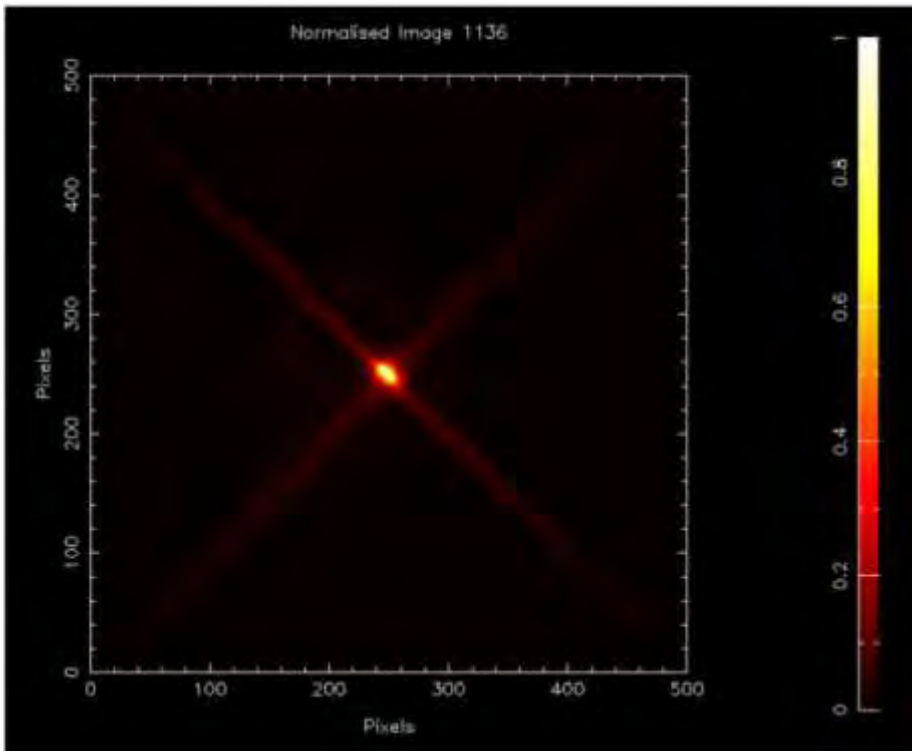

Figure A2.26 Image accumulated over a 24 hour period using the ME001-8 square-pore square-packed MCP Optic. The image has been normalised to the brightest image pixel for comparison with other images.

It is evident from this image that a greatly improved angular resolution has been achieved. The vertical cut through the focus shown in Figure A2.27 reveals a measured FWHM resolution of 3.1 arcminutes and is a significant improvement on all previous angular resolution measurements made using a square-pore square-packed MCP optic.

Table A2.6 summarises the results achieved through the analysis of the MCP Optic images analysed in this annex. Appendix I shows the images listed in Table A2.6 and the vertical cuts used to determine their FWHM angular resolution.

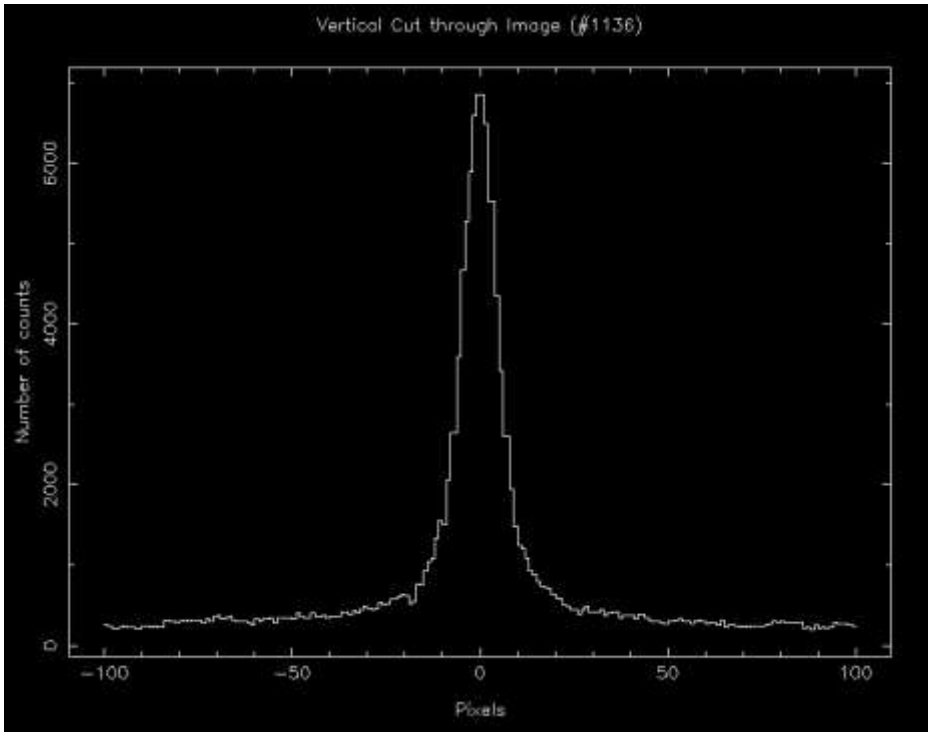

Figure A2.27 Vertical cut through image 1135. FWHM resolution is measured to be 3.1 arcminutes

Image Number	Distance of optic from detector (mm)	FWHM of peak in cut, (Arcmins)	Size of each image pixel (Arcmins)
1090	698	10.2	0.37
1120	699	10.7	0.37
1123	703	10.7	0.37
1126	685	4.8	0.38
1128	683	4.3	0.38
1130	681	3.7	0.39
1131	679	3.7	0.38
1132	677	3.4	0.39
1133	675	3.9	0.39
1135	673	4.1	0.39
1136	677	3.1	0.39

Table A2.6 Summary of FWHM Resolution Results for the various images investigated in this annex

A2.2.3.2. RESULTS: 90° ROTATION

The resolution of the MCP optic measured in Section A2.2.3.1. were in the vertical arm direction of the cruciform which is coincident with the minor axis of the elliptical X-ray source. In order to determine if the resolution of the optic is the same along the other cross arm of the image, the optic was rotated 90 degrees around the axis along X-ray beam. The slight curvature of the plate, however, meant that the allowable linear movement of the optic mount was not enough to focus the image. Figure A2.28 shows the best possible image accumulated within the restrictions of the VTF.

Figure A2.29 shows the vertical cut through Figure A2.28, demonstrating the double cross arm feature. The inability to position the optic in the correct focal length while in this orientation is indicative of a curvature different to that seen in the initial experiment and is discussed in Section A2.2.4.2.

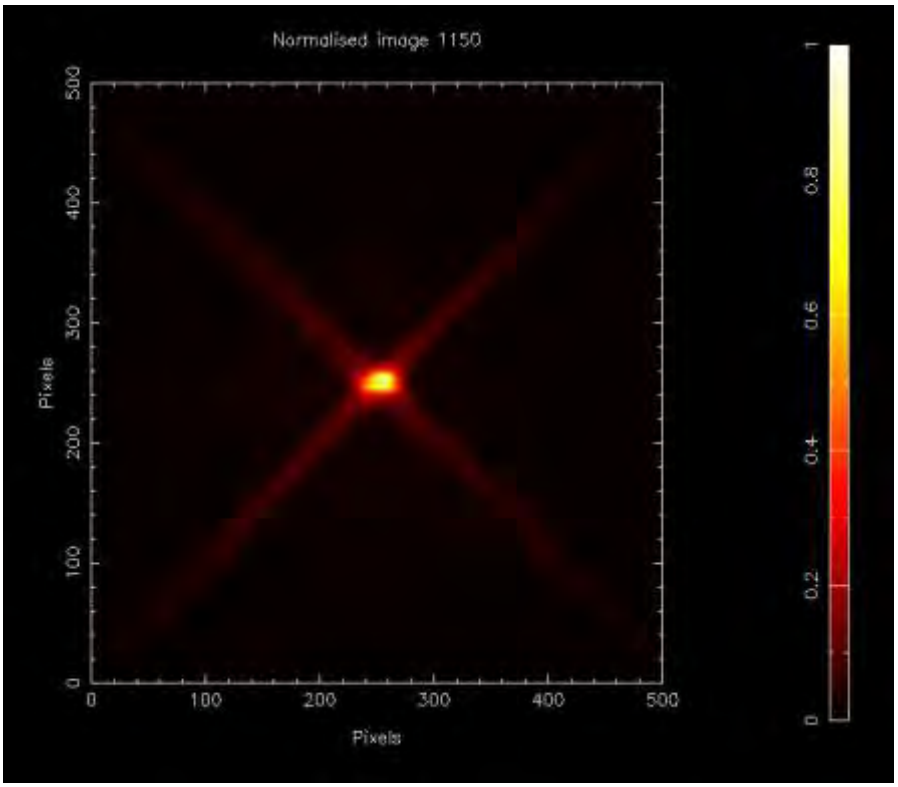

Figure A2.28 Image 1150 showing the result of a long X-ray exposure of the MCP optic rotated 90°. No further optimisation of focal length was possible within the limitations of the VTF.

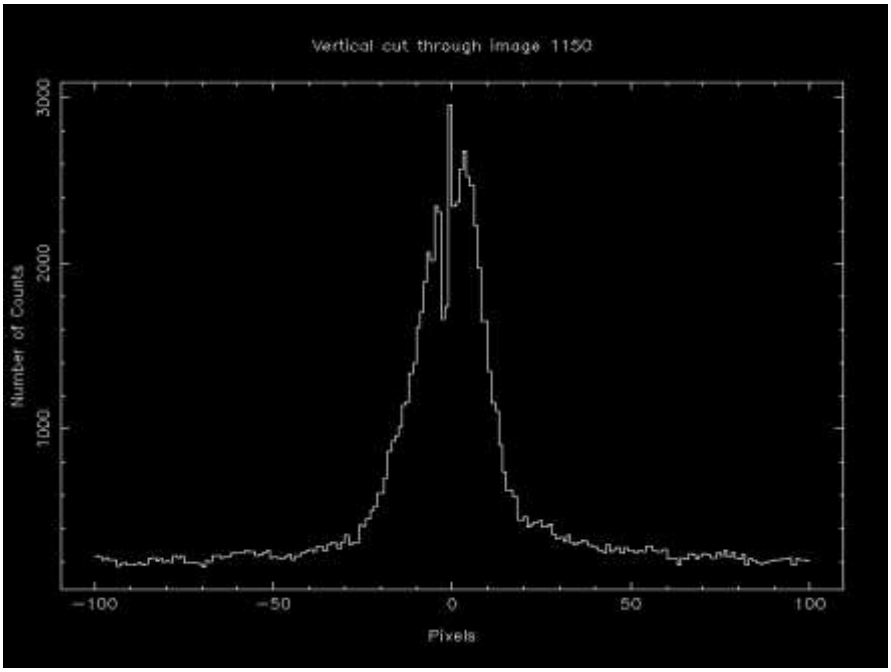

Figure A2.29 Vertical cut through image 1150 showing the double cross feature and resulting poor resolution achieved when the MCP optic was rotated 90°.

A2.2.4. DISCUSSION

A2.2.4.1. INTRINSIC OPTIC RESOLUTION

The best FWHM resolution measured in this experiment is 3.1 arcminutes, obtained from image 1136. Equation (A2.1) can be used to determine the intrinsic angular resolution of the optic by removing the other contributions to the measured angular resolution. Rearranging (A2.1) gives equation (A2.7).

$$\theta_i = \sqrt{{\theta_m}^2 - {\theta_d}^2 - {\theta_x}^2 - {\theta_s}^2} \qquad \textit{(A2.7)}$$

The depth of focus of the MCP is the result of the non-negligible thickness of the optic. From Figure A2.30 it can be seen that the red and blue X-rays travel two different path lengths when reflecting from the 1mm thick MCP optic. The red X-ray travels the shortest distance along the optical axis (1398mm) and the blue ray the furthest distance along the optical axis (1400mm). The difference between these two lengths along the optical axis is the depth of focus, 2mm, and is twice that of the MCP optic channel length of 1mm.

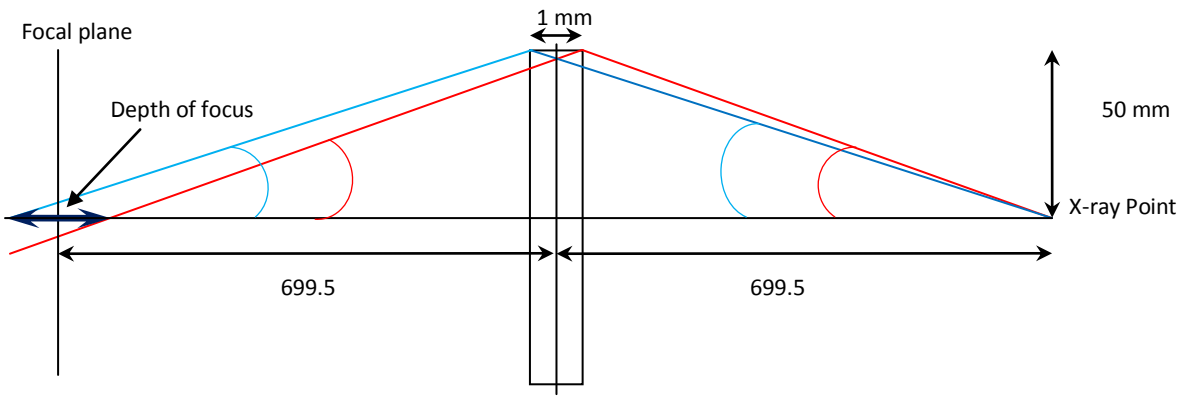

Figure A2.30 Schematic of point-to-point focusing of an MCP optic, showing the Depth of Focus

It can also be seen in Figure A2.30 that the two X-rays hit the focal plane in two different positions. This represents an increase of the point spread function and can be calculated from the above diagram using basic geometry. It was determined that, using the dimensions of the VTF and experimental setup, the spread of the point spread function due to the depth of focus of the optic is 0.012 arcminutes. Using the standard propagation of error equations, the uncertainty in this contribution is small:

Contributors to ϑ_i	Value (arcmins)	Uncertainty (arcmins)
Measured resolution, ϑ_m	3.1	0.39
Detector resolution, ϑ_d	0.39	0.02
Depth of Focus contribution, ϑ_x	0.012	0.001
Source Size contribution, ϑ_s	1.57	0.7

Table A2.7 Summary of the contributors to the intrinsic MCP optic resolution, ϑ_i

Table A2.7 summarises the contributions to the intrinsic MCP optic resolution, ϑ_i. The uncertainties in depth of focus and source size determinations were calculated using the standard error propagation formulae.

ϑ_d, the detector resolution, was 0.39 arcminutes FWHM for the setup used to obtain Figure A2.27. The depth of focus contribution, ϑ_x, is small: ~ 0.012 ± 0.001 arcminutes. The contribution from the X-ray source size, ϑ_s, is much more significant. The contribution is equivalent to the angle subtended by the X-ray spot at a distance equal to the separation from the source to the MCP optic. The source size was measured to be 320 ± 145 µm along the minor axis of the elliptical source spot. This results in a contribution of ϑ_s = 1.57 ± 0.7 arcminutes.

Substituting these values into equation (A2.7) gives a value of:

ϑ_i = 2.64 ± 0.6 arcminutes FWHM.

The quadratic addition of angular resolution contributions is based on the assumption that each component of the measured resolution is Gaussian. This is a good assumption when the intrinsic resolution, which is a combined function of MCP channel misalignment and the inner-channel surface quality, is poor, resulting in a blurred and approximately Gaussian point spread function. However, the true shape of the response of a square-pore square-packed MCP optic is triangular as shown in Figure A2.31. The images obtained with this MCP show that channel misalignment and inner-channel surface quality is such that the images are not poorly resolved and, as such, a Gaussian approximation is not wholly appropriate.

Martindale (2008) employed a more sophisticated deconvolution of the contributors to the measured resolution, based on a triangular, rather than Gaussian, intrinsic resolution combined with a top hat function representing the source size element. This analysis resulted in an intrinsic resolution of:

1.5 – 2 arcminutes FWHM

This result is obtained assuming a source size of 400µm and supports the findings of the initial analysis.

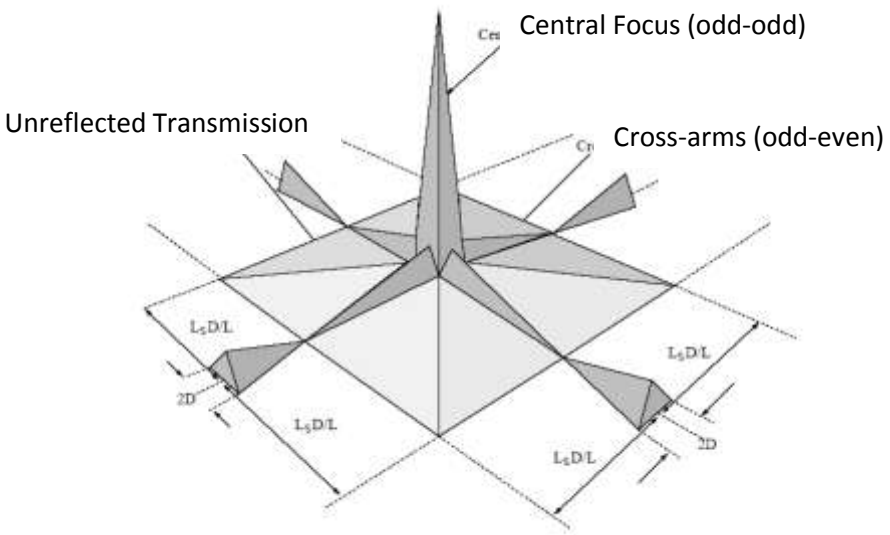

Figure A2.31 A diagram of the cruciform structure resulting from the focusing of X-rays using a planar square-pore square-packed MCP optic. The central focus is comprised of X-rays that are reflected an odd number of times from orthogonal channel walls, whereas the cross-arms are a result of an odd-even number of reflections. (Price 2001).

The resultant resolution of 1.5-2 arcminutes FWHM is an intrinsic resolution much improved on the 6-8 arcminutes FWHM measured by Price (2001) and Nussey (2005), and betters the ~4 arcminutes optic resolution requirement of the Wide Field Telescope (WFT), needed to

perform source position centroiding to a resolution <2 arcminutes [Black et. al, 2003] [Bannister and Fraser, 2003].

A2.2.4.2. MCP OPTIC CURVATURE

The double cross arm feature as seen in Figure A2.21 indicated that the MCP optic was not in the correct position for point-to-point focusing, and the accurate re-measurement of the VTF dimensions to verify the expected nominal optic position suggested that the optic, which was assumed flat, was in fact slightly curved.

The data taken when the optic was turned 90° (Figure A2.28) suggest that not only is the optic curved in this direction, also, but has a different curvature to that seen in the other axis. The optic is, therefore, slightly cylindrical in shape. This conclusion is also supported by Martindale when using the triangular-top hat deconvolution method (Martindale 2008).

Having determined the position of the optic along the optical axis which results in the best angular resolution, it is possible to estimate the amount of curvature of the optic. The lens equation for a spherically slumped MCP optic using a finite source distance is

$$\frac{2}{R} = \frac{1}{L_i} - \frac{1}{L_s} \qquad \textit{(A2.8)}$$

where L_i and L_s are the image-optic and source-optic distances respectfully. R is positive when the optic is convex from the viewpoint of the source and negative otherwise.

The optic position was measured in the VFT and suggests that the MCP optic has a curvature. The convex side faces the source and therefore R, in equation (A2.8), is positive. Using the lens equation (A2.8), the radius of curvature calculated is ~21.7m. The cylindrical curvature of the plate in two axes is equivalent, therefore, to a MCP optic with a spherical slump of ~21.7m. At such a large curvature, the sagittal depth of the plate is essentially imperceptible (~2×10^{-5}m), resulting in what looks like a flat MCP optic.

A2.2.4.3. MCP OPTIC HANDLING

The cause of the curvature seen in this experiment is a concern for the handling and use of MCP optics for both terrestrial and space applications. Similar plate deformation was seen by Martindale (2008) when analysing slumped optics for the BepiColombo MIXS instrument. Analysis of the optic holder (Martindale and Yates, 2007) showed a 38cm radius of curvature rather than the expected 75cm. It is believed that this difference in holder radius of curvature resulted in the plate deforming during tests. Such mounting stresses could have resulted in

the cylindrical deformation seen in the tests mentioned above. In these experiments, the plate was mounted in a flat holder but held in place by four corner screws, each exerting a force on the MCP optic via a spring mount. This force, which is likely to have differed for each of the screws, could have caused the deformation. (Martindale and Yates, 2007) also noted that the deformation was inelastic, with the slump radius of the optic permanently altered from its ideal shape.

The evidence from this experiment suggests that small pressure is required to result in significant alteration of the expected dimensions of MCP optics. Due care must therefore be taken when handing these optics. As a result of the tests presented, new MCP optic test mounts have been manufactured for testing the BepiColombo optics which apply minimal pressure on the optic segments, and the design of the MIXS instrument was iterated to also take this potential for deformation into account.

APPENDIX I

I-V CURVES MEASURED IN THE MIXS DIODE IRRADIATION

APPENDIX SUMMARY

There are two sets of curves presented in this Appendix: firstly, the pre-irradiation I-V curves taken by MPI-HLL prior to delivery of the diode samples and the repeat measurements made by the author at the University of Leicester and secondly: the post-irradiation curves taken at the University of Leicester.

The leakage current measurements of diode D2 on samples C03 and C05 made at the University of Leicester were found to differ from those made by MPI-HLL. Initially, it was thought that the current being measured was that of the guard ring as opposed to the diode leakage current. Close inspection of the sample pin-out showed that the current being measured was not the guard ring current, however, and that, indeed, the current measured was the leakage current of the device. A current measurement was made of the guard ring to further support this, and is shown in the curves below. These I-V curves determined which of the diodes were used for which experiment. It was decided that determining the current-related damage factor, α, was the priority test so the best performing samples were used for this. The other samples were used in the annealing experiment.

AP.1 PRE-IRRADIATION I-V CURVES, MEASURED AT LEICESTER AND MPI-HLL

AP.1.1. SAMPLE CO3

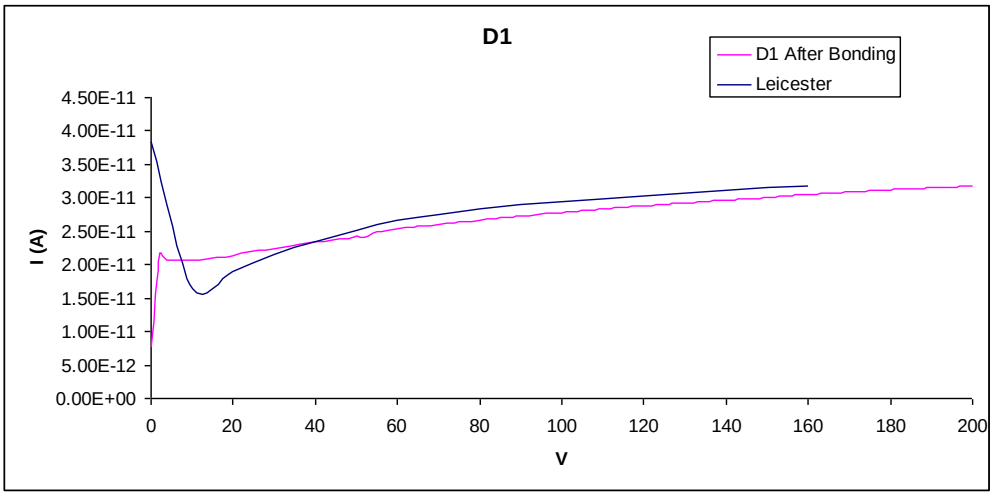

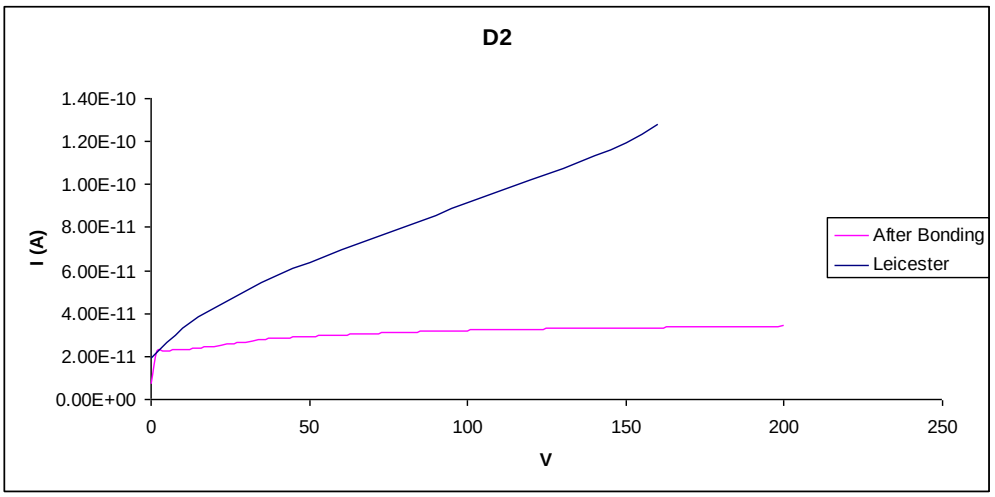

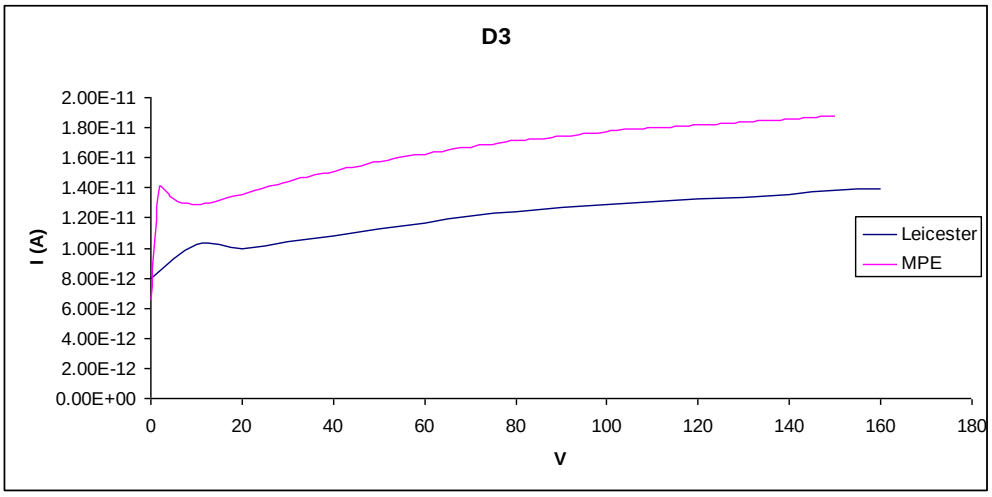

AP.1.2. SAMPLE C05

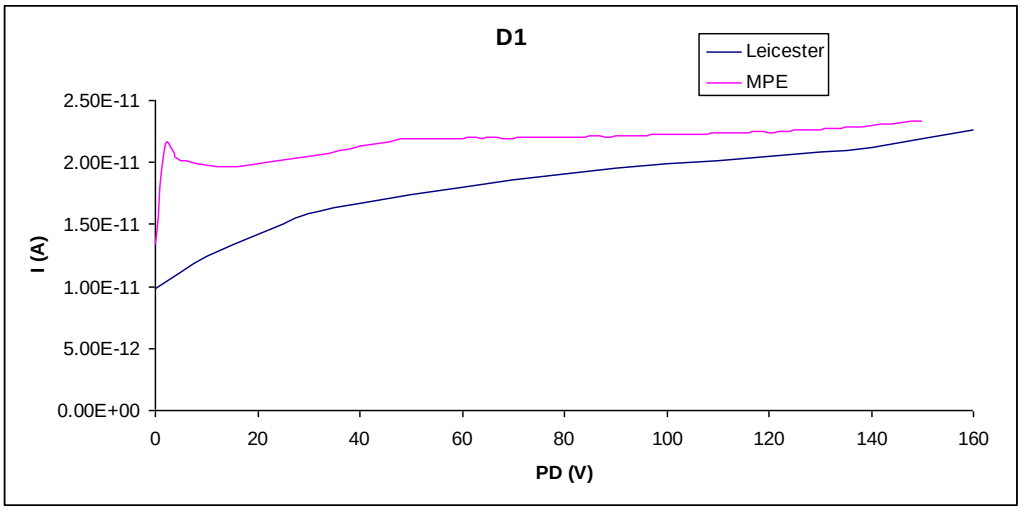

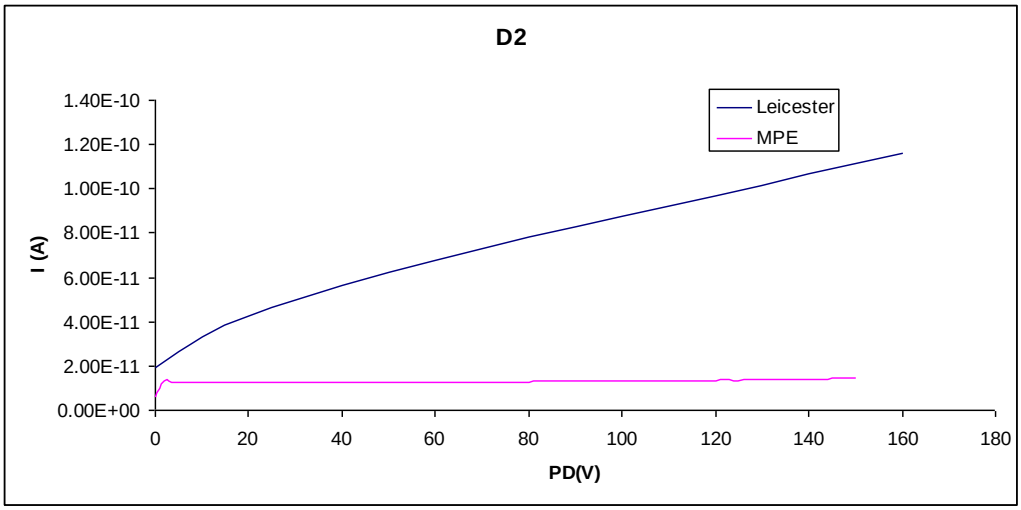

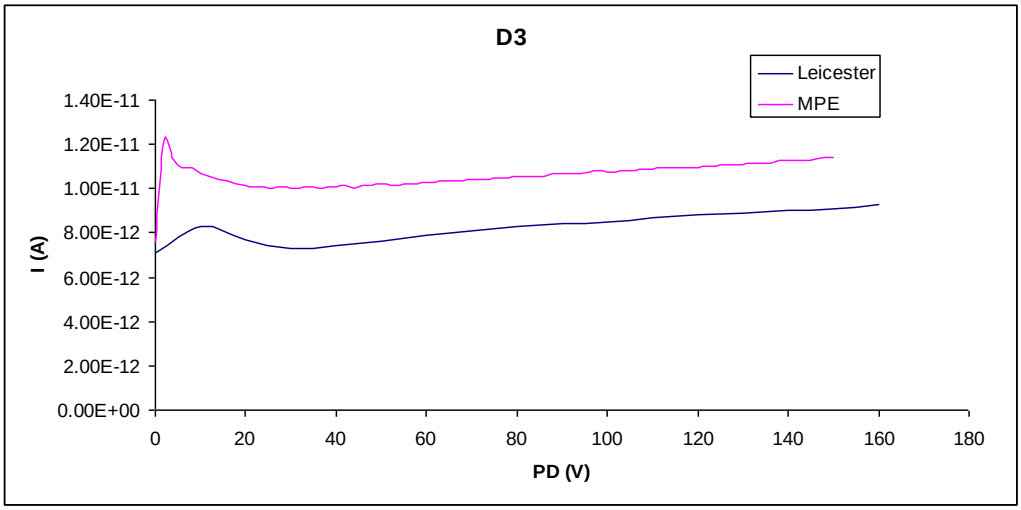

AP.1.3. SAMPLE C07

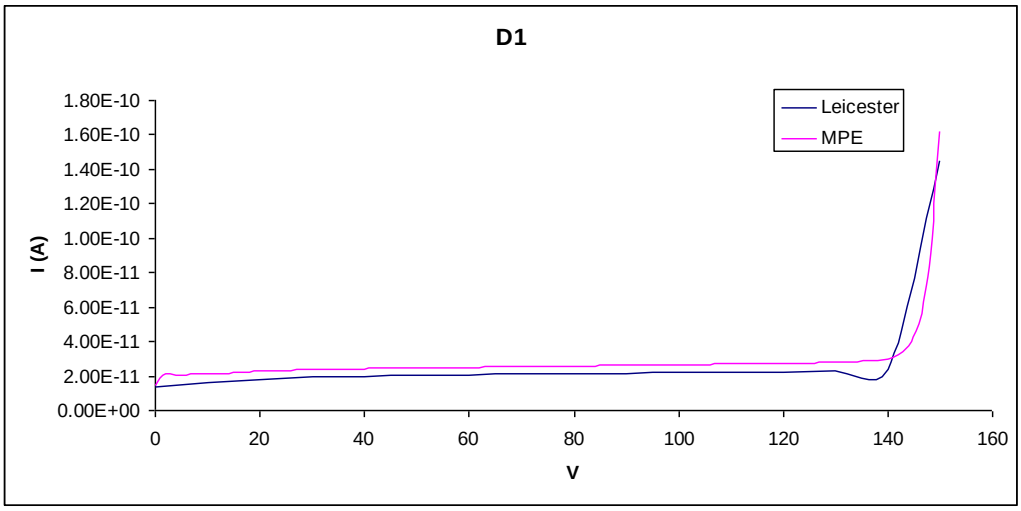

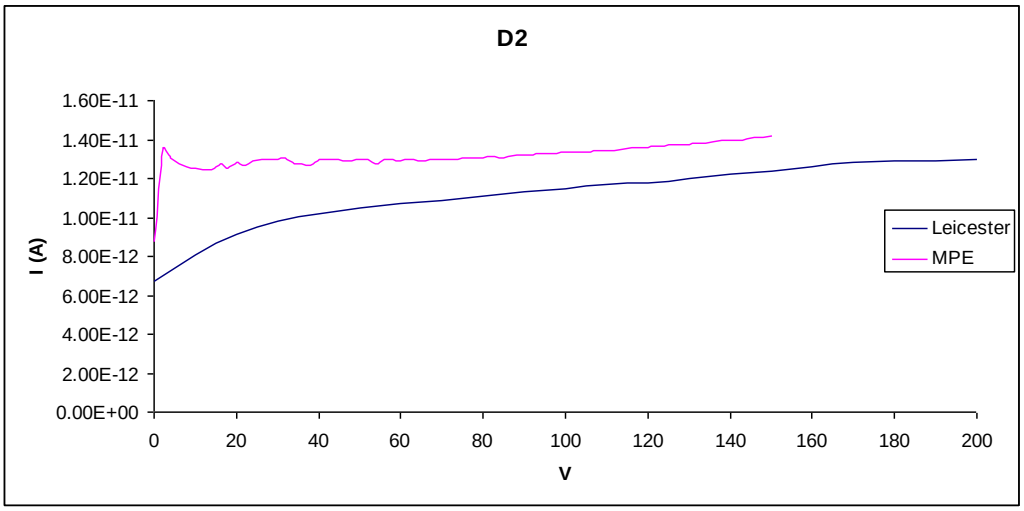

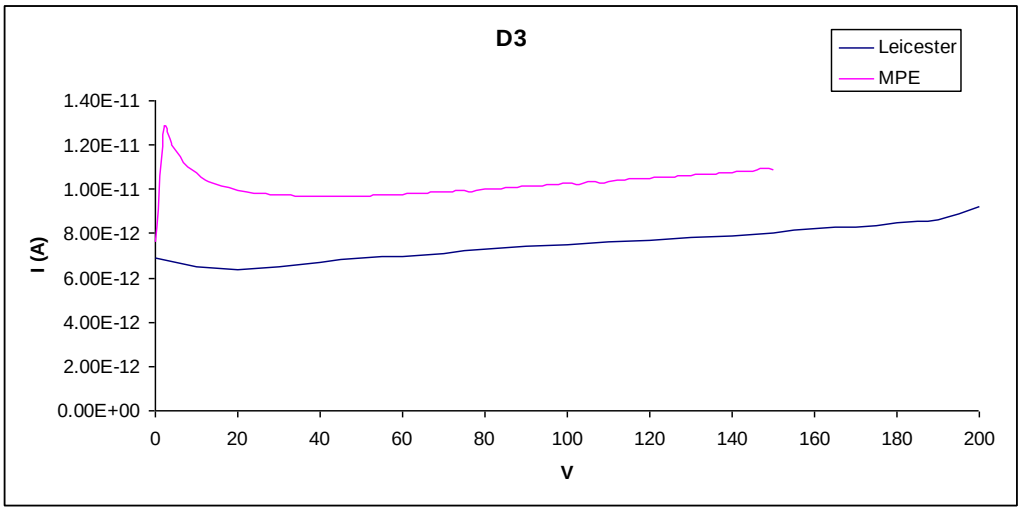

AP.1.4 SAMPLE E05

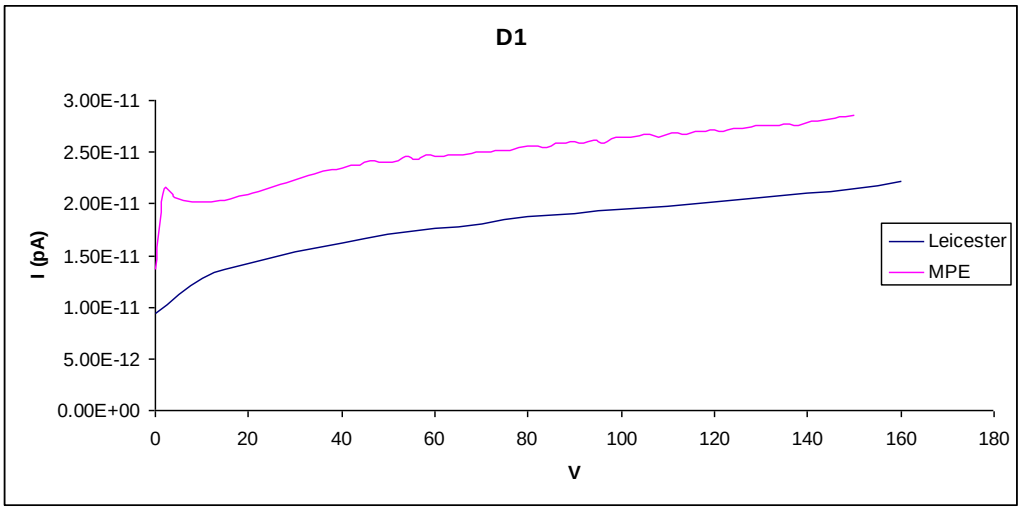

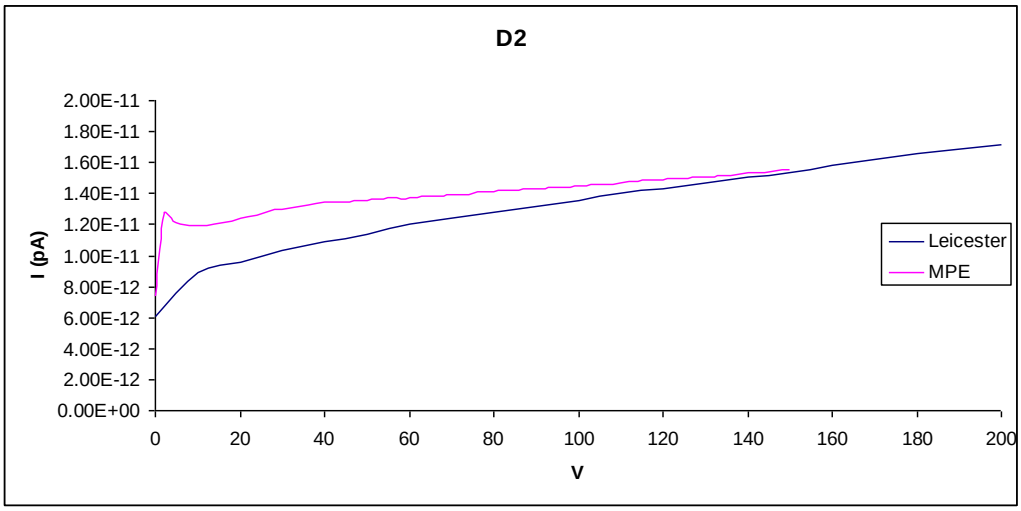

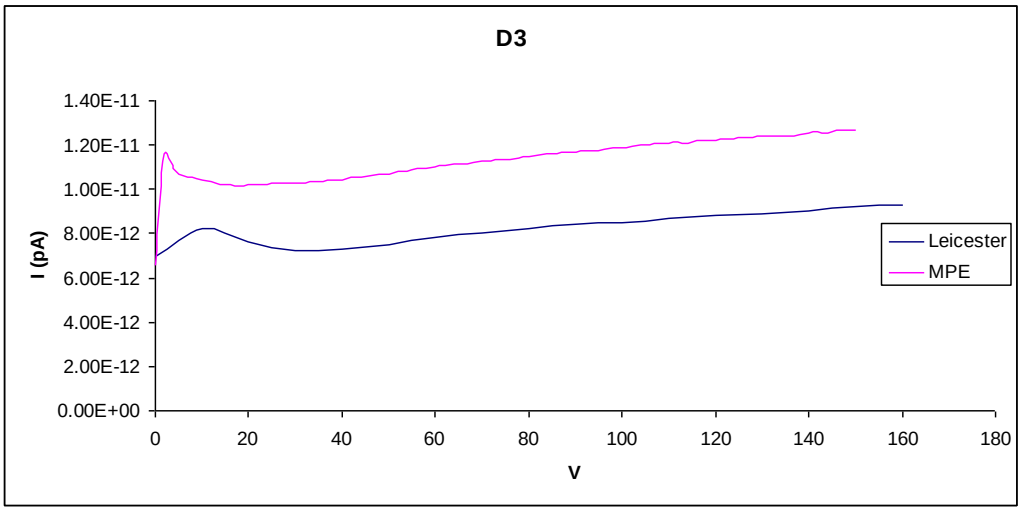

AP.1.5. SAMPLE G03

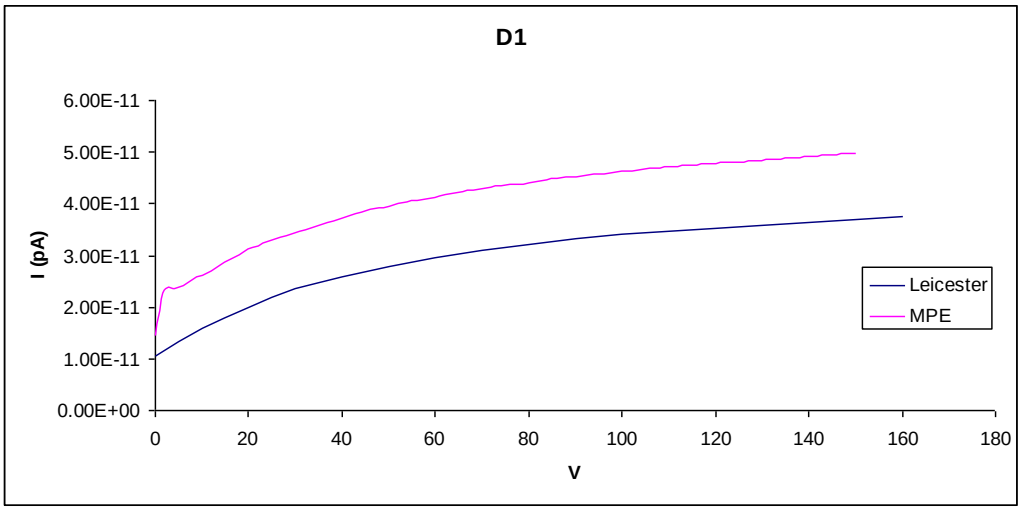

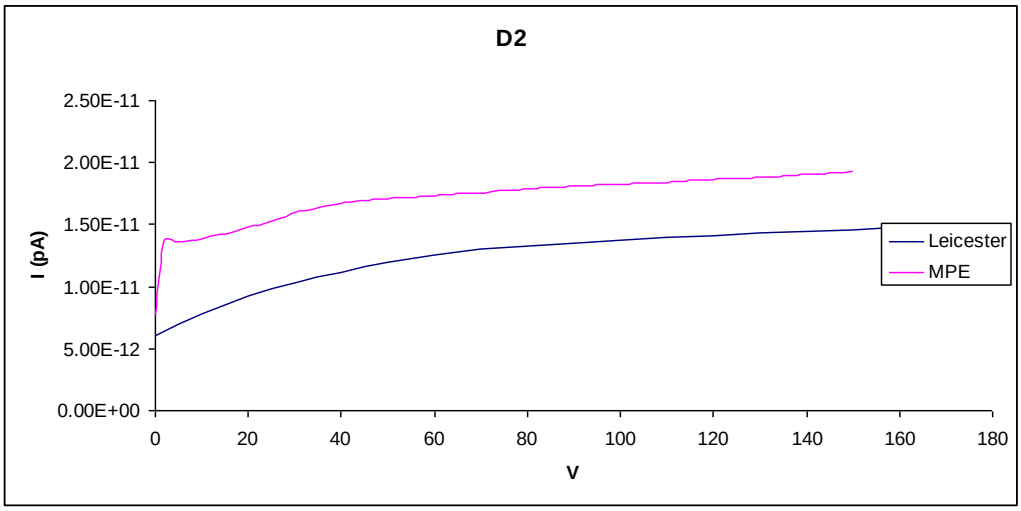

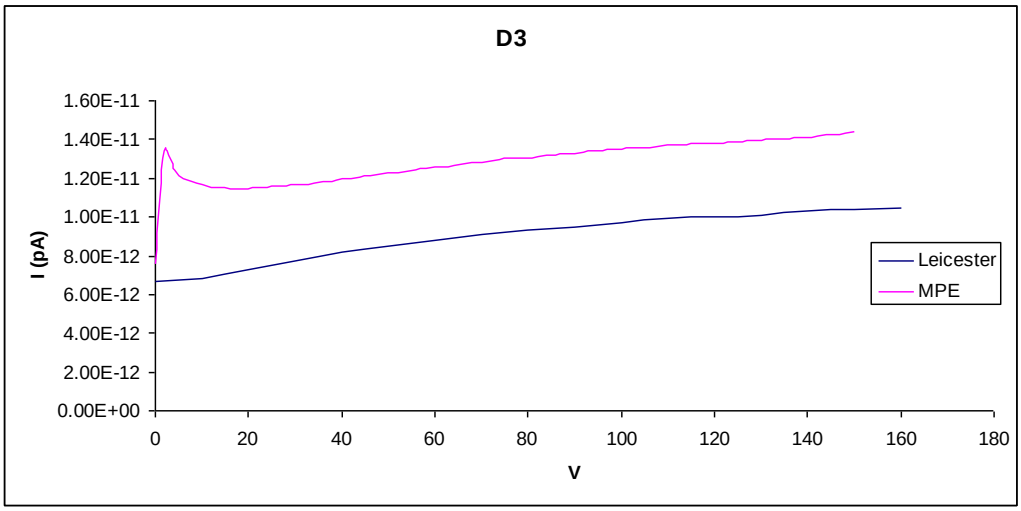

AP.1.6. GUARD RING MEASUREMENT

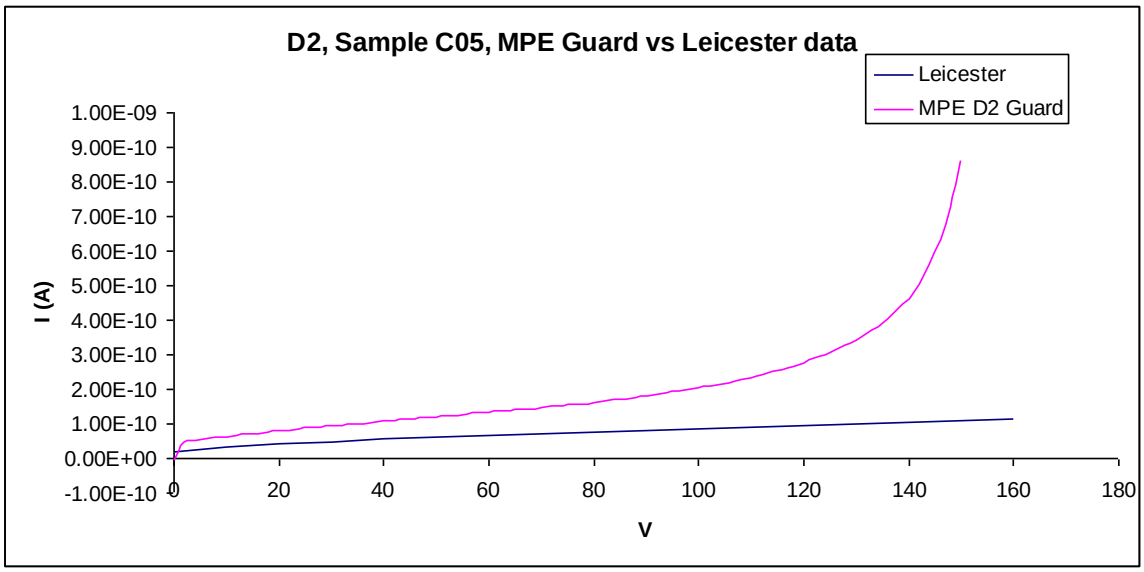

AP.1.2. POST-IRRADIATION I-V CURVES

AP.1.2.1. SAMPLE C03

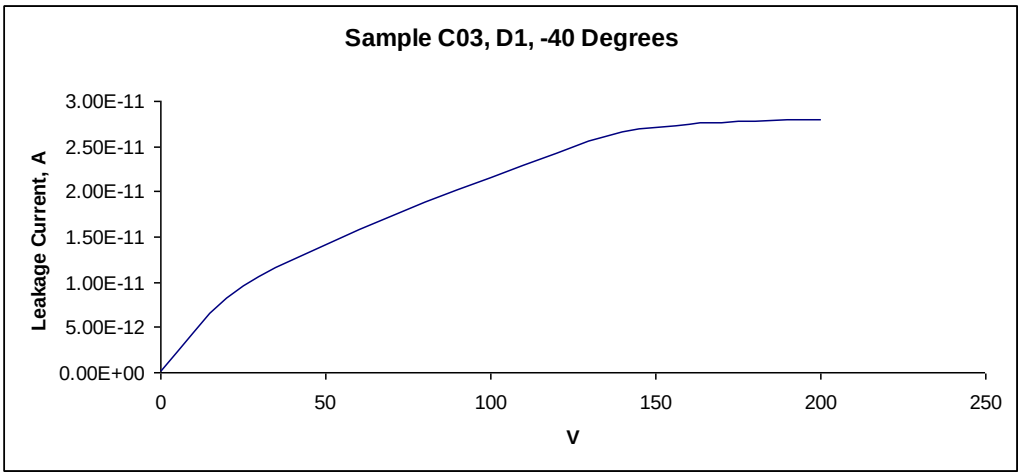

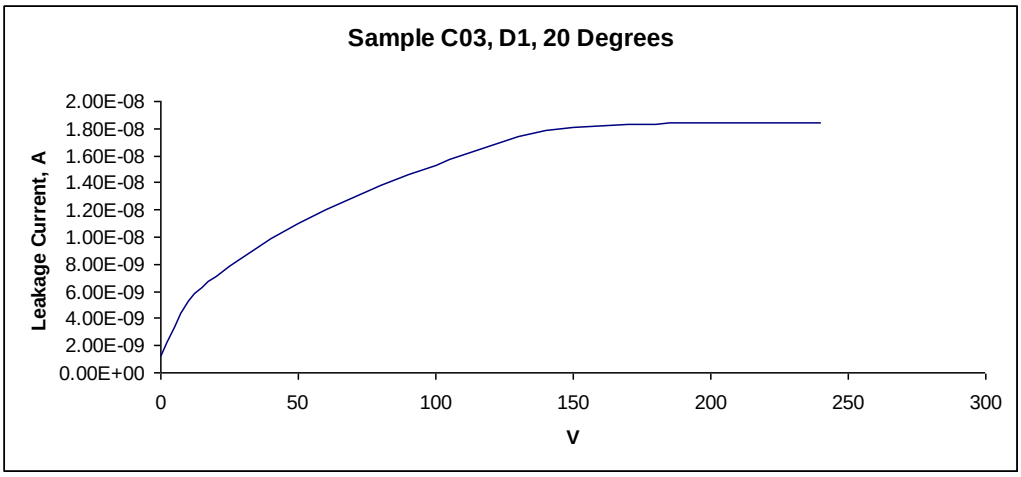

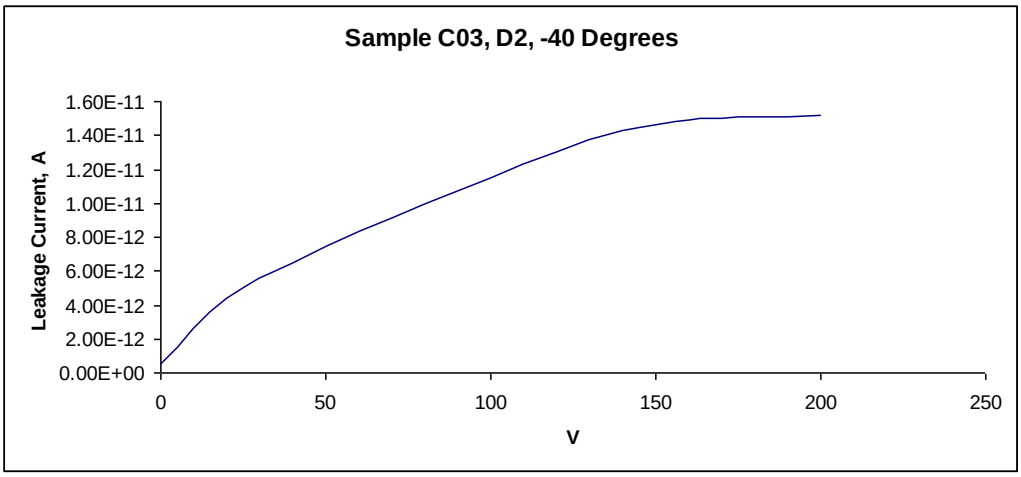

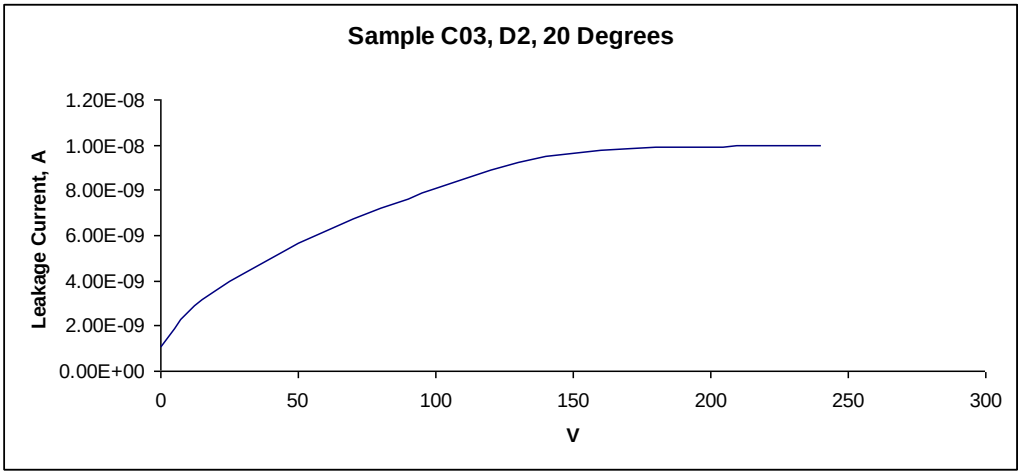
Sample C03, D2, 20 Degrees
Leakage Current, A
1.20E-08
1.00E-08
8.00E-09
6.00E-09
4.00E-09
2.00E-09
0.00E+00
0
50
100
150
200
250
300
V

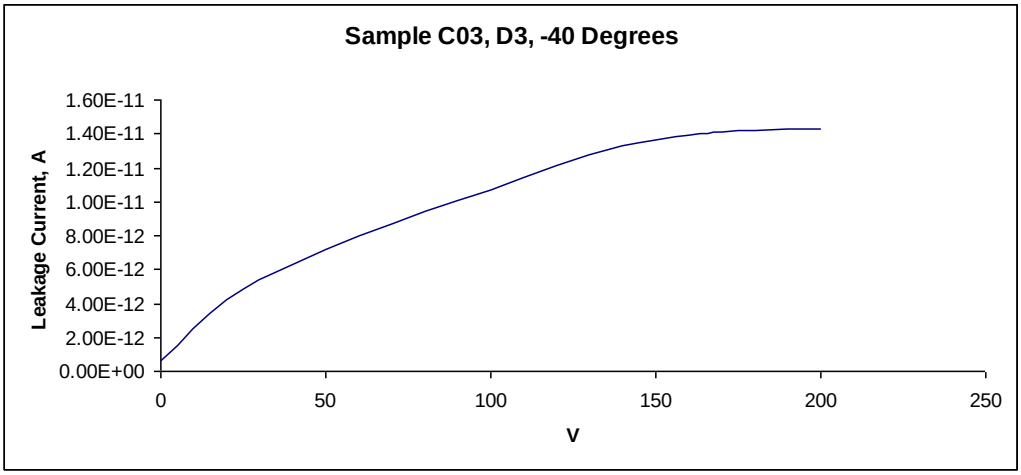
Sample C03, D3, -40 Degrees
Leakage Current, A
1.60E-11
1.40E-11
1.20E-11
1.00E-11
8.00E-12
6.00E-12
4.00E-12
2.00E-12
0.00E+00
0
50
100
150
200
250
V

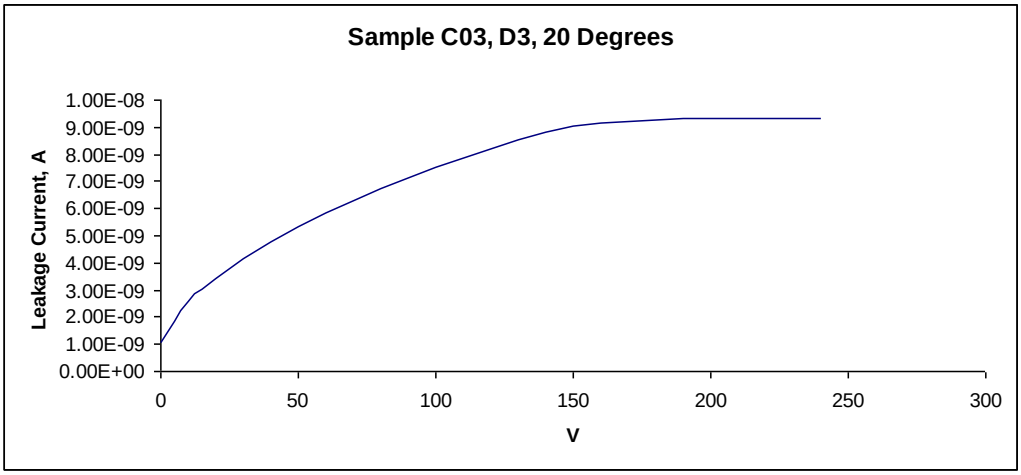
Sample C03, D3, 20 Degrees
Leakage Current, A
1.00E-08
9.00E-09
8.00E-09
7.00E-09
6.00E-09
5.00E-09
4.00E-09
3.00E-09
2.00E-09
1.00E-09
0.00E+00
0
50
100
150
200
250
300
V

AP.1.2.2. SAMPLE C07

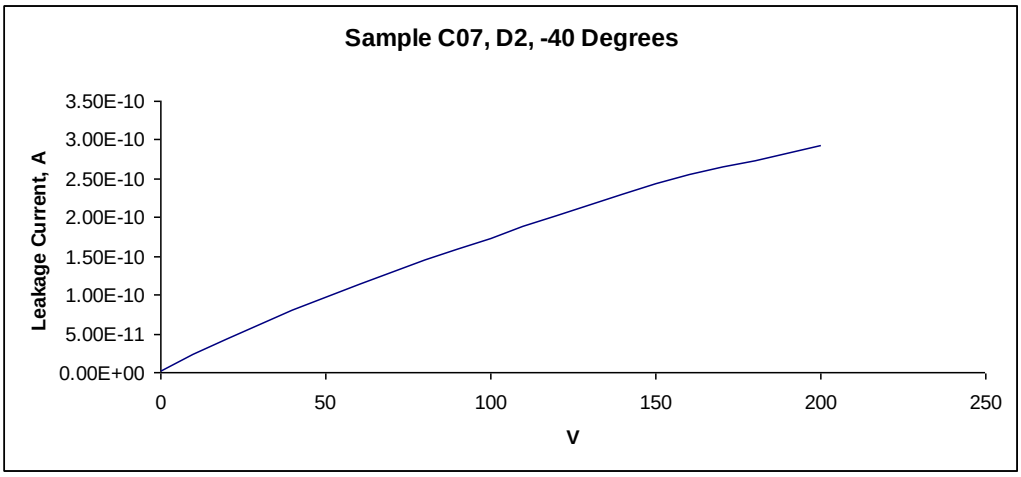

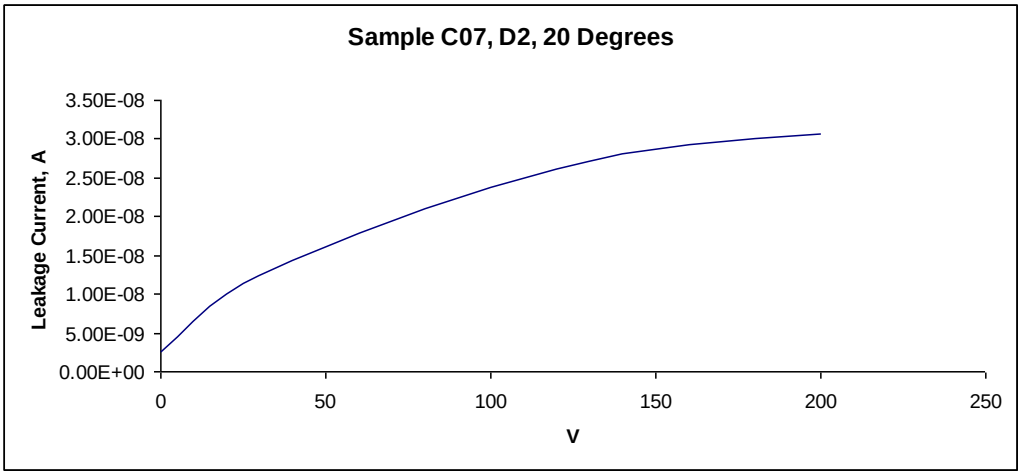

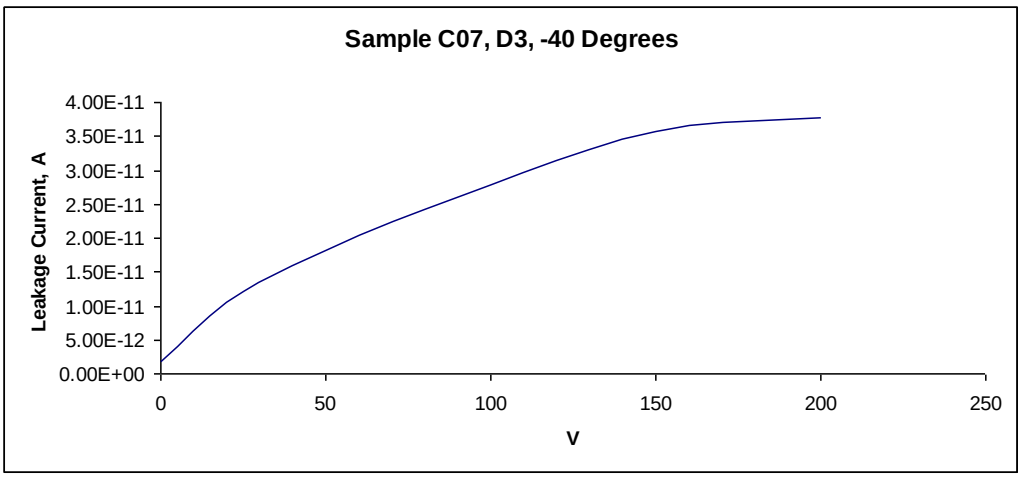

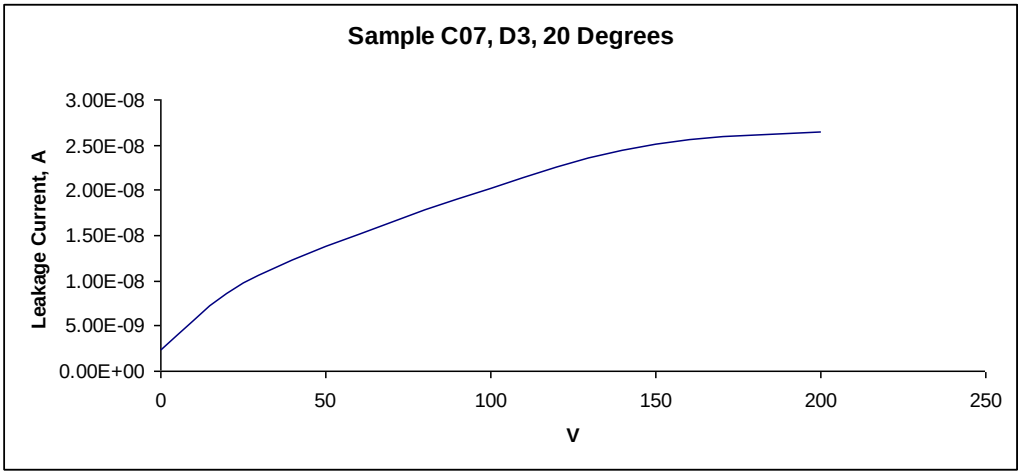
Sample C07, D3, 20 Degrees
Leakage Current, A
3.00E-08
2.50E-08
2.00E-08
1.50E-08
1.00E-08
5.00E-09
0.00E+00
0
50
100
150
200
250
V

AP.1.2.3. SAMPLE E05

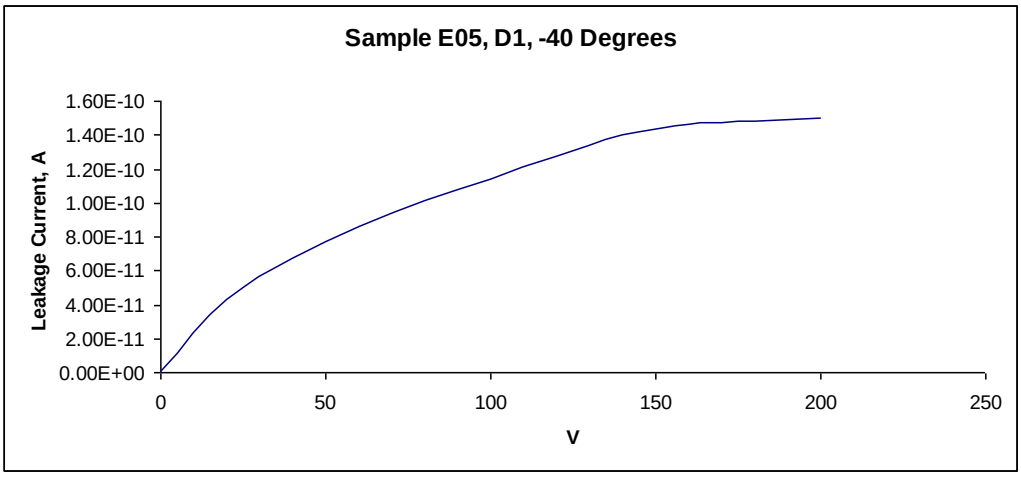

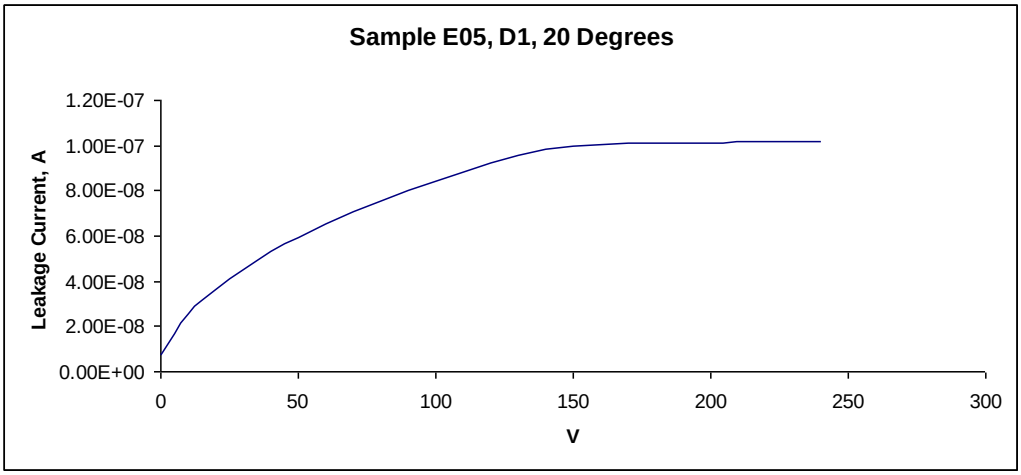

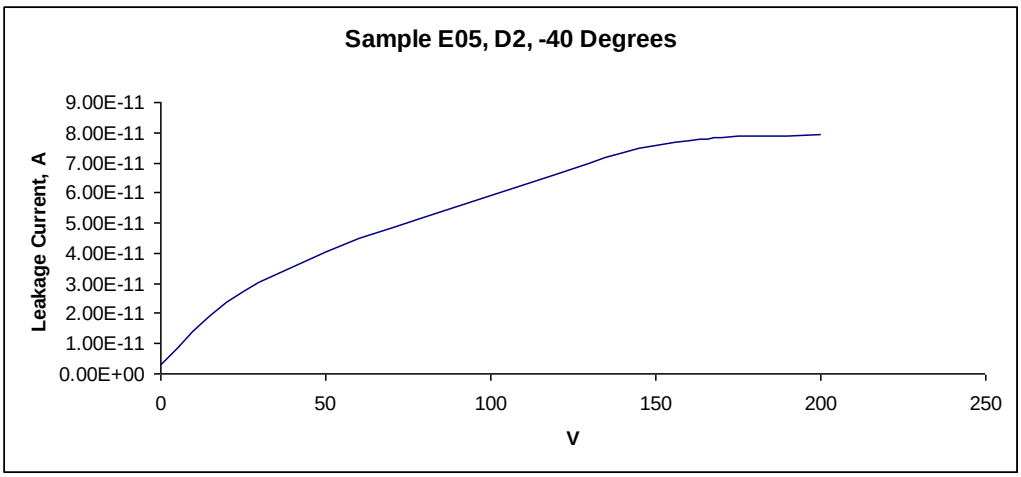

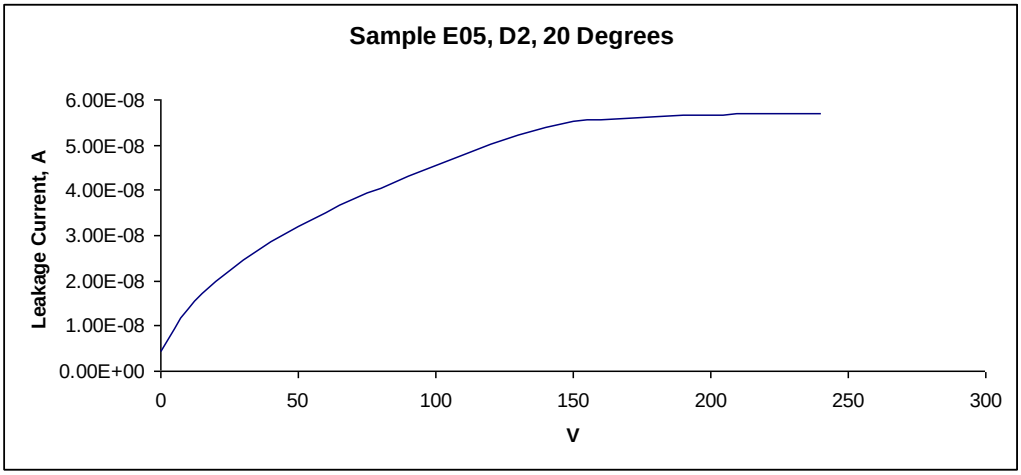
Sample E05, D2, 20 Degrees
Leakage Current, A
6.00E-08
5.00E-08
4.00E-08
3.00E-08
2.00E-08
1.00E-08
0.00E+00
0
50
100
150
200
250
300
V

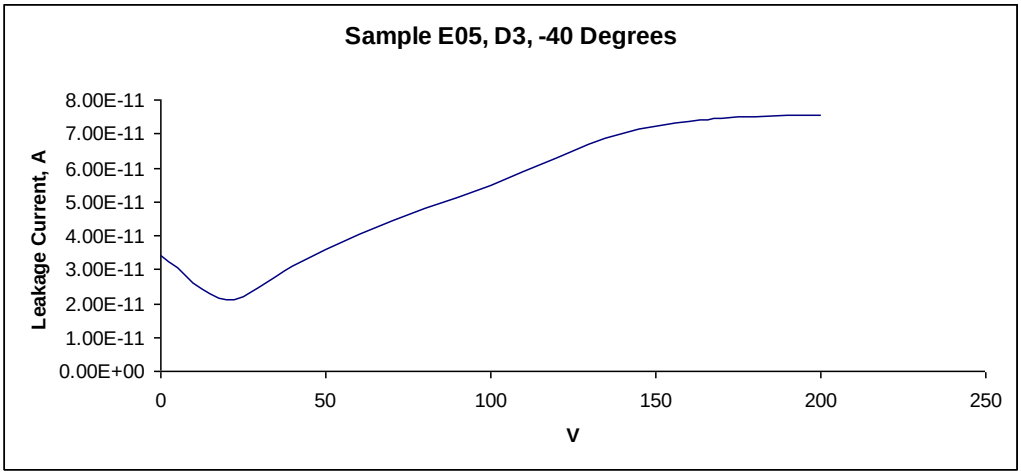
Sample E05, D3, -40 Degrees
Leakage Current, A
8.00E-11
7.00E-11
6.00E-11
5.00E-11
4.00E-11
3.00E-11
2.00E-11
1.00E-11
0.00E+00
0
50
100
150
200
250
V

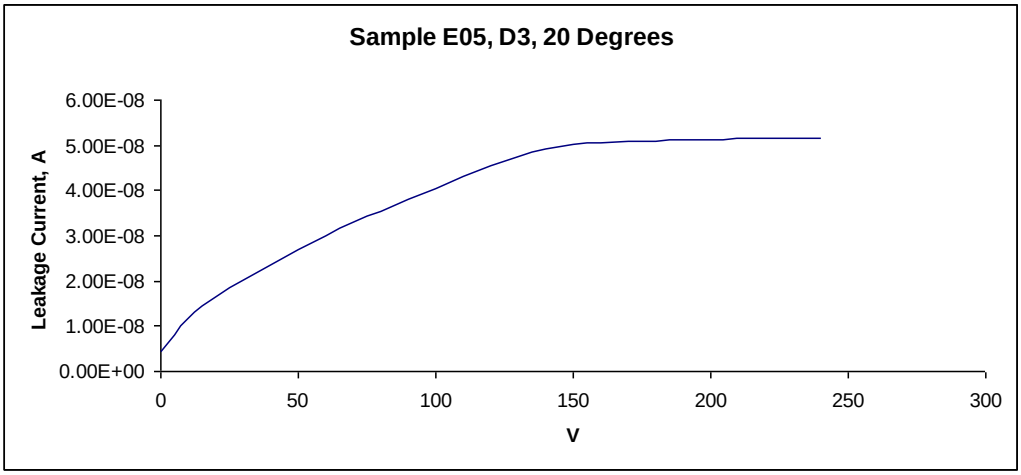
Sample E05, D3, 20 Degrees
Leakage Current, A
6.00E-08
5.00E-08
4.00E-08
3.00E-08
2.00E-08
1.00E-08
0.00E+00
0
50
100
150
200
250
300
V

AP.1.2.4. SAMPLE G03

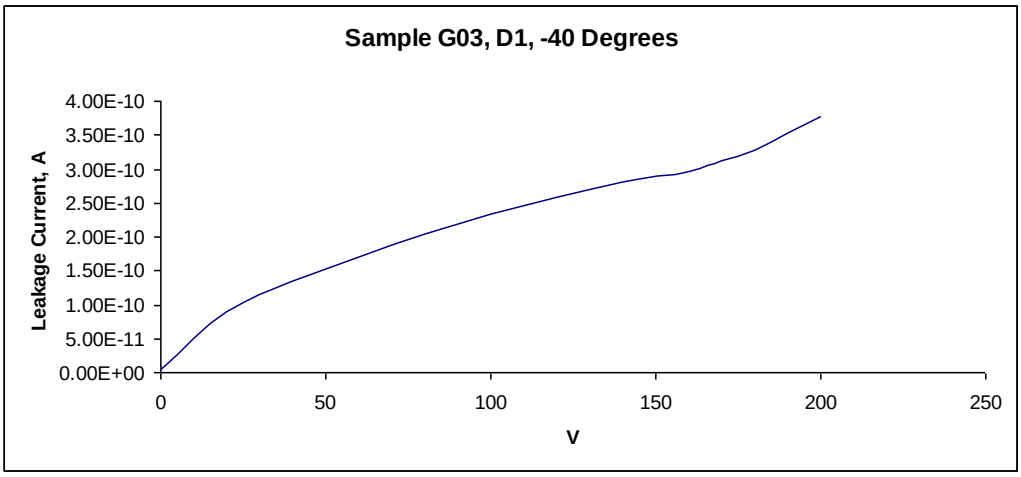

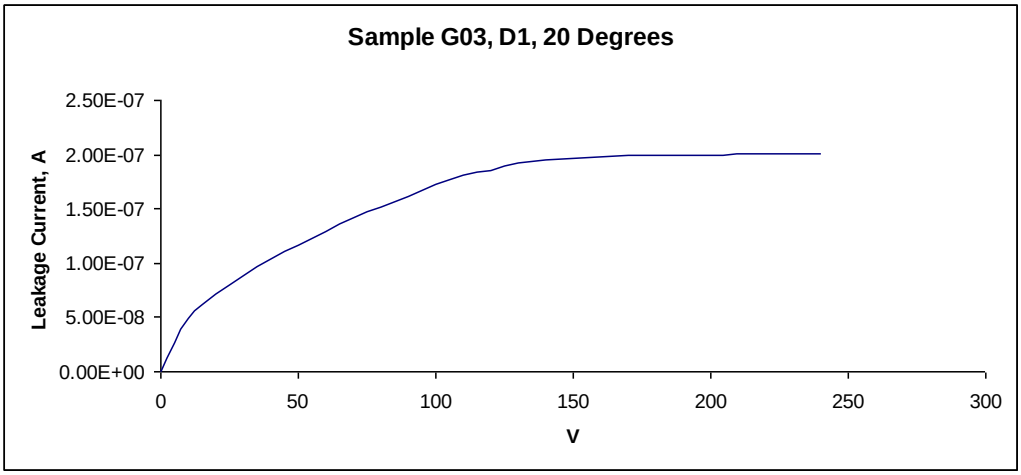

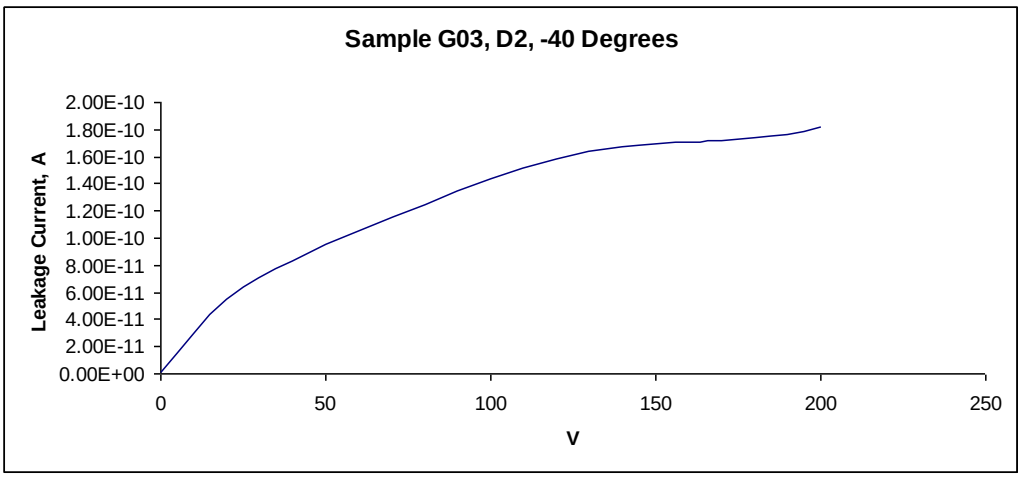

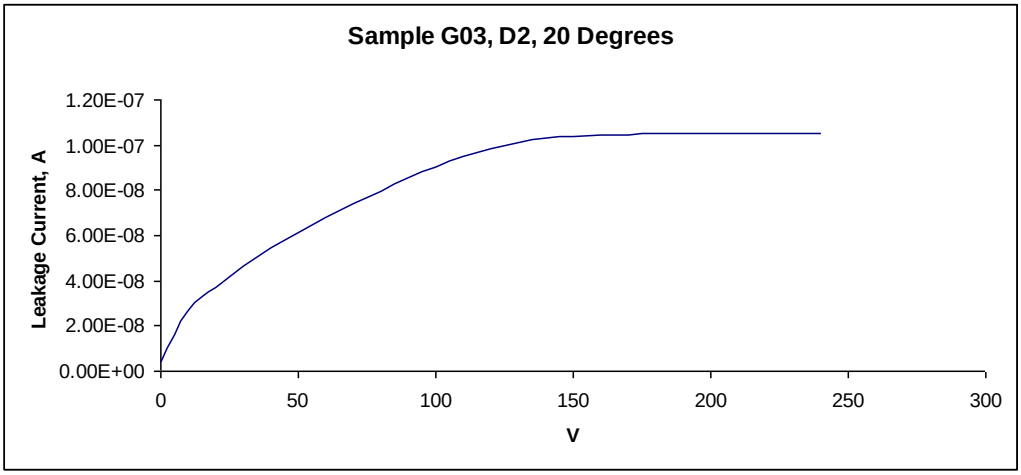
Sample G03, D2, 20 Degrees
Leakage Current, A
1.20E-07
1.00E-07
8.00E-08
6.00E-08
4.00E-08
2.00E-08
0.00E+00
0
50
100
150
200
250
300
V

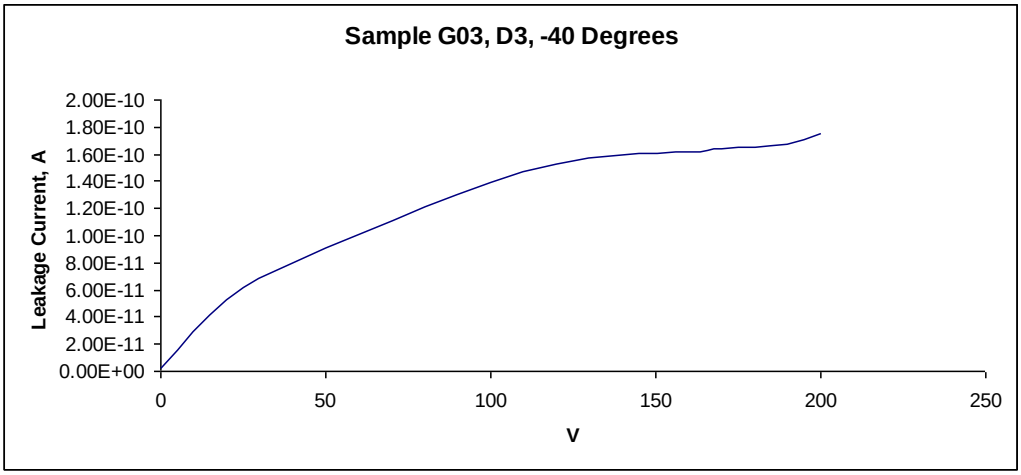
Sample G03, D3, -40 Degrees
Leakage Current, A
2.00E-10
1.80E-10
1.60E-10
1.40E-10
1.20E-10
1.00E-10
8.00E-11
6.00E-11
4.00E-11
2.00E-11
0.00E+00
0
50
100
150
200
250
V

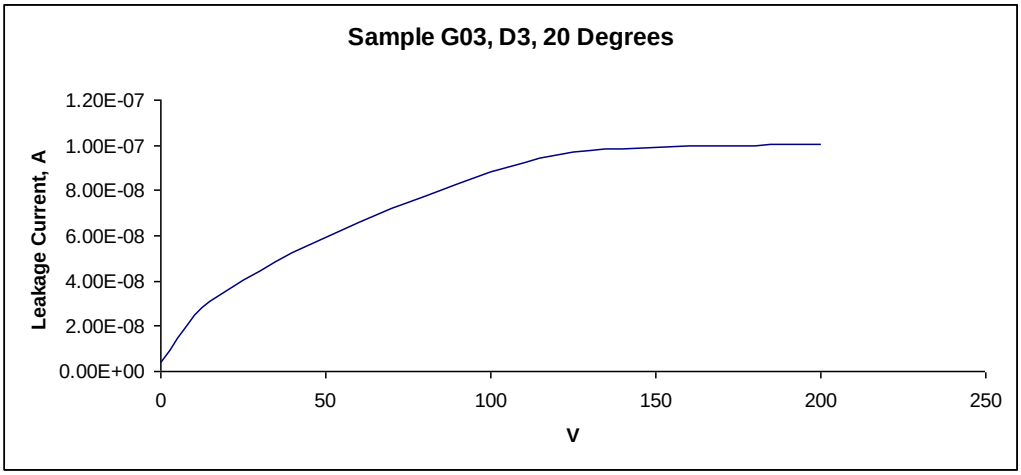
Sample G03, D3, 20 Degrees
Leakage Current, A
1.20E-07
1.00E-07
8.00E-08
6.00E-08
4.00E-08
2.00E-08
0.00E+00
0
50
100
150
200
250
V

APPENDIX 2

X-RAY SPECTRA TAKEN WITH THE CCD66 AT DIFFERENT NEGATIVE SUBSTRATE VOLTAGES

RESULTANT ISOLATED EVENT COPPER SPECTRA FOR VARYING V_{SS} LEVELS

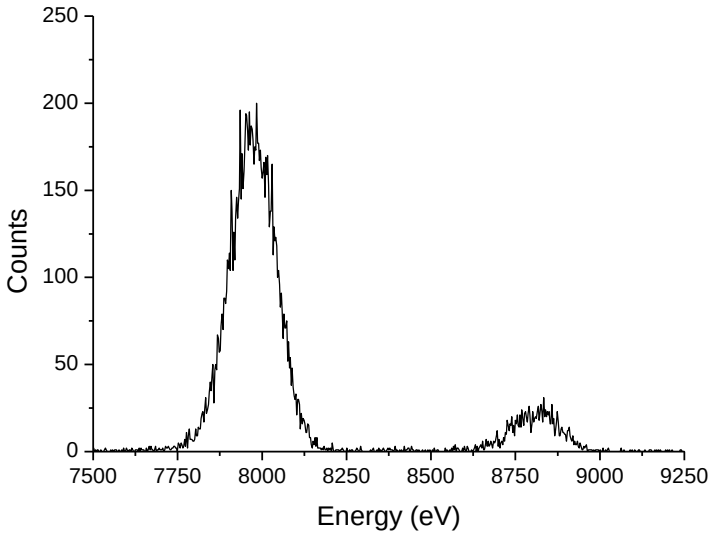

Figure AP2.1 **Copper spectra taken with the CCD66 with a V_{ss} of 0V. This shows only isolated, single pixel events**

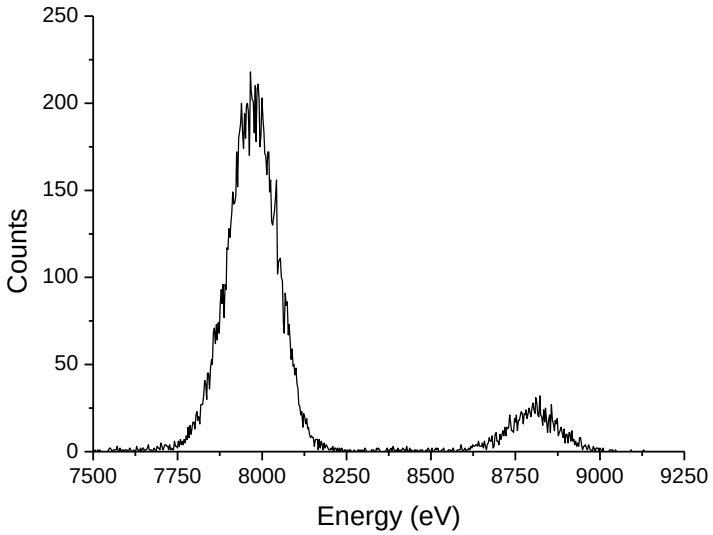

Figure AP2.2 The copper spectra taken with the CCD66 with a V_{ss} of 5V. This shows only isolated, single pixel events

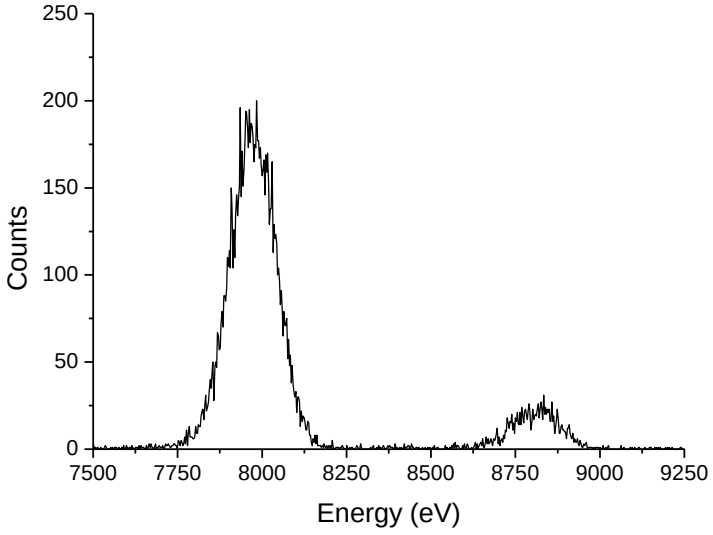

Figure AP2. 3 The copper spectra taken with the CCD66 with a V_{ss} of 10V. This shows only isolated, single pixel events

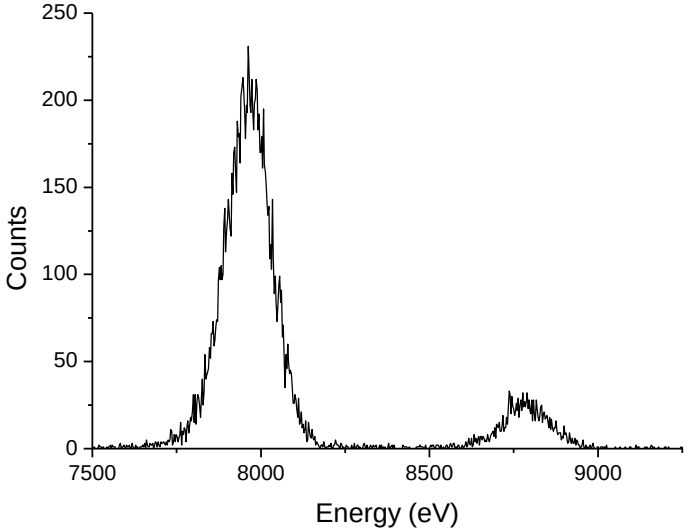

Figure AP2.4 The copper spectra taken with the CCD66 with a V_{ss} of 15V. This shows only isolated, single pixel events

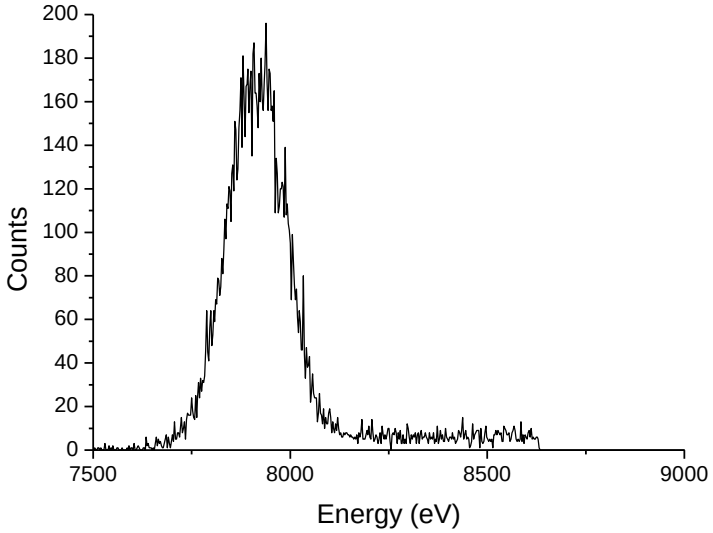

***Figure AP2.5* The copper spectra taken with the CCD66 with a V_{ss} of 20V. This shows only isolated, single pixel events**

RESULTANT SUMMED EVENT COPPER SPECTRA FOR VARYING V_{ss} LEVELS

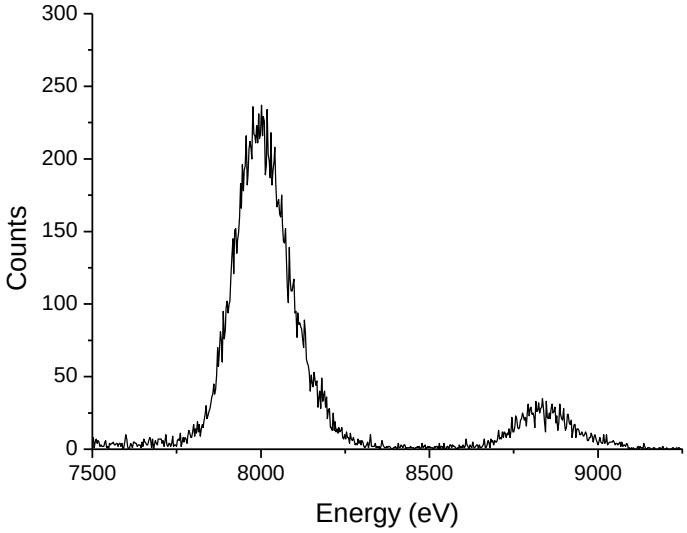

Figure AP2.6 **The copper spectra taken with the CCD66 with a V_{ss} of 0V. This shows summed pixel events**

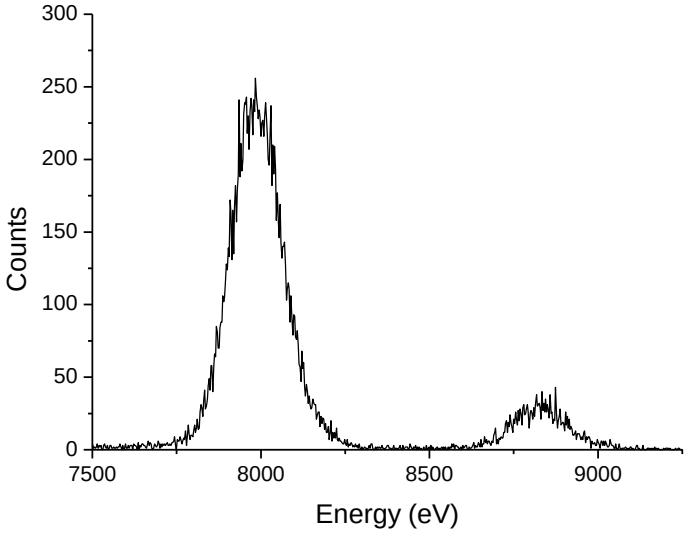

Figure AP2.7 **The copper spectra taken with the CCD66 with a V_{ss} of 5V. This shows summed pixel events**

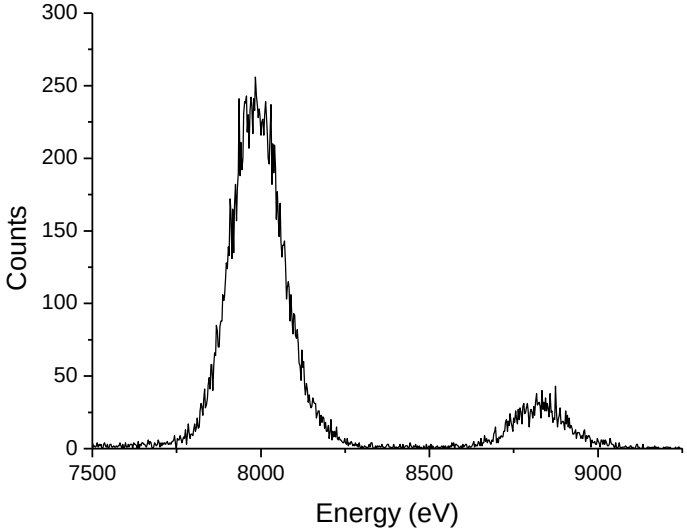

Figure AP2.8 **The copper spectra taken with the CCD66 with a V_{ss} of 10V. This shows summed pixel events**

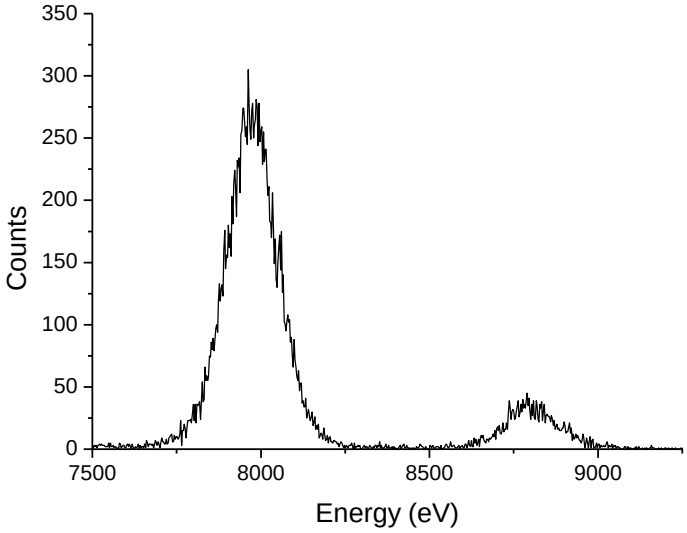

Figure AP2.9 **The copper spectra taken with the CCD66 with a V_{ss} of 15V. This shows summed pixel events**

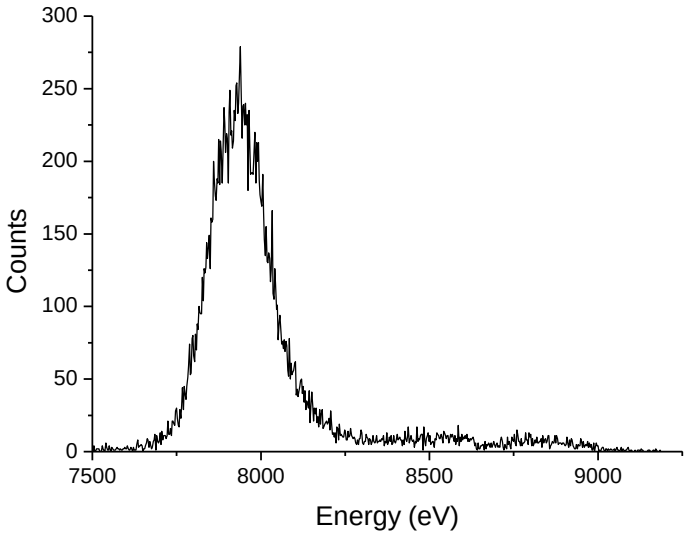

Figure AP2.10 **The copper spectra taken with the CCD66 with a V_{ss} of 20V. This shows summed pixel events**

REFERENCES

M. Ackermann et al, Performance Prediction and Measurement of Silicon Pore Optics, Proc. SPIE, Vol. 7437, 74371N (2009)

D. J. Adams, Cosmic X-ray Astronomy – Monographs on X-ray Astronomy, Adam Hilger Ltd (1980)

Adler et al, Results of the Apollo 15 and 16 X-ray Experiment, Proc. 4th Lunar Science Conference, Vol. 4, pp.2783 – 2791 (1973)

S. Agostinelli et al, Geant4 – a simulation toolkit, Nuclear Instruments and Methods A 506 250-303, (2003)

J. Allison et al, Geant4 Developments and Applications, IEEE Trans. Nucl. Sci. 53, Issue:1 Part 2 270-278 (2006)

H. Alva et al, The use of a reflective scanner to study radiochromic film response, Phys, Med. Biol. 47, 2925-2933 (2002)

R.M. Ambrosi et al, "The impact of low energy proton damage on the operational characteristics of EPIC-MOS CCDs", Nuclear Instruments and Methods in Physics Research B, 207, 175-185 (2003)

H. Aono et al, Application of Double-Sided Silicon Strip Detectors to Compton Cameras, Proc. SPIE, Col. 7021, 70211G (2008)

B. Aschenbach et al, Imaging Performance of the XMM-Newton X-ray Telescopes, SPIE 4010, paper 86 (2000)

D. Attie et al, Gas Pixel Detector for X-ray Observation, Nuclear Instruments and Methods in Physics Research A, 610 178-182 (2009)

R. S. Averback and T. Diaz de la Rubia, Displacement damage in irradiated metals and semiconductors, in Solid State Physics, edited by H. Ehrenfest and F. Spaepen, volume 51, pages 281--402, Academic Press, New York, (1998)

J. Ayers, Digital Integrated Circuits: Analysis and Design, CRC Press (2004)

N. Bannister and G. W. Fraser, The Science Case for Lobster ISS, http://www.iasfbo.inaf.it/~amati/Lobster/lob-lux-ms-008-7.pdf

M. Bavdaz et al, IXO System Studies and Technology Preparation, Proc. SPIE, Vol. 7437, 743702 (2009)

M. Bazioglou and J. Kalef-Ezra, Dosimetry with radiochromic films: a document scanner technique, neutron response, applications., Applied Radiation and Isotopes 55, 339-345 (2001)

M. Beijersbergen et al, Development of X-ray Pore Optics: Novel High-Resolution Silicon Millipore Optics for XUES and Ultralow Mass Glass Micropore Optics for Imaging and Timing, Proc. SPIE, Vol. 5539 (2004)

R. Bellazzini et al, Micropattern Gas Detector with Pixel Readout, NIM-A 513, 231-238 (2003)

R. Bellazzini and G. Spandre, Gas Pixel Detectors, ICFA Instrumentation Bulletin (2005)

R. Bellazzini et al, Gas Pixel Detectors for X-ray Polarimetry Applications, NIM-A Vol. 560, Issue 2, 425-434 (2006)

J. K. Black et al, The Imaging X-ray Detector for Lobster ISS, NIM-A 513, 123-126 (2003)

Daniela Bortoletto, Recent Resilts from RD50, NIM-A 569 69-72 (2006)

J. Bregman et al., The missing baryons in the Milky Way and Local Group, IXO Astro 2010 Decadal White Papers

C. Brown et al, Improving Quantum Efficiency and Spectral Resolution of a CCD through direct manipulation of the depletion region, Proc. SPIE, Vol 7011, 70113Z (2008)

Craig Brown, Aleksander Lyngvi, Nicola Rando, Alexander Short and Tone Peacock, "The Gamma Ray Lens Technology Reference Study", Acta Astronautica, Volume 62, Issue 12, June 2008, Pages 686-698 (2008)Mass Glass Milipore Optics for Imaging and Timing, Proc. SPIE, Vol. 5539 (2004)

BU, Birmingham University, Communication with David Parker, manager of the Birmingham University Cyclotron Facility (2007)

E. Burke, Energy Dependence of Proton Induced Displacement Damage in Silicon, IEEE Trans. Nucl. Sci. Vol. NS-33, No. 6, 1276-1281 (1986)

M. J. Butson et al, Radiochromic film for medical radiation dosimetry, Materials Science and Engineering R 41, 61-120 (2003)

J. D. Carpenter and G. W Fraser, Calculations of MIXS-C Performance, BepiColombo MIXS Technical Note, BC-MIX-TN-079 Issue 1 (2007)

J. D. Carpenter, Calculations of the MIXS-T Performance, BepiColombo MIXS Technical Note (2007)

J. Carpenter and C. Whitford, MIXS Data Rate Analysis (2007)

J. D. Carpenter et al, The MIXS Science Requirements Document, BepiColombo MIXS Technical Note (2006)

W. Cash, Astronomy: A Twisted Look at the Sky, Nature 411, 644-647 (2001)

H. N Chapman, K.A. Nugent and S. W. Wilkins, X-ray Focusing Using Square Channel Capillary Arrays, Rev. Sci. Instrum. 62, 6, 1991

P. A. Charles and F. D. Seward, Exploring the X-ray Universe, Cambridge University Press (1995)

V. Cotroneo et al, Hard X-ray Reflectivity Measurement of Broad-Band Multilayer Samples, Proc. SPIE, Vol 7437 (2009)

M. Dahlem (editor), XMM Users' Handbook Issue 1.1, ESA XMM Science Operations Centre (1999)

C. Dale and P. Marshall, Displacement Damage in Si Imagers for Space Applications, Proc. SPIE Vol. 1447, 70-86 (1991)

M. Ehle et al (Editors), XMM-Newton Handbook Issue 2.1, (2003)
http://xmm.esac.esa.int/external/xmm_user_support/documentation/uhb_2.1/index.html

ESA Advanced Studies and Payloads, X-ray and Gamma Ray Optics, ESA Webpage (2010)
http://astronomy2009.esa.int/science-e/www/object/index.cfm?fobjectid=38300&fbodylongid=1839

ESA, XMM-Newton Mission Status and Performance Indicator (2010)
http://xmm.esac.esa.int/external/xmm_news/mission_status/20040331/index.php

ESA EJSM Website, Model Payload Description, (2010)
http://sci.esa.int/science-e/www/object/index.cfm?fobjectid=42293

ESA, Mercury Environmental Specification Part II, BC-EST-TN-00113, iss. 4 (2006)

A. C. Fabian, Science with the International X-ray Observatory, AAS Meeting #213, Bulletin of the American Astronomical Society, Vol. 41, p.350 (2009)

E. Feigelson, X-ray Studies of Planetary Systems, Astro 2010 Decadal White Papers

F. Ferrari et al, New Results on Focusing of Gamma Rays with Laue Lenses, Proc. SPIE, Vol. 7437 (2009)

J. Feynman, G. Spitale, J. Wang and S. Gabriel, J. Interplanetary Proton Fluence Model: JPL 1991, Geophys. Res. 98, A8, 13281-13294 (1993)

G. W. Fraser et al, The Mercury Imaging X-ray Spectrometer (MIXS) on BepiColombo, Planetary and Space Science, Vol. 58, Issues 1-2, 79-95 (2010)

G.W. Fraser et al, LOBSTER-ISS: An Imaging X-ray All-Sky Monitor for the International Space Station, Proc. SPIE, Vol. 4497, 115 (2002)

G. Fraser, et al., The X-ray energy response of silicon Part A. Theory, Nucl. Instr. and Meth. A 350 368 (1994).

G W Fraser et al, X-ray Focusing using Square Pore Microchannel Plates: First Observation of the Cruciform Image Structure, NIM-A 324, 404-407 (1993)

C. Gabriel et al, The ESA XMM-Newton Science Operations Centre: Making Basic Space Science Available to the Whole Scientific World, Astrophysics and Space Science, Vol 305, Number 3 (2006)

G.P. Garmire et al, Advanced CCD Imaging Spectrometer (ACIS) Instrument on the Chandra X-ray Observatory, Proc. SPIE 4851, 28 (2003)

E. Gatti and Pavel Rehak, Semiconductor Drift Chamber – An Application of a Novel Charge Transport Scheme, 2nd Pisa Meeting on Advanced Detectors (1983)

N. Gehrels et al, "The Swift Gamma Ray Burst Mission", ApJ, 611, 1005 (2004)

M. Ghigo et al, Slumped Glass Option for Making the XEUS Mirrors: Preliminary Design and Ongoing Developments, Proc. SPIE, Vol. 7011, 70111F (2008)

R. Giacconi, H. Gursky, R.F. Paolini and B.B Rossi, Physical Review Letters, 9, 439-433 (1962)

M. Glaser et al, Radiation test facilities in the new PS East Hall at CERN, 5th European Conference on Radiation and its Effects on Components and Systems, RADECS 99 (1999)

O. Godet et al, Modelling the Spectral Response of the Swift-XRT Camera: Experience from In-Flight Calibration, A&A Vol. 494, Number 2 (2009)

O. Godet et al, The in-flight spectroscopic performance of the Swift XRT CCD camera during 2006-2007, Proc. SPIE 6686, 66860A, (2007)

Richard. E. Griffiths, "Requirements on ELTs from X-ray Astronomy", Proc. IAU Symposium No. 232, P209 (2005)

M. Guainazzi et al, EPIC Status of Calibration and Data Analysis, XMM-Newton Science Operations Centre Status Report (2009)

R. Gunther et al, Production of Silicon Pore Optics, Proc. SPIE, Vol. 6266, 626619 (2006)

R.N. Hall, Electron-Hole Recombination in Germanium, Phys. Rev. Vol. 87, Issue 2 (1952)

P. Hartmann and H.F. Morian, 100 Years Mirror Blanks from SCHOTT, SCHOTT anniversary commemorative paper (2003)
http://www.schott.com/rd/german/download/zeak08_fb0412.pdf

J. Hiraga et al, Direct Measurement of Sub-Pixel Structure of the EPIC MOS CCD on-board XMM/Newton Satellite, NIM-A Vol 465, Issues 2-3, 384-393 (2001)

A. Holland et al, CCD Detectors for Astronomy, X-ray Astronomy and Space Instrumentation Biennial Report for the period May 1999 to April 2001 (2001)
http://www.star.le.ac.uk/report/report.html

A. Holland et al, MOS CCDs for the Extended Wide-Field Imager of XEUS, Proc SPIE, Vol 4851, 790 (2003).

A. Holland et al, The OP-XGS Instrument ESA Mid Term Review (2010)

A. Holmes-Seidle, L. Adams, Handbook of Radiation Effects, Oxford University Press (1993)

ISPCORP Gafchromic Film Information (2007)
http://www.ispcorp.com/products/dosimetry/

IXO CDF Report, IXO ESA CDF Study, ESA, (2009)

IXO Mission Requirements Document, IXO Mission Requirements Document, ESA (2009)

IXO Payload Definition Document, IXO Payload Definition Document, IXO Assessment Study Statement of Work, ESA, (2009)

J. R. Janesick, Scientific Charged Couple Devices, SPIE Press (2001)

F. Jansen et al, XMM-Newton Observatory I: The Spacecraft and Operations, A&A 365, L1-L6 (2001)

F. Jansen et al, XMM-Newton Observatory, Astronomy and Astrophysics, Vol. 365, Number 1 (2001)

JAXA, X-ray Telescopes, Suzaku mirrors, JAXA website (2010)
http://www.astro.isas.jaxa.jp/suzaku/doc/suzaku_td/node9.html

D. Jerius et al, Orbital Measurement and Verification of the Chandra Observatory's PSF, SPIE Vol. 4012, p.17 (2000)

A. Z. Jones et al, Comparison of Indiana University cyclotron facility Faraday Cup dosimetry with radiochromic films, a calorimeter, and a calibrated ion chamber, IEEE Trans. Nucl. Sci. 46, 1762 (1999)

J.S. Kaastra, "Studying the Formation and Distribution of the Elements Using X-ray Spectroscopy", Proc. 39th ESLAB Symposium (SP-588), P91(2005)

A. Keay, A. D. Holland, D. Burt and P. Pool, Development of MOS CCDs for the next generation of X-ray observatories, NIM-A, Vol. 436, Issue 1-2, p.16-23 (1999)

P. Khare and A. Swarup, Engineering Physics: Fundamentals and Modern Applications, Jones and Bartlett Publishers (2007)

P. Kirkpatrick and A. V. Baez, Formation of Optical Images by X-rays, JOSA, Vol. 38, Issue 9, 766-773 (1948)

J. Kirz et al, 'X-ray Data Booklet', Centre for X-ray Optics, Lawrence Berkeley Laboratory, (1986)

P. Lechner et al, Novel High-Resolution Silicon Drift Detectors, X-ray Spectrometery, Vol. 33 Issue 4, 256-261 (2004)

P. Lechner et al, Silicon Drift Detectors for High Resolution, High Count Rate X-ray Spectroscopy at Room Temperature, International Centre for Diffraction Data, Advances in X-ray Analysis, Vol 47 (2004)

J Lee et al, Solid State Astrophysics – Probing Interstellar Dust and Gas Properties with X-rays, IXO Astro 2010 Decadal White Papers

M. Lester, The Science Case of the MagEX Telescope, Presentation (2007)
http://www2.le.ac.uk/departments/physics/research/src/Missions/magex/magex-publications

M. Lester et al, The Wide Field Auroral Imager (WFAI) for the KuaFu Mission, 36th COSPAR Scientific Assembly, #516 (2006)

G. Lindstrom et al, Developments for Radiation Hard Silicon Detectors by Defect Engineering – Results by the CERN RD48 (ROSE) Collaboration, NIM-A 465, Issue 1, 60-69 (2001)

M. S. Longair, High Energy Astrophysics Second Edition, Volume 1, Particles, Photons and Their Detection, Cambridge University Press (1992)

B. G. Lowe and R.A. Sareen, A Measurement of the Elecotron-Hole Pair Creation Energy and the Fano Factor in Silicon for 5.9 keV X-rays and their Temperature Dependance in the range 80-270 K, NIM-A, Vol. 576, Issue 2-3 (2007)

C. Macculi et al, TES Microcalorimeter for IXO: from Focal Plane to Anticoincidence Detector, Proc. of Science, The Extreme Sky: Sampling the Universe above 10keV (2009)

J.D. Mangus and J.H Underwood, Optical Design of a Glancing Incidence X-ray Telescope, Applied Optics, Vol. 8, Issue 1, pp. 95-102 (1969)

L. Marinangeli et al, An European XRD/XRF Instrument for the ExoMars Mission, Proc. 38th Lunar and Planetary Science Conference, No. 1338, p1322 (2007)

A. P. Martin, A. N. Brunton, G.W. Fraser and A. F. Abbey, Imaging X-ray Fluoresence Spectroscopy: Laboratory Measurements, NIM-A, 460, 316-325 (2001)

D. Martin, head of payload development for ESA Future Programmes, personal communication relating to the ESA mid-term review of the XMS instrument (2010)

A. Martindale et al, Simple filters enable X-ray Polarization Measurements, SPIE Newsroom. DOI: 10.1117/2.1200904.1585 (2009)

A. Martindale, Novel X-ray Instrumentation for Astronomy, Ph.D. Dissertation, Leicester, UK, (2008)

A. Martindale, J. Pearson and M. Evans, The Performance of a Simplified Inner-Ring Tandem for MIXS-T, BepiColombo MIXS Technical Note, BC-MIX-TN-052 (2008)

A. Martindale, Progress Presentation of the MIXS-T Tandem Tests, University of Leicester (2008)

A. Martindale and H. Yates, Profiling the Microchannel Plate Optics for BepiColombo MIXS, BepiColombo MIXS Technical Note, BC-MIX-TN-014 (2007)

Kieran J. McCarthy et al, Modelling the X-ray Response of Charge Coupled Devices, Nuclear Instruments and Methods A, 362 538-546 (1995)

H. Mercado-Uribe et al, Experimental study of the response of radiochromic films to proton radiation of low enery, NIM-B, Vol 267, Issue 10, 1849-1851, (2009)

K. Mitsuda et al, The X-ray Observatory Suzaku, PASJ, 59, 1 (2007)

M.Moll, Ph.D thesis, University of Hamburg, DESY-THESIS-1999-040 (1999)

K. Mukergee et al, Spectroscopic Performance of the Swift X-ray Telescope for Gamma-ray Burst Afterglow Studies, Proc. SPIE 5165, 215 (2004)

S. Murray et al, In-flight Performance of the Chandra High-Resolution Camera, Proc. SPIE Vol. 4012, 68 (2000)

Nandra et al, Growth of Supermassive Black Holes Across Cosmic Time, IXO Astro 2010 Decadal White Papers

NASA, IXO Flight Mirror Assembly, NASA Website, (2010)
http://ixo.gsfc.nasa.gov/technology/fma.html#Slumped-glass optics

NASA IXO: International X-ray Observatory, Science Objectives Website, 2010
http://ixo.gsfc.nasa.gov/science/goals.html

Azam Niroomand-Rad et al, Radiochromic film dosimetry: Recommendations of AAPM Radiation Therapy Committee Task Group 55, Med. Phys. 25, 11 (1998)

J. P. Nussey, Terrestrial and Space Based Applications of Microchannel Plate Optics, PhD Thesis, University of Leicester (2005)

J.P. Osborne et al, The in-flight spectroscopic performance of the Swift XRT CCD camera, Proc. SPIE Vol. 5898, 352, (2005)

A. Owens et al, The Effect of X-ray Fine Structure in Soft X=ray Astronomical Telescopes, The Astrophysical Journal, 476:924-931 (1997)

F. Paerels et al., The Behaviour of Matter Under Extreme Conditions, IXO Astro 2010 Decadal White Papers

A. Parmar, The International X-ray Observatory, Proc. High Resolution Spectroscopy: Towards IXO, Workshop, MSSL, UK (2009)

A. N. Parmar et al, "Science with XEUS: the X-ray Evolving Universe Spectroscopy mission", Proc. SPIE 5488, 388-393 (2005)

J. Pearson, personal communication, demonstration of double cruciform structure from an out of focus MCP optic using Monte Carlo ray tracing (2005)

J. Pearson, MIXS-T Performance Modelling, BepiColombo MIXS Technical Note (2006)

J. Pearson, Summary of MIXS-T Tandem Tests, BepiColombo MIXS Technical Note (2007)

G.J. Price et al, X-ray Focusing with Wolter Microchannel Plate Optics, NIM-A, Vol. 490, Issues 1-2, 276-289 (2002)

Gareth James Price, Microchannel plates in astronomy, Ph.D. Dissertation, Leicester, UK. (2001)

W. C. Priedhorsky, A. G. Peele and A. K. Nugent, Monthly Notices of the Royal Astronomical Society, 279, 733-750 (1996)

W. S. Rasband, ImageJ, U. S. National Institutes of Health, Bethesda, Maryland, USA, http://rsb.info.nih.gov/ij/, 1997-2009

P. B. Reid, Mirror Design for the International X-ray Observatory, American Astronomical Society Meeting 213, 457.04; Bulleting of the AAS, Vol. 41, p. 358 (2009)

A. Read, XMM-Newton EPIC Background Working Group (2007)
http://xmm2.esac.esa.int/external/xmm_sw_cal/background/index.shtml

A. Read and A. Abbey, Personal Communication and internal technical note, XMM-Newton In-orbit Degradation (2007)

G, Ristic, Thermal and UV annealing of irradiated pMOS dosimetric transistors, J. Phys. D: Appl. Phys. 42 135101 (2009)

ROSE, RD50 Technical Note 2003/ 03 -- Version 5 / 15.10.04 (2004)

ROSE, 3rd RD48 Status Report, The ROSE Collaboration, CERN/LHCC 2000-009, (1999)

J. H. M. M. Schmitt et al, A soft X-ray Image of the Moon, Nature 349, 583 – 587 (1991)

G. Segneri et al, Measurement of the Current Related Damage Rate at -50°C and Consequences on Macropixel Detector Operation in Space Experiments, IEEE Transactions on Nuclear Science Vol.56, Issue 6, 3732-3742, (2009)

S. Sembay, personal communication, University of Leicester, (2009)

S. Sembay, A. Read and J. Carter, MagEX: A Proposal for a Lunar-based X-ray Telescope, Presentation (2007)
http://www2.le.ac.uk/departments/physics/research/src/Missions/magex/magex-publications

Shanks et al, The Origin of the Cosmic X-Ray Background, Nature 353, 315-320 (1991)

W. Shockley and W.T. Read, Statistics of the Recombination of Holes and Electrons, Phys. Rev. Vol. 87, Issue 5 (1952)

A.D. Short, R.M. Ambrosi and M.J.L. Turner, “Spectral re-distribution and surface loss effects in Swift XRT (XMM-Newton EPIC) MOS CCDs”, Nuclear Instruments and Methods in Physics Research A, 484, 211-244 (2002)

A. Short, A. Keay and M.J.L. Turner, Performance of the XMM EPIC MOS CCD Detectors, Proc. SPIE, Vol. 3445, 13 (1998)

D.R.G. Schleicher, M. Spaans and R.S. Klessen, Probing high-redshift quasars with ALMA, A&A 513, A7 (2010)

D. Smith, E-mail and Personal Communication (2008)

S. Smith, 'The Scientist and Engineer's Guide to Digital Signal Processing', California Technical Publishing (1999)

SPENVIS, ESA Space Environment Models, (2010)
http://www.spenvis.oma.be

E. Spiller, Soft X-ray Optics, SPIE Textbook (1999)

A. Stankov, SIXS Payload Overview, BepiColombo Information Sheets, ESA RSSD (2005)

D. K. Strickland et al, Starburst Galaxies: Outflows of Metals and Energy into the IGM, IXO Astro 2010 Decadal White Papers (2010)

L. Struder et al, The European Photon Imaging Camera on XMM-Newton: The pn-CCD camera, A&A Volume 365, Number 1 First Results from XMM-Newton, (2001)

H. Su, Ph.D Thesis, University of Leicester, In Preparation (2010)

H. Su et al, Preliminary Laboratory XRD/XRF Instrument Tests and Evaluation, ESA Conference, European Mars Science and Exploration Conference: Mars Express & ExoMars (2007)

S.M. Sze, [Semiconductor Devices: Physics and Technology], John Wiley and Sons, (1985)Thompson et al, CXRO, X-ray data booklet (2001)

J. Treis et al, The Wide Field Imager for the International X-ray Observatory, Proc. SPIE, Vol. 7435, 743506 (2009)

J. Treis et al, DEPFET based X-ray Detectors for the MIXS Focal Plane on BepiColombo, Proc. SPIE, Vol. 7021, 70210Z (2008)

J. Treis, DEPFET based focal plane instrumentation for X-ray Imaging Spectroscopy in Space, IEEE Nuclear Science Symposium Conference Record, Volume 3, 2226-2235 (2007)

Personal communication with Johannes Treis, MPI-HLL Munich, 14/05/2007 (2007)

J. Treis, MPI-HLL Presentation at Leicester University, MIXS Progress Meeting, 13/09/2006 (2006)

J. Treis et.al, DEPMOSFET Active Pixel Sensor Prototypes for the XEUS Wide Field Imager, IEEE Transactions on Nuclear Science, Vol. 52, no. 4, (2005)

M. K. Tripp et al, Multilayer coating method for X-ray Reflectivity Enchancement of Polysilicon Micro-Mirrors at 1.54Å Wavelength, Micromachining Technology for Micro-Optics and Nana-Optics III, Proc. SPIE Vol 5720 (2005)

H. Tsunemi, J. Hiraga and E. Miyata, Application of a Finite Size of the Charge Cloug Shape Generated by an X-ray Photon inside the CCD, Nuclear Instruments and Methods A, 477 155-160 (2002)

H. Tsunemi et al, The Astrophysical Journal, Improvement of the Spatial Resolution of the ACIS Using Split-Pixel Events, 554: 496-504, (2001)

S. Tsuneta et al, The Soft X-ray Telescope for the SOLAR-A mission, Solar Physics, Springer Netherlands, Vol 136, Number 1 (1991)

M.J.L. Turner et al, The European Photon Imaging Camera on XMM-Newton: The MOS Cameras, A&A Volume 365, Number 1 First Results from XMM-Newton (2001)

A. Vasilescu, 3rd ROSE Workshop, DESY-Proceedings-1998-02, (1998)

P. Verhoeve et al, STJ Narrow Field Imaging Spectrometer for XEUS, Proc. SPIE 5488 (2004)

J. I. Vette, The AE-8 Trapped Electron Model Environment, NSSDC/WDC-A-R&S Report 91-24, NASA-GSFC (1991)

M. C. Weisskopf, The Chandra X-ray Observatory: An Overview, Advances in Space Research, Volume 32, Issue 10 (2004)

Chris Whitford, ESA communication with the BepiColombo MIXS System Engineer (2006b)

S. W. Wilkins et al, 1989, On the concentration, focusing, and collimation of x-rays and neutrons using microchannel plates and configurations of holes, Rev. Sci. Instrum. 60, 1026 (1989)

R. Willingale, Q Data Analysis Tool, (2010)
http://www.star.le.ac.uk/~rw/q_v6/index.html

R. Willingale, Sequential Ray Tracing Model Manual (2004)
http://www.star.le.ac.uk/~rw/q_v6/srtdoc.html

R. Willingale, G.W. Fraser, A.N. Brunton and A.P. Martin, Hard X-ray imaging with microchannel plate optics, Exp. Astron. 8pp. 281–296 (1998)

N. White et al, The International X-ray Observatory,

K Yamaoka et al, Design and In-Orbit Performance of the Suzaku Wide-Band All--Sky Monitor, PASJ 61, S35-S53 (2009)

R. Yang et al, Loss Characteristics of Silicon Substrate with Different Resistivities, Microwave and Optical Technology Letters, Vol. 48, No. 9 (2006)

C. Zhang et al, Development of DEPFET Macropixel Detectors, NIM-A, 568 207-216 (2006)

W. Zhang et al, Development of X-ray Optics for the International X-ray Observatory (IXO), AAS Meeting 213, 457.03, Bulletin of the American Astronomical Society Vol 41, p.358 (2009)

P. Zhao et al, Chandra X-ray Observatory Mirror Effective Area, Proc. SPIE Vol 5165 (2004)

J.F. Ziegler, J.P. Biersack and M.D. Ziegler, SRIM, The Stopping and Range of Ions in Matter (2010) http://www.srim.org/